

**A DESIGN PROCEDURE
AND PREDICTIVE MODELS FOR
SOLUTION CRYSTALLISATION PROCESSES**

Development and Application

**A DESIGN PROCEDURE
AND PREDICTIVE MODELS FOR
SOLUTION CRYSTALLISATION PROCESSES**

Development and Application

PROEFSCHRIFT

ter verkrijging van de graad van doctor
aan de Technische Universiteit Delft
op gezag van de Rector Magnificus prof. dr. ir. J.T. Fokkema,
voorzitter van het College voor Promoties,
in het openbaar te verdedigen
op maandag 24 maart 2003 om 13.30 uur

door

Sean Keith BERMINGHAM

scheikundig ingenieur
geboren te Terneuzen

Dit proefschrift is goedgekeurd door de promotor:
Prof. ir. J. Grievink

Samenstelling promotiecommissie:

Rector Magnificus, voorzitter
Prof. ir. J. Grievink, Technische Universiteit Delft, promotor
Dr. ir. H.J.M. Kramer, Technische Universiteit Delft, toegevoegd promotor
Prof. dr. ir. G.M. van Rosmalen, Technische Universiteit Delft
Prof. M.F. Doherty PhD, University of California, Santa Barbara
Prof. Dr.-Ing. W. Marquardt, Rheinisch-Westfälische Technische Hochschule
Aachen
Dr. ir. P.J.T. Verheijen, Technische Universiteit Delft
Dr. ir. J.-W. Verwijs, Dow Benelux N.V.

Reservelid:

Prof. dr. ir. P.J. Jansens, Technische Universiteit Delft

Published and distributed by: DUP Science

DUP Science is an imprint of
Delft University Press
P.O. Box 98
2600 MG Delft
The Netherlands
Telephone: +31 15 27 85 678
Telefax: + 31 15 27 85 706
E-mail: Info@Library.TUdelft.NL

ISBN 90-407-2395-8

Keywords: Crystallisation, Design, Modelling

Copyright © 2003 by Sean Bermingham

All rights reserved. No part of the material protected by this copyright notice may be reproduced or utilized in any form or by any means, electronic or mechanical, including photocopying, recording or by any information storage and retrieval system, without written permission from the publisher: Delft University Press.

Printed in The Netherlands

TER HERINNERING AAN MAO (1996-2002)

SUMMARY

This thesis concerns the development of a systematic design procedure and predictive models for solution crystallisation processes, with a focus on both product and process performance.

The introductory chapter starts with a discussion of the application, advantages and problems of crystallisation in the chemical process industry. Problems encountered in industrial crystallisation are related to both product quality and process performance. Although some of these problems can be solved using process control, most problems are intrinsically related to decisions taken during the design stage. However, systematic procedures and tools for the reliable design of crystallisation processes are practically non-existent. The research objective of this PhD work is hence the development of a prototype design kit, consisting of a systematic procedure and tools, for crystallisation processes. The scope of this research is defined in terms of the nature of the chemical system (relatively well soluble substances), crystallisation method (indirect-cooling, flash-cooling and evaporation), operation mode (batch, semi-batch and continuous), flowsheet configuration (single and multiple stage) and crystalliser type (stirred tank, draft tube, draft tube baffle, and forced circulation).

The relation between product quality, crystallisation mechanisms, process conditions, crystalliser geometry and operating conditions is discussed in Chapter 2. As regards product quality, a distinction is made between product performance and product composition. Customer and solid handling requirements are typically defined in terms of the prior, while crystallisation models predict product quality in terms of the latter. Next, an overview is presented of the crystallisation mechanisms that determine the product composition of crystals. Finally, requirements are outlined for a design procedure and phenomenological models that are deemed essential in order to reliably design crystallisation processes that meet their product and process performance criteria. Consequences of limited domain knowledge, limited computational power and, probably most importantly, the limitations of the human process designer are all considered.

Systematic design procedures are aimed at improving the quality of both the design and the design process. A new hierarchical procedure for the conceptual design of solution crystallisation processes is proposed in Chapter 3. The hierarchy consists of four design levels. The first two design levels have a product engineering character, whereas the last two design levels have a process engineering character. At each level of the design procedure the design specifications, design variables and the domain knowledge necessary to synthesise, analyse and optimise design alternatives are (re-)considered. The design procedure is intended to cover various scenarios as regards the destination of the crystalline product (main product, by-product or waste product) and the role of the crystallisation process (conversion, separation or purification).

Generation, evaluation and optimisation of design alternatives requires crystallisation process models that possess a predictive capability with respect to the relations between product quality and process design/operational variables. Chapter 4 concerns the development of a modelling framework that can be employed to rapidly generate consistent process models for a wide range of crystallisation processes. Separation of kinetics and hydrodynamics is considered an essential cornerstone for the development of predictive crystallisation process and product models. For this separation, two modelling approaches are investigated as a possible basis for the modelling framework, viz compartmental modelling and computational fluid dynamics. The first of these two approaches is selected as it allows for a more comprehensive description of the CSD and the process dynamics, whilst making what is considered an acceptable sacrifice in spatial resolution. Subsequently, a compartmentation procedure, i.e. a procedure for constructing a network of compartments that approximates the main hydrodynamic characteristics of a given crystalliser, is presented. The compartments represent volumes of the crystalliser within which conditions are considered uniform. The same single compartment model is used to describe each and every one of these volumes. The main body of this chapter concerns the assumptions, characteristics, equations of conservation, kinetic equations and particle settling equations of this generic compartment model. Finally, it is shown how the developed crystallisation process and product modelling framework can be applied to the range of crystallisation processes covered by the scope of this thesis.

Comprehensive crystallisation process models typically do not have analytical solutions. Chapter 5 therefore focuses on the numerical solution of these models. For this purpose, several commercially available packages are considered. The selected package is a general-purpose process modelling tool that supports steady-state and dynamic simulation, parameter estimation and optimisation using formal mathematically-based methods. Whereas this tool can solve sets of differential and algebraic equations to a predefined accuracy, this is not the case for partial differential equations, e.g. the population balance equation, and integral equations, e.g. moment calculations. In order to solve equations belonging to one of these two categories, they need to be transformed into ordinary differential equations or algebraic equations. In this work, the finite volume method is used for this transformation. The accuracy of this transformation or approximation is determined by the discretisation resolution of the crystal size domain and the formulation of the population balance equation. Investigation of these relationships reveals that the most suitable discretisation type, e.g. linear or logarithmic, depends on the employed crystallisation kinetics model. For the kinetic model of most interest for this thesis, i.e. the Gahn model, a logarithmic crystal size grid leads to the most accurate results for a given number of nodes. The optimal spacing between the nodes is determined on the basis of a trade-off between accuracy and computational performance. Initial work with the Gahn model revealed some significant pitfalls when implementing conditional equations

with respect to crystal size on a discretised crystal size domain. Smoothing these conditional equations is essential for model-based optimisation of process design and operation.

Before applying a crystallisation process model for optimal design purposes of a new chemical system, one firstly needs to estimate the values of unknown model parameters, in particular parameters of the employed kinetic model, and secondly validate the model with respect to the predictive capabilities required for design. This is the subject of Chapter 6. To this effect, experimental data is collected from two crystallisers of a different scale and type, viz a 22-litre Draft Tube crystalliser and an 1100-litre Draft Tube Baffle crystalliser, which are both equipped with online measurement techniques to characterise the evolution of the crystal size distribution during start-up and subsequent operation. Both crystallisers are operated continuously in an evaporative mode for the crystallisation of ammonium sulphate from water. In order to provide a reference frame for the descriptive and predictive capabilities of the Gahn kinetic model, parameter estimation and validation are also carried out with the kinetic models of Ottens, Eek and Ó Meadhra. The model of Ó Meadhra (eight unknown parameters) is shown to have the best descriptive value, while the model of Gahn (only two unknown parameters) has the best predictive value with respect to both changes in crystalliser scale/type and impeller frequency. Finally, it is shown how the same crystallisation process model can be applied for experiment design, by either estimating whether an additional measurement provides significant additional information and/or determining the control profiles that lead to the experiment with the highest information content.

Chapter 7 investigates the sensitivity of the predicted process behaviour and product quality on the employed compartmental model before proceeding with the use of the crystallisation process modelling framework, developed and validated in this thesis, for optimal design purposes. The first part of this chapter concerns the compartmental modelling of the UNIAK 1100-litre DTB crystalliser and a 360 m³ DTB crystalliser. For this purpose, the various compartmental models presented in Chapter 4 are employed. The resulting simulations provide a general indication of the importance of (i) the use of real dissolution kinetics as opposed to the assumption of complete dissolution for the fines removal system of a DTB crystalliser, (ii) taking into account the hold-up of the annular zone, (iii) compartmentation of the crystalliser main body, and (iv) the modelling of internal classification. The results of these simulations also serve to validate the compartmental models used in Chapter 6 to describe the 22-litre DT and 1100-litre DTB crystalliser for parameter estimation and model validation purposes. The second part of Chapter 7 is concerned with the generation of optimal crystalliser designs. For this purpose, standard mathematical optimisation techniques are used that allow a flexible formulation of constraints and an objective function. The design problem considered here involves a DTB crystalliser for the crystallisation of ammonium sulphate from water with a production capacity of 94 kton-annum⁻¹. The optimisation problem involves an

economic objective function comprising capital and operational costs, five constraints and five decision variables. The constraints include both product quality related constraints and operational constraints, whereas the decision variables relate to both design and operational aspects.

The final chapter of this thesis presents some perspectives for the use of the work described in this thesis and recommends areas for future research.

CONTENTS

SUMMARY.....	VII
CONTENTS	XI
1 INTRODUCTION	1
1.1 IMPORTANCE OF CRYSTALLISATION.....	1
1.2 PROBLEMS IN CRYSTALLISATION.....	2
1.3 LACK OF RELIABLE DESIGN PROCEDURES AND DESIGN TOOLS.....	3
1.4 RESEARCH OBJECTIVE.....	4
1.5 SCOPE OF RESEARCH	6
1.6 UNIAK PROJECT	8
1.7 STRUCTURE OF THESIS.....	9
2 ON CRYSTALS, CRYSTALLISATION, MODELLING AND PROCESS DESIGN	11
2.1 INTRODUCTION	11
2.2 CRYSTAL QUALITY – PERFORMANCE AND COMPOSITION	12
2.2.1 <i>Product performance</i>	12
2.2.2 <i>Product composition</i>	13
2.2.3 <i>Product-related design specifications</i>	13
2.3 CRYSTALLISATION MECHANISMS	14
2.3.1 <i>Nucleation</i>	15
2.3.2 <i>Crystal growth and dissolution</i>	16
2.3.3 <i>Agglomeration</i>	17
2.3.4 <i>Breakage</i>	18
2.3.5 <i>Segregation</i>	18
2.4 MODELLING AND DESIGN OF CRYSTALLISATION PROCESSES AND PRODUCTS	19
2.4.1 <i>Spatial distribution</i>	19
2.4.2 <i>Dynamic behaviour</i>	20
2.4.3 <i>Requirements for a crystallisation process and product modelling framework</i>	21
2.4.4 <i>Need for a systematic design procedure</i>	22
2.5 CONCLUSIONS	23
3 A HIERARCHICAL DESIGN PROCEDURE.....	25
3.1 INTRODUCTION	25
3.2 A DESIGN HIERARCHY	26
3.2.1 <i>Initial design specifications</i>	30
3.2.2 <i>Design of the crystalline product</i>	32
3.2.3 <i>Physical/chemical design of the crystallisation task</i>	33
3.2.4 <i>Flowsheet design of the crystallisation process</i>	36

3.2.5	<i>Design of a crystalliser stage</i>	39
3.3	DISCUSSION.....	43
3.4	CONCLUSIONS	44
4	A PREDICTIVE CRYSTALLISATION PROCESS MODEL	45
4.1	INTRODUCTION	45
4.2	PREDICTIVE REQUIREMENTS.....	47
4.2.1	<i>Kinetics</i>	47
4.2.2	<i>Overall hydrodynamics</i>	48
4.3	COMPARTMENTAL MODELLING	51
4.3.1	<i>Compartmentation procedure</i>	52
4.3.2	<i>Examples of compartmental models</i>	55
4.4	MODEL OF A SINGLE COMPARTMENT	59
4.4.1	<i>Equations of conservation</i>	62
4.4.2	<i>Kinetic model</i>	66
4.4.3	<i>Half-time for supersaturation decay</i>	74
4.4.4	<i>Classification model</i>	75
4.4.5	<i>Crystal size distribution representations</i>	81
4.4.6	<i>Thermodynamic and physical properties</i>	81
4.5	A MODELLING FRAMEWORK FOR A WIDE RANGE OF PROCESSES	81
4.5.1	<i>Crystallisation methods</i>	82
4.5.2	<i>Operation modes</i>	82
4.5.3	<i>Crystalliser types</i>	83
4.6	CONCLUSIONS	87
5	MODEL IMPLEMENTATION AND NUMERICAL ISSUES.....	89
5.1	INTRODUCTION	89
5.2	MODELLING TOOL REQUIREMENTS AND SELECTION	90
5.3	NUMERICAL SOLUTION METHODS FOR PARTIAL DIFFERENTIAL AND INTEGRAL EQUATIONS	91
5.3.1	<i>Discretisation of crystal size domain</i>	92
5.3.2	<i>Derivatives with respect to crystal size</i>	93
5.3.3	<i>Integration over crystal size</i>	97
5.3.4	<i>Logarithmic transformation of number densities</i>	98
5.4	NUMERICAL VERSUS ANALYTICAL SOLUTION – SIMPLE KINETICS	99
5.4.1	<i>MSMPR crystalliser with simple kinetics</i>	99
5.4.2	<i>Test case definition</i>	100
5.4.3	<i>Accuracy of integrals</i>	101
5.4.4	<i>Accuracy of partial derivatives</i>	102
5.4.5	<i>Combined accuracy of partial derivatives and integrals</i>	105
5.4.6	<i>Conclusions</i>	109
5.5	NUMERICAL ISSUES RELATED TO IMPLEMENTATION OF GAHN KINETIC MODEL	109
5.5.1	<i>Typical size dependency of the growth and birth/death term</i>	110
5.5.2	<i>Solving the PBE for simultaneous crystal growth and dissolution</i> .	112

5.5.3	<i>Discretisation of radial impeller co-ordinate</i>	116
5.5.4	<i>Discontinuities in Gahn kinetic model</i>	117
5.6	ACCURACY OF NUMERICAL SOLUTION - GAHN KINETIC MODEL.....	121
5.6.1	<i>Influence of grid type and resolution for crystal size discretisation</i>	123
5.6.2	<i>Influence of resolution for radial impeller co-ordinate discretisation</i>	125
5.6.3	<i>Computational requirements</i>	125
5.7	CONCLUSIONS	127
6	PARAMETER ESTIMATION, MODEL VALIDATION AND DESIGN OF EXPERIMENTS	131
6.1	INTRODUCTION	131
6.2	EQUIPMENT SET-UP	132
6.2.1	<i>Crystalliser plants</i>	132
6.2.2	<i>CSD measurement devices</i>	139
6.3	EXPERIMENTS AND MEASUREMENT DATA	139
6.3.1	<i>22-litre DT crystalliser</i>	141
6.3.2	<i>1100-litre DTB crystalliser</i>	142
6.3.3	<i>Measurement errors</i>	146
6.4	PARAMETER ESTIMATION	147
6.4.1	<i>Parameter sensitivities</i>	148
6.4.2	<i>Data window and initial conditions</i>	152
6.4.3	<i>Fitting experimental data obtained from 22-litre DT crystalliser</i> ..	155
6.5	PREDICTIVE QUALITY OF THE KINETIC MODELS.....	162
6.5.1	<i>Different operating conditions on the same crystalliser</i>	163
6.5.2	<i>Different operating conditions on a crystalliser of different type and scale</i>	165
6.6	DESIGN OF EXPERIMENTS	167
6.7	CONCLUSIONS AND RECOMMENDATIONS	170
7	OPTIMAL DESIGN	173
7.1	INTRODUCTION	173
7.2	COMPARTMENTAL MODELLING	173
7.2.1	<i>UNIAK 1100-litre DTB crystalliser</i>	175
7.2.2	<i>A 360 m³ DTB crystalliser</i>	176
7.2.3	<i>Discussion and conclusions</i>	178
7.3	OPTIMAL DESIGN OF A CONTINUOUS PROCESS	180
7.3.1	<i>Problem formulation</i>	181
7.3.2	<i>Exploring the design space</i>	184
7.3.3	<i>Mathematical optimisation</i>	186
7.3.4	<i>Conclusions</i>	191

8	RECOMMENDATIONS AND PERSPECTIVES.....	193
	REFERENCES.....	197
	LIST OF SYMBOLS	205
A	ON PRODUCT COMPOSITION.....	209
A.1	LATTICE STRUCTURE.....	209
A.2	MORPHOLOGY AND HABIT	210
A.3	CRYSTAL SIZE.....	212
A.4	CRYSTAL PURITY.....	213
A.5	SUPERFICIAL PROPERTIES.....	214
B	A PREDICTIVE CRYSTALLISATION PROCESS MODEL	217
B.1	MODEL ASSUMPTIONS	217
B.1.1	<i>Model assumptions for the general compartment model.....</i>	<i>217</i>
B.1.2	<i>Further model assumptions</i>	<i>218</i>
B.2	GENERAL COMPARTMENT MODEL.....	220
B.2.1	<i>Equations of Conservation.....</i>	<i>220</i>
B.2.2	<i>Derivative/Related/Associated States</i>	<i>222</i>
B.2.3	<i>Slurry (S/L) inlet</i>	<i>224</i>
B.2.4	<i>Slurry (S/L) outlet.....</i>	<i>224</i>
B.2.5	<i>Vapour outlet.....</i>	<i>224</i>
B.2.6	<i>Liquid Phase Reactions</i>	<i>224</i>
B.2.7	<i>Crystallisation Reactions</i>	<i>225</i>
B.3	CRYSTAL-IMPELLER COLLISION MODEL.....	226
B.3.1	<i>The velocity profile around the impeller</i>	<i>226</i>
B.3.2	<i>The chance of collision of a crystal.....</i>	<i>227</i>
B.3.3	<i>The collision velocity of a crystal.....</i>	<i>229</i>
B.4	MATERIAL PROPERTIES.....	230
B.4.1	<i>Solubility.....</i>	<i>230</i>
B.4.2	<i>Density.....</i>	<i>230</i>
B.4.3	<i>Viscosity.....</i>	<i>230</i>
B.4.4	<i>Diffusivity</i>	<i>231</i>
B.4.5	<i>Specific Heat Capacity</i>	<i>231</i>
B.4.6	<i>Additional Material Properties</i>	<i>232</i>
C	PARAMETER ESTIMATION, MODEL VALIDATION AND DESIGN OF EXPERIMENTS	233
C.1	PARAMETER SENSITIVITIES.....	233
C.2	DATA WINDOW AND INITIAL CONDITIONS	235
C.3	KINETIC MODELS OF OTTENS, EEK AND O MEADHRA	236
C.3.1	<i>Ottens</i>	<i>236</i>
C.3.2	<i>Eek.....</i>	<i>236</i>
C.3.3	<i>O Meadhra.....</i>	<i>236</i>

C.4	FITTING EXPERIMENTAL DATA OBTAINED FROM 22 LITRE DT CRYSTALLISER	238
C.5	PARAMETER CROSS-CORRELATIONS.....	240
C.6	PREDICTIVE QUALITY OF THE KINETIC MODELS.....	241
C.7	DYNAMICS IN THE GAHN KINETIC MODEL	243
C.8	INFLUENCE OF MEASUREMENT SELECTION ON PARAMETER STATISTICS.	245
D	COMPARTMENTAL MODELLING AND OPTIMAL DESIGN	247
D.1	COMPARTMENTAL MODELLING	247
D.1.1	<i>compartment numbering, locations and volumes of the compartmental models used in Chapter 7</i>	<i>247</i>
D.1.2	<i>UNIAK 1100-litre DTB crystalliser</i>	<i>248</i>
D.1.3	<i>A 360 m³ DTB crystalliser.....</i>	<i>253</i>
D.2	OBJECTIVE FUNCTION FOR OPTIMISATION.....	257
	SAMENVATTING	259
	ACKNOWLEDGMENTS.....	263
	CURRICULUM VITAE	267

1 INTRODUCTION

Application, advantages and problems of crystallisation in the chemical process industry are discussed. Problems encountered in industrial crystallisation are related to both product quality and process performance. Although some of these problems can be solved using process control, most problems are intrinsically related to decisions taken during the design stage. However, systematic procedures and tools for the reliable design of crystallisation processes are practically non-existent. The research objective of this PhD work is hence the development of a prototype design kit, consisting of a systematic procedure and tools, for crystallisation processes. The scope of this research is defined in terms of the nature of the chemical system (relatively well soluble substances), crystallisation method (indirect-cooling, flash cooling and evaporation), operation mode (batch, semi-batch and continuous), flowsheet configuration (single and multiple stage) and crystalliser type (stirred tank, draft tube, draft tube baffle, and forced circulation).

1.1 IMPORTANCE OF CRYSTALLISATION

Crystallisation involves the formation of one or more structured solid phases from a fluid phase or an amorphous solid phase. It is one of the older unit operations in the chemical industry. Crystallisation stands out from most unit operations due to the presence of a solid product. Besides chemical composition, the quality of such a product is also determined by its crystal size distribution (CSD), morphology, habit, polymorphism, etc. Within the chemical industry crystallisation is applied extensively for both separation and production purposes.

Vast quantities of crystalline substances are manufactured commercially: inorganic materials such as sodium chloride ($>10^8$ t/a), potassium chloride (fertiliser, $>10^6$ t/a), ammonium sulphate (fertiliser), and urea ($>10^6$ t/a) and organic materials such as sucrose ($>10^8$ t/a), adipic acid (raw material for nylon), paraxylene (raw material for polyester), and pentaerythritol (used for coatings).

An enormous number of and diversity in crystallisation processes is found in the pharmaceutical, organic fine chemical, and dye industries: L-ascorbine (vitamin C), L-serine (amino acid), and aspartame (sweetener). Although the production in these industries is relatively low as regards tonnages, it constitutes a substantial part of crystallisation processes from an economic point of view.

Overall, it is estimated that about 70% of the products sold by the process industry and pharmaceutical industry are solids. The main advantages of crystallisation are:

- *A high purity in one process step.* The rigid structure of the crystalline material results in a low tendency to incorporate foreign substances or solvent molecules. Therefore, high purity substances can be relatively easily produced in crystallisation. However, a lot of time is needed to grow such a rigid structure, and crystallisation is thus a rather slow

process. As a result, large vessels are generally needed to reach an acceptable yield.

- *Low level of energy consumption.* For instance, if cooling crystallisation can be used instead of distillation, a significant cost reduction is achieved.
- *Relatively mild process conditions.* This makes crystallisation a favourable unit operation for temperature sensitive or even temperature labile substances. A well-known example of an industry frequently dealing with such substances is the food sector.

1.2 PROBLEMS IN CRYSTALLISATION

Although crystallisation is one of the older unit operations in the chemical industry, crystallisation processes are notorious for the severe problems that are frequently encountered during their design and operation. These problems may be related to product quality requirements, such as filterability, caking behaviour, purity and tableting behaviour on the one hand, and process requirements, such as production capacity and plant availability on the other hand.

Many crystallisation plants frequently produce crystals, which do not satisfy the defined quality specifications. For instance, an excess of fine particles will typically result in poor filterability characteristics. Consequently increasing the cost of the downstream solid/liquid processing. Another example is the inclusion of mother liquor. After solid/liquid separation and drying of the crystalline product, e.g. during transportation or storage, mother liquor may seep from broken crystals. Subsequent re-crystallisation may cement the crystals together; a process referred to as the caking of crystals. Furthermore, a continuous crystallisation process may be at steady-state as regards the energy and material balances, but this does not have to be the case for the crystal size distribution (CSD). The dynamics in the CSD can be a result of disturbances (feed changes, blockages, utility failures), changes in operating conditions (start-up, shut down, grade changes), or simply the fact that the process is open loop unstable. The characteristic time of CSD dynamics is typically in the order of hours. Undesired CSD dynamics may therefore result in significant amounts of off-spec material.

Operational problems also constitute a large portion of the problems encountered in crystallisation processes. Firstly, scale growth or crystal deposition on heat exchanger surfaces often reduces production capacity and may even limit plant availability significantly. Secondly, plant availability may also be reduced by pipe blockages as a result of scale growth or high solids concentrations. Finally, many crystallisation processes suffer from open loop unstable behaviour.

Some of the above-mentioned problems may be solved with the help of process control. For instance, Eek (1995a) successfully demonstrated the use of both a SISO PI-controller and MPC to stabilise a continuous crystalliser, which in open loop showed an oscillatory CSD behaviour. However, even using control, the operating range with respect to attainable crystal size was still very limited. To go

beyond these limits, if at all physically feasible, requires redesign or grassroots design of the crystallisation process.

Moreover, a number of the above-mentioned problems are related to decisions taken during the design stage and can thus only be solved by redesign or grassroots design. For instance, uptake of mother liquor as a result of too high growth rates can only be reduced by increasing the crystal residence time in the crystalliser. If the production capacity is not to be sacrificed, this can only be accomplished by increasing the crystalliser volume.

1.3 LACK OF RELIABLE DESIGN PROCEDURES AND DESIGN TOOLS

Despite the importance of crystallisation, there is a relative lack of systematic procedures and design tools to ensure the design of a crystalliser that does not suffer from the before-mentioned problems.

This relative lack in comparison with vapour/liquid processes is a major omission for the chemical engineering profession (Villadsen, 1997): In November 1996, a delegation of industrialists and academics convened in Port Sunlight to discuss the future of the chemical engineering profession. They concluded that the development of and education in reliable tools and procedures for the design of structured products, such as crystalline substances, and the processes for their manufacture should be one of the main points of attention.

The need for research into design procedures and design tools for crystallisation and structured products in general was also acknowledged by Wintermantel (1999), who gave the thirteenth P.V. Danckwerts Memorial Lecture. He makes a distinction between process engineering and product engineering. Process engineering typically deals with products, which consist of relatively small molecules (as it is the case for example with basic chemicals or plastic monomers). Properties and quality of these products are essentially a function of the concentrations achieved, which in turn are determined by the correct choice of process steps and equipment. Product engineering is concerned with solid, emulsified and paste-like products, whose quality and properties are no longer determined solely by the concentrations achieved in separation operations. The physical form along the entire process route plays an even more important role. Whereas process engineering has an established body of knowledge with clear structures, which can be taught very effectively at universities and can be used by industry to pursue specific objectives, this is not at all the case for product engineering. There is still a long way to go before it will be possible to predict a structured product's physical form as a function of the relevant equipment parameters and operating conditions. For this reason, Wintermantel cannot yet even conceive of scaling up a process by a factor of 1:40.000 from the laboratory to the industrial plant, as is possible for classical chemicals.

The time lag in the development of design procedures and design tools for crystallisation processes in comparison with vapour/liquid processes is not surprising. The understanding of crystallisation processes and of solids processes

in general, is typically a degree more complex than that of most vapour/liquid processes. This added complexity mainly results from:

- The fact that the product quality specifications cannot be solely defined in terms of chemical and phase composition. A crystalline product is also characterised by its size distribution, morphology, polymorphism and the amount of strain in the crystal lattice.
- The complex thermodynamics of solid/liquid and solid/liquid/vapour systems possibly containing electrolytes, multiple solid phases and/or multiple (organic) solvents.
- The difficulties in predicting the hydrodynamics of a multi-phase flow as a function of crystalliser and impeller geometry, operating conditions, crystal properties and crystal concentrations. As a result of the hydrodynamics, the process conditions affecting the crystallisation mechanisms are rarely uniform inside industrial scale crystallisation vessels. Variations in local supersaturation levels and energy dissipation rates will affect both the final yield and crystal size distribution from the crystalliser.
- The fact that the rates with which crystals are born, grow, dissolve, are attrited, break, agglomerate, etc. are not only a function of liquid phase process conditions but also of distributed crystal properties such as size, surface structure and internal energy.

1.4 RESEARCH OBJECTIVE

Considering on one hand the sincerity of problems in crystallisation and on the other the lack of systematic design procedures and tools to overcome and/or prevent these problems, the following overall objective has been defined for this research:

development of a prototype design kit for crystallisation systems aimed at obtaining better designs in less time.

Better designs are crystallisation processes, which produce crystals of the desired quality, obey operational and SHE constraints, and have a good performance in terms of yield, energy efficiency, availability, minimal batch time, stability, controllability, etc. Consequently, both product design and process design need to be covered by this systematic design procedure. Less time refers to the fact that at present months or even years are spent on lab scale and pilot plant testing, and that long periods of troubleshooting between commissioning and satisfactory operation are often required. Reduction of these time losses is highly desirable in the light of an ever-decreasing time to market.

Besides effectivity (better designs) and efficiency (less time), use of the design kit should also result in traceable and transparent design processes. Traceability does not only involve adequate documentation of the final design but also of the rationale that led to that design. Traceability is necessary to improve on existing

process designs, design models and design procedures. A transparent design process is (among others) characterised by the mutual awareness and understanding which the members of a design team have for each other's design tasks. The importance of transparency increases with increasing size, number of disciplines and geographic distribution of the design team.

In this research, a design kit is defined as the combination of a design procedure and design tools.

The organisation of a design process (and the structuring of domain knowledge) is covered by a design procedure. Such a procedure aids by advising a user which design activity to perform next and with which design tool(s). Villadsen (1997) and Wintermantel (1999) observed that no reliable systematic design procedures exist for the design of processes involving structured products, such as crystallisation. The first research objective of this PhD work thus reads as follows:

development of a systematic design procedure to structure and simplify the design of crystallisation processes; both product design and process design are to be covered.

Design tools are tools, which represent and/or generate domain knowledge that is needed to perform one or more design activities. Domain knowledge can be present as data, models and heuristics. Examples of design tools are experimental facilities, handbooks, mathematical models, spreadsheets, flowsheet simulators and expert systems.

For some crystallisation design activities mature commercial tools are available. A major omission is a design tool for the analysis and optimisation of process design alternatives. The absence of such a tool, which must reliably scale-up molecular scale interactions from the lab scale to processes carried out in industrial equipment, is acutely felt. Many processes have to be empirically designed and a large number of process parameters must be set by experience. As a result, process yields are often disappointing and particles are frequently too small or oversized. The second research objective therefore reads:

development of a crystallisation process model that can predict the product quality and process performance as a function of crystallisation method, operation mode, equipment type and size, and operating conditions.

To achieve this goal, it is essential to be able to predict the spatially distributed, crystal size dependent and time dependent crystallisation kinetics. After all, the kinetics ultimately determine the properties of a crystalline product. To predict these kinetics requires knowledge of crystal properties, thermodynamic properties, hydrodynamic conditions and particle mechanics as well as understanding of their interactions. With respect to the predictive requirements, use of first principle models is desirable. However, at present, it is impossible to derive this knowledge and understanding from first principle models only. This may be due to a lack of physical understanding or due to computational limitations. Consequently, heuristics, tabulated data, laboratory and pilot plant scale experiments continue

to constitute a major part of the domain knowledge necessary for the design and optimisation of crystallisation processes.

Another point of attention is the concept of life cycle modelling, i.e. the use of the same model (for forward and inverse problems/simulation, parameter estimation and optimisation) throughout the lifetime of a process: research & development, grassroots design, commissioning, operation, control, redesign and decommissioning. This concept has two obvious advantages, i.e. model consistency and a decreased model development effort. Although this thesis is primarily concerned with grass roots design, life cycle modelling will be kept in mind during model development.

1.5 SCOPE OF RESEARCH

There is a large variety of crystallisation processes as regards methods, configurations, operation modes, etc. To emphasise both the generality as well as the limitations of this research, its scope is given below:

- *Chemical system.* The focus will be on the crystallisation of relatively well soluble substances like KNO_3 , NaCl , or $(\text{NH}_4)_2\text{SO}_4$. Sparsely soluble substances like CaCO_3 or BaSO_4 are mostly crystallised by precipitation, which involves a reaction mechanism that is outside the scope of this work.
- *Crystallisation method,* i.e. the method employed to generate supersaturation. Supersaturation, the driving force for crystallisation, can be created by mixing two well soluble salts resulting in an insoluble salt, the addition of an anti-solvent, and cooling or evaporation of a solution or melt. In this research crystallisation by indirect-cooling, flash-cooling and evaporation of solutions is considered.
- *Operation mode.* The whole range from batch to continuous operation is covered.
- *Flowsheet structure.* An arbitrary number of crystallisers, number of feed streams and interconnectivity is considered.
- *Crystalliser type.* A large number of crystalliser types exist in practice (Bamforth, 1965). The most common types are the stirred tank, draft tube, draft tube baffle, forced circulation and fluidised bed crystalliser. The latter crystalliser type is not taken into account because the attrition mechanisms in fluidised bed crystallisers are poorly understood.
- *Classifiers.* Many crystallisers are equipped with a fines and/or product classifier to manipulate the product crystal size distribution. Both types will be addressed.

As crystallisation is rarely a stand-alone process, it is also important to define the system boundary with respect to the overall process (see Figure 1.1).

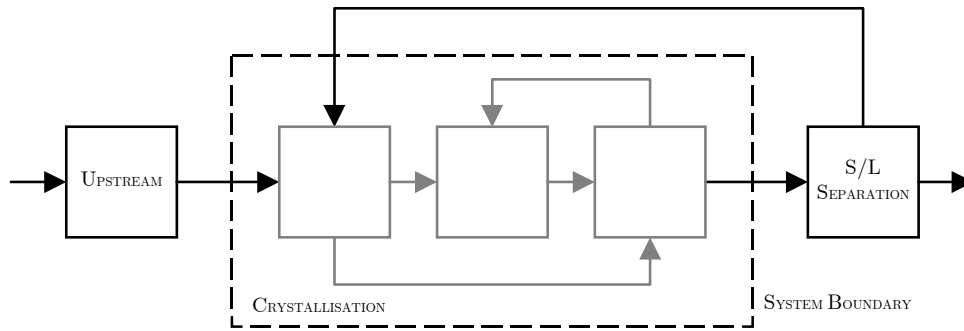


Figure 1.1: System boundary of the crystallisation process for the purpose of this thesis.

The origin of a crystallisation system's feed is the upstream part of the overall process. The exact origin is usually a reactor effluent or a product stream of a separation process. In certain cases, the mother liquor is recycled after solid/liquid separation of the crystallisation system's product. The recycled stream then constitutes a second inlet of the crystallisation system, because the solid/liquid separation lies outside the system boundary.

Both crystal free and crystal containing inlets are considered. Fluctuations in flow rates and/or composition of these inlets can have a considerable effect on process and product performance. The design procedure must be able to deal with such situations.

The product of the crystallisation system is a slurry, often also referred to as a magma, i.e. consisting of (a) liquid and solid phase(s). A solid/liquid separator is used to separate this slurry into a flow containing predominantly crystals and a flow containing predominantly liquid. The crystalline product typically carries with it adhering mother liquor that is in the range of 2-10 weight percent of the crystals (Bennett, 1993). Solid/liquid separation is usually performed with filters or centrifuges. This separation is the first step of the downstream solids processing after the crystallisation system. Subsequent steps may include washing, drying, granulation, grinding, tableting, etc.

In industry, significantly more engineering activity is concerned with retrofit, debottlenecking and optimal operation of existing equipment than with grassroots design (Industrial partners, 1995-1999). Why, one may then ask, does this thesis deal with grassroots design? The answer is that grassroots design is the most comprehensive of all above-mentioned activities as regards the degrees of freedom and diversity of required domain knowledge. As activities such as retrofit, debottlenecking and optimising operation are largely a subproblem of the grassroots design problem, it is expected that the design kit developed in this research will also be applicable to those activities.

In order not to create unnecessary confusion in this thesis, the applicability of developed design procedures and tools to other activities than grassroots design

will not be discussed during the course of this thesis, but will be addressed in the final chapter.

1.6 UNI AK PROJECT

This PhD work was carried out within the Process Systems Engineering Group and Crystallisation Group of Delft University of Technology (DUT). The research is also part of the UNI AK project, a multi-disciplinary crystallisation research project, which was initiated in 1985 and is now in its third phase. The partners of the UNI AK project represent academia, government and industry, viz The Crystallisation Group, Particle Technology Group, Systems and Control Group and Process Systems Engineering Group of Delft University of Technology, The Dutch Foundation of Technology, Akzo Nobel, BASF Aktiengesellschaft, Bayer Aktiengesellschaft, Dow Chemical Company, DSM and DuPont.

The first and second phase of the UNI AK project, i.e. UNI AK-1 (1985-1990) and UNI AK-2 (1990-1995), were mainly focused upon the development and application of measurement techniques, kinetic models and control techniques for industrial crystallisation. Design of crystallisation systems was not introduced until the current phase, because the understanding was previously considered inadequate for such an objective. This phase (UNI AK-3; 1995-2000) is further characterised by the use of more fundamental kinetic models and investigation of the hydrodynamics inside crystallisers.

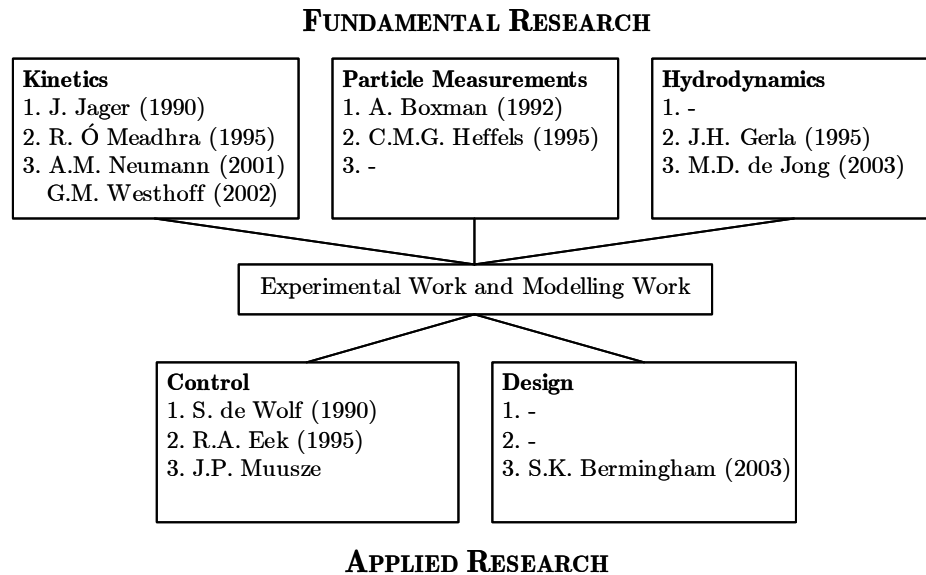


Figure 1.2: The PhD students of the UNI AK project categorised according to the five disciplines and three phases of this interdisciplinary project.

The organisation of the research within the UNIAK project over the last 15 years as well as the references to the PhD theses produced in this period are given in Figure 1.2. In this PhD work, extensive use was made of knowledge generated in the previous phases and of results obtained by fellow PhD students in the current phase.

1.7 STRUCTURE OF THESIS

Chapter 2 discusses the relationship between process and product performance on the one hand and design and operational variables on the other. It is argued that both predictive models and a systematic design procedure are required to capture this complex relationship and generate designs that satisfy predefined process and product performance criteria. The development of a hierarchical design procedure and a predictive crystallisation process modelling framework are the subjects of Chapters 3 and 4 respectively. Key elements of the modelling framework are a compartmental approach to separate the effects of kinetics and overall hydrodynamics, crystal segregation models and the most comprehensive kinetic model currently available for secondary nucleation and growth. Chapter 5 is concerned with a wide range of model implementation issues. In Chapter 6 the crystallisation modelling framework is combined with data from crystallisation experiments to estimate values for the unknown parameters of four different kinetic models, to study their descriptive capabilities and compare their predictive qualities. The first part of Chapter 7 focuses on the importance of varying modelling aspects for DTB crystallisers, such as real dissolution kinetics as opposed to complete dissolution assumption and compartmentation of the main body. The second part of this Chapter illustrates the use of standard mathematical optimisation techniques to generate optimal crystalliser designs with the same modelling framework used for parameter estimation, model validation and compartmental modelling purposes.

2 ON CRYSTALS, CRYSTALLISATION, MODELLING AND PROCESS DESIGN

The relation between product quality, crystallisation mechanisms, process conditions, crystalliser geometry and operating conditions is discussed. As regards product quality, a distinction is made between product performance and product composition. Customer and solid handling requirements are typically defined in terms of the prior, while crystallisation models predict product quality in terms of the latter. Next, an overview is presented of the crystallisation mechanisms that determine the product composition of crystals. Finally, requirements are outlined for a design procedure and phenomenological models that are deemed essential in order to reliably design crystallisation processes that meet their product and process performance criteria. Consequences of limited domain knowledge, limited computational power and, probably most importantly, the limitations of the human process designer are all considered.

2.1 INTRODUCTION

The starting point of a design process is the definition of the design specifications. Design specifications, often also called design requirements, can be categorised as process related, product related and design process related. *Process* related design specifications, such as availability, controllability and maintainability, and *design process* related design specifications, such as available time, documentation of rationale and available human resources will be discussed in Chapter 3. That leaves *product* related design specifications, which refer to both the solid and liquid phase products that result from a crystallisation process.

The purpose of the crystallisation process, e.g. purification of the liquid phase or production of a solid phase, determines which phases are the main product(s), by-product(s) or waste product(s). The specifications of a liquid phase product can be simply and uniquely expressed in terms of pressure, temperature and composition (allowed levels of by-products). In strong contrast, quality specifications of a solid crystalline product are often ambiguous, hard to quantify and difficult to measure.

This chapter focuses on (i) characterisation of crystal quality in terms of product performance and product composition (Chapter 2.2), (ii) the crystallisation mechanisms that determine the composition of a crystalline product (Chapter 2.3), (iii) the need for a predictive crystallisation process model to capture the causal chain ‘equipment geometry and operating conditions; process conditions; crystallisation kinetics; product composition’ (Chapter 2.4), and (iv) application of such a process model for the design of crystallisation processes that satisfy both product and process related design requirements (Chapter 2.4.4).

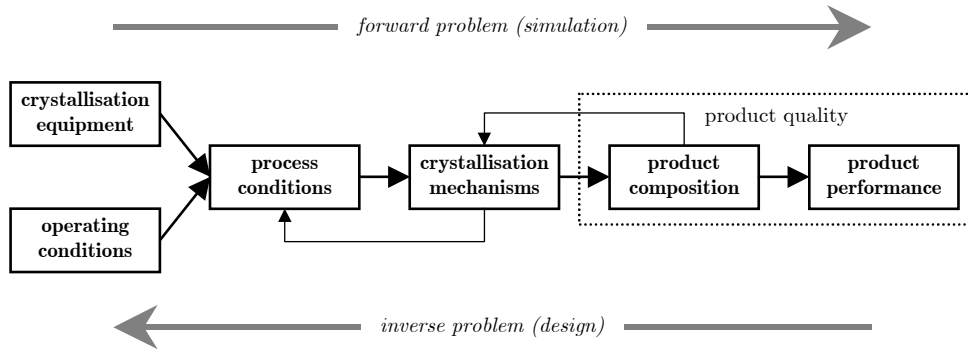


Figure 2.1: The relationship between product quality, crystallisation mechanisms, process conditions, crystallisation equipment and operating conditions.

The causal chain that needs to be captured by a predictive crystallisation process model is schematically depicted in Figure 2.1. This chain also represents the thread that runs through this chapter. Either side of the chain can be the starting point depending on the objective. Simulation of process behaviour and product quality for given crystalliser geometry and operating conditions is a forward problem, whereas optimal design and optimal control are inverse problems which start from desired product quality and process behaviour. This chapter follows the design perspective and therefore commences with crystal quality.

2.2 CRYSTAL QUALITY – PERFORMANCE AND COMPOSITION

Crystal quality can be defined in terms of product performance characteristics and product composition characteristics.

2.2.1 PRODUCT PERFORMANCE

In practice, the quality of a crystalline solid is usually expressed in terms of performance characteristics. Most crystal quality requirements are imposed by the customers and the downstream solids processing. For instance, end-consumers usually define product performance in terms of aesthetic appearance, taste, smell, feel and handling properties. Of interest for downstream solids processing are first of all the filtration, washing and drying behaviour of the crystals. Secondly, caking behaviour and flowability are important characteristics for storage and transport. Caking is usually the result of mother liquor inclusions. During transportation or storage, mother liquor may seep from broken crystals. Subsequent re-crystallisation may cement the crystals together; a process referred to as the caking of crystals.

The main problem with performance characteristics is that they are often ambiguously defined. This is clearly the case for quality assessments such as taste and feel, which are largely subjective impressions. For other characteristics, such

as crystal filterability, the ambiguous nature is not so obvious. The filtration rate using a specific piece of equipment is an objective definition of crystal filterability, but it is not universally applicable as it is equipment dependent.

2.2.2 PRODUCT COMPOSITION

For design purposes, translation of the often ill-defined performance characteristics to well-defined physical parameters is essential. Well-defined physical quantities to describe the quality of a crystalline product include size, purity, lattice structure, morphology and habit. In this work, a quality description using such terms is called the product composition of a crystalline product.

Usually the individual crystals in a crystalline product do not possess the same history as regards their formation processes. Consequently, their properties will not necessarily be the same. A product that consists of crystals with different sizes, morphologies, etc. is said to have distributed properties. As one usually considers volumes of crystalline material which are substantially larger than the volume of an individual crystal, the number of crystals is sufficiently large to justify the use of a statistical description to account for the distributed nature of the product properties. The first distributed property that jumps to mind in conjunction with industrial crystallisation is crystal size. As crystallisation usually takes place in vessels with a residence time distribution, the individual crystals will obviously have varying histories. The most noticeable result of this difference in history is usually a distribution of crystal sizes.

The most important product composition characteristics and their influence on product performance aspects are described in Appendix A.

2.2.3 PRODUCT-RELATED DESIGN SPECIFICATIONS

Defining product specifications in terms of composition instead of performance is clearly more suitable for modelling and design purposes. However, its use still raises a number of problems:

- Although product composition characteristics are well-defined, some are extremely difficult to measure, e.g. morphology and habit.
- Theoretically speaking all product composition characteristics can be uniquely defined in physical terms; however, in practice a reasonably accurate description of some characteristics would require a very substantial number of parameters.
- The lack of adequate product performance models, i.e. models predicting the performance on the basis of composition; without these models interpretation of product specifications imposed by downstream solids processing and customers remains a serious bottleneck.

These three problems are all largely related to the distributed nature of crystalline products. In addition to a size distribution, a collection of crystals will usually also possess distributions with respect to morphology, purity, etc. A comprehensive description of the product composition therefore involves a

multivariate distribution of the crystal population over the various product composition variables.

2.3 CRYSTALLISATION MECHANISMS

The product composition characteristics detailed in the previous subchapter constitute the internal states of a crystalline product. The external state of a crystal is its geometric position, and the change in this external state is given by the external velocity of the crystal, which is a function of both the hydrodynamics of the solid/liquid system and the internal states of the crystal. This subchapter focuses on the main crystallisation events or mechanisms that can change (and hence determine) the internal states of a crystalline product, viz nucleation, growth, dissolution, attrition, agglomeration and breakage. Besides influencing the internal crystal states, some of these events also change the states of the liquid phase. An overview of the states that are typically influenced by the various crystallisation events is given in Table 2.1.

Table 2.1: States typically influenced by the various crystallisation events.

crystallisation event or mechanism	internal crystal states					slurry states	
	lattice structure	morphology	size	purity	lattice strain	crystal concentration	solite concentration (supersaturation)
nucleation ; crystal formation	++	+	-	-/+	+	++	+
growth ; continuous size enlargement of a crystal	+/-	+	++	+	+	++	++
dissolution ; continuous size reduction of a crystal	-	+	++	+	+/-	++	++
agglomeration ; discontinuous size enlargement of a crystal	-	++	++	+	-	-	+
breakage ; discontinuous size reduction of a crystal; involves the fracture of a particle into two or more smaller pieces	-	++	++	-	++	-	-
attrition ; discontinuous size reduction of a crystal; involves the fracture of the particle into one slightly smaller particle and many much smaller fragments	-	+	+	++	++	+/-	+/-

The rates of these crystallisation events are largely determined by the same states they affect, i.e. the internal crystal states and slurry states. More specifically, they are a function of rate coefficients and driving forces, which are in their turn determined by slurry states or local process conditions such as supersaturation,

energy dissipation, solids concentration, pressure and temperature, as well as internal crystal states, such as size, strain and shape. In the remainder of this subchapter, a brief description is given of the physics of the various crystallisation mechanisms listed in Table 2.1 (Myerson and Ginde, 1993; Mersmann, 1995; Rosmalen et al., 2000).

2.3.1 NUCLEATION

Nucleation, the formation of new crystalline particles, is classified as being primary or secondary according to the mechanism through which it occurs.

Primary nucleation

Primary nucleation is the formation of a new solid phase from a clear liquid. This type of nucleation can be further subdivided into homogeneous and heterogeneous nucleation. In heterogeneous nucleation, nucleation starts on foreign substrates of mostly microscopic particles, e.g. dust or dirt particles. If such substrates are absent, new phase formation takes place by statistical fluctuations of solute entities clustering together, a mechanism referred to as homogeneous primary nucleation. Homogeneous nucleation rarely occurs in practice, as the presence of small quantities of microscopic particles is usually unavoidable.

The driving force for primary nucleation is the supersaturation of the crystallising substance, which is defined as the difference in chemical potential of that substance in the liquid and in the solid phase. The rate coefficient or resistance for primary nucleation is (among others) a function of the cluster-liquid interfacial tension and the diffusion coefficient. The internal states at the time of formation of the nuclei, such as size, lattice structure and purity, are also a function of supersaturation. For instance, the critical nucleus size, the size at which a nucleus is considered thermodynamically stable, is inversely proportional to the supersaturation.

Secondary nucleation

Secondary nucleation refers to the birth of new crystals at the interface of parent crystals. Contrary to the relatively high supersaturations required for primary nucleation, secondary nucleation already occurs at low to moderate values of the supersaturation. There are various types of secondary nucleation, but the most important source of secondary nuclei in crystallisation is attrition. Attrition, also referred to as contact nucleation, occurs as a result of crystal-pump, crystal-vessel wall or crystal-crystal collisions.

The driving force for attrition is determined by the concentration of the various sized crystals and their relative motion with respect to the pump blades, vessel walls or other crystals. The relative kinetic energy of a collision is determined by the size and relative velocity of the particle, which in its turn is a function of the slurry motion, viscosity and particle inertia (thus particle size). The rate coefficient or resistance for attrition is a function of the shape, surface roughness and mechanical properties of the colliding crystal. The rate coefficient is also indirectly influenced by the supersaturation, which determines factors such as surface roughness and healing of corners and surfaces damaged due to previous collisions. The supersaturation also

determines the effective secondary nucleation rate as a result of attrition: it determines the fraction of attrition fragments that actually grow out and thus 'survive'.

2.3.2 CRYSTAL GROWTH AND DISSOLUTION

Crystal growth is the addition of solute molecules from a supersaturated solution to the crystal lattice. Besides being a mechanism responsible for increasing crystal size, crystal growth, or more specifically the relative growth rates of the crystal faces, also largely determines crystal morphology. Finally, the crystal face growth rates together with the growth mechanism determine the surface structure and purity of the crystal (Rosmalen et al., 2000).

The growth rate of a particular crystal face is mostly described by its linear growth rate, which refers to the growth rate of that face in the direction normal to the face. Since the growth rates of the various crystal faces are usually not equal, an overall linear growth rate is often used.

Crystal growth is a three-step process consisting of mass transfer, surface integration and heat transfer. Mass transfer and surface integration occur sequentially and in parallel with heat transfer. Mass transfer involves the diffusion of growth units, i.e. molecules, atoms or ions, to the crystal surface. Surface integration consists of surface diffusion, orientation and the actual incorporation into the lattice. Various mechanisms exist for surface integration, the most important being spiral growth, 'birth and spread' growth and rough growth. Spiral growth is the most encountered growth mechanism under normal operating conditions (Rosmalen et al., 2000). Heat transfer is often a rate-limiting step in melt crystallisation, but this is practically never the case in solution crystallisation. Supersaturation is the driving force for both mass transfer and surface integration. The rate of mass transfer has a first order supersaturation dependency. The supersaturation dependency of the surface integration step is determined by the mechanism: a second, exponential and first order dependency for respectively spiral growth, 'birth and spread' growth and rough growth. It is important to note that the supersaturation, i.e. the difference in chemical potential of the crystallising substance in the liquid and solid phase, need not be the same for each crystal. While the chemical potential in the liquid phase may be the same, the chemical potential of two neighbouring crystals may differ due to differences in lattice structure and/or lattice strain. As a result, similarly sized crystals exposed to identical growth conditions can exhibit different growth rates. This phenomenon is called growth rate dispersion and has been experimentally observed by among others Ristic et al. (1990). The mass transfer rate coefficient is a function of the diffusion coefficient, crystal size and local hydrodynamics. Besides on the surface integration mechanism, the rate coefficient for surface integration also depends on the size of the growth units (because of surface diffusion and steric orientation) and the lattice structure.

Crystal dissolution is not the exact opposite of crystal growth: dissolution does not require surface diffusion and orientation of atoms, ions or molecules, and is therefore

in general limited by mass transfer. Crystal dissolution thus has a first order dependency on the supersaturation, its driving force. The rate coefficient for dissolution is a function of the diffusion coefficient, crystal size and local hydrodynamics. Because dissolution is usually mass transfer limited, dissolution at crystal edges and corners is faster due to steric favouring. For this reason, crystals are easily rounded off once dissolution starts.

2.3.3 AGGLOMERATION

An agglomerate is defined as the mass formed by the cementation of individual particles, probably by chemical forces (Randolph and Larson, 1988). A mass formed by a group of particles held together by only interparticle forces is called an aggregate.

Agglomerates are usually undesirable because they contain mother liquor between the primary crystals that form the agglomerate. This liquor is hard to remove during drying, and promotes caking of the product during storage. Furthermore, agglomerates also tend to break more easily than solid crystals, during which they also release solvent. There are however also cases where agglomeration is stimulated, namely when the primary particles are too small for acceptable downstream solids handling.

Agglomeration first of all requires the collision of two or more crystals. The collision mechanism depends on the sizes of the crystals involved: perikinetic (due to Brownian motion; small particles), orthokinetic (due to fluid shear) or inertia (due to differences in relaxation time; differently sized particles). Next, these crystals must form an aggregate as a result of interparticle forces, such as Van der Waals (attractive), electrostatic (repulsive) and steric (repulsive) forces. Finally, cementation of these crystals as a result of growth, before the aggregate is disrupted, is required to create an agglomerate.

The driving force for agglomeration is the supersaturation. Without supersaturation, aggregates can be formed but agglomerates cannot. The rate coefficient or kernel for agglomeration is a function of the number of particles (collision chance), the sizes of the particles involved (agglomeration mechanism), and in the case of orthokinetic agglomeration the fluid shear or energy dissipation (collision chance, time between collision and disruption). An example of the shear rate dependency of the orthokinetic agglomeration rate constant is shown in Figure 2.2.

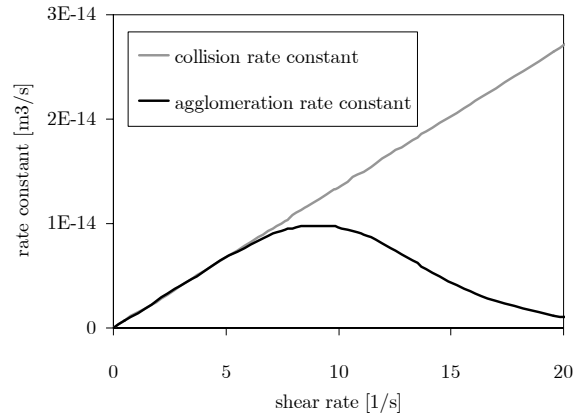


Figure 2.2: Shear rate dependence of the rate constant for the orthokinetic agglomeration of Calcium Oxalate after Mumtaz et al. (1997).

The collision frequency increases with increasing shear rate, but if the shear rate becomes too high, aggregates are disrupted before sufficient cementation has taken place. As a result, the rate constant for orthokinetic agglomeration first increases and subsequently decreases with shear rate.

2.3.4 BREAKAGE

Similar to attrition, breakage can occur as a result of crystal-pump, crystal-vessel wall or crystal-crystal collisions. The difference between breakage and attrition is not a distinct one. The fracture of a particle into one slightly smaller particle and many much smaller fragments is defined as attrition. Breakage involves the fracture of a particle into two or more pieces. To accomplish the total fracture of a particle requires considerably more energy than that needed for attrition. If the impact energy of a single collision is not sufficient, repeated collisions, which result in accumulation of crystal stress, are required for breakage.

The driving force and rate coefficient for breakage are mainly a function of the same process conditions and particle properties as discussed for attrition. In addition, the rate coefficient or resistance for breakage is also influenced by the collision history of the particles involved.

2.3.5 SEGREGATION

Segregation is not a crystallisation mechanism in the sense that it forms a particle, increases its size or reduces its size. However, as it can have a significant effect on the final product quality it is discussed here. Particle segregation is a result of slip with respect to the liquid motion. An important effect that can only be described if segregation is taken into account, is the non-uniform distribution of solids in a

crystalliser. For instance, if the circulation intensity is lowered in a crystalliser, the relative amount of solids in the lower part of the crystalliser will increase.

Particle segregation is a function of particle size, liquid velocity, solids concentration, and the difference in material density between the liquid and solid phase.

2.4 MODELLING AND DESIGN OF CRYSTALLISATION PROCESSES AND PRODUCTS

As outlined in subchapter 2.2, the product composition or internal state of a crystalline product is determined during its formation by a combination of crystallisation mechanisms or events. Furthermore, crystalline products are of a distributed nature, i.e. they possess a range of values for the internal states of the individual crystals constituting the product. The distributed nature is a result of these individual crystals having different formation histories, i.e. during their stay in a crystalliser they do not all experience the various crystallisation mechanisms at the same time and at the same rate. The rates of the crystallisation mechanisms are a function of both the process conditions (slurry states) experienced by the individual crystal and its crystal properties (internal crystal states).

2.4.1 SPATIAL DISTRIBUTION

Process conditions, such as supersaturation, energy dissipation, pressure, temperature and the concentration of particles with certain properties, will rarely be uniformly distributed in a crystalliser. Non-uniformity will increase with increasing crystalliser scale and/or increasing rates of crystallisation mechanisms that change one or more of these process conditions. The process condition with the strongest gradients is typically the energy dissipation followed by the supersaturation. Prediction of product composition thus requires knowledge about the crystal's whereabouts, the process conditions in the various regions of a crystalliser, and the process condition dependencies of the rates of the various crystallisation mechanisms.

Although process conditions are far from uniformly distributed in most crystallisers, geometrically lumped descriptions of the crystallisation processes in a vessel still prevail. Such descriptions will rarely provide reliable predictions of product quality for scale-up purposes, as the following examples illustrate:

- The mean specific power input of the impeller, which is often used to predict secondary nucleation due to crystal-impeller collisions, contains no information on the velocity gradients in the vicinity of the impeller. As a result, the differences in collision velocities (magnitude and angle) using two different impellers operated at the same mean specific power input are not taken into account.
- A geometrically lumped description only yields one average value for the supersaturation, thus ignoring possible peak values. In evaporative crystallisers, the supersaturation will be above average in the boiling zone and lower, possibly undersaturated, after the heat exchanger.

Near feed points of a cooling crystalliser, where a saturated stream is mixed with the much cooler contents of the vessel, high supersaturation values can be expected, possibly leading to primary nucleation and/or scaling. In both these examples, a lumped description of the crystallisation process will probably ignore or definitely underestimate the occurrence of certain phenomena, such as dissolution and primary nucleation.

- Whenever there is a difference in material density of the solid and liquid phase, particle segregation will occur to some extent. To what extent depends on the internal circulation rate induced by the pump or impeller. If particle segregation is such that large crystals will have a significantly shorter residence time in the boiling zone, the growth rate of these crystals will appear to be below average. In a geometrically lumped description of such a process, this effect can only be described by lowering the growth rate constant of the larger crystals. The error in this approach becomes evident when the internal circulation rate is increased, particle segregation decreases and the growth rate of these particles approaches average values.

These examples also obviate the problems encountered in practice when a kinetic model, of which the parameters were estimated from experiments on a non-ideally mixed crystalliser, is applied to another crystalliser scale or type. Those kinetic parameters will undoubtedly contain hydrodynamic information, such as the above-mentioned particle segregation effect, which is crystalliser and operating conditions specific.

2.4.2 DYNAMIC BEHAVIOUR

Process conditions may vary with time. Consequently, the product quality resulting from a crystallisation process will not always be constant in time. Dynamics in product quality are usually most noticeable in the crystal size distribution. Batch processes are inherently dynamic, but continuous processes can also exhibit dynamic behaviour (Qian and Botsaris, 1996; Eek et al., 1995b). Dynamics in continuous processes do not only occur as a result of process disturbances or set point changes, but can also occur when the process inputs are kept constant and no disturbances occur. In the latter case, unstable process behaviour is usually a result of the interaction between crystallisation mechanisms such as nucleation and growth. For instance, a period of low nucleation rates will result in a decrease in the volume specific crystal surface area available for growth, which will lead to an increase in the level of supersaturation and hence in the crystal growth rate. As the same crystal mass is being deposited on a smaller number of crystals, the average crystal size will increase. The increase in supersaturation and crystal size can respectively lead to an increase in primary and secondary nucleation rates. Consequently, the supersaturation level and average crystal size will decrease, thus leading to a new period of low nucleation rates.

As decisions taken during design determine to a great extent the controllability of a process, the effect of process dynamics on product quality and process performance should not be postponed to the control system design stage. Dynamic modelling of crystallisation processes is therefore essential from the process design stage onwards.

2.4.3 REQUIREMENTS FOR A CRYSTALLISATION PROCESS AND PRODUCT MODELLING FRAMEWORK

Design purposes require a predictive modelling framework that captures the causal chain ‘equipment geometry and operating conditions; process conditions; crystallisation kinetics; product composition; product performance’, which has been discussed throughout this chapter and is depicted in Figure 2.1. A second requirement is related to practical considerations such as computational times, robustness, maintainability, configurability, etc. The balance between these two categories of requirements depends on the type of engineering activity. For instance, the requirement for a predictive model decreases as one shifts the emphasis from the design of process, equipment and operating policy to the design of a new operating policy and further to model-based control, i.e. adhering to a given operating policy. At the same time, the need for short computational times (or more importantly a guaranteed solution time) and robustness are significantly more important for control than off-line design purposes.

The main focus in this work is on the design of crystallisation processes. Consequently, the primary focus here is on a modelling framework with predictive capabilities. As has become apparent in this chapter, industrial crystallisation is a spatially distributed and time dependent process involving a product with distributed properties. A comprehensive crystallisation process and product model should therefore consist of a framework providing resolution with respect to (i) the external co-ordinates representing the geometric space of the crystalliser, (ii) the internal co-ordinates such as crystal size, shape and internal energy, and (iii) the time co-ordinate. This framework would be populated with components such as:

- First principle thermodynamic models to calculate phase equilibria (S/L/V), attachment energies (morphology prediction) and periodic bond chain analysis (polymorph prediction).
- First principle kinetic models for primary nucleation, secondary nucleation, growth, attrition, breakage and agglomeration.
- First principle hydrodynamic models to calculate liquid motion, particle motion, fluid shear, energy dissipation rates, etc.
- Equations of conservation: component mass balances, energy balances and population balances. Population balances are used to statistically describe the evolution of distributed properties, such as size, lattice strain and purity, amongst a crystal population. The number of distributed properties taken into account determines the number of internal co-ordinates.

Use of such a process and product model would involve first principle modelling of all crystallisation phenomena from the nano scale right up to the macro scale and with time scales varying from microseconds to days.

Unfortunately, use of such a model is currently not feasible for at least two reasons. First of all, it is at present impossible to derive the knowledge and understanding of all these phenomena from first principle models only. Consequently, heuristics, tabulated data, laboratory and pilot plant scale experiments continue to constitute a major part of the domain knowledge necessary for the design and optimisation of crystallisation processes. Secondly, for certain crystallisation phenomena, present computational capabilities are barely sufficient to perform simulations let alone optimisation calculations (as required for design purposes) using a first principle model of that single phenomenon. For instance, stand-alone morphology predictions and hydrodynamic simulations often require computations in the order of days or even weeks.

Any crystallisation process model that is developed now or in the near future will therefore need to (i) be of a hybrid nature, i.e. a combination of first principle and heuristic models, and (ii) encompass model decomposition and/or model reduction steps, if it is to be practical for design purposes. Depending on the model application, certain shackles of the causal chain will be modelled in great detail while the remaining shackles are represented by simplified models.

Nevertheless, even if there were first principle models for all crystallisation phenomena and no computational limitations, would an all-inclusive process and product model be ideal for engineering purposes? This is one of the questions that will be addressed in the next paragraph.

2.4.4 NEED FOR A SYSTEMATIC DESIGN PROCEDURE

This chapter has illustrated the need for a predictive process and product model to reliably and efficiently design crystallisation processes that meet their product and process performance criteria. However, as will be argued in this final sub chapter, the development of such a product and process model is not sufficient. Equally important is the availability of a systematic procedure to guide the design process. A systematic design procedure can improve the quality of designs and speed up the design process by serving the following purposes:

- Organise design tasks such as collecting design specifications, domain knowledge acquisition, synthesis (generating design alternatives) and analysis (evaluating designs).
- Improve reproducibility of the design process by capturing the design rationale in order to improve not only future designs but also the employed design procedure and/or crystallisation process and product model.
- Decompose the design problem to reduce the number of specifications and degrees of freedom that need to be considered simultaneously.

The second purpose, reduction of the number of design specifications and degrees of freedom that need to be considered simultaneously, is typically achieved by focussing on fragments of the causal chain in sequence as opposed to considering the entire chain simultaneously. This reduction has two advantages. Firstly, it does not require numerical solution of the overall crystallisation process and product modelling framework, thus providing a scope for reduction in required computational efforts, which is essential to enable the generation of design alternatives within an acceptable timeframe. Secondly, it aids the evaluation of design alternatives by a human process designer. Dealing with a smaller subset of design specifications and degrees of freedom facilitates judgment on the basis of the designer's domain knowledge and intuition as regards the crystallisation process. Even when computational limitations disappear, it is expected that this last advantage will remain a very compelling reason for decomposition of design problems.

It is the author's opinion that a systematic and sufficiently detailed procedure is not yet available for the design of crystallisation processes. One of the reasons for the lack of activity in this research area is undoubtedly the lack of predictive models for analysis and optimisation of design alternatives. However, some very relevant work has been done in both the fields of process design and crystallisation. Based on the pioneering work of Douglas (1985) concerning the conceptual design of vapour/liquid processes, Rajagopal et al. (1992) developed a hierarchical design procedure for solids processes in general. More specific design procedures have been developed for fractional crystallisation (Dye and Ng, 1995), reactive crystallisation (Berry and Ng, 1997) and the interactions between the crystallisation step and the downstream processing (Rossiter and Douglas, 1986). These procedures mainly focus upon the synthesis and (economic) evaluation tasks of the design process. A comprehensive overview of the state-of-the-art of systematic design procedures for chemical engineering processes in general is given by Gavrilu (1998) and Herder (1999).

The development of a detailed systematic design procedure for crystallisation processes and products is the subject of the next chapter.

2.5 CONCLUSIONS

The quality of a crystalline product is in practice defined in terms of product performance characteristics, which are typically of a qualitative nature and equipment dependent, whereas first principal crystallisation models predict crystal quality in terms of size, morphology and purity. Bridging the gap between product performance and product composition is a challenging step in the design of crystallisation processes and products.

A fully predictive model for crystallisation processes and products requires a framework that provides resolution in external co-ordinates, internal co-ordinates and the time co-ordinate. This framework needs to be populated with equations of conservation, first principle models for the thermodynamics and kinetics, and performance models in order to capture the causal chain 'equipment geometry and

operating conditions; process conditions; crystallisation kinetics; product composition; product performance’.

Numerical solution of such a comprehensive process and product model is currently infeasible within an acceptable timeframe. At the same time, the number of design specifications and degrees of freedom involved in the overall crystallisation process design problem is too large for evaluation by a human process designer, even when guided by a systematic design procedure. The logical solution for both these problems is a decomposition of the design problem, which allows one to focus on fragments of the causal chain in sequence as opposed to considering the entire chain simultaneously.

3 A HIERARCHICAL DESIGN PROCEDURE

Systematic design procedures are aimed at improving the quality of both the design and the design process. A new hierarchical procedure for the conceptual design of solution crystallisation processes is proposed. The hierarchy consists of four design levels. The first two design levels have a product engineering character, whereas the last two design levels have a process engineering character. At each level of the design procedure the design specifications, design variables and the domain knowledge necessary to synthesise, analyse and optimise design alternatives are (re-)considered. The design procedure is intended to cover various scenarios as regards the destination of the crystalline product (main product, by-product or waste product) and the role of the crystallisation process (conversion, separation or purification).

3.1 INTRODUCTION

As argued in the previous chapter, predictive process and product models are necessary but not sufficient for the design of crystallisation processes and products that meet the specified performance criteria. In addition to models, there is a need for a systematic design procedure outlining the various steps in the design process and advising on when to use which design tools, models, data, etc. Typical benefits to arise from the use of a systematic design procedure are:

- The ability to deliver crystallisation process designs of a consistently high quality (*design effectivity*).
- A reduction in the duration of the overall design process, e.g. by removing the need for pilot scale experiments for scale-up purposes (*design efficiency*). This helps meet one of the increasingly more important design requirements, viz the available time-to-market, which is decreasing continuously.
- Reproducibility of the design process (*traceability of design decisions and rationales*). This is essential to improve on existing designs and identify any remaining errors in the applied domain knowledge and/or design procedure.
- A mutual awareness in a design team of the tasks that the various members have in the various stages of the design process.

It is the author's opinion that a systematic and sufficiently detailed procedure is not yet available for the design of crystallisation processes. One of the reasons for the lack of activity in this research area is undoubtedly the lack of predictive models for analysis and optimisation of design alternatives. This opinion is most probably also shared by Villadsen (1997) and Wintermantel (1999), who both identified a lack of systematic procedures and design tools for structured products in general. However, some very relevant work has been done in both the fields of process design and crystallisation.

Starting with the field of systematic design procedures for chemical engineering processes in general, Rajagopal et al. (1992) developed a hierarchical design procedure for solids processes in general. This procedure is based on the pioneering work of Douglas (1985) concerning the conceptual design of vapour/liquid processes. More specific design procedures have been developed for fractional crystallisation (Dye and Ng, 1995), reactive crystallisation (Berry and Ng, 1997) and the interactions between the crystallisation step and the downstream processing (Rossiter and Douglas, 1986). These procedures mainly focus upon the synthesis and (economic) evaluation tasks of the design process.

Design procedures originating from the field of crystallisation include work by de Jong (1984), Bennett (1984, 1993) and Mersmann (1988). These procedures contain many useful elements with respect to process and equipment design, but pay little attention to product design. Whereas these procedures obviously incorporate more detailed crystallisation knowledge than those developed by Douglas, Ng and co-workers, they lack some significant elements. For instance, following one of the procedures developed by de Jong, Bennett and Mersmann can lead to a considerable number of implicit decisions. Furthermore, if the design resulting from one of these procedures does not satisfy all the design specifications, there is usually no methodology for generating design alternatives.

The systematic design procedure presented in the remainder of this chapter contains many elements from both the field of systematic design procedures for chemical engineering processes in general as well as the field of crystallisation. Models used within this procedure are of both a rigorous and empirical nature. Heuristics are considered useful because their application is usually rapid and relatively simple. Furthermore, heuristics are often the only alternative for domains where fundamental knowledge is not available or applicable. This chapter is largely a more comprehensive description of the design procedure presented by Bermingham et al. (2000).

3.2 A DESIGN HIERARCHY

One of the conclusions drawn from Chapter 2, states that the design of crystallisation products and processes encompasses too many design specifications and degrees of freedom to be considered simultaneously. This is illustrated by Figure 3.1, which shows a large number of degrees of freedom or design variables that can affect the filterability, which is merely one of the many possible design specifications for crystallisation.

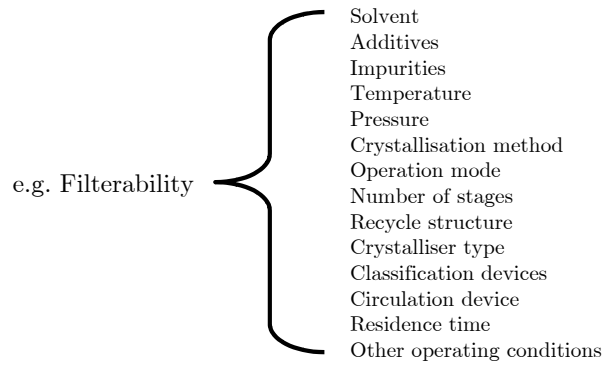


Figure 3.1: Design complexity illustrated.

The first step in the development of a systematic design procedure for crystallisation processes and products, aimed at delivering the benefits outlined at the beginning of the introduction, is to decompose the design process into sub problems concerned with fewer design specifications and degrees of freedom. Here a hierarchical decomposition is chosen that largely resembles the causal chain ‘equipment geometry and operating conditions; process conditions; crystallisation kinetics; product composition; product performance’ discussed in Chapter 2. The proposed design hierarchy consists of one level at which the initial design specifications are formulated and four design levels (see Table 3.1).

Table 3.1: Proposed level decomposition.

0	Initial design specifications
I	Design of the crystalline <i>product</i>
II	Physical/chemical design of the crystallisation <i>task</i>
III	Flowsheet design of the crystallisation <i>process</i>
IV	Design of a crystallisation <i>stage</i>

Returning to the filterability example, Figure 3.2 shows how the hierarchical decomposition of the design process limits the number of design variables under consideration by focusing on one design level at a time. Later it will also become clear how this hierarchical decomposition reduces the number of design specifications and the amount of knowledge that needs to be considered simultaneously.

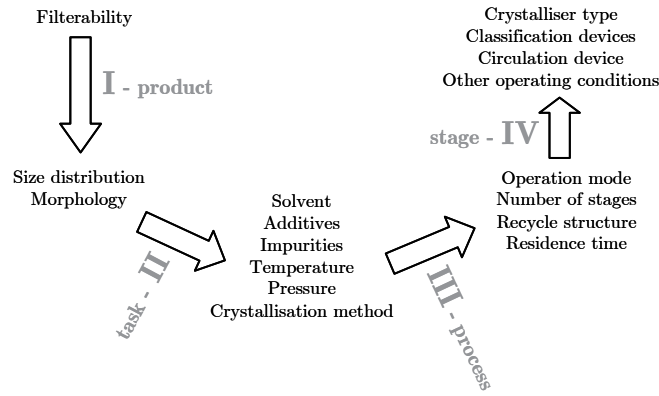


Figure 3.2: Illustration of hierarchical decomposition

Design levels I through IV are aimed at finding design alternatives that meet the initial design specifications. As the designer progresses from one level to the next the emphasis shifts from product design (levels I and II) to process design (levels II and III) and ultimately to crystalliser design (level IV). In contrast with methodologies as proposed by Douglas (1985), the degree of detail does not automatically increase with each level. For product related issues it actually decreases, and for process and equipment related topics it increases when progressing to the next design level.

At all four design levels the same tasks are performed, i.e. definition of design space and specifications, assessing domain knowledge, synthesis, analysis, evaluation and optimisation. (see Figure 3.4). These tasks will be discussed briefly below and further on they will be exemplified at each level.

The first step at each level is to make an inventory of applicable design specifications and to identify the design space. The specifications consist of relevant initial design specifications from level 0 and design specifications propagated from a previous level. Propagated design specifications are in fact design variables, which are fixed after completion of a previous level. The design space is defined by the available design variables and operational variables.

The second step is to gather domain knowledge that relates the design variables and operational variables to the behaviour of a design alternative. This knowledge may consist of heuristics, experimental data and behavioural models. If parts of the domain knowledge are considered inadequate, additional experimental and modelling efforts may be required.

The third step, the synthesis task, involves the creation of design alternatives. A design alternative is characterised by its structure and its scale. In this design procedure, we will classify design and operational variables that determine the structure as discrete, and those that define the scale as continuous design and operational variables.

The fourth step is the analysis of the physical behaviour of the design alternatives. Subsequently, the set of behavioural results is evaluated (step five).

The evaluation first of all concerns the compliance of the design alternatives' behaviour with the design specifications. If this evaluation is positive, the design alternative is propagated to a next design level, accompanied by new design specifications. These propagated specifications are in fact design variables and operational variables set at a previous level. This interaction between subsequent levels of the design hierarchy is again illustrated for the filterability example (see Figure 3.3).

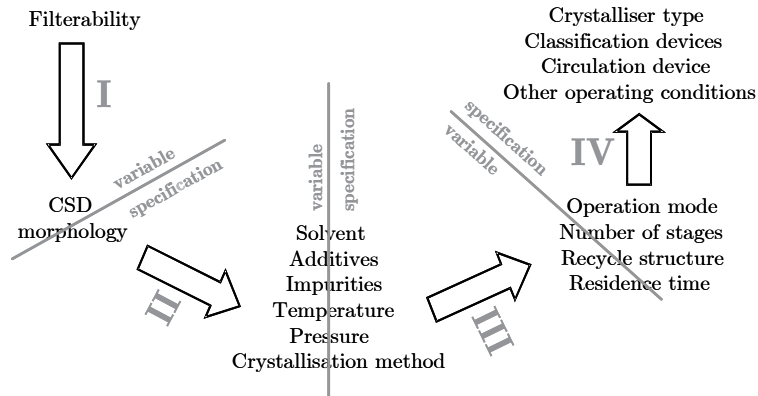


Figure 3.3: Illustration of interactions between levels, i.e. propagation of design variables from a previous level to a next level where they are treated as a design specification.

If the design alternatives fail the evaluation step, their performance is optimised by modifying their structure and scale, i.e. by returning to the synthesis step. Normally, a screening of the economic potential will be part of any evaluation step. However, such screening is not covered in this chapter. Secondly, the evaluation phase may be used to judge the quality of the applied domain knowledge. If a part of the knowledge is considered inadequate, additional experimental and modelling efforts may again be called for.

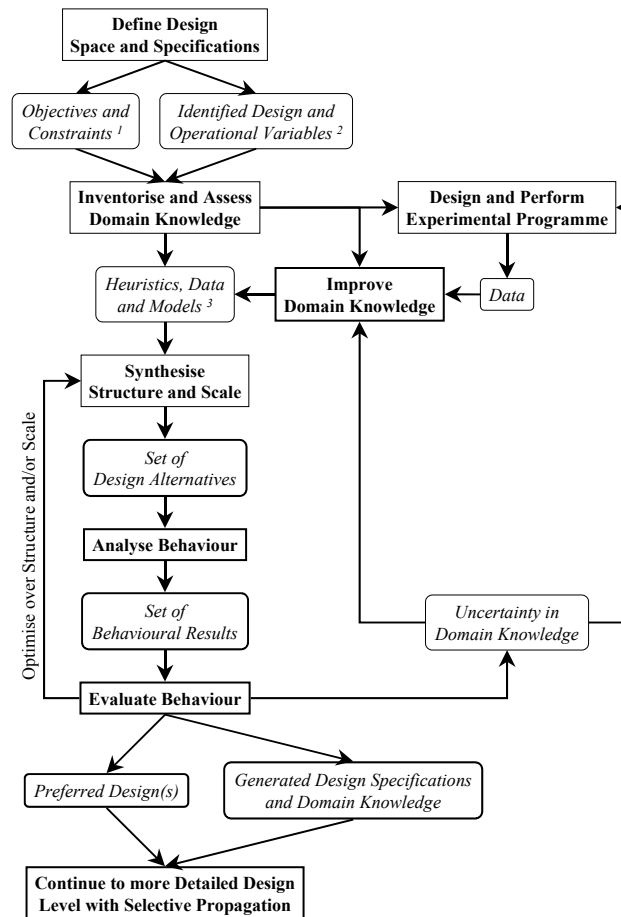


Figure 3.4: Typical sequence of design tasks and the outcome of these tasks. The superscripts refer to the column numbers of Table 3.3 through Table 3.7.

A comprehensive execution of all the above-mentioned tasks at all four design levels, while considering all the design specifications listed in Table 3.2, will obviously lead to very lengthy design trajectories. Assigning importance to the various initial design specifications is thus crucial, as the specifications taken into consideration largely determine the amount of effort put into each design level.

3.2.1 INITIAL DESIGN SPECIFICATIONS

Table 3.2 shows the types of requirements considered at level 0. Depending on the nature of the crystalline product (main product, by-product or waste product) and the role of the crystallisation process (conversion, separation or purification) some design specifications will be deemed necessary, desirable or irrelevant.

Table 3.2: Level 0 - Initial design specifications.

Product performance requirements
<i>In the crystalliser:</i> no flotation, suspendability
<i>Downstream handling:</i> filterability, washability, dryability, dissolution rate, pneumatic handling, freedom from dust, flowability, mechanical strength
<i>Customer application:</i> no caking in storage, dissolution rate, mechanical strength, freedom from dust, bulk density or porosity, aesthetic appearance
Process requirements
feed composition, battery limits and conditions, production capacity, yield, energy consumption, controllability, reproducibility, resiliency, availability, SHE considerations
Design process requirements
design budget, time to market, in-house or licensed technology, available skilled design staff, traceability, explicitness of design decisions

The product performance requirements listed in the table above are examples of criteria used in practice to specify the required quality of a crystalline product. A description of some of these requirements can be found in Chapter 2.

Most of the process related requirements are self-explanatory, but there are a few that merit elaborating on. First of all, the yield of a crystallisation process. For cooling crystallisation processes, the yield is calculated from the initial or feed solution composition and the solute solubility at the final or product temperature for respectively batch or continuous operation. For evaporative crystallisation, the amount of solvent removed also has to be taken into account in the yield calculation. If the crystalline product is a hydrate, account must be taken of the water incorporated in the crystal lattice, since this water is not available for retaining the solute in solution (Bennett, 1993). The yield is also influenced in most processes by the removal of some mother liquor as a result of adherence to the crystal surface during solid/liquid separation. The adhering mother liquor is typically in the range of two to 10 percent of the crystal weight (Bennett, 1984). Secondly, the availability or reliability of the crystallisation process. The main phenomena to determine a crystallisation process' availability are fouling and blockage. For many processes, controlling the fouling is the determining factor in improving their economic performance (see for instance Bermingham et al, 1999). Whether fouling or encrustation will occur depends firstly on the solubility characteristics of the fouling component. The location in the crystalliser where fouling occurs, depends on the method of supersaturation generation, e.g. on heat exchange surfaces in cooling crystallisers and on the walls and agitator shaft at the vapour release surface in evaporative crystallisers.

As regards the design process requirements, these are also largely self-explanatory and are mainly taken into account implicitly in the remainder of this chapter.

3.2.2 DESIGN OF THE CRYSTALLINE PRODUCT

At this design level (see Table 3.3), the aim is to determine which product composition is required to meet the product performance criteria, i.e. the product related initial design specifications. Some examples of the relationship between product performance and product composition criteria are:

- Filterability and freedom of dust are strongly related to the content of fine particles. Reduction of the fines content is a common requirement in practice, in order to increase the throughput and availability of downstream solids handling.
- Aesthetic appearance is usually related to particle size uniformity.
- The colour of certain inorganic pigments obtained by precipitation depends on the product's crystal size distribution.
- Although large crystals are preferred for many applications, there are also cases where small crystals are favoured, e.g. for fast dissolution.
- The liquor inclusion content is in its turn related to crystal size or more specifically to the surface area per unit crystal mass. As small crystals have a relatively large surface area, they will typically contain more adhering mother liquor after filtration than larger crystals.
- The bulk density is determined by the polymorphism and morphology of the crystals.
- The caking tendency in storage is related to the liquor inclusion content.

Table 3.3: Design Level I - Design of the crystalline product.

Design specifications Objectives and Constraints	Design Variables	Domain knowledge
<i>Product:</i> <ul style="list-style-type: none"> • Filterability • No caking in storage • No flotation • Suspendability • Washability • Dryability • Dissolution rate 	<ul style="list-style-type: none"> • SHE considerations • Pneumatic handling • Freedom from dust • Flowability • Mechanical strength • Abrasion resistance • Bulk density or porosity • Aesthetic appearance 	<ul style="list-style-type: none"> • Polymorphism <i>Continuous:</i> <ul style="list-style-type: none"> • Morphology • Crystal size distribution • Purity • Maximum inclusion content
		<ul style="list-style-type: none"> • Filterability tests and models: permeability and compressibility • Shear tests • Indentation tests • Caking tests • Flowability tests • Safety aspects

Most of the relevant domain knowledge for this design level belongs to the field of particle technology, and has a strong empirical character. This is mainly due to the fact that product performance criteria are often equipment specific and hence cannot be defined generically. The development of fundamental knowledge in this field is further complicated by the need to account for distributed properties, seeing as a collection of particles can rarely be described by one size, one

morphology, one purity, etc. Depending on the importance of the product performance criteria, much experimental work may be needed for this design level. The design alternatives, i.e. sets of design variables, are propagated to design level II, where they are treated as design specifications.

3.2.3 PHYSICAL/CHEMICAL DESIGN OF THE CRYSTALLISATION TASK

The design specifications of level II, the physical/chemical design of the crystallisation task, are composed of process requirements from level 0 and propagated product composition characteristics from level I. Consult Table 3.4 for a list of specifications.

Table 3.4: Design Level II - Physical/chemical design of the crystallisation task.

Design specifications Objectives and Constraints	Design and Operational Variables	Domain knowledge
<p><i>Process:</i></p> <ul style="list-style-type: none"> • Production capacity • Feed composition • Yield • Energy consumption • Availability • SHE considerations <p><i>Product:</i></p> <ul style="list-style-type: none"> • Polymorphism • Morphology • Crystal size distribution • Purity • Maximum inclusion content 	<p><i>Discrete:</i></p> <ul style="list-style-type: none"> • Crystallisation method • Feed purification • Recrystallisation step • Solvent(s) • Additive(s) • Material of construction <p><i>Continuous:</i></p> <ul style="list-style-type: none"> • Pressure range • Temperature range • Concentration solvent(s) • Concentration additive(s) 	<ul style="list-style-type: none"> • Thermodynamic activity of species/components in solid, liquid and vapour phase • Adsorption (energy) of components/species on the various crystal faces • Scaling or encrustation tendency of components/species • Metastable zone with respect to homogeneous and heterogeneous primary nucleation • Physical properties, e.g. material densities and specific heats • Safety aspects

3.2.3.1 Solvent, additives and impurities

The polymorphism and morphology of the crystalline product are influenced by the choice of solvent and additives, crystallisation temperature and crystal growth rates. The domain knowledge required for this selection issue was traditionally obtained from experimental work, but the latter is increasingly being replaced by molecular modelling. This modelling technique involves first principles calculations for the adsorption energy of a component on a specific crystal face. The same knowledge is also essential to determine the sensitivity of the crystal purity, morphology and polymorphism for impurities in the feed, and hence determine the need for feed purification. Another possible source of impurities is the construction material used for the crystalliser, auxiliary equipment and piping. Some examples of changes in morphology due to the presence of an additive or impurity are listed in Table 3.5.

Table 3.5: Examples of changes in morphology due to the presence of an additive or impurity (after Bennett, 1984).

Material crystallised	Additive / Impurity	Effect	Concentration
NaCl	urea	formation of octahedral	Small
NaClO ₃	Na ₂ SO ₄ , NaClO ₄	formation of tetrahedrons
Na ₂ CO ₃ ·H ₂ O	SO ₄ ²⁻	reduces L/D ratio	0.1-1.0%
Na ₂ B ₄ O ₇	casein, gelatine	forms flat crystals
(NH ₄) ₂ HPO ₄	H ₂ SO ₄	reduces L/D ratio	7%
(NH ₄) ₂ SO ₄	Cr ⁺³ , Fe ⁺³ , Al ⁺³	formation of needles	50 ppm
	H ₂ SO ₄	formation of needles	2-6%
	oxalic acid, citric acid	formation of chunky crystals	1000 ppm
	H ₃ PO ₄ , SO ₂	formation of chunky crystals	1000 ppm
pentaerythritol	acetone solvent	forms plates
urea	biuret	reduces L/D ratio	2-7%
	NH ₄ Cl	reduces L/D ratio	5-10%
naphthalene	from cyclohexane	formation of needles
	from methanol	formation of plates

Solvent selection also has a significant influence on the attainable size range of a crystalline product. Selecting a solvent that results in a high solubility for a given solute typically leads to low relative supersaturations, low primary nucleation rates, high crystal growth rates and hence to large crystal sizes (Mersmann and Kind, 1988). These relations are depicted in Figure 3.5.

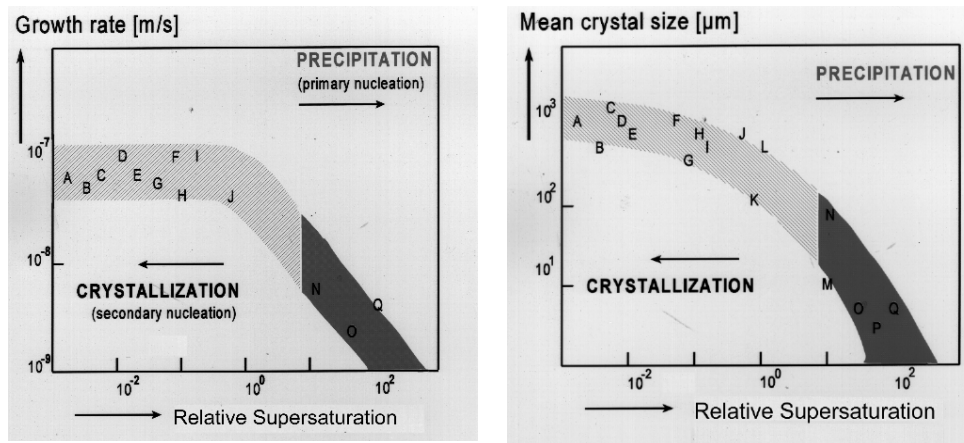


Figure 3.5: Growth rate and mean crystal size versus relative supersaturation for a number of salts (Mersmann and Kind, 1988). A: KCl, B: NaCl, C: (NH₂)₂CS, D: (NH₄)₂SO₄, F: Na₂SO₄, G: K₂SO₄, H: (NH₄)Al(SO₄)₂, I: K₂Cr₂O₇, N: CaCO₃, O: TiO₂, P: CaF₂, Q: BaSO₄

3.2.3.2 Crystallisation method

The crystallisation method is mainly selected on the basis of the thermodynamics of the solid/liquid equilibrium. For many systems, e.g. those involving electrolytes, these equilibria still need to be determined experimentally. A heuristic scheme for this selection process, based upon melt temperatures, T_{melt} , and equilibrium concentrations, C_{eq} , is given in Figure 3.6.

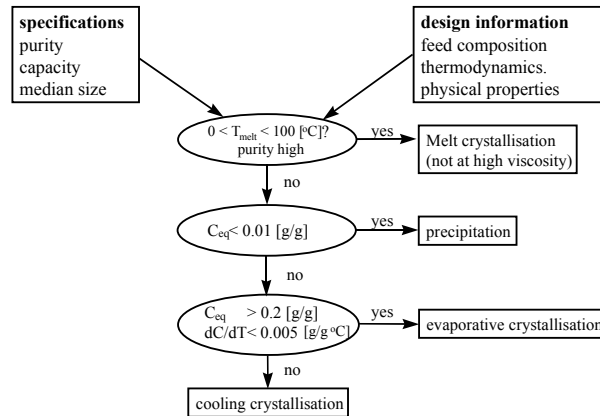


Figure 3.6: Crystallisation method selection
(after Kramer et al., 1999).

Other factors influencing this selection are the scaling tendencies of components present in the solution and the production capacity. For instance, the availability of a direct cooling crystallisation process can be reduced significantly by scaling on the cooling surface. Depending on the added value of the product, this loss in availability may or may not be considered a problem. Another example, a crystallisation method requiring a vacuum system is very inconvenient for low capacity processes.

Melt crystallisation

Crystallisation from a melt is chosen when high product purity is required and the use of a solvent poses problems due to safety or environmental problems. This crystallisation method may pose problems at high melting temperatures or when the melt possesses a high viscosity.

Precipitation

When the solubility of a component in a solvent is lower than approximately one weight%, precipitation is the appropriate crystallisation method. Because of the low solubility, high relative supersaturation values are required to obtain a reasonable production rate. These high supersaturations are obtained by adding two streams containing separate reactants that form a product with a very low solubility.

Evaporative crystallisation

Evaporative crystallisation is economically more favourable than cooling crystallisation if the solute's solubility has a very small temperature dependence. However, the operation of such a process is usually more demanding as it typically takes place at sub atmospheric pressures and hence requires a vacuum system.

Cooling crystallisation

This crystallisation method is energetically favourable and simple to operate. However, the prevention of fouling on the cooling surfaces and at the feed point may require major attention.

Flash cooling crystallisation

As an alternative for direct cooling using a heat exchanger, evaporative flash cooling can be used, which solves most of the fouling problems at the expense of a more complicated installation.

3.2.3.3 Other design variables

Operating conditions such as pressure and temperature are chosen such to obtain the highest possible yield, while obeying SHE constraints. Purity considerations determine the necessity for recrystallisation steps and the maximum crystal growth rate. With increasing growth rates the tendency of components to co-crystallise and entrapment of mother liquor increase. This introduces an upper limit for the supersaturation. The maximum allowable supersaturation also depends on the metastable zone. When the concentration significantly exceeds this zone, excessive primary nucleation may occur, which is usually undesirable as it decreases the average crystal size.

3.2.4 FLOWSHEET DESIGN OF THE CRYSTALLISATION PROCESS

The realisations of the design and operational variables from design level II are propagated to design level III, the flowsheet design of the crystallisation process. Together with relevant initial design specifications from level 0, they constitute the objectives and constraints for level III. An overview of the design specifications, design and operational variables and domain knowledge for this level is given in Table 3.6. Note that at this level all product related specifications except the CSD have disappeared. If relevant, they are now present as operating windows for pressure, temperature and supersaturation. These operating windows are used, because it is currently unfeasible to incorporate calculations of product properties, such as morphology and polymorphism, into dynamic process models including population balances.

To analyse the consequences of the choices at this design level on the CSD, a predictive process model consisting of thermodynamics, kinetics, mass, energy and population balances is required. As mentioned before, kinetic models cannot yet be derived from first principles only. Experimental design, experimentation and parameter estimation are hence an intrinsic step in crystallisation design. The

next chapter of this thesis is concerned with the development of a general crystallisation process model for analysis and optimisation with respect to the CSD as well as domain knowledge acquisition concerning the kinetics.

Table 3.6: Design Level III - Flowsheet design of the crystallisation process.

Design specifications Objectives and Constraints	Design and Operational Variables	Domain knowledge
<p><i>Process:</i></p> <ul style="list-style-type: none"> • Production capacity • Feed composition • Crystallisation method • Yield • Pressure range • Temperature range • Supersaturation range • Energy consumption • Availability, controllability and Resiliency • SHE considerations <p><i>Product:</i></p> <ul style="list-style-type: none"> • Crystal size distribution 	<p><i>Discrete:</i></p> <ul style="list-style-type: none"> • Operation mode • Number of stages • Feed configuration • Recycle structure • Location purge stream(s) <p><i>Continuous:</i></p> <ul style="list-style-type: none"> • Residence time in each stage or batch time • Recycle flow rates • Purge flow rate • Pressure and/or temperature in each stage • Heating/cooling duty or trajectory • Heat exchange rates 	<ul style="list-style-type: none"> • Thermodynamic activity of species/components in solid, liquid and vapour phase • Physical properties, e.g. material densities, specific heats and viscosities • Crystallisation kinetics, i.e. rate expressions for the nucleation, growth, attrition, agglomeration and breakage of crystals • Fouling kinetics • Shape factors of the crystalline components • Fire and explosion index

If a predictive crystallisation process model is not available or a quick calculation is required, a first estimate for the residence time of a continuous process, τ , can be obtained from the following simple function involving the desired median crystal size, L_{50} , and an estimate for the crystal growth rate, G , (for instance taken from Figure 3.5):

$$\tau = \frac{L_{50}}{3.67 \cdot G} \quad [3.1]$$

Another analysis, especially important for multiple stage evaporative crystallisation processes, involves the energy consumption and heat exchange surface area for the required heat exchange rates. The steam consumption and the total heat exchange surface area of an evaporative process consisting of N stages are proportional to respectively $1/N$ and N . Large deviations of the relationship for the surface area occur when a system exhibits significant boiling point elevations (BPE). When components with a high fouling tendency are present, time variant heat transfer coefficients need to be taken into account when sizing heat exchangers. For this purpose, another predictive model has been developed (Birmingham et al., 1999), which is not discussed any further in this thesis.

The resulting flowsheet design alternatives are propagated to level IV. If the suggested flowsheets contain multiple crystallisation stages, the relevant information for each stage is propagated to different instances of design level IV.

3.2.4.1 Operation mode

Criteria to select batch or semi-batch operation include a low production capacity, a short time-to-market, a short product lifetime, high value products, severe encrustation problems and a narrow CSD. According to Bennett (1993), continuous operation is typically only economically viable for relatively large production rates, viz from approximately 50 tonnes of product per day and upward. Nevertheless, a bulk product such as sugar is still produced batch wise because it leads to much narrower crystal size distributions than can be obtained from continuous processes. Another reason for producing bulk crystalline materials via batch operation is the presence of materials that have a very strong fouling tendency and consequently lead to frequent interruption of an otherwise continuous operation. Batch crystallisation is also employed when temperature or product characteristics require unusual precautions, or where very expensive materials are being handled and losses must be minimised, or when the cooling range is very wide (Bennett, 1984). Finally, batch operated processes provide more flexibility with respect to feedstock and product requirements as they can be more easily adapted.

3.2.4.2 Staged operation

A continuous crystallisation process can be employed in a single or multiple stage configuration. Multiple stage or multi-effect operation can be attractive when evaporative requirements exceed the capabilities of a single vessel and/or energy costs dictate staging of the operation (Moyers, 1987). Theoretically, the energy consumption and heat transfer area required for a multiple stage process are respectively inversely proportional and proportional to the number of stages. However, boiling point elevation decreases the temperature difference between the stages thus requiring an increased heat transfer area to maintain the same production capacity.

Multiple stage operation can also be economically interesting for cooling crystallisation processes. A typical case is when a large flow at a high temperature and concentration is cooled and the mother liquor is returned from the final stage to a dissolving or leaching station for reconcentration. In such systems, multiple stage cooling is used to allow the mother liquor from the final crystalliser to be heated by the upstream crystallisers (Bennett, 1993).

Another possible reason to opt for a multiple stage configuration is the requirement to produce a narrow CSD. By operating a multiple stage process in series, the residence time distribution and hence the crystal size distribution will be narrower than the CSD produced in the same volume of crystallisers in parallel or in a single crystalliser of the same volume. The feed configuration of a multiple stage process is not only governed by the required CSD but also by the feed temperature. A description of the various feed modes, viz forward, mixed, parallel and backward, is given by Mullin (1993).

Another potential advantage of multiple stage operation is the fact that crystal growth kinetics are usually favoured at higher temperatures. Because all stages

except the last can be operated at a higher temperature than the corresponding single stage process, multiple stage operation can result in an enhanced overall crystal size distribution (Moyers, 1987).

3.2.5 DESIGN OF A CRYSTALLISER STAGE

Practically all the design specifications from the previous level are present at this design level. The set is extended with equipment related specifications and with design and operational variables propagated from the previous level (see Table 3.7). All product related specifications except the CSD appear implicitly in the form of operating windows for pressure, temperature and supersaturation.

Table 3.7: Design Level IV - Design of a crystallisation stage.

Design specifications Objectives and Constraints	Design and Operational Variables	Domain knowledge
<p><i>Process:</i></p> <ul style="list-style-type: none"> • Production capacity • Feed composition • Crystallisation method • Yield • Operation mode • Pressure and temperature range • Supersaturation range • Residence time (distribution) • Heat exchange rates • No boiling in heat exchanger • No entrainment of droplets by vapour • Suspension criterion • Availability, controllability and resiliency • SHE considerations <p><i>Product:</i></p> <ul style="list-style-type: none"> • Crystal size distribution 	<p><i>Discrete:</i></p> <ul style="list-style-type: none"> • Crystalliser type • Fines classification and dissolution/clear liquor advance • Product classification • Heat exchanger type • Circulation device <p><i>Continuous:</i></p> <ul style="list-style-type: none"> • Equipment dimensions • Feed location • Product removal location • Solids concentration • Circulation flow rate • Operating conditions of classification devices • Flow rate through heat exchanger 	<ul style="list-style-type: none"> • Equipment characteristics • Hydrodynamics • Thermodynamic activity of species/components in solid, liquid and vapour phase • Physical properties, e.g. material densities, specific heats and viscosities • Crystallisation kinetics, i.e. rate expressions for the nucleation, growth, attrition, agglomeration and breakage of crystals • Fouling kinetics • Shape factors of the crystalline components

At this level, hydrodynamics is added to the fields of domain knowledge. Applications of this knowledge include the sizing and operation of classification devices, determination of minimum circulation rates for adequate particle suspension and optimisation of the product removal location. The use of computational fluid dynamics (CFD) packages to obtain hydrodynamic information is on the increase for crystallisation processes. However, it is not yet possible to combine CFD techniques with population balance modelling. To analyse the influence of kinetic-hydrodynamic interactions on the product CSD, the general crystallisation model mentioned at the previous design level can be

used in a compartmental manner to account for spatially distributed process conditions.

The final design alternative can be propagated to a next level, design of instrumentation and control. This design level is not considered in this thesis. However, Westhoff (2002) has extended the hierarchical design procedure presented here with two new levels, viz design of instrumentation and control and design of soft sensors.

3.2.5.1 Crystalliser type, circulation device, heat exchanger and classification

The first selection at this level involves the crystalliser type, e.g. fluidised bed crystalliser, draft tube baffle crystalliser, draft tube crystalliser, forced circulation crystalliser or simply a mixed tank. The order in which these crystallisers are mentioned here, usually coincides with decreasing crystal size for a certain crystallisation system. This trend is also depicted in Figure 3.7.

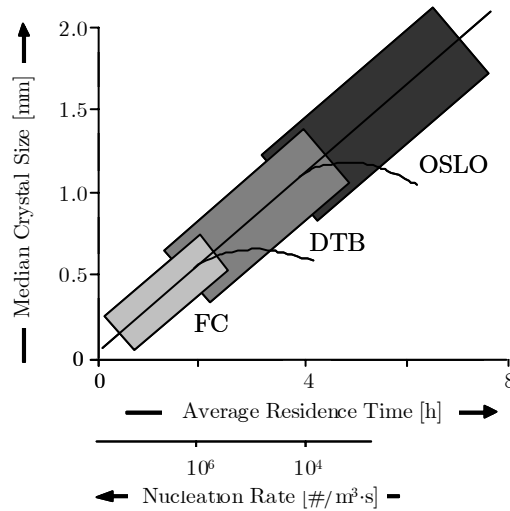


Figure 3.7: Expected median crystal size range for three basic crystalliser types as a function of residence time and nucleation rate (after Wöhlk et al., 1991).

The type of circulation device, impeller or pump, is determined by the crystalliser type and the mechanical properties of the crystals. For brittle materials, a device with a high pumping number must be selected to prevent excessive attrition.

Criteria for heat exchanger selection are low-pressure drops, to avoid flashing in heat exchanger, and fouling. If severe fouling is to be expected, a scraped surface heat exchanger should be considered. Alternatively, the heat exchanger will need to be cleaned regularly, in which case an external heat exchanger is preferable to an internal heat exchanger.

Fines or product classification can be employed to increase the average crystal size and/or stabilise the crystalliser with respect to the CSD. Fines classification with subsequent fines destruction is used to control the number of nuclei in a

crystallisation process. Fines classification can only be achieved in certain crystalliser types, as it requires a settling zone, e.g. the annular zone of a draft tube baffle crystalliser and the upper part of the suspension chamber in a fluidised bed crystalliser. Product classification may be performed internally or externally. Internal product classification is induced by the use of an elutriation leg, in which the product flow is withdrawn counter currently from the crystalliser with respect to the feed/circulation stream. Devices that can be used for external product classification include vibrating screens, hydrocyclones and hydrosizers (Gerla, 1995).

The different characteristics of the main crystalliser types with respect to the hydrodynamics, feed and product withdrawal configuration, mass and heat transfer are discussed below (after Neumann, 2001).

Agitated draft tube crystalliser

After the agitated vessel, the draft tube (DT) crystalliser is the most commonly employed design in industry. This is mainly due to its simple design and good mixing characteristics. It is operated predominantly in batch or fed-batch mode, as vacuum or cooling crystalliser. An overview of practical and theoretical knowledge with respect to draft tube design and impeller selection is given by EKATO (1991). A more detailed analysis of the relationship between process and product performance on the one hand and crystalliser scale, impeller design and operating conditions on the other is given by Jancic and Grootsholten (1984) and Mersmann and Rennie (1995).

Forced circulation crystalliser

The Forced Circulation (FC) crystalliser is the most common crystalliser type for continuous crystallisation processes in industry. Distinguishing feature of this equipment type is an external circulation circuit. Typically, FC crystallisers are designed to operate at residence times of up to two hours and solid densities within the range of 15 to 25 weight percent. Under these circumstances, the attainable median crystal size is in the range of 0.2 to 0.6 mm, which is comparable to that of the DT crystalliser. Generally speaking, the product obtained from commercial FC crystallisers is smaller and less uniform than that produced in DTB or fluidised bed crystallisers. The FC crystalliser is therefore used for simple crystallisation operation, where large crystal size is not a requirement. For further reading concerning design and operation of forced circulation crystallisers, the reader is referred to Bamforth (1965), Jancic and Grootsholten (1984), and Bennett (1993).

Draft tube baffle crystalliser

The Draft Tube Baffle (DTB) crystalliser is employed to obtain larger average crystal sizes and narrower size distributions than can be produced in a DT or FC crystalliser. The main characteristics of this crystalliser are the removal and subsequent destruction of fine crystals in combination with relatively low volume specific attrition rates. Note that a prerequisite for operating a fines destruction system is an appreciably large density difference between solids and mother liquor. DTB units are designed to operate at residence times in the range of three

to four hours and solid densities up to 25 weight percent. Under these circumstances the attainable median crystal sizes is in the range of 0.5 to 1.5 mm. More detailed information on this crystalliser type can be found in Bamforth (1965) and Bennett (1993).

Fluidised bed crystalliser

A coarser crystalline product can be obtained by using a fluidised bed (FB) or Oslo crystalliser. This is a result of the fact that an FB crystalliser does not have a pump displacing the crystal suspension, such as the circulation pump in an FC crystalliser or the agitating device in a DT/DTB crystalliser. Instead, the crystals are kept in suspension in a fluidised bed, which is maintained by a large circulation flow of clear mother liquor. FB crystallisers typically operate at residence times of up to eight hours and solid densities of up to 40 weight percent. The resulting median crystal size is usually within the range of 0.6 to 2.5 mm. Note that successful operation of this crystalliser type also requires an appreciably large density difference between solids and mother liquor.

3.2.5.2 Dimensioning and operating conditions

Before using a comprehensive predictive crystallisation process and product model to find the optimal crystalliser geometry and operating conditions, a number of empirical (shortcut) calculations can be performed to obtain initial guesses for these degrees of freedom. These calculations lead to a so-called basic crystalliser design (van Rosmalen et al., 1997).

Crystalliser volume

The crystalliser volume is simply calculated from the desired production capacity, the maximum solids concentration that the equipment can handle and the residence time.

Area for heat exchange

The area required for heat exchange is a function of the production capacity, the selected crystallisation method, the selected heat transfer mechanism and the system's thermodynamics. The selected crystallisation method determines the maximum allowable temperature difference between the process and utility side. In cooling crystallisation very small temperature differences, in the order of one to three Kelvin, have to be used to avoid fouling on the heat exchange surface. For evaporative crystallisation the temperature difference is much less restricted provided the solubility curve of the crystallising component has a positive derivative with respect to temperature. However, care must be taken to avoid flashing in the heat exchanger, which requires the heat exchanger to be placed well below the liquid level in the crystalliser. In practice this poses few problems and as a result temperature differences of up to 25 to 30 Kelvin are possible.

Cross-sectional area for evaporation

The diameter of an evaporative crystalliser has to be chosen such that entrainment of liquid droplets into the condenser zone is prevented. Formulas to calculate the maximum superficial velocity of the vapour and subsequently the

minimum diameter that satisfies this criterion can be found in van Rosmalen et al. (1997) and Mersmann and Rennie (1995).

Circulation flow rate

Initial estimates for circulation flow rates in crystallisers are typically obtained using empirical correlations for criteria such as a suspension criterion. To meet this criterion, the flow rate generated by a pump or impeller must be sufficient to keep most crystals in a suspended state. This implies that the local superficial velocity of the solution must exceed the settling velocity of a swarm of particles. A wide variety of relations are available in the literature to calculate this settling velocity, see for instance Mersmann (1988). A second criterion for the minimum required circulation flow rate or degree of macro mixing is related to liquid phase mixing. In order to prevent steep supersaturation gradients within the crystalliser, which may lead to excessive primary nucleation in certain areas and low crystal growth rate than others, the characteristic time for macro mixing must be less than the characteristic time for supersaturation depletion. Relationships for the calculation of these characteristic times are given by Garside (1985), Ploß (1985) and Mersmann (1988).

Flow through heat exchanger

There are two aspects to the flow rate through a crystalliser's heat exchanger, viz the flow rate and superficial velocity. The flow rate is a function of the required heat duty and hence the process' production capacity as well as the temperature increase of the process stream per pass. As regards superficial fluid velocities, values in the range of 1.5 to 3.0 ms⁻¹ are recommended to minimise fouling of heat exchanger surfaces and plugging of heat exchanger tubes (Moyers, 1987; Mersmann and Rennie, 1995).

3.3 DISCUSSION

Although the scope of this thesis as a whole does not include crystallisation methods such as precipitation, melt crystallisation and super critical crystallisation, it is the author's opinion that the hierarchical design procedure presented in this chapter is equally applicable to these crystallisation methods as it is to cooling, flash cooling and evaporative crystallisation.

Similarly, whereas the main focus of this thesis is on (grass roots) design of crystallisation processes, the presented hierarchical procedure should also be of use for other engineering activities, such as debottlenecking and optimising the operation of an existing plant.

The design procedure was well received by industry and academia when first presented at the 1999 FOCAPD conference (Birmingham et al., 2000). However, the real validation of this hierarchical design procedure requires (industrial) case studies. Recently, Westhoff (2002) presented the first real crystalliser design based upon this procedure. He found the design procedure useful to structure the design process of a pilot plant crystalliser and to identify design problems at an early stage. An interesting alternative for further testing of the proposed design

procedure is to let rather inexperienced designers use this procedure and see whether they can come up with designs that are considered of a high-quality by experienced designers.

3.4 CONCLUSIONS

The hierarchical decomposition used in the design procedure presented in this chapter is believed to provide a rational and useful breakdown of the crystallisation process and product design problem. However, so far this has only been confirmed by one application (Westhoff, 2002).

The hierarchical design procedure allows one to systematically deal with the large number of initial design specifications, design and operational variables and the wide variety of domain knowledge involved. Structuring of the relevant specifications, variables and knowledge at each design level simplifies the design problem and provides valuable insights for designers. It also ensures that design decisions are taken explicitly, which is of essence for the reproducibility of the design process. Furthermore, the design procedure also serves to highlight major shortcomings in design knowledge, i.e. product performance/composition relations (level I) and predictive models for the concise analysis of flowsheets (level III) and comprehensive analysis of single crystallisers (level IV) with respect to the CSD and supersaturation. The hierarchical decomposition does not imply a once-through process with respect to the design levels.

The value of heuristics and shortcut models on the one hand and rigorous first principle models on the other are both acknowledged. The heuristics and shortcut models as used in many conventional design procedures for crystallisation are valuable synthesis tools as they allow a rapid development of a base case design, in particular with respect to most of the discrete design decisions. Rigorous first principle models play an important role in both synthesis (mathematical optimisation) and analysis (simulation).

The ultimate aim of this design procedure, viz better designs in less time, cannot be guaranteed until the procedure as a whole is validated by means of industrial case studies. Main achievements so far are improved understanding of the design process and identification of bottlenecks in domain knowledge.

Finally, although the design procedure has been presented in the light of grassroots design, it can also be largely applied to retrofit and optimisation of process operation. One should think of synthesis at levels I and II and analysis tools at all levels.

4 A PREDICTIVE CRYSTALLISATION PROCESS MODEL

Generation, evaluation and optimisation of design alternatives requires crystallisation process models that possess a predictive capability with respect to the relations between product quality and process design-/operational variables. This chapter concerns the development of a modelling framework that can be employed to rapidly generate consistent process models for a wide range of crystallisation processes. Separation of kinetics and hydrodynamics is considered an essential cornerstone for the development of predictive crystallisation process and product models. For this separation, two modelling approaches are investigated as a possible basis for the modelling framework, viz compartmental modelling and computational fluid dynamics. The first of these two approaches is selected as it allows for a more comprehensive description of the CSD and the process dynamics, whilst making what is considered an acceptable sacrifice in spatial resolution. Subsequently, a compartmentation procedure, i.e. a procedure for constructing a network of compartments that approximates the main hydrodynamic characteristics of a given crystalliser, is presented. The compartments represent volumes of the crystalliser within which conditions are considered uniform. The same single compartment model is used to describe each and every one of these volumes. The main body of this chapter concerns the assumptions, characteristics, equations of conservation, kinetic equations and particle settling equations of this generic compartment model. Finally, it is shown how the developed crystallisation process and product modelling framework can be applied to the range of crystallisation processes covered by the scope of this thesis.

4.1 INTRODUCTION

The design procedure presented in the previous chapter can be considered to be a work plan to structure the sequence of the various design activities. Hence, to perform a design in practice, the design procedure needs to be combined with tools incorporating specific domain knowledge. This knowledge can be present in various forms, i.e. data, models and heuristics.

Examples of domain knowledge required at the various design levels of the hierarchical procedure are listed in Table 4.1. The last column of this table concerns the commercial availability of tools incorporating the domain knowledge required to perform a certain design task. The lack of dedicated tools for certain domain knowledge areas can be seen as a reflection of the areas, which constitute the major bottlenecks in the reliable design of crystallisation, processes.

Let us consider the design of a crystallisation process for a relatively simple system, such as the crystallisation of ammonium sulphate from water (used as model system throughout this thesis). For this system the various phase equilibria and physical properties can be measured or calculated sufficiently accurate for

design purposes. The lattice structure and morphology can be predicted using molecular modelling techniques or determined experimentally. The crystallisation kinetics of this system can be determined from laboratory scale experiments. However, the scale up of processes on the basis of these kinetics alone is typically very unreliable. This is a result of the fact that the relations between crystalliser type, scale and operation on the one hand and crystal size distribution, lattice structure and morphology on the other are hard to quantify and therefore poorly understood. Quantification of these relations requires firstly a process modelling framework for integrating kinetics, thermodynamics and hydrodynamics and secondly sufficient computational power to perform simulations and optimisations with this framework. Other relations that are difficult to quantify, concern the performance of the crystalline product outside the crystallisation system, i.e. in further downstream solids processing (filterability, washability, dryability, etc.), transport and in its final application. Research into the relations between these performance characteristics and composition characteristics such as lattice structure, morphology and size belongs to the field of particle technology. The author therefore considers particle technology and process modelling to be the weakest links in the chain of domain knowledge required for the reliable design of crystallisation processes and products. Despite the clear importance of particle technology, no further attention is paid to this subject. This is a direct consequence of the fact that downstream solids processing does not lie within the physical scope of this thesis, as defined in Chapter 1.5.

Table 4.1: Typical forms in which domain knowledge is present at the various levels of the hierarchical design procedure presented in Chapter 3.

design level	domain knowledge	dedicated tool available?	
I product	particle technology	no	
II process	thermodynamics (S/L equilibria)	yes	e.g. OLI, MultiFlash
	thermodynamics (morphology)	yes	e.g. Cerius ²
	physical properties	yes	e.g. OLI, MultiFlash
III flowsheet	thermodynamics (S/L equilibria)	yes	e.g. OLI, MultiFlash
	physical properties	yes	e.g. OLI, MultiFlash
	kinetics	no	
	process modelling (combining 3 above)	no	
IV crystalliser	thermodynamics (S/L equilibria)	yes	e.g. OLI, MultiFlash
	physical properties	yes	e.g. OLI, MultiFlash
	kinetics	no	
	hydrodynamics	yes	e.g. Fluent, CFX
	process modelling (combining 3 above)	no	

This chapter describes the development of a crystallisation process model aimed at providing the predictive properties required for design purposes. First the predictive requirements are addressed (4.2). Next the concept of compartmental modelling is introduced (4.3). Then we turn to the model of a single compartment, i.e. the building block for compartmental models (4.4). Finally, a

framework is presented which facilitates the use of the compartmental approach and the single compartment model for the modelling of the wide variety of processes included in the scope of this thesis (4.5).

4.2 PREDICTIVE REQUIREMENTS

For design purposes a model is required to predict the relations between crystalliser geometry and operating conditions on the one hand and production capacity and crystal quality on the other.

In Chapter 2.4 it was concluded that the predictive capabilities of existing crystallisation models have either been proven very limited or can be reasoned to be very limited. This is mainly related to the use of empirical kinetic models and the assumption of perfect mixing in crystallisers. In strong contrast, an ideal crystallisation process model as outlined in Chapter 2.4 consists of rigorous kinetic models and a framework providing resolution in 1) external co-ordinates representing the geometric space of the crystalliser vessel, in 2) internal crystal co-ordinates such as size, shape and internal energy, and in 3) the time co-ordinate.

The following two subparagraphs are concerned with two modelling approaches, viz computational fluid dynamics and compartmental modelling of processes, which provide differing degrees of resolution for the external co-ordinates. As regards the time co-ordinate, this definitely needs to be accounted for when considering batch processes, as these are intrinsically dynamic. Although less obvious, continuous processes often also merit a dynamic description. Continuous processes do not only exhibit dynamic behaviour during start-up or shutdown, but sometimes also during undisturbed operation, experimental evidence of which will be presented in Chapter 6 of this thesis. Finally, although crystal shape and internal energy will be taken into account in the model development, no independent co-ordinate systems will be used for these internal states.

4.2.1 KINETICS

As regards the crystallisation kinetics, models with a rigorous physical basis are required. Relevant information for rigorous or first principle kinetic models typically includes thermodynamic driving forces, physical properties, mechanical properties and *local* hydrodynamic conditions, but no dependencies on the *overall* hydrodynamics. Local (micro-scale) hydrodynamics is at the scale of the individual crystals, influencing processes such as mass transfer and crystal collisions, whereas the residence time and circulation time of crystals and liquid are influenced by the overall (meso-scale) hydrodynamics. Concluding, kinetic relations may contain only internal crystal states and local slurry states, and must be causal, i.e. kinetics only depend on past and present.

Another point of attention is the number of model parameters, as parameter estimation is often an intrinsic part of the design process. Empirical models typically have far less equations than first principle models, but often have many more parameters. They are therefore relatively computationally efficient for simulation and optimisation purposes. However, this is not necessarily so for

parameter estimation where the number of parameters is often more important than the number of equations. Furthermore, a large number of parameters is usually less favourable from a statistical point of view, as this tends to lead to more cross-correlation and larger confidence intervals for the estimated parameters.

Unfortunately, kinetic models that meet the above-mentioned criteria are non-existent for most if not all crystallisation processes. One must therefore scrutinise the quality of the available kinetic models on a case-by-case basis. However, in general it can be said that the predictive modelling of phenomena such as growth and secondary nucleation is more advanced than that of primary nucleation and agglomeration.

4.2.2 OVERALL HYDRODYNAMICS

For the separation of kinetics and *overall* hydrodynamics a spatial description of the crystalliser is needed. In practice, two approaches are encountered to achieve this separation, computational fluid dynamics and compartmental modelling. Both these approaches are described and compared in the following subsections.

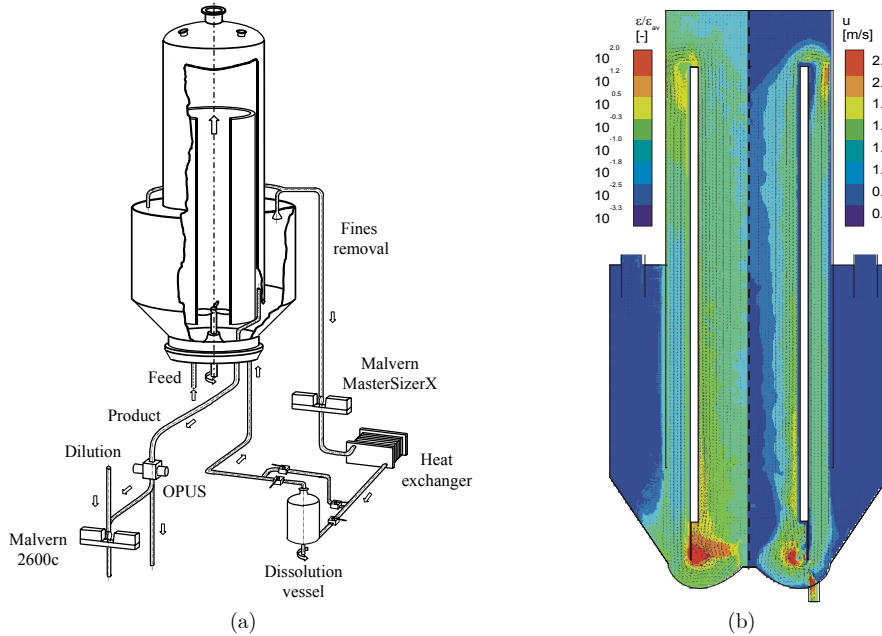


Figure 4.1: The 1100-litre DTB crystalliser at Delft University of Technology (a). Energy dissipation rate (b; left) and velocity profile in a vertical plane (b; right).

4.2.2.1 Computational fluid dynamics

Computational fluid dynamics (CFD) packages are currently the obvious choice when a high spatial resolution is required. CFD calculations involve solution of

the Navier-Stokes equations and result in detailed information on the hydrodynamics, such as velocity profiles and energy dissipation rate profiles.

Although insights into the relationship between crystalliser geometry and operating conditions on the one hand and hydrodynamic conditions on the other are clearly necessary, they are not sufficient. As outlined in Chapter 3, design specifications for a crystallisation process typically concern product and process performance and not, for instance, requirements with respect to energy dissipation rates. To bridge this gap most CFD packages allow incorporation of user-defined kinetic routines. However, with present computational power the price paid for the spatial resolution is such that incorporation of crystallisation kinetics, component mass balances, an energy balance and a population balance leads to simulation times that are impractical for design purposes. For example, ten Cate et al. (2000) required a week-long simulation on 8 PIII-500 MHz processors to simulate one second real-time flow behaviour of a 1100-litre DTB crystalliser (Figure 4.1). The calculations were done using a lattice-Boltzmann method with a LES¹ turbulence model. Note that this calculation method is computationally more demanding than $k-\varepsilon$ or Reynolds stress approaches. On the other hand, this example concerned a relatively small crystalliser and solution of the Navier-Stokes equations alone. Furthermore, these simulations are pseudo-single phase only, i.e. they only account for the presence of two phases (mother liquor and crystals) by means of an apparent viscosity. Such an approach cannot take into account the slip or relative motion between the two phases. However, prediction of this relative motion is of great importance in systems where significant particle segregation may occur. The degree of segregation increases with crystal size and the material density between the two phases.

Concluding, despite the valuable information provided by CFD methods, in their current status they can clearly not be used *directly* for the evaluation and optimisation of design alternatives. For design purposes, one needs to be able to calculate the dynamic process behaviour (~ days real-time) for several configurations within a practical time frame (~ hours CPU time).

4.2.2.2 Compartmental modelling

Compartmental modelling is a technique that has long been used in chemical reactor engineering (Kramers and Westerterp, 1963; Levenspiel, 1972), but relatively short in crystallisation (Garside, 1985; Klein, 1991, Jager et al., 1991). This technique comprises the division of the crystalliser into a number of units with well-defined flow patterns (plug flow, perfectly mixed) and was introduced to treat non-ideal flow and mixing problems. Such a problem is defined as one in which fluid dispersion causes the residence time distribution to deviate from that of either ideal extremes, plug flow or perfectly mixed. The non-ideal flow problem is dealt with by introducing a network of coupled units that have ideal flow characteristic. The objective is to find the combination of interconnected units that best reproduces the measured residence time distribution. These units are

¹ LES: Large Eddy Simulation

also called ‘cells’ or ‘compartments’. As the spatial resolution of a network of compartments is typically a few orders of magnitude less than used in CFD techniques, enough computational power is retained to include crystallisation kinetics, population balances and process dynamics.

However, the use of compartmental models introduces new model parameters that need to be determined, e.g. the number of compartments, the size of the compartments, and the exchange rates between the compartments. The values for these parameters determine whether the influence of crystalliser geometry and operating conditions on the hydrodynamics will be captured correctly. Obtaining correct values for these parameters is thus a key issue in compartmental modelling.

4.2.2.3 CFD vs. compartmental modelling

Both the CFD and compartmental modelling approach can provide resolution in the time, external and internal co-ordinates. However, considering the present computational power and the intended application of these approaches for design purposes, neither can provide the degree of resolution in all co-ordinates required for a general rigorous description of crystallisation processes. One must therefore deliberate upon the dominant crystallisation mechanisms for each crystallisation system, and subsequently determine the resolutions with which the various co-ordinates will be described.

In cooling and evaporative crystallisation, applied for easily soluble compounds, the supersaturation normally remains low and does not vary considerably over the vessel, while large crystals (500-5000 μm) are formed. Nuclei (new crystals) are mostly formed by the attrition of larger crystals, the rate of which is determined by the local energy dissipation rate and the surface roughness of the parent crystals. The surface roughness of a crystal is determined by the supersaturation levels it has experienced in the different crystalliser regions. The survival chance of the nuclei depends on the local supersaturation experienced during and shortly after formation. The healing of attrited crystals and the formation of liquid inclusions are also related to local supersaturation and energy dissipation rate values. The growth rate is dependent upon supersaturation and for the smaller crystals also upon the remaining stress from the attrition process. In suspension crystallisation, the rates of the dominant mechanisms typically have low order energy dissipation rate and supersaturation dependencies. Small changes in supersaturation and/or energy dissipation rates will therefore have a minor effect on the kinetics, thus reducing the need for a high spatial resolution. Furthermore, as relatively large crystals are formed in most suspension crystallisation process, particle segregation is often an important phenomenon that needs to be accounted for. Concluding, a compartmental approach is deemed suitable for the description and prediction of process behaviour and product quality of most cooling and evaporative crystallisation processes involving easily soluble compounds.

In precipitation processes, the mixing conditions and thus the local supersaturation and energy dissipation rate values, have long been recognised to dominate the final product specifications. This is a direct consequence of the high relative

supersaturations and the high order supersaturation dependencies of primary nucleation and aggregation, the dominant mechanisms in most precipitation processes. When a process is scaled-up, completely different local supersaturation and energy dissipation rate values may arise, resulting in different CSDs and often even the development of other polymorphic forms. The dynamics of precipitation processes are less pronounced because there is no direct dependency of the nucleation rates on the crystal size distribution. The above indicates a higher need for spatial resolution than a dynamic description of the process. For this reason, CFD packages, supplemented with elementary kinetic routines are nowadays used for the detailed modelling of precipitation processes.

The typical differences between suspension crystallisation and precipitation processes are summarised in Table 4.2.

Table 4.2: Suspension crystallisation versus precipitation; typical differences in physical characteristics and in the subsequent modelling approach.

	suspension crystallisation	precipitation
<i>physical characteristics</i>		
material's solubility	high	low
relative supersaturation	low	high
dominant nucleation mechanism	secondary	primary
supersaturation dependency of kinetics	low order	high order
crystal size [μm]	500-5000	1-50
solids content [vol.%]	10-20	
<i>modelling approach</i>		
hydrodynamics	2 or 3 phase flow 1-100 compartments	one phase flow 10^4 - 10^6 cells
kinetics	size dependent	size independent
crystal size distribution	discretised	moments

4.3 COMPARTMENTAL MODELLING

So far, this thesis has covered both suspension crystallisation and precipitation. However, the remainder of this thesis is primarily focused upon suspension crystallisation. Consequently, the compartmental modelling approach is adopted to account for the spatial distribution of process conditions, such as the supersaturation, energy dissipation and CSD, throughout a crystalliser. This approach provides a rough separation of the *local* intrinsic kinetics and the *overall* hydrodynamics, which also allows for a computationally feasible description of the process dynamics as well as a more detailed description of the CSD. In this work, the perfectly mixed compartment model is the only building block used for the construction of compartmental models. The characteristics, assumptions and equations of the perfectly mixed compartment model are subject of the next subchapter (4.4). A plug flow compartment model was not developed for the following reasons:

- Plug flow can be approximated by a cascade of perfectly mixed compartments.
- Dispersion or back-mixing in a mainly plug flow region can be accounted for more flexibly using a number of CSTRs in series; and
- Modelling a plug flow compartment that takes into account an axial and optionally radial distribution, involves solution of PDEs as opposed to ODEs for the dynamic conservation equations and introducing additional partial derivatives in the population balance equation. Numerical solution methods for PDEs are not guaranteed to be robust under all circumstances; using a cascade of CSTRs avoids this problem.

However, development of a plug flow compartment model should be considered for future work as it provides scope for a potential reduction in the number of variables/equations by using high order numerical methods to approximate the partial derivatives with respect to spatial co-ordinates. Note that a cascade of CSTRs is only a first order approximation.

In this paragraph, an approach is outlined for the derivation of compartmental models for suspension crystallisation systems. All compartments in a *compartmental* model are described with the same generic *compartment* model, i.e. the same equations of conservation, physical and thermodynamic property relations, kinetic rate expressions and parameters. Differences between compartments with respect to nucleation, growth, dissolution, attrition, breakage and aggregation rates are therefore purely a result of varying process conditions.

To justify the use of a compartmental modelling approach, compartmental models must be set up such that the compartments contain no or negligible internal gradients in supersaturation, energy dissipation and CSD. Considerable gradients may of course exist between the various compartments. The magnitude of these gradients is influenced by the kinetics and material properties of the material to be crystallised, the geometry of the crystalliser vessel and the operating conditions. Consequently, a compartmental model is not specific for a certain crystalliser, but may need to be re-derived for different operating conditions or another model system.

4.3.1 COMPARTMENTATION PROCEDURE

A compartmental model is characterised by the structure of the compartments (number, location, volume and shape) and the connectivity of the compartments (source and destination, flux and exchange area of the flows). In this work, the following compartmentation procedure, i.e. a procedure to construct compartmental models, was employed:

1. Introduce compartments to account for zones in the crystalliser, including external circulation loops, that have clearly identifiable specific functions and finite hold-ups, e.g. the main body (crystal

growth), annular zone (segregation with respect to crystal size) and fines loop (crystal dissolution).

This step mainly serves to account for the different residence times in the main functional zones of the crystalliser.

2. Create compartments for circulation devices such as impellers and pumps, where the highest energy dissipation rates are typically found.

This step is important for systems that require an accurate description of crystal collisions with impellers and pumps. Such is the case for most solution crystallisation processes, including the crystallisation of ammonium sulphate from water, where these collisions are considered the dominant source of secondary nuclei (Mersmann et al., 1988). A model for crystal-impeller collisions will be presented later in this chapter. This step is also of importance for systems with significant agglomeration, as described under step five.

3. Define compartments to represent the main circulation flow pattern within the crystalliser.

This step is rather arbitrary, even if flow patterns have been determined experimentally or calculated by means of CFD. However, that is not a matter for serious concern, because this step functions primarily as a precursor for refinement in the following steps.

4. Check all compartments for the presence of internal supersaturation gradients, or in other words, analyse the degree of liquid phase mixing.

For this purpose, an engineering rule of thumb is used: the half-time for supersaturation decay must be one order of magnitude larger than the residence time in the compartment. If this is not the case, further subdivision of that compartment is needed. Calculation of this half-time is discussed in section 4.4.3. Large supersaturation gradients are typically found near crystalliser inlets, e.g. feed point and fines return, in the vicinity of cooling surfaces, and in the boiling zone.

However, one can reason that compartmentation with respect to supersaturation provides little added value, if (i) secondary nucleation is the dominant nucleation mechanism, (ii) crystal growth is size independent and first order in supersaturation, and (iii) there are no undersaturated regions in the crystalliser. This reasoning is analogue to classical reaction engineering where the conversion is the same for a CSTR and PFR if the reaction kinetics are first order in the reactants.

5. Check all compartments for further gradients in the local energy dissipation.

Strong gradients may also be expected near feed locations, the edges of a draft tube and the edge of a skirt baffle. If they are indeed present, one or more of the compartments will be split up. This step cannot be performed unambiguously if no detailed hydrodynamic information is available, from either experiments or CFD modelling. This step is of special importance for systems where agglomeration is an important mechanism (Hollander, 1999). Rates of other crystallisation

mechanisms, such as primary nucleation and growth, typically have a low order dependency on the energy dissipation.

6. Now the number, location and size of compartments is known, distribute the overall heat or cooling duty of the crystalliser among the relevant compartments.

A rough approximation is to distribute according to the fraction of a heat exchanger surface that is present in each compartment; and

7. Calculate classification functions to describe the non-uniform distribution in the crystalliser of the solids phase due to particle segregation.

These functions act upon the flows connecting the individual compartments, and effectively render the residence time of crystals in a compartment particle size dependent. The classification function of a slurry stream is related to its superficial flow velocity, flow direction, viscosity and density difference between the liquid and solid phase. A model for calculating these functions is given in subparagraph 4.4.4. Note that although a compartment may have classified exit streams, its contents are always considered to be perfectly mixed.

At each step of the procedure, the connectivity of the compartments is determined by the magnitude and direction of the liquid flow in the various uniformly mixed regions. Of all flow rates in a compartmental model, knowledge of the flow rate induced by an internal circulation device is arguably most important. The magnitude of the circulation flow has a strong influence on both the spatial distribution of process conditions throughout the crystalliser and the collision frequency of crystals with the impeller or pump. For certain combinations of pump type and surrounding geometry the relation between pump frequency and flow rate, often given by the pumping number, can be obtained from equipment manufacturers or found in handbooks (Mersmann, 1995, p.226). If such a relation is doubtful or not available from these sources, the alternative is the use of CFD calculations. A good approximation for the flow rate at a certain pump frequency can be obtained from the velocity profiles.

For other flow rates than the main circulation flow rate, e.g. short circuiting flows, CFD results are the only practical source of information. The same holds for the values of local energy dissipation rates. Examples of work illustrating the use of CFD to aid the compartmentation process are de Jong et al. (1998), Urban and Liberis (1999), ten Cate et al. (2000). The work of Urban and Liberis is of special interest, as part of the compartmentation information, i.e. flow rates and energy dissipation rates, is regularly updated on the basis of new CFD simulations during the actual process simulation.

As discussed earlier, CFD cannot (yet) be used for the direct analysis and optimisation of design alternatives. However, its indirect use, i.e. by aiding the compartmentation process, is of great value. In doing so, caution must be exercised when interpreting CFD results, as long as proper description of two-phase (S/L) flow is not possible yet, let alone three-phase (S/L/V) hydrodynamics. Furthermore, some

CFD packages are known to overestimate energy dissipation rates considerably (Derksen and Van Den Akker, 1999).

The detailed shape of a compartment is mostly not of great interest when creating compartmental models. Usually only certain areas of certain compartments need to be specified within a reasonable accuracy, viz areas related to heat fluxes and/or mass fluxes. For example, to calculate the classification function of the fines flow to the annular zone requires knowledge of the flow direction and the area available for flow perpendicular to that direction. Also, to calculate the undercooling at a heat exchanger surface requires knowledge of the heat flux as well as the available area for heat exchange.

4.3.2 EXAMPLES OF COMPARTMENTAL MODELS

The proposed compartmentation procedure will now be illustrated for the UNIAK 1100-litre DTB crystalliser, an evaporative crystalliser with a fines destruction loop (Figure 4.1.a). Recall that there is not a unique compartmental model for a certain crystalliser, because the compartment structure and connectivity depends on the model system and the applied operating conditions. Here we will derive a compartmental model for this crystalliser and the model system ammonium sulphate and water. In order to avoid re-compartmentation for different operating conditions, the compartmental model is derived for those operating conditions that will result in the largest spatial non-uniformity, e.g. lowest possible pump frequency (constrained by suspension criterion) and lowest fines flow at the highest envisaged heat input (constrained by flashing criterion).

As can be seen from Figure 4.1.a, a DTB crystalliser has three distinct regions: a main body, an annular zone and a fines dissolution loop.

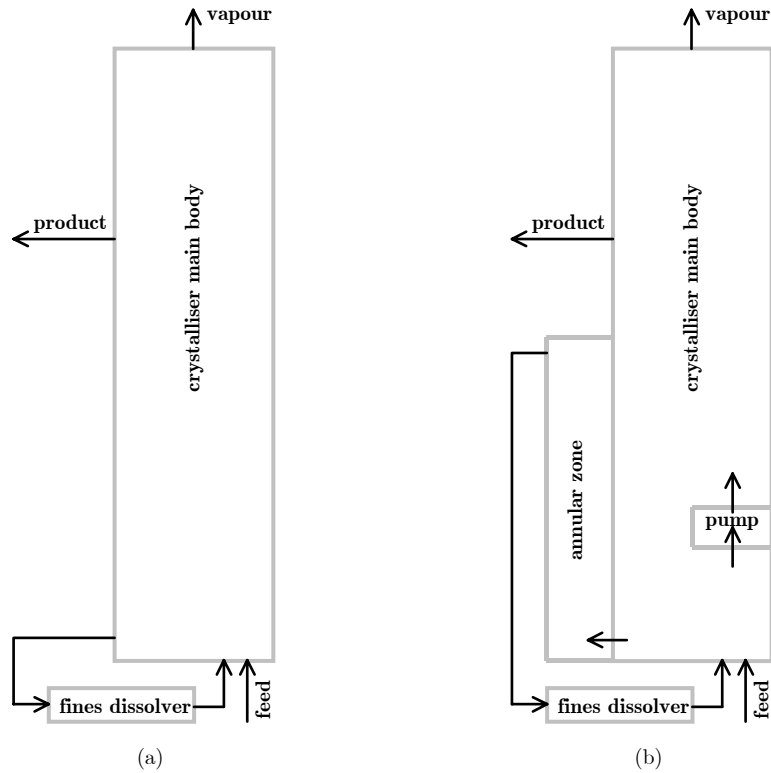


Figure 4.2: Two compartmental models for an evaporative DTB crystalliser: *R*-model (a) and after step one of the compartmentation procedure (b).

The most basic compartmental model for this crystalliser type is the so-called *R*-model, a model of a MSMPR crystalliser with fines destruction, introduced by Randolph and Larson (1988). This model consists of two compartments: one for the main body and one for the fines dissolution loop (Figure 4.2.a). There is no compartment for the annular zone because:

- The crystal growth in that zone is considered negligible. This assumption is based on the fact that the solids concentration and residence time in the annular zone are typically much lower than in the main body; and
- This model was developed for steady-state purposes, hence the delay effect of the hold-up in the annular zone could also be neglected.

The only significant effect of the annular zone, its classification behaviour, is captured by means of a classification function on the stream from the main body to the fines dissolver. Note that the *R*-model is usually considered a one-compartment model because the fines dissolution loop compartment is modelled without hold-up whilst assuming complete dissolution.

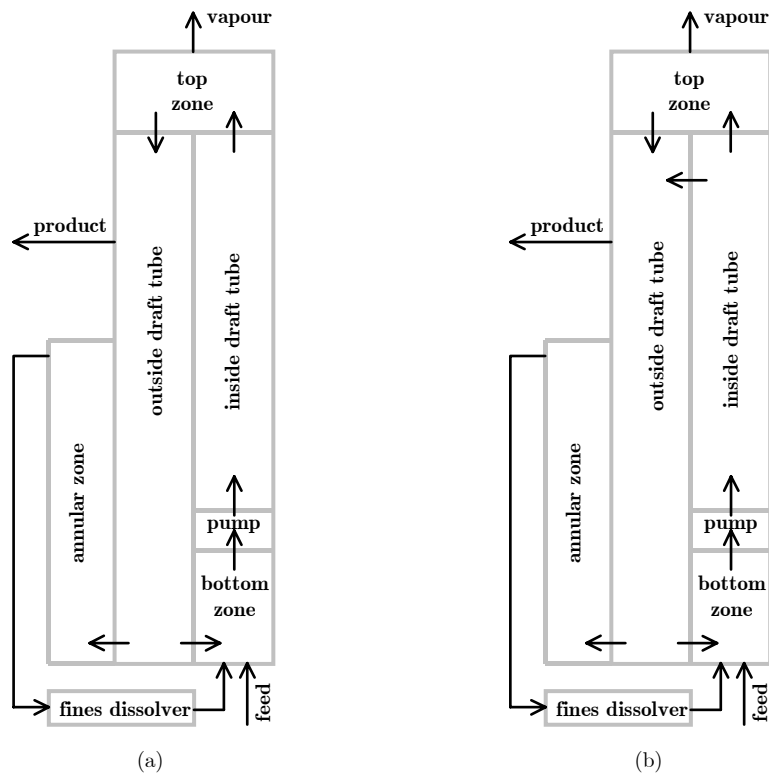


Figure 4.3: Two compartmental models for an evaporative DTB crystalliser: after step two of the compartmentation procedure without (a) and with (b) short circuiting flow.

Now a compartmental model will be set up using the compartmentation procedure presented in the previous subparagraph.

1. As prescribed by step one of the procedure, an additional compartment is introduced for the annular zone to account for process dynamics resulting from hold-up in this zone. This additional compartment is also of importance when modelling industrial crystallisers where the assumption of low solids concentrations in the annular zone may not hold.
2. Following step two of the procedure results in a separate compartment for the internal circulation pump (Figure 4.2.b). As contact nucleation is the dominant nucleation mechanism in the ammonium sulphate/water system, nucleation will primarily occur in this compartment of the crystalliser. Note that no additional compartments were added for the fines and product pump. There are two reasons for the omission of a separate compartment for the fines pump. Firstly, only small particles pass through the fines pump and these are much less prone to attrition than larger particles. Secondly, if any attrition

fragments are formed in the fines pump, they will be the first particles to dissolve in the fines loop, i.e. these fragments will not contribute to effective nucleation. As regards the product pump, all particles do pass the product pump, but only once. If a proper pump is used, the attrition caused by this pump will be negligible in comparison with attrition resulting from collisions with the internal circulation pump. For this specific crystalliser, which is operated at a product residence time of 75 minutes and turnover time of approximately five seconds, all crystals pass the circulation pump in the order of 1000 times.

3. Proceeding to step three of the procedure, the main body of the crystalliser is further divided into four compartments to represent the main circulation flow pattern (Figure 4.3.a). The volume of these compartments can be roughly determined from the crystalliser dimensions. The main circulation flow rate is either calculated using a known pumping number or with the aid of CFD results. If CFD results are available, the connectivity can be extended with a so-called short circuiting flow (Figure 4.3.b). The magnitude of this flow will influence the residence time in the top zone and hence the supersaturation.
4. The next step requires calculation of the half-time for supersaturation decay for this model system at the intended solids concentration. In this specific case, the half-time is in the range of 30 to 80 seconds (Birmingham et al., 1998), which is at least one order of magnitude larger than the residence time in the largest compartment. Therefore, the compartmental model derived in step two is not modified in step four of the procedure.
5. Step five comprises the further compartmentation with respect to spatial gradients in the local energy dissipation. For this purpose, the CFD calculations previously presented in Figure 4.1.b are used. The resulting compartmental model, derived by ten Cate et al. (2000), is depicted in Figure 4.4. The model consists of 22 compartments for the main body, one for the internal circulation pump, one for the annular zone and one for the fines dissolution loop. This compartmentation is not expected to be particularly meaningful for this crystallisation set-up, as none of the mechanisms dominating the crystallisation of ammonium sulphate from water has rate expressions that include a high order dependency on the local energy dissipation;
6. Distribution of the overall heat input (step six) is straightforward. All heat for evaporation is added via the heat exchanger in the fines dissolution loop; and
7. As regards classification functions, the most important one acts on the flow from the outside draft tube compartment to the annular zone compartment. This is a region where the superficial velocities are purposely low to enable the segregation of especially larger particles.

Typical values for the compartment volumes, exchange flow rates, exchange areas, distribution of heat or cooling duty, and classification functions can be found in Chapter 7, where the various compartmental models presented here are applied.

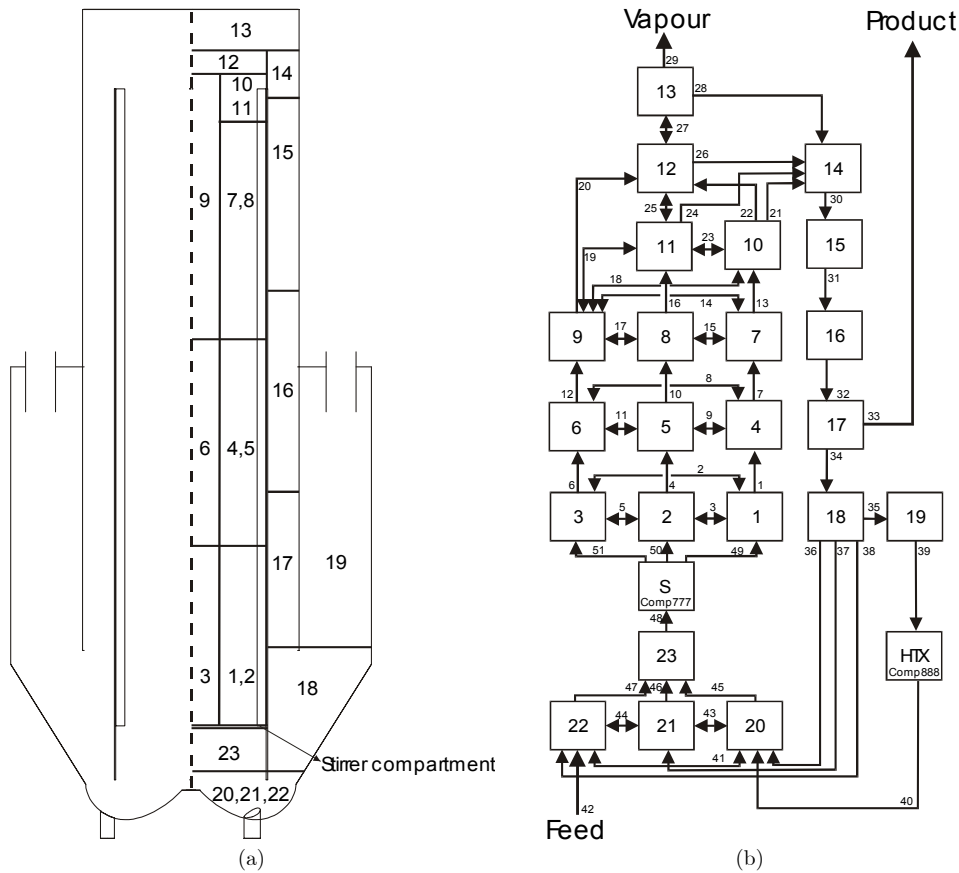


Figure 4.4: Comprehensive compartmental model for the 1100-litre DTB crystalliser: location of compartments (a) and connectivity diagram (b).

4.4 MODEL OF A SINGLE COMPARTMENT

The model of a single compartment, i.e. the compartment model, is the building block for the construction of compartmental models. A compartment represents a perfectly mixed zone/volume with respect to process conditions such as supersaturation, energy dissipation rate, CSD, temperature and pressure. The attributes of a compartment as used in this thesis work are listed below, while the main modelling assumptions can be found in Appendix B.1.1:

- Its position and orientation in space.
- Its size in terms of volume.

- As many surfaces as outgoing fluxes.
- The various kind of fluxes allowed through each of its surfaces.
- Intensive properties (pressure, temperature, liquid phase composition, volume fraction occupied by liquid phase, the crystal size distribution and the energy dissipation rate).
- Uniformly distributed intensive properties with respect to the spatial domains within the compartment.
- Equations of conservation to calculate (changes in) all intensive properties except pressure and the energy dissipation rate.
- The pressure follows from simplified flow versus pressure drop relationships for the main fluxes between the compartments.
- The energy dissipation rate is either calculated from the specific power input of the circulation device(s) or from CFD results.
- Hydrodynamic regime prevailing in the compartment.
- Expressions for physical properties.
- Rate expressions for the various crystallisation mechanisms.
- Expression for solid/liquid flux between compartments as a function of the pressure difference between these compartments.
- Expression for vapour flux leaving system as a function of the difference between the compartment's temperature and the saturation temperature in the condenser; and
- Fluxes going through a surface are assumed to be uniform over that surface.

A compartmental model for a crystalliser must be set up such that negligible gradients in process conditions exist within the compartments. Considerable gradients may of course exist between the various compartments. To ensure consistency and a minimal model development effort, all regions of a crystalliser should be described with the same compartment model, i.e. the same equations of conservation, physical and thermodynamic property relations, kinetic rate expressions and parameters. Differences between compartments with respect to nucleation, growth, dissolution, attrition, breakage and aggregation rates are therefore purely a result of varying process conditions. Furthermore, in order to maintain model consistency and facilitate the modelling of a wide variety of design alternatives, it was also deemed necessary to use the same single compartment model for:

1. Cooling, flash cooling and evaporative crystallisation.
2. Batch and continuous processes.
3. Different crystalliser types; and
4. Single and multiple compartment descriptions of crystallisers.

This wide range of process types and configurations poses the following requirements for the development of a generally applicable model of a single compartment:

- The model must have the ability to deal with both the presence and absence of a vapour phase and vapour flow.
- The model should be able to cope with fixed and free volumes.
- Setting up compartmental models, i.e. a flowsheet consisting of single compartments, requires a model that allows an arbitrary number of inlet and outlet streams; and
- Describing all the regions of a crystalliser with the same compartment model implies that a compartment will typically have many more functionalities than it actually requires. Functionalities include feed insertion, product withdrawal, heating, cooling, pumping, attrition, growth, classification, etc. For each instance of the single compartment model in a crystalliser's compartmental model, different combinations of functionalities need to be activated.

A single compartment model, aimed at satisfying the above-mentioned needs, is schematically depicted in Figure 4.5. An arbitrary number of inlet streams and outlet streams respectively enter and exit the compartment. Each flow is characterised by an overall flow rate, component mass flow rates, crystal number densities and an enthalpy flow rate. The vapour flow, present in each compartment but zero in most compartments, is described by a mass flow rate and enthalpy flow rate only. The states in a compartment are the mass quantities of each component, crystal number densities (i.e. CSD) and enthalpy. The heat input of a compartment can be positive (heating), negative (cooling) or zero.

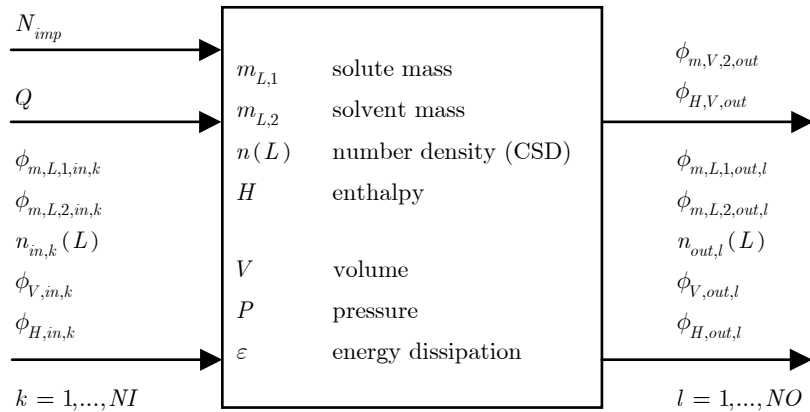


Figure 4.5: Compartment model - variables and structure.

In order to predict the rates of the various crystallisation processes and the resulting product composition in a compartment requires knowledge of:

- The crystallisation kinetics. These are captured by the kinetic models covered in subparagraph 4.4.2.
- Convective transport into and out of the compartment. The overall flow rates are obtained from operating conditions and/or CFD

calculations. Classification functions that account for the slip of crystals with respect to the liquid are treated in subparagraph 4.4.4.

- Thermodynamic and physical properties. These are discussed in subparagraph 4.4.6; and
- Operating conditions, such as the heat input of the compartment and if applicable the pump frequency.

The combined effect of the kinetics, convective transport and operating conditions on the dynamic process and product behaviour is determined by the equations of conservation. These equations are introduced in the next subparagraph.

4.4.1 EQUATIONS OF CONSERVATION

In Appendix B.2.1, the comprehensive equations of conservation are derived for a crystallisation system of volume V at temperature T and pressure P . The system consists of one liquid phase containing NC_L components and NP_S solid (crystalline) phases. There are NI inlet streams, NO outlet streams, one vapour outlet stream and a heat transfer stream. NR_L reactions occur in the liquid phase, and it is assumed that each solid phase is created or depleted via one crystallisation reaction only.

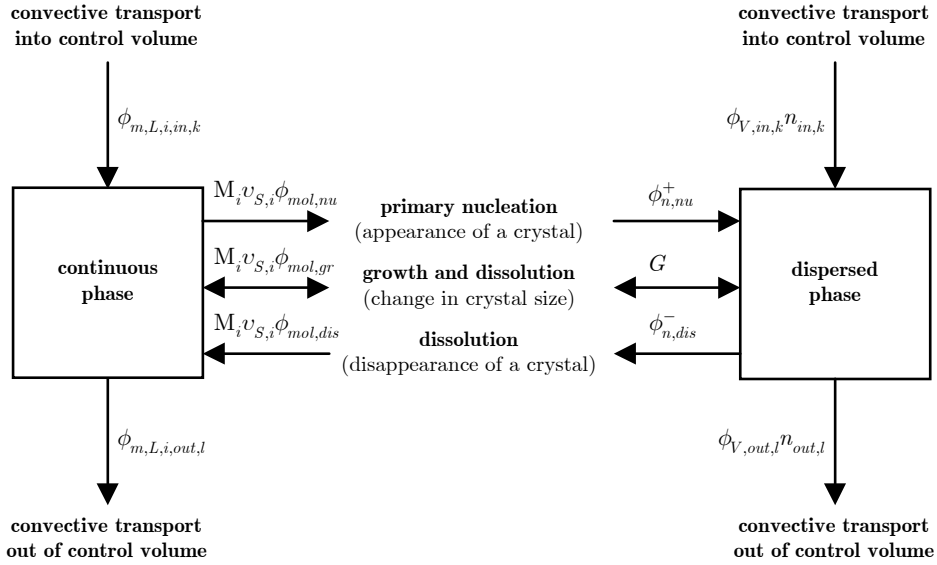


Figure 4.6: Link between the mass balances for the continuous phase components and the population balances for the dispersed phases(s).

The equations of conservation consist of the mass balances for the liquid phase components, population balance(s) for the solid phase(s) and the enthalpy balance. The population balance is in fact a distributed mass balance for a solid or dispersed phase, and is linked to the liquid or continuous phase component mass balances via the crystallisation kinetics (see Figure 4.6).

Here, we present the equations of conservation for a single-solute single-solvent system, such as the crystallisation of ammonium sulphate from water. This system is used for all experimental and modelling work in the remainder of this thesis. Hence we have two liquid phase components ($NC_L = 2$), one solid phase ($NP_s = 1$) and no liquid phase reactions ($NR_L = 0$).

Liquid phase component 1	solute (A)
Liquid phase component 2	solvent (B)
Solid phase	crystals (C)

As only one solid phase is present, we can simplify the set of comprehensive equations listed in Appendix B.2.1 by introducing the following definitions:

$$\begin{aligned} \phi_{mol,nucl} &= \phi_{mol,nucl,1} , & \phi_{mol,grow} &= \phi_{mol,grow,1} , & \phi_{mol,dis} &= \phi_{mol,dis,1} , \\ v_{S,1} &= v_{S,1,1} , & v_{S,2} &= v_{S,1,2} , & n(L) &= n_1(L) , \\ G &= G_1 , & \phi_n^\pm(L) &= \phi_{n,1}^\pm(L) \end{aligned}$$

Using these definitions, the crystallisation reaction in the above-mentioned system can be written as follows:

$$v_{S,1}A + v_{S,2}B + C = 0 \quad [4.1]$$

For the crystallisation of ammonium sulphate from water, stoichiometric coefficients $v_{S,1}$ and $v_{S,2}$ are equal to minus one and zero respectively.

Mass balance for solvent

With these newly introduced definitions, we can rewrite the liquid phase component mass balance for the solvent as follows:

$$\begin{aligned} \frac{\overbrace{dm_{L,2}(t)}^{\text{mass rate of accumulation}}}{dt} &= \overbrace{\sum_{k=1}^{NI} \phi_{m,L,2,in,k}(t) - \sum_{l=1}^{NO} \phi_{m,L,2,out,l}(t) - \phi_{m,V,2,out}(t)}^{\text{mass rates in and out via convective transport}} \\ &\quad \underbrace{\phi_{mol,nucl}(t) + \phi_{mol,grow}(t) - \phi_{mol,dis}(t)}_{\text{interphase mass flux due to crystal growth and due to primary nucleation and dissolution at the critical nucleus size}} \\ &\quad + M_2 v_{S,2} \left[\phi_{mol,nucl}(t) + \phi_{mol,grow}(t) - \phi_{mol,dis}(t) \right] \end{aligned} \quad [4.2]$$

Initial condition:

$$m_{L,2}(t = 0) = m_{L,2,0}$$

Mass balance for solute

By assuming that the vapour flow only contains solvent, we obtain the following equation for the mass accumulation rate of solute in the liquid phase:

$$\begin{aligned}
\overbrace{\frac{dm_{L,1}(t)}{dt}}^{\text{mass rate of accumulation}} &= \overbrace{\sum_{k=1}^{NI} \phi_{m,L,1,in,k}(t) - \sum_{l=1}^{NO} \phi_{m,L,1,out,l}(t)}^{\text{mass rates in and out via convective transport}} \\
&\quad \underbrace{\text{interphase mass flux due to crystal growth and due to primary nucleation and dissolution at the critical nucleus size}} \\
&\quad + M_1 v_{S,1} \left[\phi_{mol,nucl}(t) + \phi_{mol,grow}(t) - \phi_{mol,dis}(t) \right]
\end{aligned} \tag{4.3}$$

Initial condition:

$$m_{L,1}(t = 0) = m_{L,1,0}$$

Population balance for crystals

As discussed in Chapter 2, crystalline products may have a distributed nature with respect to internal states, such as size, morphology, internal energy and purity. A comprehensive description of the product composition of a crystalline material therefore involves a multivariate distribution of the crystal population over the various product composition variables. For practical reasons, as outlined earlier in this chapter, only one independent co-ordinate system will be used to describe the internal state of the crystals, viz crystal size. Crystal shape and internal energy are taken into account in the model development, but not as independent co-ordinate systems. The time evolution of a crystal size distribution (CSD) is given by the population balance equation (PBE). This equation was introduced to crystallisation by Randolph in 1962 (Randolph and Larson, 1988). The PBE is encountered in many forms. The amount of particles can be expressed in terms of number, volume or mass densities, whereas particle size is usually expressed in terms of length or volume. Volume is typically used for particle size when agglomeration and/or breakage play an important role, because these crystallisation mechanisms must obey mass conservation and the density of the solid phase is assumed constant. Furthermore, the PBE can easily be extended to include external co-ordinates (Randolph and Larson, 1988).

The PBE for a uniformly mixed volume, with the amount and the size of particles expressed in terms of number density and particle length respectively, can be written as follows:

$$\begin{aligned}
\frac{\overbrace{\frac{\partial(n(L,t)V(t))}{\partial t}}^{\text{number rate of accumulation}}}{\partial t} &= -V(t) \frac{\overbrace{\frac{\partial(n(L,t) \cdot G(L,t))}{\partial L}}^{\text{rate of number gain due to crystal growth and dissolution}}}{\partial L} \\
&+ \sum_{k=1}^{\overbrace{NI}^{\text{number rate in}}} \overbrace{\phi_{V,in,k}(t)n_{m,k}(L,t)}^{\text{number rate in}} - \sum_{l=1}^{\overbrace{NO}^{\text{number rate out}}} \overbrace{\phi_{V,out,l}(t)n_{out,l}(L,t)}^{\text{number rate out}} \\
&+ \overbrace{\left[\phi_{n,nucl}^+(L,t) - \phi_{n,dis}^-(L,t)\right]V}^{\text{number production rate due to primary nucleation and dissolution at the critical nucleus size}} \\
&+ \overbrace{\left[\phi_{n,attr}^\pm(L,t) + \phi_{n,break}^\pm(L,t) + \phi_{n,aggl}^\pm(L,t)\right]V}^{\text{number production rate due to attrition, breakage and agglomeration}}
\end{aligned} \tag{4.4}$$

Initial condition:

$$n(L, t = 0) = n_0(L)$$

The initial condition can be used to express a trivial situation such as a clear liquid (no crystals) or a size distribution of seed crystals (often used in batch processes).

Boundary conditions for the population balance

The classical boundary condition with respect to crystal size for the population balance equation is:

$$n(L = 0, t) = \frac{B_0(t)}{G(L = 0, t)} \qquad G(L) \geq 0 \text{ for all } L, \quad G(L=0) > 0$$

This boundary condition is applicable and sufficient when the crystal growth rate is positive for all crystal sizes. B_0 denotes the birth rate of crystals of size zero. Note that this rate is not a distributed variable such as $\phi_{n,nucl}^+$ and $\phi_{n,attr}^\pm$. Depending on the employed kinetic model, nucleation is either modelled using a birth rate at the boundary (e.g. Ploß et al., 1985; Jager, 1990) or as a distributed process with respect to crystal size (e.g. Ó Meadhra et al., 1996; Gahn and Mersmann, 1999a). In the latter case, the birth rate of crystals of size zero is equal to zero.

If the growth rate is negative for all crystal sizes, a boundary condition at infinite length is required and sufficient. As crystals of infinite size do not exist, the following boundary condition can be used.

$$n(L = \infty, t) = 0 \qquad G(L) < 0 \text{ for all } L$$

If the growth rate is negative for certain crystal size intervals and positive for others, the PBE requires more than one boundary condition with respect to crystal size. For such systems, one could define a separate PBE for each size interval within which the growth rate of all crystals have the same sign.

As an example, consider a system where:

- The growth rate equals zero for crystals of size L_{eq} .

- The growth rate of crystals smaller than L_{eq} is negative; and
- The growth rate of crystals larger than L_{eq} is positive.

In this case, there are two size intervals, i.e. one from zero to L_{eq} , and one from L_{eq} to infinity. As the growth rate in the first interval is negative, the PBE requires a boundary condition at the upper bound of this interval: L_{eq} . The growth rate in the second interval is positive and as a result, the PBE requires a boundary condition at the lower bound of this interval: also at L_{eq} .

Kinetic rate terms present in both the mass balances and population balance

The kinetic rate terms in the component mass balances and population balance are coupled by the following three equations:

$$\phi_{mol,nucl}(t) = \frac{k_v \rho_S}{M_S} V(t) \int_0^{\infty} \phi_{n,nucl}^+(L,t) L^3 dL \quad [4.5]$$

$$\begin{aligned} \phi_{mol,grow}(t) &= \frac{k_v \rho_S}{M_S} \int_0^{\infty} \left. \frac{\partial(n(L,t)V(t))}{\partial t} \right|_{\text{growth}} L^3 dL \\ &= -\frac{k_v \rho_S}{M_S} V(t) \int_0^{\infty} \frac{\partial(n(L,t)G(L,t))}{\partial L} L^3 dL \end{aligned} \quad [4.6]$$

$$\phi_{mol,dis}(t) = \frac{k_v \rho_S}{M_S} V(t) \int_0^{\infty} \phi_{n,dis}^-(L,t) L^3 dL \quad [4.7]$$

Expressions for the number density fluxes, $\phi_{n,nucl}^+$, and, $\phi_{n,dis}^-$, as well as the growth rate, G , follow from the kinetic models treated in the next subparagraph.

Enthalpy balance

Finally, the dynamics of the temperature are given by the energy balance. In Appendix B.2.1 it is shown how the energy balance can be transformed into the enthalpy balance assuming that kinetic energy, potential energy and shaft work can be neglected. The resulting balance is as follows:

$$\begin{array}{ccc} \text{rate of enthalpy} & \text{rate of total enthalpy in} & \text{net rate} \\ \text{accumulation} & \text{and out by convection} & \text{of heat} \\ \frac{d\widehat{H}(t)}{dt} & = \overbrace{\sum_{k=1}^{NI} \phi_{H,in,k}(t) - \sum_{l=1}^{NO} \phi_{H,out,l}(t) - \phi_{H,V,out}(t)} & + \widehat{Q}(t) \end{array} \quad [4.8]$$

Initial condition:

$$H(t=0) = H_0$$

4.4.2 KINETIC MODEL

The crystallisation process modelling framework being developed here is intended primarily for design purposes. Hence, kinetic models that are useful for control

purposes because they have good descriptive capabilities, but lack adequate predictive properties will be of little use for this work.

The industrial crystallisation of well soluble substances is often dominated by secondary nucleation, in particular contact nucleation, and crystal growth (Mersmann et al., 1988). This is also the case for the crystallisation of ammonium sulphate from water.

The formation of secondary nuclei is a complex process depending on the hydrodynamics inside a crystalliser, the attrition behaviour of the crystalline material and the outgrowth (survival) of the attrition fragments. In draft tube, draft tube baffle and forced circulation crystallisers the attrition is mainly caused by collisions between crystals and the pump or impeller, whereas in fluidised bed crystallisers collisions between crystals are considered the dominating source of attrition.

Over the years, quite a number of kinetic models have been developed for secondary nucleation and growth dominated systems. Ó Meadhra (1995) discussed the models of Ottens et al. (1972), Ploß et al. (1985), Jager (1990) and van der Heijden et al. (1994). He found that only models with nucleation rates depending on the number and size of the parent crystals present were able to fit observed dynamics in the CSD. The two kinetic models developed in the previous phase of the UNIAK project contained similar relations between nucleation rates and CSD (Eek et al., 1995b; Ó Meadhra et al., 1996). Both also include the effect of size dependent attrition on the effective crystal growth rate. More importantly, Ó Meadhra was the first to physically model the retarding effect of lattice strain on the crystal growth rate. However, all these models are largely of an empirical nature: they do not contain the particle mechanics of importance for attrition and they miss the vital link between the attrition process and the hydrodynamic conditions inside the crystalliser. As a result, many of the parameters need to be re-determined for different crystalliser and/or pump geometries and sometimes even for different operating conditions, thus making these models unreliable for scale-up.

More recently, Gahn and Mersmann (1999a; 1999b) have developed a model framework for attrition, secondary nucleation and growth. This framework contains a more physical basis than any previous work: the secondary nucleation rate caused by crystal-impeller collisions is calculated largely from first principles. Consequently, the number of kinetic parameters is significantly less. More importantly, these parameters are not of an empirical nature, i.e. they have a physical meaning. One can therefore expect this model to have the predictive properties required for design purposes. As this model is expected to possess the best predictive properties at this moment in time, it is selected for implementation in the general crystallisation process modelling framework.

The model framework of Gahn and Mersmann can be seen as a synthesis of three sub-models (Neumann et al., 1998a):

1. A procedure to determine the total number of crystals colliding per second with the faces and edges of the impeller blades, and the

corresponding impact energy per collision (Mersmann et al., 1988; Ploß et al., 1989).

2. A relation between the impact energy and the attrition volume produced due to a single collision of a crystal corner with a hard, flat surface and the resulting number and size distribution of resulting attrition fragments (Gahn et al., 1997); and
3. A relation to derive the growth rate of the fragments formed by the attrition process (van der Heijden, 1992; Zacher, 1995; Gahn, 1997).

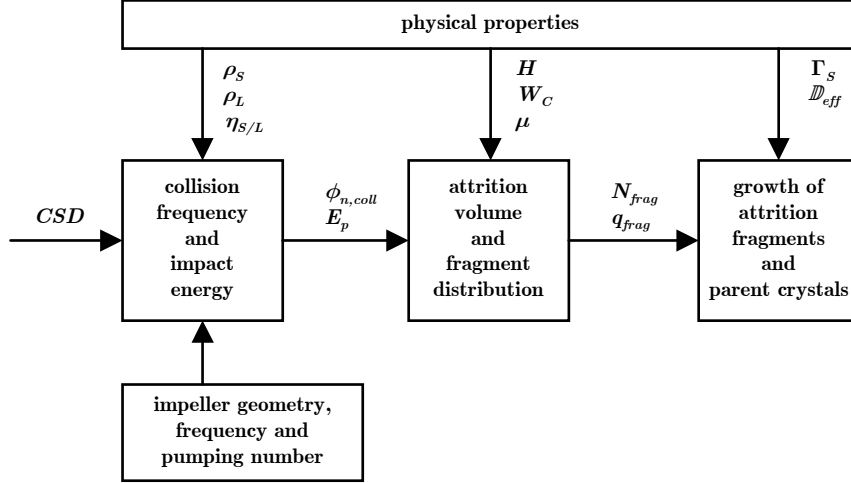


Figure 4.7: Model structure of the framework of Gahn and Mersmann (1999a).

4.4.2.1 Collision frequency and impact energy

The chance and impact velocity of a crystal-impeller collision are calculated using a geometrically simplified model developed by Ploß et al. (1989), which provides an approximation for the complex two-phase flow pattern in the vicinity of the impeller. Both the chance and impact velocity are a function of the distance from the impeller axis. Therefore, in addition to the discretisation of the crystal size coordinate, the impeller needs to be discretised along its radius. The chance and impact velocity calculations are performed independently for the faces and edges of the impeller blades.

The collision rate of crystals of size, L , with the face and the edge of the impeller blade at radial position, r , is given by:

$$\phi_{n,\text{coll,edge/face}}(L,r) = n(L) \phi_{V,\text{dt}} \eta_{\text{coll,edge/face}}(L,r) \quad [4.9]$$

The collision efficiencies, $\eta_{\text{coll,edge}}$ and $\eta_{\text{coll,face}}$, are measures for the chance of a crystal of size, L , being on a streamline towards and actually colliding at radial position, r , with the impeller edge and face respectively. The calculation of collision efficiencies and collision velocities is given in Appendix B.3. It is this part of the model that limits its application to crystallisers with impellers in draft

tubes or pipes. De Jong (2003) is therefore developing a CFD based procedure to determine target and geometric efficiencies of crystal-wall collisions in arbitrary geometries. Furthermore, using their procedure they can check the validity of the geometrically simplified model used by Ploß et al. as an approximation for the flow pattern in the vicinity of the impeller.

From this point onwards, the calculations are identical for the edge and face of the impeller blades. The collision impact energy, E_p , is calculated using the following equation:

$$E_{p,edge/face}(L,r) = \frac{1}{2} \rho_s k_v L^3 v_{coll,edge/face}^2(L,r) \quad [4.10]$$

4.4.2.2 Attrition volume and fragment distribution

Removed attrition volume

The attrition volume, V_{attr} , removed from a parent crystal as a result of a single collision with an impeller is related to the impact energy, E_p , of the crystal via a number of material properties, viz hardness, H , shear modulus, μ , and effective fracture surface energy, Γ/K_r .

Of all the material properties used in this kinetic model framework, the effective fracture surface energy is the most difficult property to obtain (Gahn and Mersmann, 1999a). Gahn and Mersmann (1997) have presented a method to estimate this material property from a Vickers indentation test. Assuming idealised radial and lateral crack formation, the effective fracture surface energy, Γ/K_r , can be related to the critical work of indentation for crack formation, W_C :

$$\frac{\Gamma}{K_r} \approx \frac{1}{5.2} \frac{W_C^{1/3} H^{5/3}}{\mu} \quad [4.11]$$

The assumptions concerning the crack patterns around the indentation make the calculation of the effective fracture surface energy the most uncertain link in this attrition model. Gahn and Mersmann (1999a) therefore attribute observed deviations between model predictions and experimental results to this material property. Consequently, they modified the proportionality constant in Eq. 4.11 by a factor of two:

$$\frac{\Gamma}{K_r} = \frac{1}{10} \frac{W_C^{1/3} H^{5/3}}{\mu} \quad [4.12]$$

In order for an impact to cause fracture and to remove material from a crystal, the impact energy must exceed a certain minimum impact energy. This energy is solely a function of the material properties and thus a constant for a given substance:

$$E_{p,min} \approx 64 \frac{\mu^3}{H^5} \left(\frac{\Gamma}{K_r} \right)^3 = \frac{64}{1000} W_C \quad [4.13]$$

Combining equations 4.10 and 4.13 shows that the required minimal collision velocity is only a function of crystal length for a given substance:

$$v_{coll,min}(L) \approx \sqrt{128 \frac{\mu^3}{\rho_s k_v L^3 H^5} \left(\frac{\Gamma}{K_r} \right)^3} = \sqrt{\frac{128}{1000} \frac{W_C}{\rho_s k_v L^3}} \quad [4.14]$$

The attrition volume resulting from a single collision is given by:

$$\begin{aligned} V_{attr}(L, r) &= C E_p^{4/3}(L, r) & E_p(L, r) &\geq E_{p,min} \\ V_{attr}(L, r) &= 0 & E_p(L, r) &< E_{p,min} \end{aligned} \quad [4.15]$$

where C is the attrition constant, which is defined as:

$$C \approx \frac{2}{3} \frac{H^{2/3}}{\mu} \frac{K_r}{\Gamma} = \frac{20}{3} \frac{1}{W_C^{1/3} H} \quad [4.16]$$

According to Neumann (2001), an important assumption made in this model is that a damaged crystal corner will have sufficient time to heal before a subsequent collision of the same corner takes place. If this healing process is not completed in time, the corners of the crystal will become more and more rounded-off. As a result, the attrition resistance of these crystals will increase, leading to a higher value for the effective fracture resistance and consequently to a lower value for the attrition constant, C . This assumption can have serious consequences for scale-up, because the time between subsequent collisions is strongly related to the turnover time in a crystalliser. As the turnover time typically decreases with crystalliser scale, the above-mentioned healing assumption will rather be violated in a laboratory scale crystalliser than in an industrial scale crystalliser.

Number and distribution of fragments

The attrition volume removed from a parent crystal consists of a plastically and an elastically deformed part. The attrition fragments from the plastically deformed volume have such a high internal stress content, that these are assumed to dissolve instantaneously. The total number of attrition fragments in the elastically deformed part, N_{frag} , and their normalised number density distribution, $q_{frag}(L)$, are given by the following two equations:

$$N_{frag}(L, r) \approx \frac{\pi}{21} \frac{H^{1/2}}{k_v \mu^{3/4}} \left(\frac{K_r}{\Gamma} \right)^{3/4} \left(L_{frag,min}^{-2.25} - L_{frag,max}^{-2.25}(L, r) \right) E_p(L, r) \quad [4.17]$$

$$\begin{aligned} q_{frag}(L, r, L_{frag}) &= \frac{2.25 L_{frag}^{-3.25}}{L_{frag,min}^{-2.25} - L_{frag,max}^{-2.25}(L, r)} & L_{frag,min} &\leq L_{frag} \leq L_{frag,max}(L, r) \\ q_{frag}(L, r, L_{frag}) &= 0 & L_{frag} &< L_{frag,min} \vee L_{frag} > L_{frag,max}(L, r) \end{aligned} \quad [4.18]$$

Note that each combination of parent crystal size, L , and radial position, r , results in a number of attrition fragments, N_{frag} , with their own size distribution, q_{frag} . It is therefore essential to distinguish between the fragment crystal size, L_{frag} , and parent crystal size, L .

The size of the smallest attrition fragments is only a function of material properties:

$$L_{frag,min} = \frac{32}{3} \frac{\mu}{H^2} \frac{\Gamma}{K_r} = \frac{32}{30} \left(\frac{W_C}{H} \right)^{1/3} \quad [4.19]$$

Whereas the size of the largest attrition fragments is also determined by the magnitude of the impact energy:

$$L_{frag,max}(L,r) = \frac{1}{2} \left(\frac{H^{2/3}}{\mu} \frac{K_r}{\Gamma} \right)^{1/3} E_p^{4/9}(L,r) = \frac{1}{2} \left(\frac{10}{W_C^{1/3} H} \right)^{1/3} E_p^{4/9}(L,r) \quad [4.20]$$

4.4.2.3 Growth of attrition fragments and parent crystals

Driving force

As mentioned above, the plastically deformed attrition fragments are assumed to dissolve instantaneously due to their high internal stress. The elastically deformed attrition fragments also contain a certain amount of internal stress resulting from the collision of their parent crystal with the impeller. Their solubility, c_{real}^* , is therefore increased in comparison to the solubility, c^* , of an ideal, stress free crystal.

$$c_{real}^*(L) = c^* \exp\left(\frac{\Gamma_s}{RTL}\right) \quad [4.21]$$

thus reducing their absolute supersaturation, Δc , the driving force for crystallisation:

$$\Delta c(L) = c - c_{real}^*(L) \quad [4.22]$$

The surface related energy increase, Γ_s , is said to be a material constant which can be derived using CSD data from crystallisation experiments.

Due to a decreased driving force, the growth rate of the fragments will be lowered and it might even result in dissolution of fragments. On the other hand, as an attrition fragment grows out it will contain less and less stress at the surface, thus lowering its solubility and increasing its growth rate.

Growth rate

Assuming a combined mass transfer and second order surface reaction controlled growth, the growth rate of a crystal is defined as:

$$\frac{G(L)}{2k_d(L)} = \frac{\Delta c(L)}{c_s} + \frac{k_d(L)}{2k_r c_s} - \sqrt{\left(\frac{k_d(L)}{2k_r c_s}\right)^2 + \frac{k_d(L)}{k_r c_s} \frac{\Delta c(L)}{c_s}} \quad \Delta c(L) > 0 \quad [4.23]$$

This equation contains the second parameter that also needs to be derived from experimental CSD data: the rate coefficient for surface integration, k_r . Chapter 6 focuses on the estimation of Γ_s and k_r from CSD data.

From a physical point of view, dissolution is not simply the opposite of growth. Crystal growth requires the orientation of ions or molecules at the crystal surface prior to integration into the lattice. This often time-consuming orientation step is not required for dissolution. As a result, crystal dissolution is not expected to be limited by surface ‘de-integration’:

$$\frac{G(L)}{2k_d(L)} = \frac{\Delta c(L)}{c_s} \quad \Delta c(L) \leq 0 \quad [4.24]$$

The mass transfer coefficient can be calculated using a Sherwood type relation developed by Herndl (1982):

$$k_d(L) = \frac{D_{AB}}{L} \left[2 + 0.8 \left(\frac{\bar{\varepsilon} L^4}{v_L^3} \right)^{1/5} \left(\frac{v_L}{D_{AB}} \right)^{1/3} \right] \quad [4.25]$$

The mean specific power input of the impeller follows from:

$$\bar{\varepsilon} = \frac{Ne N_{imp}^3 D_{imp}^5}{V} \quad [4.26]$$

It is well known that the energy dissipation induced by the impeller's power input is distributed highly non-uniformly throughout a stirred vessel. However, it is expected that using the same mean specific power input for all compartments in a crystalliser is a valid assumption as this quantity is only raised to a very small power.

4.4.2.4 Kinetic source and sink terms in PBE

The dominant mechanisms in the crystallisation of ammonium sulphate from water are secondary nucleation and growth (including dissolution). Other mechanisms, such as primary nucleation, breakage and agglomeration are not included in the model framework developed and used in this thesis². As a result, the source and sink terms in the PBE related to primary nucleation, $\phi_{n,nucl}^+$, breakage, $\phi_{n,break}^\pm$, and agglomeration, $\phi_{n,aggl}^\pm$, will be zero. The remaining kinetic source and sink terms are calculated using the following set of equations:

$$\phi_{n,dis}^-(L) = \delta(L - L_{crit}) D_{dis} \quad [4.27]$$

D_{dis} is the rate at which crystals of the critical nucleus size disappear from the PBE as a result of dissolution. This rate has the units $[\text{m}^3 \cdot \text{s}^{-1}]$ and should be chosen sufficiently high to avoid crystal accumulation at size L_{crit} . The dirac function is a distribution with units $[\text{m}^{-1}]$, which is zero when its argument is non zero, and has the following property:

$$\int_{L=0}^{\infty} \delta(L - L_{crit}) dL = 1 \quad [4.28]$$

Note that dissolution is present in the PBE as both a convective term (crystal size reduction) and a sink term (crystal disappearance). The latter is shown above.

² Note that these mechanisms may need to be included in future to cover other systems than the crystallisation of ammonium sulphate from water.

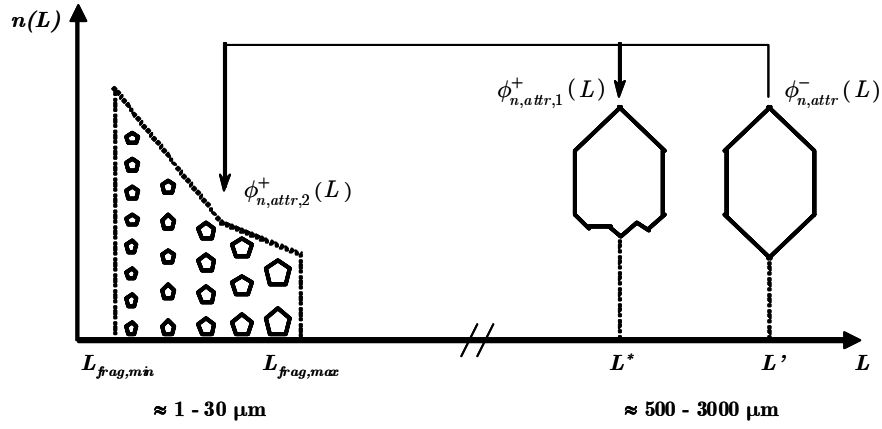


Figure 4.8: Relationship between the attrition related sink and source terms in the population balance equation (after Mitrovic, 2002).

The net source term as a result of attrition, $\phi_{n,attr}^{\pm}$ is composed of three terms (see Figure 4.8), which relate to the various steps of the attrition process: a sink term for the parent crystals that are subject to attrition, $\phi_{n,attr}^{-}$, a source term reflecting the birth of a single crystal, slightly smaller than the parent crystal, $\phi_{n,attr,1}^{+}$, and a source term for the attrition fragments, $\phi_{n,attr,2}^{+}$.

$$\phi_{n,attr}^{\pm}(L) = -\phi_{n,attr}^{-}(L) + \phi_{n,attr,1}^{+}(L) + \phi_{n,attr,2}^{+}(L) \quad [4.29]$$

The collision rate of crystals with size, L , at radial position, r , is given by Eq. 4.9. However, not all these collisions will necessarily result in attrition of the parent crystal. The other condition that must be satisfied to initiate an attrition event is a collision energy exceeding the minimum collision energy as given by Eq. 4.13. The effective rate of collisions leading to attrition can thus be calculated using the following expression:

$$\phi_{n,coll,eff,edge/face}(L,r) = \phi_{n,coll,edge/face}(L,r) h(E_{p,edge/face}(L,r) - E_{p,min}) \quad [4.30]$$

The sink term for parent crystals subject to attrition, $\phi_{n,attr}^{-}$, is obtained by integrating the radial, effective collision rate over the impeller radius:

$$\phi_{n,attr}^{-}(L) V = \int_{r=0}^{D_{imp}/2} \phi_{n,coll,eff}(L,r) dr \Big|_{edge} + \int_{r=0}^{D_{imp}/2} \phi_{n,coll,eff}(L,r) dr \Big|_{face} \quad [4.31]$$

The source term reflecting the birth of crystals slightly smaller than the parent crystals, $\phi_{n,attr,1}^{+}$, is obtained similarly.

$$\begin{aligned} \phi_{n,attr,1}^+(L) V = & \int_{r=0}^{D_{imp}/2} \int_{L'=L}^{\infty} \delta(L - L^*(L',r)) \phi_{n,coll,eff}(L',r) dL' dr \Big|_{edge} \\ & + \int_{r=0}^{D_{imp}/2} \int_{L'=L}^{\infty} \delta(L - L^*(L',r)) \phi_{n,coll,eff}(L',r) dL' dr \Big|_{face} \end{aligned} \quad [4.32]$$

In this equation, L' , denotes the size of the parent crystal and, L^* , is the size of the parent crystal's remnant after the attrition event. The size of this remnant is a function of the parent crystal's size prior to the collision and the volume of the attrition fragments formed by that collision:

$$L^*(L',r) = \sqrt[3]{L'^3 - \frac{V_{attr}(L',r)}{k_v}} \quad [4.33]$$

Note that this equation assumes the same mass density for the parent crystal, its remnant and the attrition fragments. Furthermore, the parent crystal and its remnant are assumed to have the same volumetric shape factor.

The source term for the formed attrition fragments, $\phi_{n,attr,2}^+$, is given by the following equation:

$$\begin{aligned} \phi_{n,attr,2}^+(L) V = & \int_{r=0}^{D_{imp}/2} \int_{L'=L}^{\infty} \left[h(L - L_{frag,min}) - h(L - L_{frag,max}(L',r)) \right] \\ & N_{frag}(L',r) q_{frag}(L',r,L) \phi_{n,coll,eff}(L',r) dL' dr \Big|_{edge} \\ & + \int_{r=0}^{D_{imp}/2} \int_{L'=L}^{\infty} \left[h(L - L_{frag,min}) - h(L - L_{frag,max}(L',r)) \right] \\ & N_{frag}(L',r) q_{frag}(L',r,L) \phi_{n,coll,eff}(L',r) dL' dr \Big|_{face} \end{aligned} \quad [4.34]$$

In this equation, L and L' , respectively denote the size of an attrition fragment and a parent crystal.

4.4.3 HALF-TIME FOR SUPERSATURATION DECAY

Step three of the compartmentation procedure presented in subparagraph 4.3.1 concerns the refinement of the compartment structure with respect to internal supersaturation gradients. For this purpose, a half-time for supersaturation decay is a useful quantity. Gradients in the supersaturation are expected to be negligible if the residence time within a compartment is short compared to the time required to deplete half of the available supersaturation by growth or nucleation.

Garside (1985) derived analytical solutions to determine the half-time for supersaturation decay in crystallisation systems with size independent growth ($G = k_g \Delta c^g$), constant volume and void fraction within the half-time:

$$t_{\Delta c,1/2} \approx \frac{0.6\varepsilon}{k_g A_T} \quad \text{for } g=1 \quad [4.35]$$

$$t_{\Delta c,1/2} = \frac{(2^{g-1} - 1)\varepsilon}{(g - 1)k_g\Delta c_i^{g-1}A_T} \quad \text{for } g \neq 1 \quad [4.36]$$

Despite the fact that crystal growth is often not size independent, the trends given by these analytical solutions will remain true: the half-time increases for increasing void fraction and decreasing crystal surface area. For exact calculations of half-times in systems with size dependent growth rates ($k_g=k_g(L)$) numerical solutions are needed. The half-time for supersaturation depletion $t_{\Delta c,1/2}$ will then not only depend on the specific crystal surface area A_T but also on the shape of the crystal size distribution.

In general, $t_{\Delta c,1/2}$ appears to vary from a few seconds to several minutes (Garside, 1985).

4.4.4 CLASSIFICATION MODEL

Whenever there is a material density difference between the solid and liquid phase, crystals will not always follow the stream lines of the liquid phase. As a result, the flow pattern and distribution of solids in the crystalliser will differ from the liquid phase. This phenomenon increases with increasing particle size and increasing density difference. To correctly account for this effect, requires two-phase computational fluid dynamics, i.e. simultaneous solution of the equations of motion for the liquid phase and for the various particle sizes in the solid phase, while taking into account particle-particle and particle-liquid interactions as well as equipment related boundary conditions.

However, as discussed earlier (section 4.2.2.1), it is currently not practically feasible to directly use CFD methods in a crystallisation process modelling framework for the evaluation and optimisation of design alternatives. Therefore, we adopt a simplified approach that can be implemented in the compartmental modelling framework. The approach comprises the calculation of classification functions, to account for the difference in flow pattern of the liquid and solid phase due to particle slip.

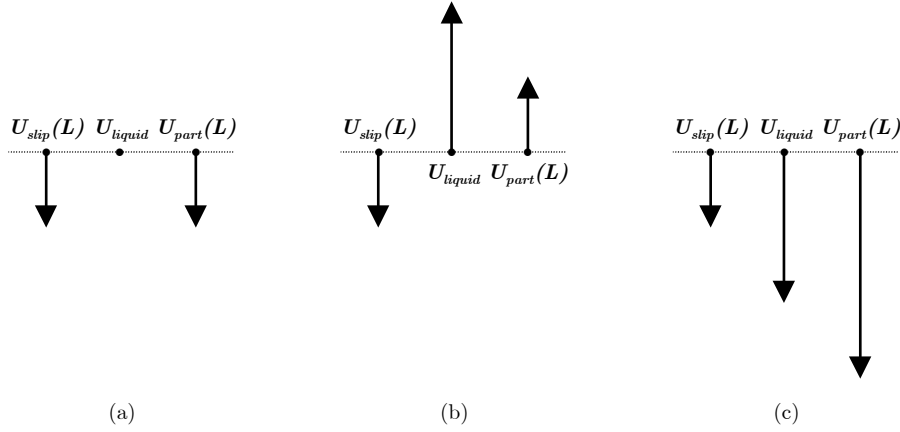


Figure 4.9: Particle slip velocity, U_{slip} , absolute liquid velocity, U_{liquid} , and absolute particle velocity, U_{part} , in three different scenarios: stagnant liquid (a), upward moving liquid (b) and downward moving liquid (c).

4.4.4.1 Particle slip velocity

The slip of a particle is defined as its relative motion with regard to the liquid. As slip is a result of inertia, the slip velocity of a particle depends on its size. Besides particle size, the slip velocity also depends on the density difference between the solid and liquid phase, particle shape and the dynamic viscosity of the liquid phase. Furthermore, if multiple particles are present, the volume fraction of solids and the particle size distribution also influence the particle slip velocity.

There are various models in literature for the calculation of slip velocities (e.g. Richardson and Zaki, 1954; Barnea and Mizrahi, 1973; Zimmels, 1983). Usually these models are called settling or sedimentation models as they were originally developed for particle settling in a stationary liquid. In that case, i.e. liquid velocity equal to zero, the absolute particle (settling) velocity equals the particle slip velocity (see Figure 4.9.a). In order to apply these models for a moving liquid, the absolute particle velocity, U_{part} , is defined as the sum of the absolute liquid velocity, U_{slip} , and the particle slip velocity, U_{liquid} :

$$U_{part}(L) = U_{liquid} + U_{slip}(L) \quad [4.37]$$

Note that the settling velocities or slip velocities calculated by the above-mentioned models are terminal velocities, i.e. the velocities corresponding to the steady-state solution of the force balance on a particle.

Bouma (1997) compared the model predictions of the various models and found little difference between them. The result of this study was to use the model of Barnea and Mizrahi (1973) for the calculation of particle slip velocities. It was chosen over Richardson and Zaki (1954) because it can be used over a wider flow regime, i.e. the Stokes, Transition and Turbulent regimes. It was also chosen in favour of Zimmels' approach (1983), which is in fact an extension of the Barnea

and Mizrahi model, because its added complexity relating to polydispersity only leads to significantly different model predictions at solids concentrations exceeding 20 vol%, but does require significantly more computational effort.

Using the model of Barnea and Mizrahi, the slip velocity of a particle is calculated using the following set of eight equations:

$$U_{slip}(L) = \left(\frac{-B(L) + \sqrt{B(L)^2 + AC(L)}}{C(L)} \right)^2 \quad [4.38]$$

where parameters A , B and C are defined as follows:

$$A = \sqrt{\alpha_1} \quad [4.39]$$

$$B(L) = 0.5\sqrt{\alpha_2}\alpha_4 \quad [4.40]$$

$$C(L) = \sqrt{\alpha_2}\alpha_3 \quad [4.41]$$

and α_1 , α_2 , α_3 and α_4 are given by:

$$\alpha_1 = g \frac{\rho_S - \rho_L}{\rho_S + \rho_L} \quad [4.42]$$

$$\alpha_2(L) = \frac{3}{4} \frac{1 + (1 - \varepsilon)^{1/3}}{(\rho_S + \rho_L)L^2\varepsilon} \quad [4.43]$$

$$\alpha_3(L) = 0.63\sqrt{L\rho_L} \quad [4.44]$$

$$\alpha_4 = 4.80\sqrt{\eta_L} \exp\left[\frac{5}{6} \frac{1 - \varepsilon}{\varepsilon}\right] \quad [4.45]$$

4.4.4.2 Classification function

Classification functions account for the difference in flow pattern of the liquid and solid phase by rendering the residence time of crystals in a compartment size dependent. For a compartment with one outlet stream, the crystal residence time is defined as:

$$\tau(L) = \frac{V n(L)}{\phi_{V,out} n_{out}(L)} \quad [4.46]$$

The ratio of the crystal number density in a certain outlet stream and in the compartment is defined as the classification function of that stream:

$$h_{out}(L) = \frac{n_{out}(L)}{n(L)} \quad [4.47]$$

The introduction of a classification function allows one to have compartments that are perfectly mixed internally but not necessarily with respect to the outlet streams. The latter only refers to the crystal size distribution; the temperature

and liquid phase composition of the outlet stream are always assumed to be equal to the temperature and composition within the compartment.

Using the definition of the classification function, the size dependent residence time of crystals in a compartment with a single outlet can be expressed as:

$$\tau(L) = \frac{V}{h_{out}(L)\phi_{V,out}} \quad [4.48]$$

Consider a compartment describing the bottom region of a crystalliser. As a result of gravity, the crystal concentration is typically higher in the bottom regions of a crystalliser than the top regions. This phenomenon becomes more pronounced with increasing crystal size. Or in terms of classification functions: for an upward stream leaving this compartment, the value of the classification function will decrease with increasing crystal size. As can be seen from Equation 4.48, a lower classification function value implies a higher residence time, i.e. a lower tendency to leave the compartment. Classification functions thus provide a simple but effective way to describe a non-uniform crystal size distribution throughout a crystalliser.

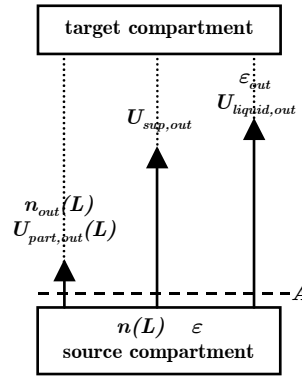


Figure 4.10: Particle velocity, superficial velocity, liquid velocity, crystal size distribution and cross-sectional area of a flow connecting two compartments.

By assuming flat profiles for the particle, liquid and superficial velocities in flows connecting compartments, classification function values can be calculated using the following equation:

$$h_{out}(L) = \frac{U_{part,out}(L)}{U_{sup,out}} \quad [4.49]$$

$$U_{sup,out} = \frac{\phi_{V,out}}{A} \quad [4.50]$$

The ratio of the particle velocity, $U_{part,out}(L)$, and superficial or average flow velocity, $U_{sup,out}$, is equal to the ratio of the average residence time, τ , and the size dependent residence time of the crystal, $\tau(L)$. As expected, this ratio is equal to the classification function:

$$\tau = \frac{V}{\phi_{V,out}} \quad [4.51]$$

$$\frac{\tau}{\tau(L)} = \frac{V/\phi_{V,out}}{V/(h_{out}(L)\phi_{V,out})} = h_{out}(L) \quad [4.52]$$

Combining Eq. 4.49 and Eq. 4.37 gives the following expression for the classification function:

$$h_{out}(L) = \frac{U_{liquid,out} + U_{slip}(L)}{U_{sup,out}} \quad [4.53]$$

For a given total volumetric flow rate and given material properties, the superficial velocity and particle slip velocity can be directly calculated using equations presented earlier in this section. The last piece of information required for the calculation of classification functions is thus the liquid velocity. Calculation of this velocity may seem trivial, but that is only the case when the solids concentration is very low. In such a situation, the liquid velocity may be approximated by the superficial velocity. A more general expression for the liquid velocity must account for the concentration and velocity of the various sized crystals. Such an expression is derived below:

$$\phi_{V,out} = \phi_{V,liquid,out} + \phi_{V,part,out} \quad [4.54]$$

The total volumetric flow rate is the sum of the liquid and solid phase flow rates. The flow rates of the individual phases are given by the following two equations:

$$\phi_{V,liquid,out} = U_{liquid,out} \varepsilon_{out} A \quad [4.55]$$

$$\phi_{V,part,out} = A \int_{L=0}^{\infty} U_{part,out}(L) n_{out}(L) L^3 dL \quad [4.56]$$

Using Eq. 4.37 the above equation can be written as follows:

$$\begin{aligned} \phi_{V,part,out} &= A \int_{L=0}^{\infty} (U_{liquid,out} + U_{slip}(L)) n_{out}(L) L^3 dL \\ &= A U_{liquid,out} \int_{L=0}^{\infty} n_{out}(L) L^3 dL + A \int_{L=0}^{\infty} U_{slip}(L) n_{out}(L) L^3 dL \\ &= U_{liquid,out} (1 - \varepsilon_{out}) A + A \int_{L=0}^{\infty} U_{slip}(L) n_{out}(L) L^3 dL \end{aligned} \quad [4.57]$$

Substituting Eq. 4.55 and Eq. 4.57 into Eq. 4.54 leads to the following expression for the total volumetric flow rate:

$$\begin{aligned}
\phi_{V,out} &= \phi_{V,liquid,out} + \phi_{V,part,out} \\
&= U_{liquid,out} \varepsilon_{out} A + U_{liquid,out} (1 - \varepsilon_{out}) A + A \int_{L=0}^{\infty} U_{slip}(L) n_{out}(L) L^3 dL \\
&= U_{liquid,out} A + A \int_{L=0}^{\infty} U_{slip}(L) n_{out}(L) L^3 dL
\end{aligned} \tag{4.58}$$

Combining this equation with the relationship between the total volumetric flow rate and the superficial velocity (Eq. 4.50) gives:

$$U_{sup,out} = U_{liquid,out} + \int_{L=0}^{\infty} U_{slip}(L) n_{out}(L) L^3 dL \tag{4.59}$$

Replacing the liquid velocity in Eq. 4.53 with the equation above results in an expression for the classification function that only contains the superficial velocity and particle slip velocities, both of which are known:

$$\begin{aligned}
h_{out}(L) &= \frac{U_{sup,out} - \int_{L=0}^{\infty} U_{slip}(L) n_{out}(L) L^3 dL + U_{slip}(L)}{U_{sup,out}} \\
&= 1 + \frac{U_{slip}(L) - \int_{L=0}^{\infty} U_{slip}(L) n_{out}(L) L^3 dL}{U_{sup,out}}
\end{aligned} \tag{4.60}$$

This equation can be simplified by considering the classification function for crystals of size zero. These crystals have no inertia and thus no slip. They consequently have the same flow behaviour as the liquid. The value of the classification function for these crystals is thus equal to the ratio of the volume fraction liquid in the outlet and within the compartment:

$$h_{out}(L = 0) = 1 + \frac{0 - \int_{L=0}^{\infty} U_{slip}(L) n_{out}(L) L^3 dL}{U_{sup,out}} = \frac{\varepsilon_{out}}{\varepsilon} \tag{4.61}$$

From these two equations, we obtain the following expression for the integral:

$$\int_{L=0}^{\infty} U_{slip}(L) n_{out}(L) L^3 dL = U_{sup,out} \left(1 - \frac{\varepsilon_{out}}{\varepsilon}\right) \tag{4.62}$$

Replacing the integral in Eq. 4.60 with the expression above gives:

$$\begin{aligned}
h_{out}(L) &= 1 + \frac{U_{slip}(L) - U_{sup,out} \left(1 - \frac{\varepsilon_{out}}{\varepsilon}\right)}{U_{sup,out}} = \frac{U_{slip}(L) + U_{sup,out} \frac{\varepsilon_{out}}{\varepsilon}}{U_{sup,out}} \\
&= \frac{U_{slip}(L)}{U_{sup,out}} + \frac{\varepsilon_{out}}{\varepsilon}
\end{aligned} \tag{4.63}$$

Note that this result differs from that given by Eek (1995a), which is believed to be wrong.

4.4.5 CRYSTAL SIZE DISTRIBUTION REPRESENTATIONS

So far, the number density distribution has been used to represent the amount of crystals present as well as the size distribution of these crystals. In practice, many different representations are used depending on which aspect of the size distribution is of most interest. The same holds for this thesis, and for convenience the various representations used throughout this work are listed and defined in the table below.

Table 4.3: Crystal size distribution representations used in this thesis.

description	mathematical definition
cumulative number density distribution	$N(L) = \int_0^L n(L) dL$
volume density distribution	$v(L) = n(L)k_v(L)L^3$
cumulative volume density distribution	$V(L) = \int_0^L v(L) dL$
normalised cumulative volume density distribution	$\tilde{V}(L) = \frac{V(L)}{V(L = \infty)}$
moments of the (number based) distribution	$M_i = \int_0^{\infty} n(L)L^i dL \quad , \quad i = 0, \dots, 3$
quantiles of the distribution	$\frac{q}{100} = \tilde{V}(L_q)$

4.4.6 THERMODYNAMIC AND PHYSICAL PROPERTIES

Equations and values for the thermodynamic, physical and mechanical properties used within this framework are given in Appendix B.4.

4.5 A MODELLING FRAMEWORK FOR A WIDE RANGE OF PROCESSES

This paragraph addresses the modelling of the wide variety of crystallisation processes included in the scope of this thesis. This range of processes can be conveniently characterised by the employed:

1. Crystallisation method (cooling, flash-cooling or evaporative).
2. Operation mode (batch, semi-batch or continuous).
3. Configuration (single or multiple stage); and
4. Crystalliser type (stirred vessel, DT, DTB, FC or Oslo).

The modelling flexibility required to deal with this variety of processes in a consistent manner is achieved by setting up a process modelling framework:

- Based on the compartmental modelling approach in order to account for the influence of crystalliser type and scale on process behaviour and product quality.
- Using the single compartment model as the general building block of compartmental model; and
- Which allows the modeller to switch functionalities on and off per compartment and within the compartmental model as a whole. As discussed in paragraph 4.4, all compartments are to be modelled with the same compartment model. This implies that the compartment model must cater for the highest possible denominator, i.e. contain all functionalities that may be required in one or more compartments.

The remainder of this paragraph discusses which functionalities need to be switched on and off for different process configurations.

4.5.1 CRYSTALLISATION METHODS

The modelling of different crystallisation methods, e.g. cooling, flash-cooling and evaporative, using the same process modelling framework is relatively trivial. The differences that need to be accounted for in the modelling framework are listed in Table 4.4. The first two differences, viz feed temperature and heat input, are model inputs that can simply be assigned by the user. In contrast, the presence of a vapour liquid equilibrium and thus of a vapour flow is taken care of internally by the framework.

Table 4.4: Differences in crystallisation methods that need to be accounted for in a general crystallisation process modelling framework.

crystallisation method	feed temperature	heat input	vapour liquid equilibrium
cooling	$> T_{cryst}$	< 0	no
flash-cooling	$> T_{cryst}$	0	yes
flash-cooling with additional evaporation	$> T_{cryst}$	> 0	yes
evaporative	$\leq T_{cryst}$	> 0	yes

4.5.2 OPERATION MODES

The modelling of different operation modes, e.g. batch, semi-batch and continuous, using the same process modelling framework is more demanding than that of different crystallisation methods. The differences that need to be accounted for in the modelling framework are listed in Table 4.5.

In batch operation, the feed and product flow rates are zero and the crystalliser volume may vary due to density changes. During semi batch operation the product flow rate is also zero, but variations in crystalliser volume due to density

changes are compensated for using a controller manipulating the feed flow. A volume or level controller is also used in continuous operation. The manipulated variable may be either the feed flow rate or the product flow rate. The flow rate that is not manipulated is assigned by the user.

Table 4.5: Differences in operation mode that need to be accounted for in a general crystallisation process modelling framework.

operation mode	feed flow rate	product flow rate	crystalliser volume
batch	0	0	free
semi-batch	> 0 (MV)	0	controlled (CV)
continuous	> 0 (MV)	> 0	controlled (CV)

An additional complication may arise when modelling a batch crystalliser using a compartmental model. As the volume of the crystalliser changes during the batch, certain compartments may be only partially full or even empty. This may also occur when considering the start-up or shutdown of a continuous crystalliser. The modelling framework in its current state only allows one compartment to have a fluctuating volume; the volumes of all other compartments are fixed in time. This was not a limitation for the modelling activities performed for this thesis work. However, it is recommended that this is addressed as it is likely to be a limiting factor for future applications.

4.5.3 CRYSTALLISER TYPES

Using the concept of compartmental modelling, the same modelling framework can be used to describe different crystalliser types. This is illustrated in this section for a draft tube baffle crystalliser, forced circulation crystalliser and fluidised bed crystalliser (Oslo crystalliser), by setting up compartmental models according to the compartmentation procedure presented in section 4.3.1.

4.5.3.1 Draft tube baffle crystalliser

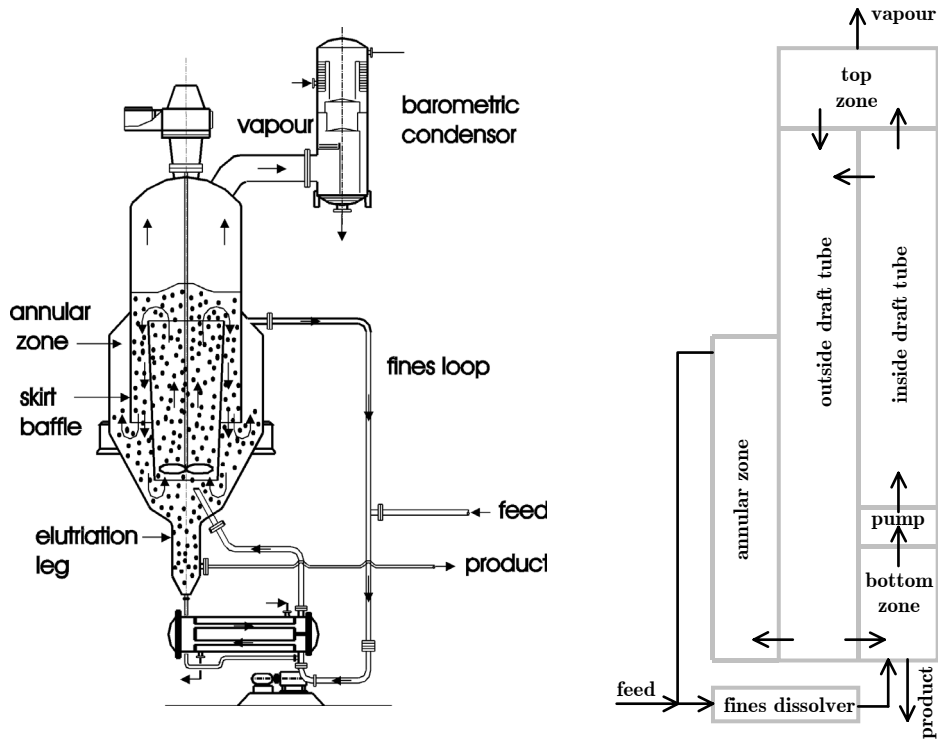


Figure 4.11: Draft tube baffle crystalliser and its possible compartmental model.

The compartmental model of the draft tube baffle crystalliser shown in Figure 4.11, can take into account phenomena such as:

- Enhanced settling of larger particles in the boiling zone and in the upward stream through the draft tube.
- Supersaturation in the boiling zone (growth).
- Undersaturation in the external heat exchanger, to model dissolution of the fine particles; and
- Majority of attrition taking place in the mixing zone where the impeller is located. The nucleation rate as a result of this attrition process may be strongly reduced as a consequence of very low supersaturation levels or even undersaturated conditions.

4.5.3.2 Forced circulation crystalliser

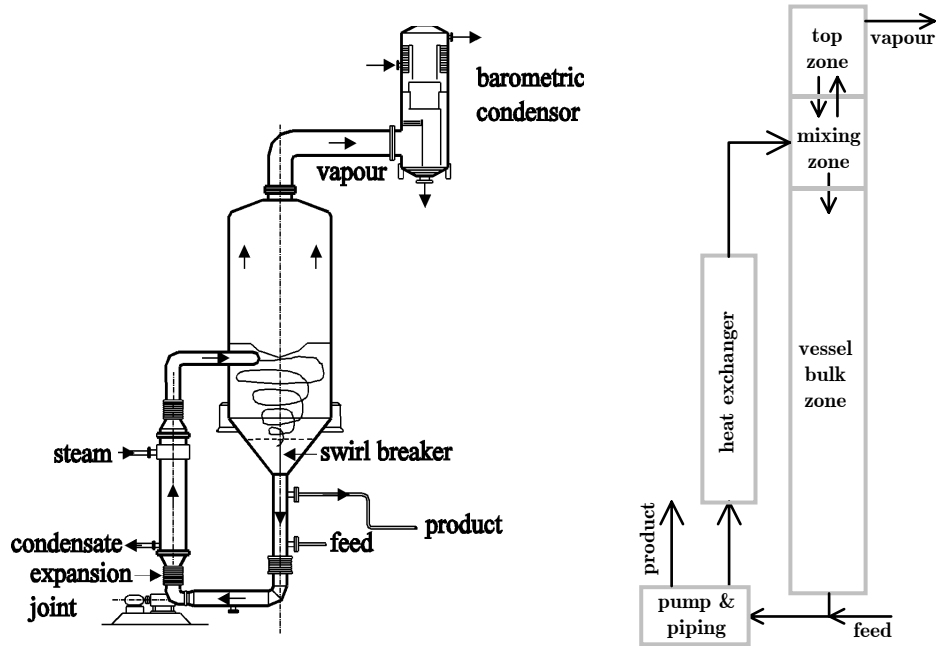


Figure 4.12: Forced circulation crystalliser and its possible compartmental model.

The compartmental model (Figure 4.12) of the forced circulation crystalliser can describe:

- Enhanced settling of larger particles in the boiling zone and the main crystalliser body.
- Supersaturation in the boiling zone (growth) and possibly undersaturation in the heat exchanger. The latter is again related to the internal dissolution of fine particles; and
- Majority of attrition in the circulation pump. The effective birth rate is influenced by the level of super- or undersaturation subsequently experienced by the attrition fragments in the heat exchanger.

4.5.3.3 Oslo (fluidised bed) crystalliser

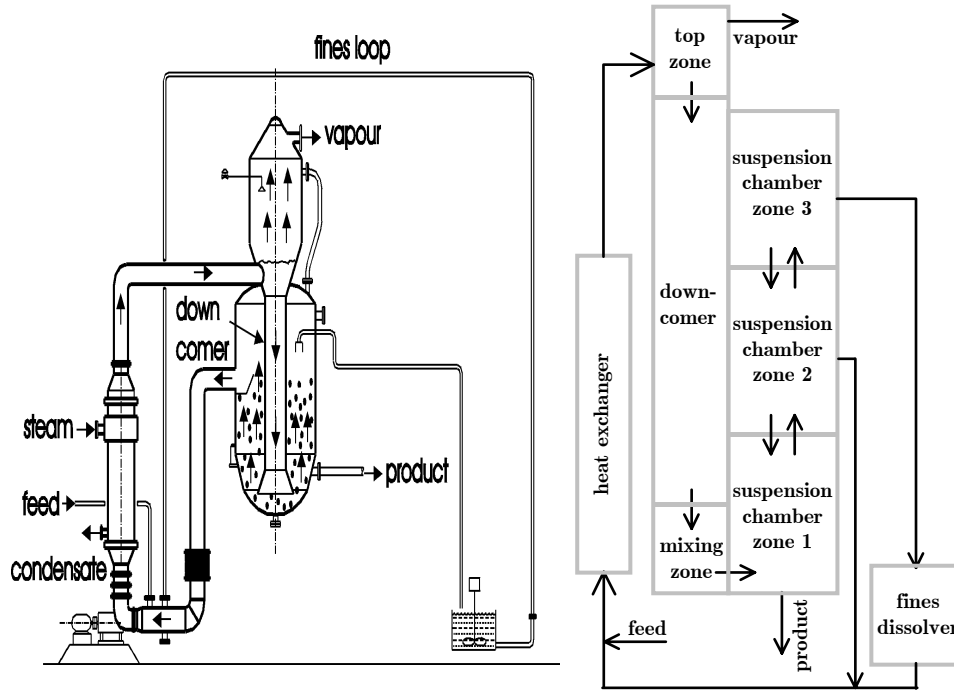


Figure 4.13: Oslo (fluidised bed) crystalliser and its possible compartmental model.

The compartmental model of the Oslo crystalliser presented below (Figure 4.13), can among others describe the following effects:

- High supersaturation in the boiling zone, in the presence of no or very few particles.
- Classification of particles in the fluidised bed (suspension chamber); and
- Influence of changes in the circulation flow rate on the residence time in the heat exchanger and the temperature rise of the process fluid per pass. Both effects influence the degree of dissolution of the fine particles.

A major difference between an Oslo crystalliser and other crystalliser types, for crystallisation systems where secondary nucleation is an important source of crystal birth, is the nature of the dominant secondary nucleation source. Because the larger crystals do not pass through the external circulation loop in a properly operated Oslo crystalliser, the dominant source for secondary nucleation cannot be crystal-impeller collisions but will be crystal-crystal collisions. As a result, the collisions sub model of the secondary nucleation model presented in this chapter is not applicable to this crystalliser type.

4.6 CONCLUSIONS

Due to computational limitations, it is currently not practically feasible to model crystallisation or precipitation processes with high spatial resolutions, as provided by CFD packages, whilst taking into account the time domain and internal co-ordinates of the crystalline product, such as crystal size. For solution crystallisation processes, a high resolution for the time domain (in the order of days) and the crystal size co-ordinate are considered more important than a high spatial resolution. Consequently, a compartmental modelling approach is adopted to provide a separation between kinetics and overall hydrodynamics. Application of this technique to crystallisation is not a novelty; the added value of the compartmental modelling framework presented here is:

- The inclusion of process dynamics.
- The use of detailed kinetic models with a physically sound basis.
- The use of classification functions to account for the size dependent spatial distribution of solids; and
- The combination of the above to obtain the predictive properties needed for design purposes.

The compartmentation procedure presented in this chapter involves heuristics in many of its steps. Depending on the availability of CFD results, the procedure's reliance on heuristics may be substantially decreased. When CFD calculations have been performed, interpretation of these results may be done on the basis of engineering insights or using an automatic zoning technique that makes the compartmentation procedure significantly less ambiguous. Nevertheless, caution must be exercised when interpreting CFD results. For instance, predicted energy dissipation rates may be considerably higher than measured values.

It should be noted that the compartmentation procedure presented here reflects an analysis oriented way of thinking rather than one driven by synthesis. It deals with some a priori given hydrodynamic situation that has to be approximately modelled in the best possible manner for analysis purposes. In the synthesis oriented way of thinking one would rather ask the inverse question: *'What is the best way of creating sources for secondary nucleation, what is the preferred way of staging heat transfer and fluid circulation to get the best possible product composition at the lowest capital and operational costs?'* Having determined the optimal compartment configuration and connectivity, the next step would be to derive an actual geometry and hydrodynamic situation that approximates the optimal compartment configuration as closely as possible.

The Gahn kinetic model is implemented to describe crystal growth, crystal attrition due to crystal-impeller collisions and the outgrowth of the resulting attrition fragments (secondary nucleation). It was chosen over other secondary nucleation and growth models by Ottens, Eek and Ó Meadhra, because it has a significantly sounder physical basis, as a result of which it has an explicit dependency of the kinetic rates on crystalliser geometry, impeller geometry and impeller frequency. Nevertheless, there is one significant shortcoming worth

noting, viz the fact that the driving force for crystallisation is expressed in terms of concentration and not activity. This shortcoming is not expected to affect the work in this thesis as a feedstock with a consistently high purity was used for all experimental work. However, in industrial practice the use of concentration based driving forces may significantly limit the predictive value of the model with respect to changes in feed composition.

The crystallisation process modelling framework, which consists of the compartmentation procedure and a general compartment model, allows rapid generation of consistent process models that cover the wide range of processes included in the scope of this work. However, the existence of this framework and the use of rigorous kinetic models do not in themselves ensure good predictive capabilities. These capabilities will be investigated in Chapter 6.

5 MODEL IMPLEMENTATION AND NUMERICAL ISSUES

Comprehensive crystallisation process models typically do not have analytical solutions. For the numerical solution of these models, several commercially available packages are considered. The selected package is a general-purpose process modelling tool that supports steady-state and dynamic simulation, parameter estimation and optimisation using formal mathematically-based methods. Whereas this tool can solve sets of differential and algebraic equations to a predefined accuracy, this is not the case for partial differential equations, e.g. the population balance equation, and integral equations, e.g. moment calculations. In order to solve equations belonging to one of these two categories, they need to be transformed into ordinary differential equations or algebraic equations. In this work, the finite volume method is used for this transformation. The accuracy of this transformation or approximation is determined by the discretisation resolution of the crystal size domain and the formulation of the population balance equation. Investigation of these relationships reveals that the most suitable discretisation type, e.g. linear or logarithmic, depends on the employed crystallisation kinetics model. For the kinetic model of most interest for this thesis, i.e. the Gahn model, a logarithmic crystal size grid leads to the most accurate results for a given number of nodes. The optimal spacing between the nodes is determined on the basis of a trade-off between accuracy and computational performance. Initial work with the Gahn model revealed some significant pitfalls when implementing conditional equations with respect to crystal size on a discretised crystal size domain. Smoothing these conditional equations is essential for model-based optimisation of process design and operation.

5.1 INTRODUCTION

In the previous chapter, the use of the same crystallisation model for a wide range of crystallisation processes was emphasised. This objective was achieved by means of a general crystallisation process modelling framework using a general single compartment model as its sole building block. Here the focus is on selecting a single modelling tool that can be used (i) to implement this compartment model and thus to model the crystallisation processes covered by the scope defined in Chapter 1.5, (ii) for all model-based activities in the design process and (iii) if possible, for off-line and on-line model-based activities related to process operation.

5.2 MODELLING TOOL REQUIREMENTS AND SELECTION

In the previous chapters a number of requirements have already been (implicitly) formulated with respect to a modelling tool to be used for the design of crystallisation processes and products.

- Time domain: steady-state and dynamic modelling (see Chapters 2.4.2 and 4.2); and
- Nature of the mathematical problem: numerical solution of a crystallisation process and product model based upon the framework presented in the previous chapter involves solution of algebraic equations, ordinary differential equations, partial differential equations and integral equations.

Using a modelling framework in the different stages of a plant's life cycle, i.e. design, (de-)commissioning, operation and control, requires a modelling tool that supports a number of model-based activities:

- Parameter estimation (to acquire design information).
- Simulation (to explore the design space); and
- Process optimisation (to find the best design and operating conditions).

Simulation is relatively the easiest of these activities as it 'only' involves the solution of a so-called *forward problem*: given a model, model parameters and inputs, calculate the model output, i.e. the behaviour of a crystallisation process and the quality of the resulting product. Model inputs typically include equipment dimensions and operating conditions.

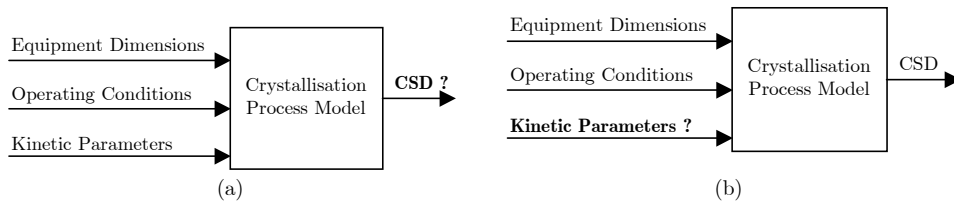


Figure 5.1: Schematic depiction of the simulation (a) and parameter estimation (b) problem. Unknown model inputs and outputs are shown in bold.

Parameter estimation and optimisation are *inverse problems*. This class of problems is typically much harder to solve than forward problems because it requires the determination of certain model inputs given a desired model output. Parameter estimation can be defined as: given measured process output (e.g. CSD and supersaturation), a model and model inputs, determine the values of the unknown model parameters in order to maximise the probability that the predicted model output will correspond to the measured output. Process optimisation can be defined similarly: given a desired process output (e.g. production capacity and CSD), a model and model parameters, determine the

optimal values for inputs related to design (e.g. crystalliser type and scale) and/or operating conditions (e.g. residence time and pump frequency).

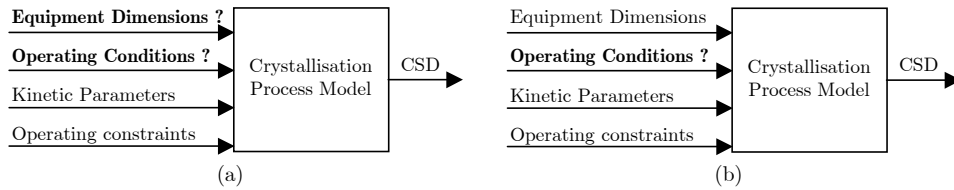


Figure 5.2: Schematic depiction of the optimisation of design and operation (a) and the optimisation of operation alone (b). Unknown model inputs are shown in bold.

In practice, *inverse problems* are usually solved by manually 'tweaking' model inputs and doing hundreds of simulations, i.e. solving hundreds of *forward problems*. Besides from being very laborious, this approach has several major drawbacks: (1) even for small problems it is difficult to manually satisfy all constraints, (2) even if feasibility is achieved, there is no guarantee of optimality, and (3) it is difficult to determine the statistical significance of a solution.

A more time- and cost-efficient as well as effective method for the solution of inverse problems embraces formal, mathematically-based methods. A modelling tool containing such methods is obviously desirable.

Based on the requirements listed above, three commercial dynamic modelling tools were considered for this work: Matlab (MathWorks, 1995), SpeedUp (Pantelides, 1988; AspenTech, 1995) and gPROMS (Barton and Pantelides, 1994; Process Systems Enterprise Ltd, 2002). Matlab was dismissed because it is not as computationally efficient in dealing with large DAE systems. gPROMS was chosen over SpeedUp because (i) it has a more powerful modelling language, (ii) it has better support for hierarchical modelling and (iii) it has a longer track record on solving optimisation and parameter estimation problems using its built-in mathematically-based optimisation methods.

5.3 NUMERICAL SOLUTION METHODS FOR PARTIAL DIFFERENTIAL AND INTEGRAL EQUATIONS

gPROMS is a modelling tool that can simultaneously solve mixed systems of algebraic equations (AEs) and ordinary differential equations (ODEs) with respect to time. These systems are conveniently referred to as systems of differential-algebraic equations (DAEs). Besides AEs and ODEs, the crystallisation model presented in the previous chapter also comprises of a partial differential equation (PDE), i.e. the population balance, and a number of integral equations (IEs) for the calculation of among others the total crystal volume fraction and characteristics of the crystal size distribution such as quantiles. In order to solve these equations in gPROMS they must be reduced to a set of DAEs. These reductions concern all derivatives with respect to independent variables other

than time, as well as all integrals over other independent variables than time. The independent variables of interest for this work are the crystal size or crystal length, L , and radial impeller co-ordinate, r . In order to perform the reductions, the independent variable domains need to be discretised.

The next sections successively discuss the discretisation of the crystal size domain (5.3.1), the reduction to DAEs of the population balance, which contains a partial derivative with respect to crystal length (5.3.2), and the reduction to DAEs of integrals over crystal length (5.3.3).

The discretisation of the radial impeller co-ordinate and the reduction to AEs of integrals over this independent variable are presented in section 5.5.3.

5.3.1 DISCRETISATION OF CRYSTAL SIZE DOMAIN

Discretisation of the crystal size domain involves at least three aspects:

- The lower bound of the domain, L_{min} .
- The upper bound of the domain, L_{max} ; and
- The discretisation resolution.

To begin with the last aspect, for given lower and upper bounds, the resolution is not only determined by the number of elements or nodes, but also by the spacing between these nodes. The simplest spacing is equidistant, but sometimes it may be more convenient to have a smaller spacing (i.e. higher resolution) in certain parts of the domain and a larger spacing in other parts of the domain. However, most numerical methods for the reduction of PDEs and integral equations to DAEs only apply to equally spaced nodes.

Depending on the employed crystallisation kinetics models, e.g. size dependent or size independent growth, birth of single-sized crystals or birth of crystals with a size distribution, etc. the use of a crystal size domain, L , with non-equidistant spacing is favourable. In order to be able to use numerical methods only applicable to equally spaced nodes, we introduce a normalised crystal size domain, z . This normalised domain has a lower bound of zero, an upper bound of one and nodes that are by definition equidistantly spaced. The reduction of PDEs and integral equations to DAEs now requires the following two steps:

1. Take the original derivative or integral with respect to L and rewrite it as a derivative or integral with respect to z , e.g.:

$$\frac{\partial [n(L,t)G(L,t)]}{\partial L} = \frac{\partial [n(z,t)G(z,t)]}{\partial z} \frac{dz}{dL} \quad [5.1]$$

$$\int_{L_{min}}^{L_{max}} n(L,t)L^3 dL = \int_0^1 n(z,t)L(z)^3 \frac{dL}{dz} dz \quad [5.2]$$

2. Apply the numerical method for the reduction to a system of DAEs to the derivative or integral with respect to z . This step is subject of sections 5.3.2 and 5.3.3.

The first step only requires L as a function of z and the derivative of L with respect to z . This makes it easy to implement different discretisation schemes. In this work only a linear and logarithmic scheme are used, but the addition of a user-defined scheme is clearly trivial. The linear scheme is given by:

$$L = L_{min} + z(L_{max} - L_{min}) \quad [5.3]$$

$$\frac{dL}{dz} = L_{max} - L_{min} \quad [5.4]$$

The logarithmic scheme is defined as:

$$L = L_{min} \exp\left(z \ln\left(\frac{L_{max}}{L_{min}}\right)\right) \quad [5.5]$$

$$\frac{dL}{dz} = \ln\left(\frac{L_{max}}{L_{min}}\right) L_{min} \exp\left(z \ln\left(\frac{L_{max}}{L_{min}}\right)\right) = \ln\left(\frac{L_{max}}{L_{min}}\right) L \quad [5.6]$$

Finally, the choice of the lower bound of the domain, L_{min} , and the upper bound of the domain, L_{max} . The lower bound should be equal to or smaller than the critical nucleus size and equal to or larger than zero. The upper bound should be chosen such that the concentration of crystals at this point can be assumed to be zero:

$$n(L_{max}, t) \approx 0 \quad \forall t \geq 0 \quad [5.7]$$

The location of L_{max} thus depends on the rates of the various crystallisation mechanisms as well as the residence time for continuous processes or batch time for batch processes. Consequently, whenever one changes to a new chemical system, another crystalliser or a different set of operating conditions, the location of the lower and upper bound need to be reconsidered.

5.3.2 DERIVATIVES WITH RESPECT TO CRYSTAL SIZE

The dynamic form of the PBE is a PDE and thus needs to be reduced to a set of DAEs to be solved numerically. To this end, numerical methods belonging to the family of the Method of Lines are frequently used (Oh, 1995).

5.3.2.1 Method of Lines

This family comprises a number of finite difference, finite volume and weighted residual methods. The latter group of methods contains among others the (orthogonal) collocation method, least-squares method and Galerkin method. These weighted residual methods are often applied on finite elements.

The Method of Lines involves the discretisation of the non-temporal variable domains and the use of piecewise local or global functions to approximate the derivatives with respect to the non-temporal variables. After which the resulting ODEs, one for each grid point, are integrated over time along lines parallel to the time axis in the time-space domain; hence the name of this method. The methods belonging to the family of the Method of Lines differ in the grid discretisation

and/or in the approximation functions for the spatial, i.e. non-temporal, derivatives.

This section does not aim to provide a comprehensive review of the various numerical methods proposed in the past for solving PBEs. For that purpose, the interested reader is referred to Wójcik and Jones (1998), Hill and Ng (1997) or Kumar and Ramkrishna (1996).

Whether a numerical method is appropriate for the reduction of the PBE to a set of DAEs is foremost determined by the dominant crystallisation mechanisms.

If there is no crystal growth, e.g. only agglomeration and/or breakage occur, the PBE is not a PDE but an ODE with a time derivative of a distributed variable. In this case, there is no need for approximation functions for partial derivatives. However, accurate methods for the piecewise-constant approximation of the continuous birth and death terms in the PBE are required to ensure conservation of mass and other properties of the size distribution (Hounslow et al., 1988).

If crystal growth occurs, the PBE has a convective character and is classified as a hyperbolic PDE. Hyperbolic PDEs are best solved with an upwind finite difference method (Muhr et al., 1996) or a finite volume method (Gerstlauer et al., 2001). In the past, central finite difference methods have also been applied to the numerical solution of hyperbolic forms of the PBE (Eek, 1995a; Muhr et al., 1995). However, use of this method leads to negative values for the crystal concentrations (Muhr et al., 1996). This is hardly surprising since central difference in space and backward difference in time is known to be unconditionally unstable (Lapidus and Pinder, 1982). Although first order upwind finite difference and finite volume methods do not suffer from numerical instabilities when used correctly, they do invariably exhibit numerical diffusion (Lapidus and Pinder, 1982). As a result, acceptable solutions require relatively fine grids. More efficient methods, which are numerically more stable and exhibit less numerical diffusion, are orthogonal collocation on finite elements using an adaptive size grid for error control (Nicmanis and Hounslow, 1998) and a finite difference method combined with the method of characteristics (Kumar and Ramkrishna, 1997). These two methods cannot be directly implemented in a DAE solver such as gPROMS because they both involve a changing number of equations during the simulation. Based on the positive experience of Gerstlauer et al. (2001) with the finite volume method for the solution of the PBE in combination with the Gahn kinetic model, the same approach is used for this work.

5.3.2.2 Finite volume method

The first step of the finite volume method is the definition of a grid for the crystal size domain. This is done for the normalised crystal size domain, z , with an equidistant spacing between the grid points. As explained in section 5.3.1, the use of this intermediate, normalised domain enables a straightforward way of using grids with non-equidistant spacing on the real crystal size domain, L . Thus avoiding added complexity in the numerical method.

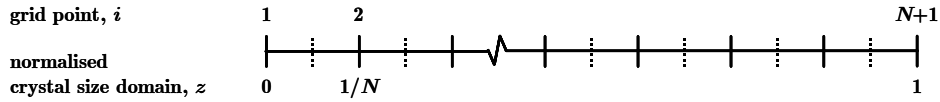


Figure 5.3: Crystal size grid — grid points.

The grid points form the boundaries of so-called control volumes (CVs). Next, computational nodes are assigned to the geometric centres of the CVs (see Figure 5.4). Note the contrast with finite difference methods where the grid points also constitute the computational nodes. Consequently, there are no computational nodes on the domain boundaries.

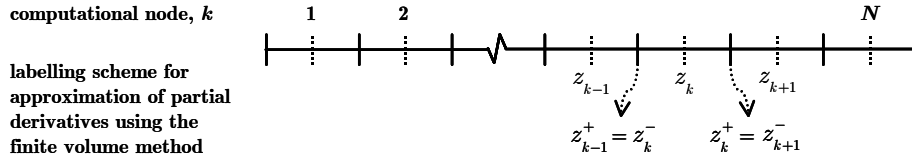


Figure 5.4: Crystal size grid — computational nodes and labelling scheme.

For the numerical approximation of the partial derivative in the PBE, we adopt the labelling scheme shown in Figure 5.4. By integrating each term of the PBE, written in terms of z , from z_k^- to z_k^+ the following approximation of the partial derivative with respect to z is obtained (Patankar, 1980):

$$\left. \frac{\partial nG}{\partial z} \right|_{z_k} = \frac{(nG)|_{z_k^+} - (nG)|_{z_k^-}}{z_k^+ - z_k^-} = \frac{(nG)|_{z_k^+} - (nG)|_{z_k^-}}{\Delta z_k} \tag{5.8}$$

Calculation of the partial derivative at the computational nodes, z_k , requires the values of the number densities and growth rates at the boundaries of the CVs, i.e. at the grid points. This is trivial for the growth rates as these can be obtained directly from the kinetic rate expressions, but this is not so for the number densities. A computational node is by definition the geometric centre of the control volume in which it lies. Hence, the value of the number density at the computational node is a representative value for the CV:

$$n(z) = n(z_k) \qquad z_k^- < z < z_k^+ \tag{5.9}$$

However, this relationship excludes the boundaries (see also Figure 5.5). Consequently, the values of the number densities at the boundaries of the CVs are still unknown at this point. Their values can be obtained by interpolation formulae, which are often referred to as profile assumptions. Common formulae are upwind interpolation, linear interpolation and quadratic upwind interpolation. Linear and quadratic upwind interpolation formulae provide approximations of an order higher than one and may therefore produce oscillatory solutions (Ferziger and Peric, 1996). Consequently, the upwind interpolation formula, a first order approximation, is used here.

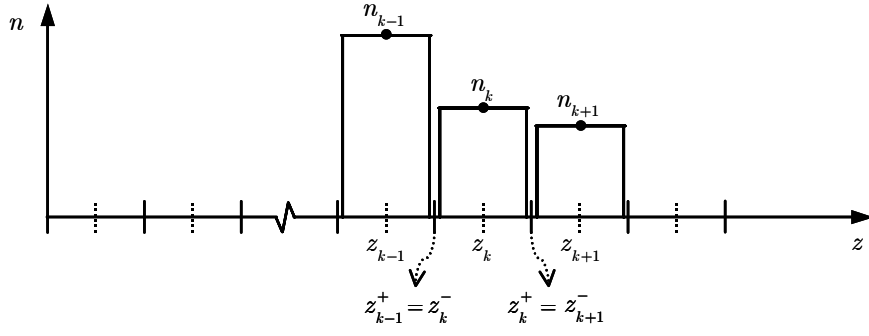


Figure 5.5: The need for profile assumptions to determine the number densities at the boundaries of the control volumes.

Upwind interpolation considers the direction i.e. sign of the convective term in the partial derivative, in this case the crystal growth rate. The values of $n(z_k^-)$ and $n(z_k^+)$ are simply approximated by those of the computational nodes upstream of z_k^- and z_k^+ respectively:

$$n(z_k^-) = \begin{cases} n(z_{k-1}) & G(z_k^-) > 0, & k = 2 \dots N \\ n(z_k) & G(z_k^-) \leq 0, & k = 1 \dots N \end{cases} \quad [5.10]$$

$$n(z_k^+) = \begin{cases} n(z_k) & G(z_k^+) \geq 0, & k = 1 \dots N \\ n(z_{k+1}) & G(z_k^+) < 0, & k = 1 \dots N - 1 \end{cases} \quad [5.11]$$

This approximation is equivalent to using a first order backward or forward difference approximation for the partial derivative (depending on the flow direction):

$$\left. \frac{\partial nG}{\partial z} \right|_{z_k} = \begin{cases} \frac{n(z_k)G(z_k^+) - n(z_{k-1})G(z_k^-)}{\Delta z_k} & G(z_k^-) > 0, G(z_k^+) \geq 0 \\ & k = 2, \dots, N \\ \frac{n(z_{k+1})G(z_k^+) - n(z_k)G(z_k^-)}{\Delta z_k} & G(z_k^-) \leq 0, G(z_k^+) < 0 \\ & k = 1, \dots, N - 1 \\ \frac{n(z_k)G(z_k^+) - n(z_k)G(z_k^-)}{\Delta z_k} & G(z_k^-) \leq 0, G(z_k^+) \geq 0 \\ & k = 1 \dots N \\ \frac{n(z_{k+1})G(z_k^+) - n(z_{k-1})G(z_k^-)}{\Delta z_k} & G(z_k^-) > 0, G(z_k^+) < 0 \\ & k = 2 \dots N - 1 \end{cases} \quad [5.12]$$

The approximations for the values of $n(z_k^-)$ and $n(z_k^+)$ as given by equations 5.10 and 5.11 exclude $n(z_1^-)$ and $n(z_N^+)$ when $G(z_1^-)$ and $G(z_N^+)$ are respectively

positive and negative. These cases reflect the active boundary conditions of the PBE as discussed in section 4.4.1.

Boundary condition at lower domain bound

If the growth rate at the lower boundary, $G(z_1^-)$, is positive, $n(z_1^-)$ is taken to be equal to the number density at the lower boundary ($z=0$):

$$n(z_1^-) = n(z = 0), \quad G(z_1^-) > 0 \quad [5.13]$$

This number density follows from the boundary condition:

$$n(z = 0) = \frac{B_0}{G(z = 0)} \quad [5.14]$$

Depending on the sign of the growth rate at the boundary of the first and second CV, z_1^+ , the partial derivative at the first computational node ($k=1$) is given by:

$$\left. \frac{\partial n G}{\partial z} \right|_{z_1} = \begin{cases} \frac{n(z_1)G(z_1^+) - B_0}{\Delta z_k}, & G(z_1^+) \geq 0 \\ \frac{n(z_2)G(z_1^+) - n(z_1)G(z_1^-)}{\Delta z_k}, & G(z_1^+) < 0 \end{cases} \quad [5.15]$$

Boundary condition at upper domain bound

When the growth rate at the upper boundary, $G(z_N^+)$, is negative, $n(z_N^+)$ is taken to be equal to the number density at the upper boundary ($z=1$):

$$n(z_N^+) = n(z = 1), \quad G(z_N^+) < 0 \quad [5.16]$$

Assuming that the location of the domain's upper bound, L_{max} , has been chosen correctly (see section 5.3.1), $n(z = 1)$ is zero:

$$n(z = 1) = n(L = L_{max}) \approx 0 \quad [5.17]$$

This results in the following expression for the partial derivative at computational node N :

$$\left. \frac{\partial n G}{\partial z} \right|_{z_N} = \begin{cases} \frac{0 - n(z_N)G(z_N^-)}{\Delta z_k}, & G(z_N^-) \leq 0 \\ \frac{n(z_N)G(z_N^+) - n(z_{N-1})G(z_N^-)}{\Delta z_k}, & G(z_N^-) > 0 \end{cases} \quad [5.18]$$

5.3.3 INTEGRATION OVER CRYSTAL SIZE

As the value of the number density at a computational node is a representative value for the CV containing that computational node, integrals with respect to the normalised crystal size, z , can be calculated using a Riemann summation, e.g.:

$$\int_0^1 n(z, t) L(z)^3 \frac{dL}{dz} dz = \sum_{k=1}^N n(z_k, t) L(z_k)^3 \frac{dL}{dz}(z_k) \Delta z_k \quad [5.19]$$

5.3.4 LOGARITHMIC TRANSFORMATION OF NUMBER DENSITIES

Another degree of freedom with respect to the numerical solution of the PBE is the form in which the number density appears in the PBE: in terms of ‘normal’ number densities or logarithms of the number densities. The most obvious advantage of taking the logarithms of the number densities is numerical scaling. A less obvious advantage is the fact that it provides a different approximation of the partial derivative term: linear in the logarithm of the number density instead of linear in the ‘normal’ number density. The transformation required to obtain a PBE in terms of logarithms of number densities is illustrated in the remainder of this subparagraph. The PBE as presented in chapter 4 (Eq. 4.4) is taken as a starting point:

$$\begin{aligned} \frac{\partial[n(L,t)V(t)]}{\partial t} = & -V(t) \frac{\partial[n(L,t)G(L,t)]}{\partial L} \\ & + \phi_{V,in}(t)n_{in}(L,t) - \phi_{V,out}(t)n_{out}(L,t) + \phi_n^\pm(L,t)V(t) \end{aligned} \quad [5.20]$$

Note that the terms relating to the convective transport into and out of the compartments have been simplified to account for one flow only, and that the various number production rate terms have been lumped into one. These simplifications have only been made for illustrative purposes; they are not necessary for this transformation.

The next step involves splitting the partial derivative:

$$\begin{aligned} \frac{\partial[n(L,t)V(t)]}{\partial t} = & -V(t) \left[n(L,t) \frac{dG(L,t)}{dL} + G(L,t) \frac{\partial n(L,t)}{\partial L} \right] \\ & + \phi_{V,in}(t)n_{in}(L,t) - \phi_{V,out}(t)n_{out}(L,t) + \phi_n^\pm(L,t)V(t) \end{aligned} \quad [5.21]$$

After which each term is multiplied by $d \ln n(L,t) / dn(L,t)$:

$$\begin{aligned} \frac{d \ln n(L,t)}{dn(L,t)} \frac{\partial[n(L,t)V(t)]}{\partial t} = & \\ & -V(t) \left[n(L,t) \frac{d \ln n(L,t)}{dn(L,t)} \frac{dG(L,t)}{dL} + G(L,t) \frac{d \ln n(L,t)}{dn(L,t)} \frac{\partial n(L,t)}{\partial L} \right] \\ & + \phi_{V,in}(t)n_{in}(L,t) \frac{d \ln n(L,t)}{dn(L,t)} - \phi_{V,out}(t)n_{out}(L,t) \frac{d \ln n(L,t)}{dn(L,t)} \\ & + \phi_n^\pm(L,t)V(t) \frac{d \ln n(L,t)}{dn(L,t)} \end{aligned} \quad [5.22]$$

Using the following relationships:

$$\frac{d \ln n(L,t)}{dn(L,t)} = \frac{1}{n(L,t)} \quad [5.23]$$

$$\frac{d \ln n(L,t)}{dn(L,t)} \frac{\partial n(L,t)}{\partial L} = \frac{\partial \ln n(L,t)}{\partial L} \quad [5.24]$$

Eq. 5.22 can be written as:

$$\begin{aligned} \frac{\partial [n(L,t)V(t)]}{\partial t} = & -n(L,t)V(t) \left[\frac{dG(L,t)}{dL} + G(L,t) \frac{\partial \ln n(L,t)}{\partial L} \right] \\ & + \phi_{V,in}(t)n_{in}(L,t) - \phi_{V,out}(t)n_{out}(L,t) + \phi_n^\pm(L,t)V(t) \end{aligned} \quad [5.25]$$

This completes the transformation of the partial derivative term in the PBE. Finally, all other number densities are also written in terms of logarithms:

$$\begin{aligned} \frac{\partial [\exp(\ln(n(L,t)V(t)))]}{\partial t} = & -\exp(\ln(n(L,t)V(t))) \left[\frac{dG(L,t)}{dL} + G(L,t) \frac{\partial \ln n(L,t)}{\partial L} \right] \\ & + \phi_{V,in}(t) \exp(\ln n_{in}(L,t)) - \phi_{V,out}(t) \exp(\ln n_{out}(L,t)) \\ & + \exp(\ln(\phi_n^\pm(L,t)V(t))) \end{aligned} \quad [5.26]$$

To obtain the numerical scaling advantage, the implemented model equations should not contain n , n_{in} and n_{out} as variables, but $\ln n$, $\ln(nV)$, $\ln n_{in}$ and $\ln n_{out}$. Whereas values for n may range from 1e-20 to 1e20, the corresponding values for $\ln n$ will only range from -46 to 46. Obviously care must be taken to avoid number densities of zero ($\ln n = -\infty$).

5.4 NUMERICAL VERSUS ANALYTICAL SOLUTION – SIMPLE KINETICS

This paragraph investigates the effect of the grid discretisation scheme (linear or logarithmic), discretisation resolution (number of grid points) and form of the partial derivative term in the population balance equation (in terms of normal number densities or logarithms of the number densities) on the accuracy of the numerical solutions obtained with the finite volume method. To this effect, numerical solutions of the crystal size distribution in terms of number densities and (normalised) cumulative volume density distributions will be compared with the corresponding analytical solutions of the PBE for a so-called MSMPR crystalliser with simple kinetics.

5.4.1 MSMPR CRYSTALLISER WITH SIMPLE KINETICS

A MSMPR crystalliser is the crystallisation community's equivalent of the CSTR, and can be characterised as follows:

<i>Operation</i>	<i>Kinetics</i>
steady state: $\mathcal{A}(nV)/\partial t = 0$	size-independent growth: $G \neq G(L)$
one feed, crystal free: $n_{in}(L) = 0$	crystal birth at size zero: $B(L) = 0; B_0 \geq 0$
one product, unclassified: $n_{out}(L) = n(L)$	no death of crystals: $D(L) = 0$

Taking the PBE presented in the previous chapter as a starting point and applying the characteristics listed above results in a strongly simplified PBE:

$$0 = -VG \frac{\partial n(L)}{\partial L} - \phi_{V,out} n(L), \quad [5.27]$$

This can be rewritten as:

$$\frac{dn(L)}{n(L)} = -\frac{\phi_{V,out}}{VG} dL \quad [5.28]$$

Integrating both sides from L equals zero to L produces the following result:

$$\ln\left(\frac{n(L)}{n_0}\right) = -\frac{L}{G\tau} \quad [5.29]$$

This can be rewritten to give the well-known analytical solution for the number density distribution in a MSMPR crystalliser:

$$n(L) = n_0 \exp\left(-\frac{L}{G\tau}\right) \quad [5.30]$$

The cumulative volume density distribution is obtained from the number density distribution using the following equation:

$$V(L) = \int_0^L n(L)k_v(L)L^3 dL \quad [5.31]$$

Substituting $n(L)$ in the above equation with the expression given in Eq. 5.30, assuming a volumetric shape factor of unity for all crystal sizes, and subsequent rewriting lead to the following analytical solution for the cumulative volume density distribution in a MSMPR crystalliser:

$$\begin{aligned} V(L) = & -G\tau n_0 \exp\left(-\frac{L}{G\tau}\right)L^3 - 3G^2\tau^2 n_0 \exp\left(-\frac{L}{G\tau}\right)L^2 \\ & - 6G^3\tau^3 n_0 \exp\left(-\frac{L}{G\tau}\right)L - 6G^4\tau^4 n_0 \exp\left(-\frac{L}{G\tau}\right) + 6G^4\tau^4 n_0 \end{aligned} \quad [5.32]$$

The third moment of the crystal size distribution is defined as the value of the cumulative volume density distribution at a crystal size of infinity, and is thus given by the following analytical solution:

$$M_3 = V(L = \infty) = \int_0^\infty n(L)L^3 dL = 6G^4\tau^4 n_0 \quad [5.33]$$

5.4.2 TEST CASE DEFINITION

The comparison of numerical and analytical solutions of the number density distributions and (normalised) volume density distributions is performed for a MSMPR crystalliser operating at the following conditions:

- A residence time, τ , of 1000 s.
- A linear growth rate, G , of $2 \cdot 10^{-7}$ m·s⁻¹; and
- A nucleation rate, B_0 , of 10^6 m⁻³·s⁻¹.

For the numerical solutions a crystal size grid is used with an upper bound, L_{max} , of $3 \cdot 10^{-3}$ m and a lower bound, L_{min} , of 0 m when using a linear grid and 10^{-7} m when using a logarithmic grid.

5.4.3 ACCURACY OF INTEGRALS

The accuracy of numerically calculated integrals with respect to crystal size is studied by comparing the analytical cumulative volume density distribution (Eq. 5.32) with the corresponding distribution obtained by numerical integration of the analytical number density distribution (Eq. 5.30).

Figure 5.6 shows the numerically calculated *cumulative volume density distributions* obtained with 25, 50, 100, 200, 400 and 800 grid points on both linear and logarithmic size grids.

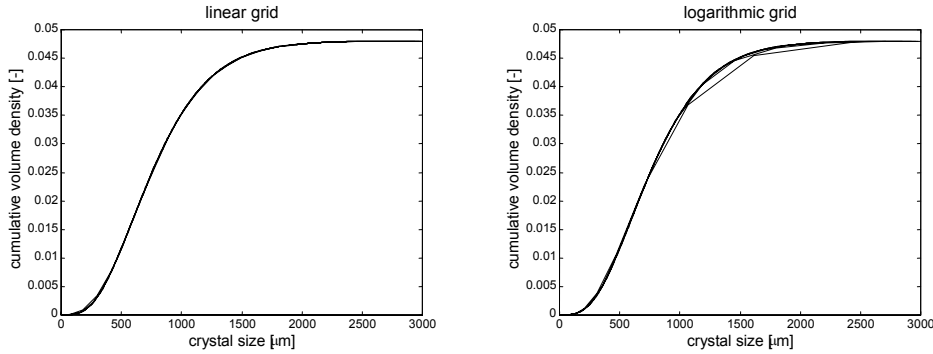


Figure 5.6: *Cumulative volume density distributions* obtained by numerical integration of the analytical number density distribution on linear and logarithmic size grids with 25, 50, 100, 200, 400 and 800 grid points.

This figure reveals that even for as few as 25 grid points a (visually) reasonable accuracy is obtained. This impression is confirmed by the results listed in Table 5.1, which denote the relative deviation between analytical and numerical third moments of the CSD for varying numbers of grid points.

Table 5.1: Relative deviation [%] between analytical M_3 and M_3 obtained by integrating the analytical number density distribution on a linear and logarithmic size grid.

number of grid points	25	50	100	200	400	800
linear grid	-0.0150	-0.0010	0.0000	0.0000	0.0000	0.0000
logarithmic grid	-0.1941	-0.0242	-0.0040	-0.0008	0.0000	0.0000

The comparison in this table only provides information with respect to the total amount of crystals and not their distribution with respect to size, i.e. the shape of the crystal size distribution. For this purpose, a criterion suggested by Verheijen and Merkus (1999) is used: the maximum difference in the normalised cumulative volume density distributions.

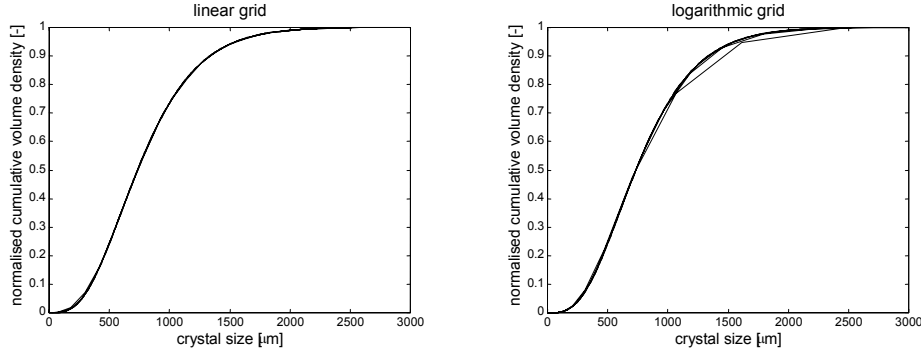


Figure 5.7: *Normalised cumulative volume density distributions* obtained by numerical integration of the analytical number density distribution on linear and logarithmic size grids with 25, 50, 100, 200, 400 and 800 grid points.

Figure 5.7 shows the *normalised cumulative volume density distributions* obtained by numerical integration with 25, 50, 100, 200, 400 and 800 grid points on both linear and logarithmic size grids. The maximum deviation between the analytical and numerically calculated normalised cumulative volume density distributions is shown in Table 5.2.

Table 5.2: Maximum deviation between the analytical normalised cumulative volume density distribution and that obtained by integrating the analytical number density distribution on a linear and logarithmic size grid.

number of grid points	25	50	100	200	400	800
linear grid	0.003674	0.000978	0.000253	0.000212	0.000212	0.000213
logarithmic grid	-0.012852	-0.003639	-0.000807	0.000231	0.000209	0.000229

The largest deviation is obtained using a logarithmic grid with 25 grid points, and is merely 1% of the function range of the cumulative distribution. This indicates a high accuracy for the numerically calculated integrals at each point of the size distribution, even when a mere 25 grid points are used.

5.4.4 ACCURACY OF PARTIAL DERIVATIVES

The accuracy of numerically calculated partial derivatives is studied by comparing the analytical solution of the number density distribution with that obtained by numerical solution of the PBE.

Figure 5.8 depicts the influence of the discretisation resolution (25, 50, 100, 200, 400 and 800 grid points) on the accuracy of the *number density distribution*, for linear and logarithmic grids and for the partial derivative term in the PBE in terms of ‘normal’ number densities and logarithms of the number densities.

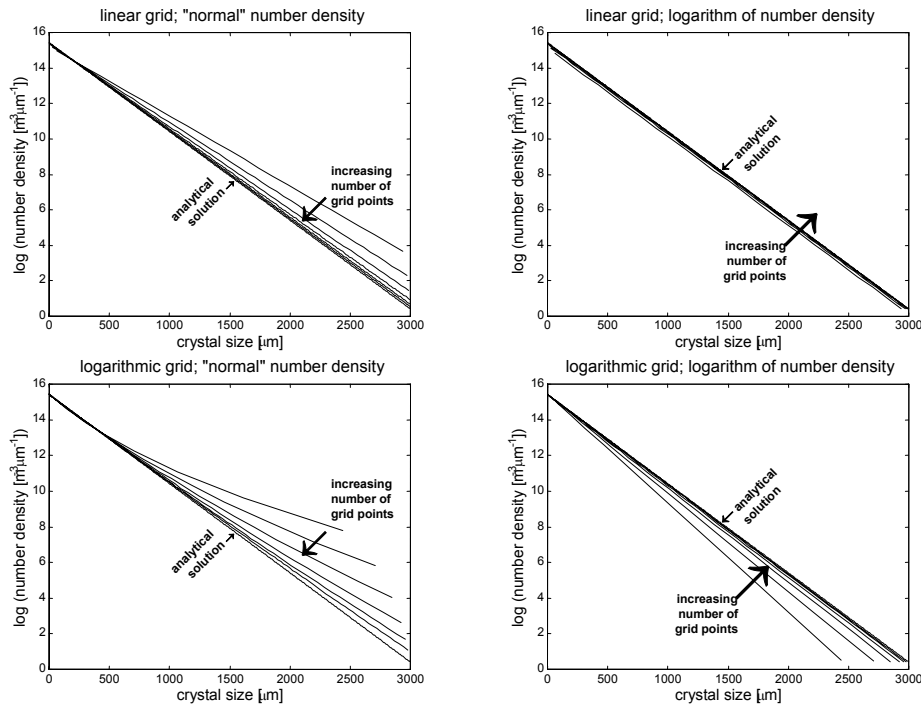


Figure 5.8: Numerical solutions of the *number density distribution* for (1) linear and logarithmic grids, (2) the partial derivative term in the PBE in terms of ‘normal’ number densities and logarithms of the number densities, and (3) various discretisation resolutions (25, 50, 100, 200, 400 and 800 grid points).

From these plots, it is apparent that:

- When using the same number of grid points and the same form for the number density in the PBE, the accuracy of the numerical solution obtained on a linear grid is better than that obtained on a logarithmic grid.
- When using the same number of grid points and the same type of grid, the accuracy of the numerical solution obtained when using the logarithm of the number density in the PBE is better than that obtained with the ‘normal’ number density; and
- As expected, when using the same type of grid and the same form for the number density in the PBE, the accuracy of the numerical solution increases with the number of grid points.

The number density distribution may be the variable that appears in the PBE, however, plotting this variable does not provide a convenient indication of the average crystal size and the width of the size distribution. For that purpose, mass or volume density distribution plots are more appropriate. Figure 5.9 therefore shows the influence of the discretisation resolution (25, 50, 100, 200, 400 and 800

grid points) on the accuracy of the *volume density distribution*, for linear and logarithmic grids and for the partial derivative term in the PBE in terms of ‘normal’ number densities and logarithms of the number densities.

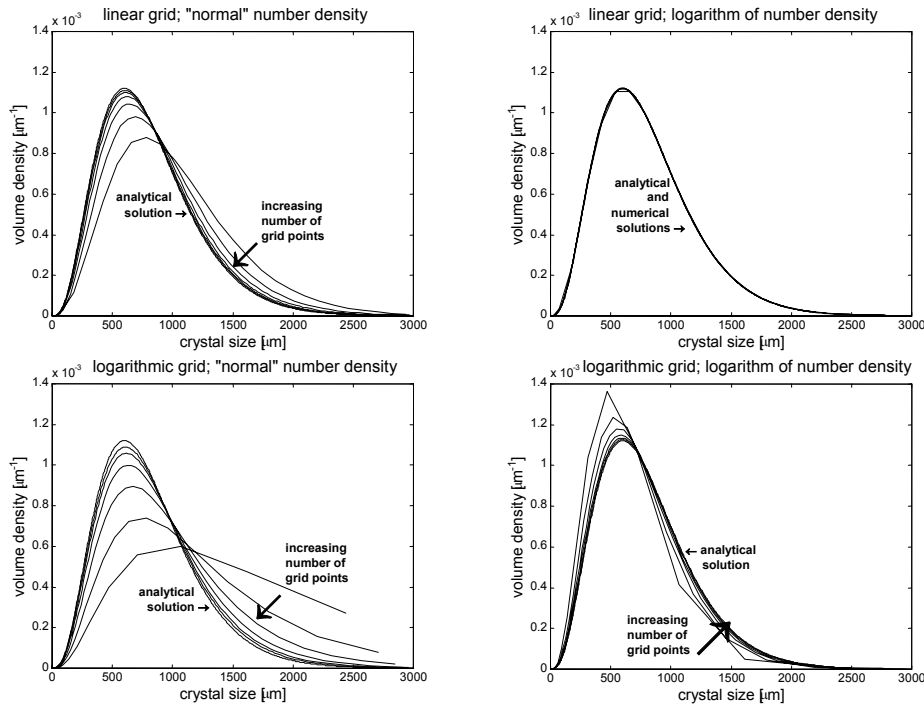


Figure 5.9: Numerical solutions of the *volume density distribution* for (1) linear and logarithmic grids, (2) the partial derivative term in the PBE in terms of ‘normal’ number densities and logarithms of the number densities, and (3) various discretisation resolutions (25, 50, 100, 200, 400 and 800 grid points).

These volume density distribution plots indeed provide an easy means of qualitatively studying the influence of the number of grid points, type of grid and form of the number density in the PBE on the location and width of the crystal size distribution:

- Regardless of the type of grid, when using the ‘normal’ number density in the PBE, the location of the size distribution shifts to lower crystal sizes with increasing discretisation resolution.
- Regardless of the type of grid, when using the logarithm of the number density in the PBE, the location of the size distribution shifts to larger crystal sizes with increasing discretisation resolution; and
- Regardless of the type of grid and form in which the number density appears in the PBE, the width of the distribution increases with increasing discretisation resolution.

5.4.5 COMBINED ACCURACY OF PARTIAL DERIVATIVES AND INTEGRALS

This subparagraph provides a quantitative analysis of the influence of the number of grid points, type of grid and form of the number density in the PBE on the location and width of the crystal size distribution. This analysis is done in a separate subparagraph because it is based upon cumulative volume density distributions and quantiles of the distribution, and therefore requires both numerically calculated partial derivatives and numerically calculated integrals.

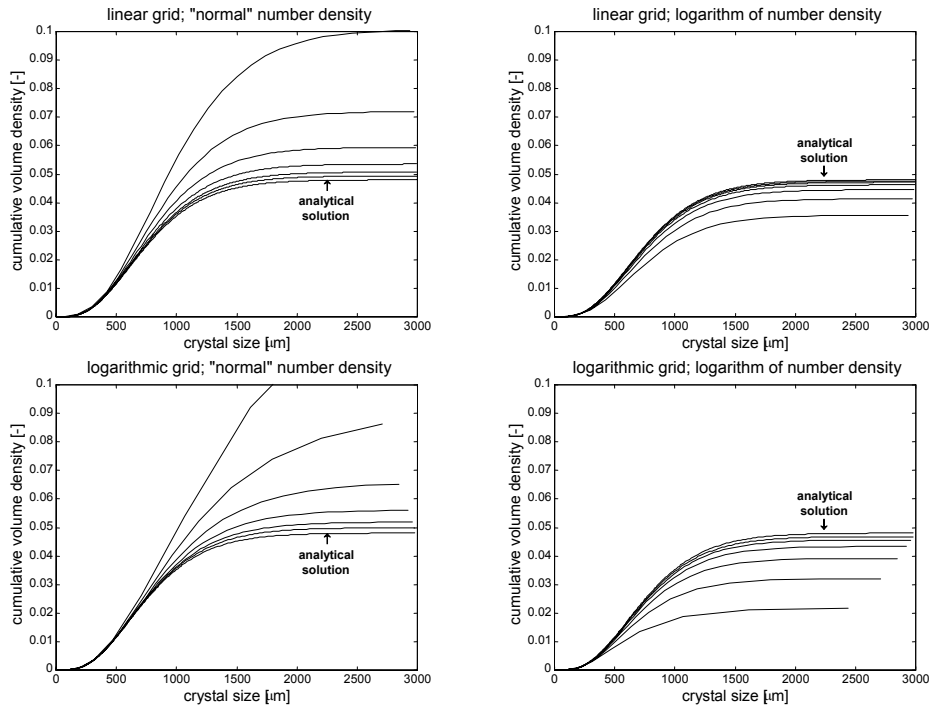


Figure 5.10: Numerical solutions of the *cumulative volume density distribution* for (1) linear and logarithmic grids, (2) the partial derivative term in the PBE in terms of ‘normal’ number densities and logarithms of the number densities, and (3) various discretisation resolutions (25, 50, 100, 200, 400 and 800 grid points).

The previous two subparagraphs focused on the accuracy of numerically calculated integrals and partial derivatives respectively. The results from those two studies indicate that the inaccuracies in the partial derivative calculations are significantly larger than those in the integral calculations. Consequently, the combined accuracy of numerically calculated partial derivatives and integrals will approximate the accuracy of the numerically calculated partial derivatives. As such, the quantitative comparisons on the basis of cumulative volume density

distributions and quantiles, presented in the remainder of this subparagraph, can be seen as a quantitative study into the accuracy of the partial derivatives alone. Figure 5.10 shows the influence of the discretisation resolution (25, 50, 100, 200, 400 and 800 grid points) on the accuracy of the *cumulative volume density distribution*, for linear and logarithmic grids and for the partial derivative term in the PBE in terms of ‘normal’ number densities and logarithms of the number densities. The cumulative volume density distributions are calculated from the volume density distributions using one of the equations given in Chapter 4.4.5. These cumulative volume density distribution plots clearly show that the total amount (volume/mass) of crystals is overestimated when the ‘normal’ number density is used in the PBE and underestimated when the logarithm of the number density is used. As expected, the overestimation respectively underestimation decreases with increasing grid resolution. This trend is shown quantitatively in Table 5.3 where the relative deviations between the analytical and numerical solution for the third moment of the CSD, M_3 , are listed for all combinations of grid type (linear/logarithmic), form of the number density in the PBE (‘normal’/logarithmic) and grid resolution (25, 50, 100, 200, 400 and 800 grid points). The third moment of the CSD is equivalent to the total volume of crystals contained within the CSD.

Table 5.3: Relative deviation [%] between analytical M_3 and M_3 obtained by numerical integration of the numerical solution of the number density distribution.

number of grid points	25	50	100	200	400	800
linear grid; ‘normal’ number density	109.3	49.8	23.7	11.5	5.7	2.8
linear grid; logarithm of number density	-25.9	-13.9	-7.2	-3.7	-1.9	-0.9
logarithmic grid; ‘normal’ number density	173	79.9	35.8	16.7	8	3.9
logarithmic grid; logarithm of number density	-54.8	-33.3	-18.5	-9.8	-5	-2.5

In comparison with Table 5.1 many more grid points are required for an accurate solution. When the M_3 is calculated by numerical integration of the *analytical* solution of the number density relative deviations of less than 1% are already obtained with 25 grid points. However, a similar accuracy for a M_3 obtained by numerical integration of the *numerical* solution of the number density requires at least 800 grid points.

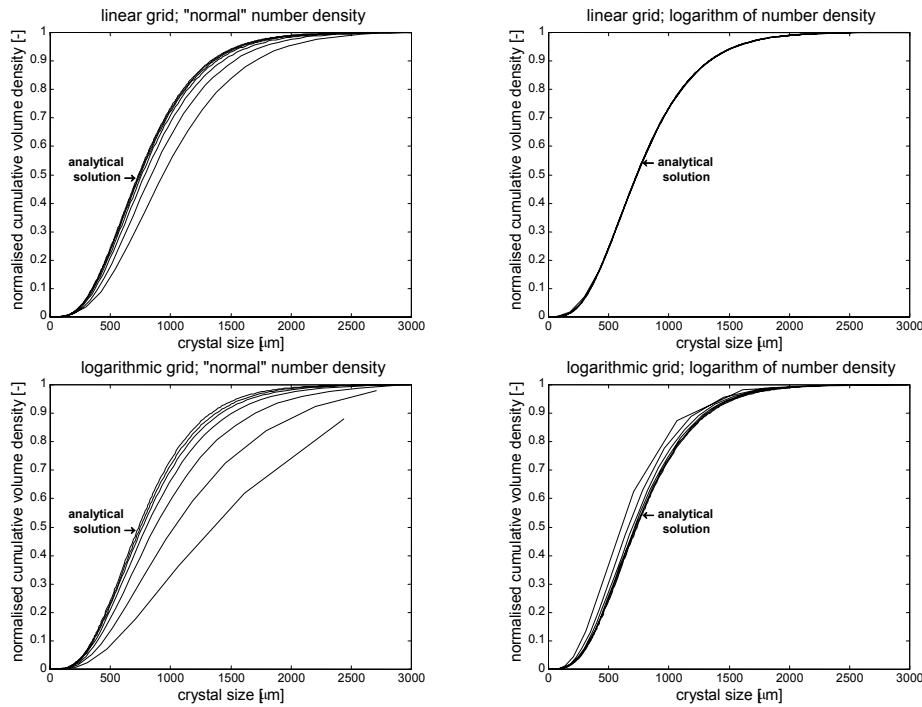


Figure 5.11: Numerical solutions of the *normalised cumulative volume density distribution* for (1) linear and logarithmic grids, (2) the partial derivative term in the PBE in terms of ‘normal’ number densities and logarithms of the number densities, and (3) various discretisation resolutions (25, 50, 100, 200, 400 and 800 grid points).

The amount of crystals is only one aspect of a CSD. To investigate the accuracy with respect to the shape of the distribution, the cumulative distributions are converted to *normalised cumulative volume density distributions* (see Figure 5.11). Next, the maximum difference between analytical and numerical normalised cumulative volume density distributions is determined. This difference is listed in Table 5.4 for all combinations of grid type (linear/logarithmic), form of the number density in the PBE (‘normal’/logarithmic) and grid resolution (25, 50, 100, 200, 400 and 800 grid points).

The choice of an acceptable inaccuracy is obviously arbitrary, but for practical reasons, e.g. accuracy of CSD measurements, a maximum difference of 5% may well be considered appropriate. From Table 5.4 it follows that the minimum number of grid points required to obtain this accuracy ranges from approximately 25 to 400 depending on the type of grid and the form of the number density in the PBE.

Table 5.4: Maximum deviation between the analytical normalised cumulative volume density distribution and that obtained by integrating the numerical number density distribution on a linear and logarithmic size grid.

number of grid points	25	50	100	200	400	800
linear grid; 'normal' number density	-0.188271	-0.104124	-0.055012	-0.028261	-0.014285	-0.007138
linear grid; logarithm of number density	0.003674	0.000978	0.000253	0.000212	0.000212	0.000213
logarithmic grid; 'normal' number density	-0.417059	-0.252975	-0.138550	-0.071325	-0.036030	-0.018041
logarithmic grid; logarithm of number density	0.150941	0.077956	0.039873	0.020108	0.010150	0.005141

This comparison involves the overall shape of the CSD. In practice, a simpler representation is often used, which typically consists of a quantity indicating the location of the distribution and a quantity denoting the width of the distribution. In this work, the crystal median size and a quantile ratio are used to represent respectively the location and width of the CSD. Note that the median size is in fact the 50 percent quantile of a distribution, and that quantiles are defined according to one of the equations given in Chapter 4.4.5.

Table 5.5: Relative deviation [%] between analytical L_{50} and L_{50} obtained by numerical integration of the numerical solution of the number density distribution.

number of grid points	25	50	100	200	400	800
linear grid; 'normal' number density	27.3	14.2	7.3	3.7	1.8	0.9
linear grid; logarithm of number density	-0.2	0.0	0.0	0.0	0.0	0.0
logarithmic grid; 'normal' number density	83.2	40.4	18.9	9.0	4.4	2.2
logarithmic grid; logarithm of number density	-18.3	-9.8	-5.0	-2.5	-1.3	-0.7

Using an acceptable inaccuracy of 5% for the numerically calculated median crystal size, L_{50} , it follows from Table 5.5 that the minimum number of required grid points also ranges from approximately 25 to 400 depending on the type of grid and the form of the number density in the PBE.

The ratio of the 90 percent quantile and 10 percent quantile is used in this work as a measure of the size distribution's width. From Table 5.6 it follows that a maximum inaccuracy of 5% in the numerically calculated values of this ratio, again requires a minimum number of grid points ranging from approximately 25 to 400.

Table 5.6: Relative deviation [%] between analytical L_{90}/L_{10} and L_{90}/L_{10} obtained by numerical integration of the numerical solution of the number density distribution.

number of grid points	25	50	100	200	400	800
linear grid; 'normal' number density	0.9	0.2	0.0	0.0	0.0	0.0
linear grid; logarithm of number density	2.7	0.6	0.1	0.0	0.0	0.0
logarithmic grid; 'normal' number density	21.4	21.7	12.6	6.4	3.1	1.5
logarithmic grid; logarithm of number density	7.7	1.8	0.4	0.1	0.0	0.0

Summarising, the combined accuracy of numerically calculated partial derivatives and integrals is clearly determined by the accuracy of the partial derivatives.

5.4.6 CONCLUSIONS

For the MSMPR case, size independent growth and nucleation at the lower bound only, it is apparent that the combination of a linear crystal size grid and the number density expressed in terms of its logarithm requires the lowest grid resolution to obtain a given accuracy. However, there is no guarantee that this combination will always outperform others. The three other combinations of size grid and form of number density will therefore not be secluded from further investigations.

5.5 NUMERICAL ISSUES RELATED TO IMPLEMENTATION OF GAHN KINETIC MODEL

In this paragraph, numerical issues related to the incorporation of the Gahn kinetic model in the crystallisation process modelling framework (see Chapter 4.4.2) will be discussed. The main differences with the MSMPR case, as regards the solution of the PBE, are:

- Size dependent growth as opposed to size independent growth.
- Moreover, at one moment in time the growth rate may be positive for some crystal sizes and negative for others; and
- A birth/death term, which is non-zero for a range of crystal sizes instead of for one size only. This term describes the attrition of large crystals and the subsequent generation of secondary nuclei.

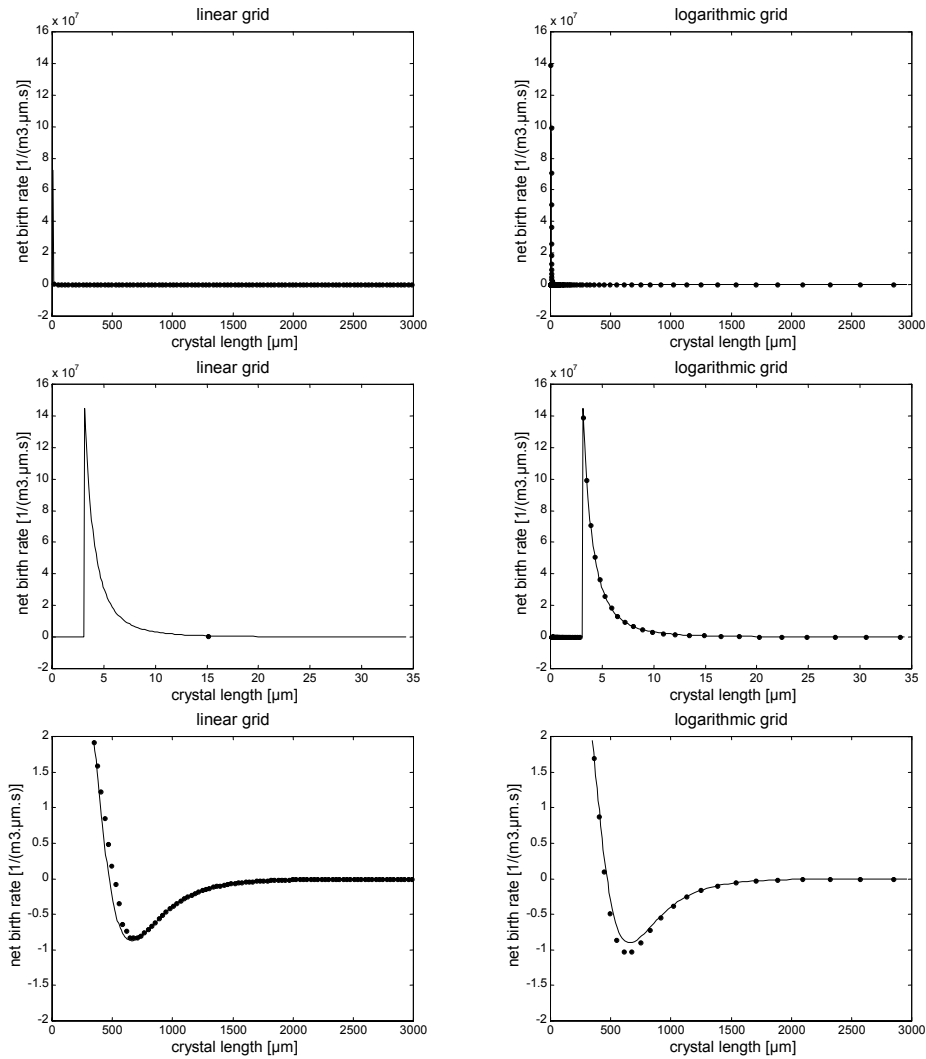


Figure 5.12: Typical size dependency of the combined birth and death term in the Gahn kinetic model. This term describes the attrition of large crystals and the subsequent generation of secondary nuclei. Results shown are for 100 grid points and a crystal size domain ranging from 0.1 to 3000 μm .

5.5.1 TYPICAL SIZE DEPENDENCY OF THE GROWTH AND BIRTH/DEATH TERM

As can be seen from Figure 5.12 and Figure 5.13, the size dependency of the growth and birth terms is most pronounced in the smaller crystal size range. It is

for this reason that the logarithmic crystal size grid was introduced as an alternative to the linear grid in paragraph 5.3.1.

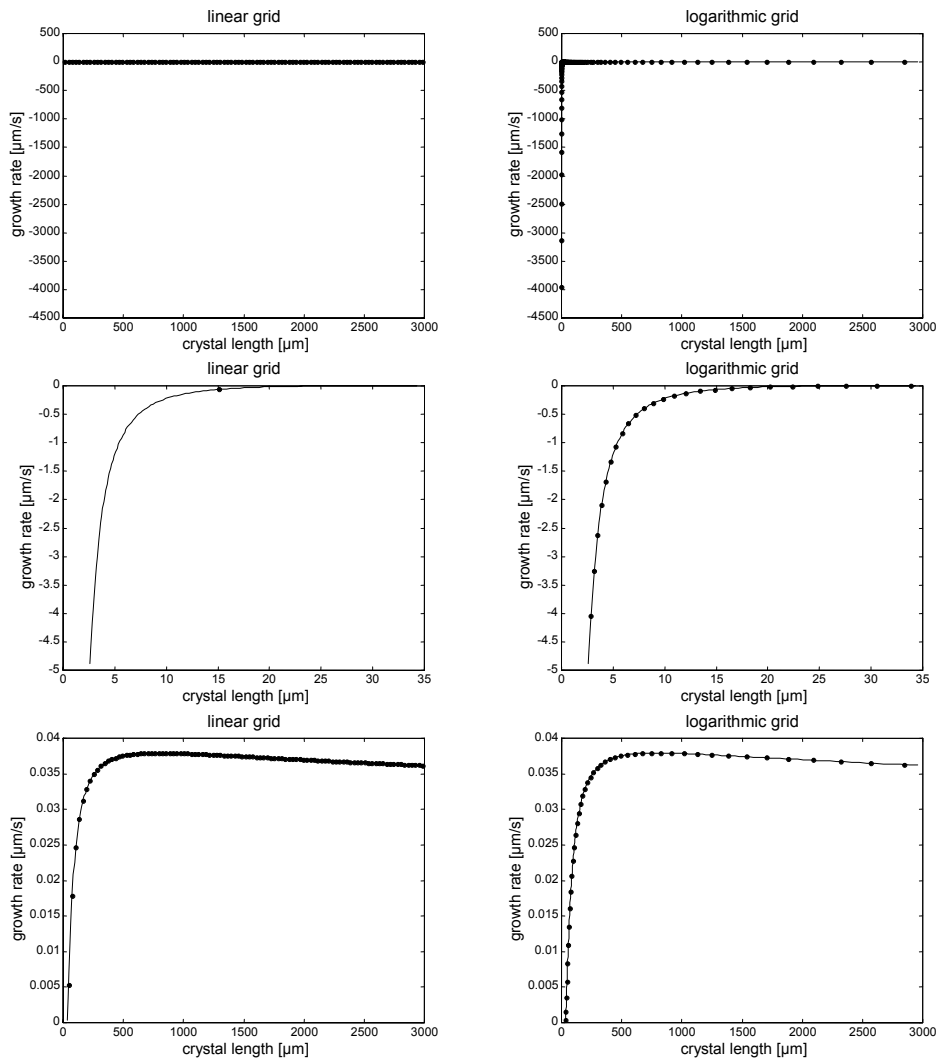


Figure 5.13: Typical size dependency of the growth rate term in the Gahn kinetic model. Results shown are for 100 grid points and a crystal size domain ranging from 0.1 to 3000 μm .

Using a same number of grid points, the logarithmic grid clearly captures the size dependency of the growth and birth/death term more precisely than the linear grid. It may be argued that the extra resolution provided by a logarithmic grid in the small crystal size range is not important because the majority of the crystals

in this range will dissolve even under ‘normal’ growth conditions. However, there are roughly two reasons why this resolution is indeed needed.

Firstly, an accurate description of the size distribution of small crystals that do ‘survive’ as well as their generation is unarguably of paramount importance for an accurate prediction of the product CSD. The birth of small crystals or nuclei that do survive is usually referred to as the effective nucleation rate in a crystallisation system. For instance, in this example crystals larger than approximately $35\ \mu\text{m}$ will grow out whilst crystals below this size will dissolve. A closer look at the net birth rate distribution, i.e. in a size range above $35\ \mu\text{m}$, indicates the possible advantage of using a logarithmic grid instead of a linear grid (see Figure 5.14).

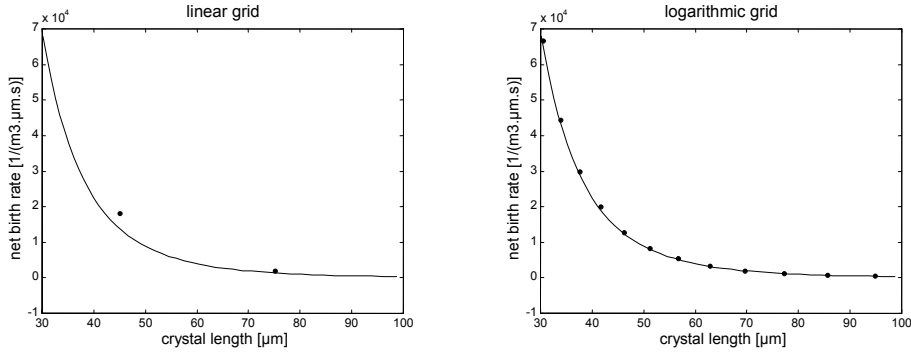


Figure 5.14: Advantage of using a logarithmic crystal size grid to capture the net birth rate distribution.

Secondly, the fact that small crystals will practically always dissolve does not in itself warrant a limited resolution in the small crystal size range. For instance, whenever a crystal slurry is removed from a crystalliser and separated from its liquid, the small crystals contained in this slurry will no longer dissolve and thus form an intrinsic part of the product, which may have a significant effect on its performance. Another example, in case of compartmental modelling, crystals that dissolve in one compartment may grow in another as a result of supersaturation gradients between the various compartments.

The performance of the linear and logarithmic grid for solving PBEs in combination with the Gahn kinetic model will be compared in paragraph 5.6.

5.5.2 SOLVING THE PBE FOR SIMULTANEOUS CRYSTAL GROWTH AND DISSOLUTION

As regards the numerical solution of the PBE in combination with the Gahn kinetic model, two distinct cases can be distinguished:

- ‘Normal’ growth conditions, i.e. crystals above a certain size grow and below a certain size they dissolve; and
- Overall dissolution, i.e. all crystals dissolve.

Solution of the second case is straightforward: a boundary condition at the upper bound of the crystal size domain, as discussed in Chapter 4.4.1, and an upwind finite volume method, i.e. forward discretisation.

Several options were considered for the first case. One option, suggested in Chapter 4, encompasses the definition of one PBE for each size interval within which the growth rate of all crystals have the same sign. This would result in (1) a PBE with a boundary condition at its upper bound and a forward discretisation scheme for the dissolving crystals, and (2) a PBE with a boundary condition at its lower bound and a backward discretisation scheme for the growing crystals. Note that the upper bound of the first domain, which encompasses the smaller crystals, coincides with the lower bound of the second domain, which contains the larger crystals. Both are defined as the crystal size at which the growth rate is zero. This approach would be easy to implement if it were not for the fact that this crystal size may change from simulation to simulation and more importantly during a dynamic simulation. As can be seen from the equations given in Chapter 4.4.2.3, the crystal size at which the growth rate is zero, L_{eq} , depends on the overall supersaturation. This quantity does not only vary with operating conditions but also due to the dynamic behaviour observed in batch processes and also in many continuous processes. The upper respectively lower bound of the two PBEs are thus time-variant, and solution of these PBEs thus constitutes a moving boundary problem. Although it is no problem to formulate such a problem mathematically, it does result in an increased number of time-variant quantities. Variables such as the crystal length, L , and the derivative of the crystal length with respect to the normalised crystal size, dL/dz , would no longer be time-invariant. Furthermore, an additional partial derivative term needs to be added to each PBE to account for the varying locations of the grid points as well as the varying class widths. It was anticipated that the use of two PBEs would result in such a considerable increase in computational requirements, that it was decided not to implement this approach.

The second option for the first case involves the use of one PBE with zero, one or two boundary conditions, depending on the sign of the growth rate at the lower and upper bound of the crystal size domain. In this case, the lower bound, upper bound and grid point locations are time-invariant, but the direction of the discretisation scheme used for the finite volume method depends on the sign of the time-variant growth rate. This direction needs to be determined for each grid point and at each moment in time, as the sign of the growth rate may switch during the simulation.

$$\left. \frac{\partial nG}{\partial z} \right|_{z_k} = \begin{cases} \frac{n(z_k)G(z_k^+) - n(z_{k-1})G(z_k^-)}{\Delta z_k} & G(z_k^-) > 0, G(z_k^+) \geq 0 \\ & k = 2, \dots, N \\ \frac{n(z_{k+1})G(z_k^+) - n(z_k)G(z_k^-)}{\Delta z_k} & G(z_k^-) \leq 0, G(z_k^+) < 0 \\ & k = 1, \dots, N-1 \\ \frac{n(z_k)G(z_k^+) - n(z_k)G(z_k^-)}{\Delta z_k} & G(z_k^-) \leq 0, G(z_k^+) \geq 0 \\ & k = 1 \dots N \\ \frac{n(z_{k+1})G(z_k^+) - n(z_{k-1})G(z_k^-)}{\Delta z_k} & G(z_k^-) > 0, G(z_k^+) < 0 \\ & k = 2 \dots N-1 \end{cases} \quad [5.34]$$

As this scheme contains a large number of discontinuities, it may result in frequent reinitialisation during a dynamic simulation. It was therefore decided to simplify this scheme as follows:

$$\left. \frac{\partial nG}{\partial z} \right|_{z_k} = \alpha(z_k) \frac{n(z_k)G(z_k^+) - n(z_{k-1})G(z_k^-)}{\Delta z_k} + (1 - \alpha(z_k)) \frac{n(z_{k+1})G(z_k^+) - n(z_k)G(z_k^-)}{\Delta z_k} \quad [5.35]$$

$$\alpha(z_k) = \frac{1}{1 + \exp(\beta \cdot \Delta c(z_k))} \quad [5.36]$$

This sigmoid function serves to smooth the discontinuity associated with the switching of the discretisation scheme (forward to backward or vice versa). The value of this function is 0.5 if the absolute supersaturation, $\Delta c(z_k)$, equals zero. The function value is zero or one if $\Delta c(z_k)$ equals respectively minus or plus infinity. When α equals 0.5 for a grid point z_k , the partial derivative at that grid point is calculated using a central finite difference scheme. As discussed in paragraph 5.3.2 of this chapter, using such a scheme may result in unstable solutions. It is therefore crucial to ensure that the difference schemes for all other grid points are either backward (growth) or forward (dissolution), or in terms of $\alpha(z_k)$ one or zero. This can be achieved by choosing a value of minus or plus infinity for β . However, this will in fact reintroduce the discontinuity that we want to smooth using this sigmoid function. On the other hand, too low a value for β will result in more grid points having central-like finite difference schemes. What then is an appropriate value for β ? In the following an expression is derived for β , which will ensure that $\alpha(z_{k+1}) \approx \alpha_n$ and $\alpha(z_{k-1}) \approx 1 - \alpha_n$ if $\alpha(z_k) = 0.5$, regardless of the location of grid point z_k . The value of α_n should be either slightly larger than zero or slightly smaller than one, but its exact value should be determined by the user. The most important step in the derivation of β is to realise that the product of β and $\Delta c(z_{k+1})$ should be the same regardless of the

location of the grid point z_k at which the growth rate is zero. To achieve this, the value of β needs to be inversely proportional to the derivative of $\Delta c(z)$ with respect to z at z_{eq} :

$$\frac{1}{\beta} \propto \left. \frac{d(\Delta c(z))}{dz} \right|_{z_{eq}} \quad [5.37]$$

z_{eq} is the normalised crystal size for which $\Delta c(z)$ equals zero, and L_{eq} is the corresponding non-normalised crystal size. These two crystal sizes, L_{eq} and z_{eq} , are related as follows:

$$L_{eq} = z_{eq} \left. \frac{dL}{dz} \right|_{L_{eq}} \quad [5.38]$$

Note that z_{eq} and L_{eq} are continuous variables, whereas the values of z_k coincide with discrete grid points. The crystal size dependency of the absolute supersaturation is obtained by substituting Eq. 4.21 into Eq. 4.22:

$$\Delta c(L) = c - c^* \exp\left(\frac{\Gamma_S}{RTL}\right) \quad [5.39]$$

Solving this equation for $\Delta c(L)$ equals zero results in the following expression for L_{eq} :

$$L_{eq} = \frac{\Gamma_S}{RT} \frac{1}{\ln(c/c^*)} \quad [5.40]$$

The derivatives of Δc with respect to z and L at respectively z_{eq} and L_{eq} are related as follows:

$$\left. \frac{d(\Delta c(z))}{dz} \right|_{z_{eq}} = \left. \frac{d(\Delta c(L))}{dL} \right|_{L_{eq}} \left. \frac{dL}{dz} \right|_{L_{eq}} \quad [5.41]$$

The derivative of $\Delta c(L)$ with respect to L is obtained by differentiation of Eq. 5.39:

$$\frac{d(\Delta c(L))}{dL} = \frac{\Gamma_S c^*}{RTL^2} \exp\left(\frac{\Gamma_S}{RTL}\right) \quad [5.42]$$

Substituting L with the solution for L_{eq} (Eq. 5.40) in the above equation gives:

$$\left. \frac{d(\Delta c(L))}{dL} \right|_{L_{eq}} = \frac{RTc}{\Gamma_S} \left(\ln\left(\frac{c}{c^*}\right) \right)^2 \quad [5.43]$$

Using the relationship represented by Eq. 5.41 results in the following expression for the derivative of $\Delta c(z)$ with respect to z at z_{eq} :

$$\left. \frac{d(\Delta c(z))}{dz} \right|_{z_{eq}} = \frac{RTc}{\Gamma_S} \left(\ln\left(\frac{c}{c^*}\right) \right)^2 \left. \frac{dL}{dz} \right|_{L_{eq}} \quad [5.44]$$

The steepness parameter β of sigmoid function $\alpha(z)$ depends on the location of L_{eq} via the ratio of the time-variant solute concentration, c , and time-invariant

saturation concentration for stress-free crystals, and on the type of grid via the dL/dz term:

$$\frac{1}{\beta} \propto \frac{RTc}{\Gamma_S} \left(\ln \left(\frac{c}{c^*} \right) \right)^2 \frac{dL}{dz} \Big|_{L_{eq}} \quad [5.45]$$

However, this expression does not account for changes in the grid spacing or class width Δz . When the grid resolution is increased, a steeper sigmoid function $\alpha(z)$ is required to ensure that $\alpha(z_{k+1}) \approx \alpha_n$ and $\alpha(z_{k-1}) \approx 1 - \alpha_n$ if $\alpha(z_k) = 0.5$. Making β inversely proportional to both $d(\Delta c(z))/dz$ and Δz will provide an expression that will account for changes in the location of the lower bound, upper bound and/or number of grid points:

$$\frac{1}{\beta} \propto \frac{RTc}{\Gamma_S} \left(\ln \left(\frac{c}{c^*} \right) \right)^2 \frac{dL}{dz} \Big|_{L_{eq}} \Delta z \quad [5.46]$$

or

$$\frac{1}{\beta} = \text{const} \cdot \frac{RTc}{\Gamma_S} \left(\ln \left(\frac{c}{c^*} \right) \right)^2 \frac{dL}{dz} \Big|_{L_{eq}} \Delta z \quad [5.47]$$

The value of the constant in this equation merely needs to be tuned to provide the desired α_n , i.e. steepness of the sigmoid function.

5.5.3 DISCRETISATION OF RADIAL IMPELLER CO-ORDINATE

In the Gahn kinetic model, the chance and energy of a crystal-impeller collision are calculated as a function of the radial position on the impeller. Calculation of quantities such as the total collision rate of crystals of a given size thus requires integration of terms containing the collision rate density over the impeller radius, $D_{imp}/2$. As mentioned in paragraph 5.3, integral equations need to be transformed to algebraic equations to be solved numerically. This transformation is achieved by discretisation of the radial impeller co-ordinate.

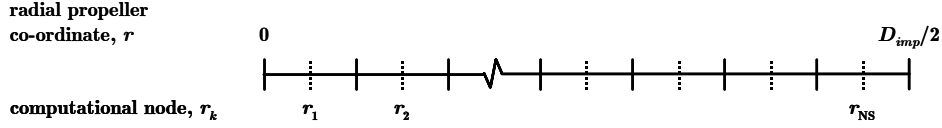


Figure 5.15: Discretisation of radial impeller co-ordinate.

The radial impeller co-ordinate is discretised into NS equally-sized impeller segments, i.e. with a constant segment width, Δr . This segment width is defined as:

$$\Delta r = \frac{D_{imp}}{2NS} \quad [5.48]$$

Similar to the discretisation approach used for the solution of the PBE with the finite volume method, the computational nodes are placed in the centres of the impeller segments. The radial position of these nodes is given by:

$$r_k = \left(k - \frac{1}{2}\right)\Delta r \quad [5.49]$$

The variable value at a computational node is a representative value for the impeller segment containing that computational node. Integrals with respect to the radial impeller co-ordinate, such as Eq. 4.31, can thus be calculated using a Riemann summation:

$$\phi_{n,attr}^-(L) V = \sum_{k=1}^{NS} \phi_{n,coll,eff}(L, r_k) \Delta r \Big|_{edge} + \sum_{k=1}^{NS} \phi_{n,coll,eff}(L, r_k) \Delta r \Big|_{face} \quad [5.50]$$

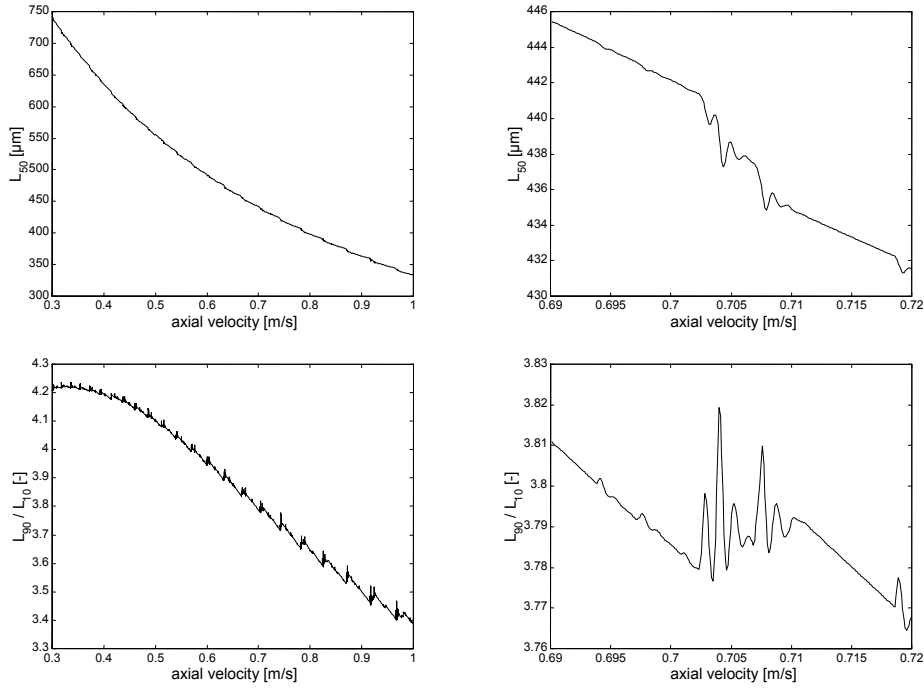


Figure 5.16: Axial velocity dependence of the median size (above) and a quantile ratio (below) as predicted with the first implementation of the Gahn kinetic model.

5.5.4 DISCONTINUITIES IN GAHN KINETIC MODEL

Initial work with the Gahn kinetic model revealed unexpected changes in the CSD when (1) the discretisation resolution for the crystal size domain was varied and

(2) the crystalliser geometry, impeller geometry and/or frequency was changed during model based optimisation of operation and design. This unexpected behaviour is illustrated in Figure 5.16, where some steady-state characteristics of the CSD are plotted as a function of the axial velocity induced by the impeller. These results were produced with a continuation method in which the axial velocity was gradually increased from 0.3 to 1 m/s. Based on intuition, one would expect a monotonous decrease in median size with increasing impeller frequency. The overall trend shown in Figure 5.16 is indeed a decreasing one, but closer inspection reveals small, local increases.

The origin of this irregular behaviour was tracked down to two conditional equations in the Gahn kinetic model, viz Eq. 4.15 and Eq. 4.18:

$$\begin{aligned} V_{attr}(L, r) &= 0 & E_p(L, r) &< E_{p,min} \\ V_{attr}(L, r) &= C E_p^{4/3}(L, r) & E_p(L, r) &\geq E_{p,min} \end{aligned} \quad [4.15]$$

$$\begin{aligned} q_{frag}(L, r, L_{frag}) &= \frac{2.25 L_{frag}^{-3.25}}{L_{frag,min}^{-2.25} - L_{frag,max}^{-2.25}} & L_{frag,min} &\leq L_{frag} \leq L_{frag,max}(L, r) \\ q_{frag}(L, r, L_{frag}) &= 0 & L_{frag} &< L_{frag,min} \vee L_{frag} > L_{frag,max}(L, r) \end{aligned} \quad [4.18]$$

5.5.4.1 Attrition volume equation

The first of these two equations states that a crystal-impeller collision will only result in attrition if the impact energy exceeds a certain minimum impact energy. Let $L_{parent,min}$ be the size of the smallest parent crystal contributing to the attrition process at impeller position r and impeller frequency N . An infinitesimally small increase in the impeller frequency will then result in crystals in an infinitesimally small size range between a ‘new’, smaller $L_{parent,min}$ and the ‘old’ $L_{parent,min}$ joining the attrition process at impeller position r . This reasoning is based on the presumption that crystal size is a continuous variable at the microscopic scale. However, the crystallisation model developed in this work involves crystal size as a discrete variable. An obvious implementation of Eq. 4.15 on a discrete crystal size domain is given by:

$$\begin{aligned} V_{attr}(L_k, r) &= \alpha_1(L_k, r) C E_p^{4/3}(L_k, r) \\ \alpha_1(L_k, r) &= 0 & E_p(L_k, r) &< E_{p,min} \\ \alpha_1(L_k, r) &= 1 & E_p(L_k, r) &\geq E_{p,min} \end{aligned} \quad [5.51]$$

This implementation gives rise to discontinuities in the attrition behaviour because an infinitesimally small increase in the impeller frequency will now result in either no crystals or a whole volume element of crystals joining the attrition process. The first case arises when there is no computational node, L_k , between the ‘old’ and ‘new’ $L_{parent,min}$, whereas the second case is a result of $L_{parent,min}$ moving past a computational node. The other condition for this discontinuous behaviour is the fact that, provided $E_{p,min}$ is not zero, the attrition volume of the crystals

that have just joined the attrition process is not zero but a finite positive amount. In this work, the following implementation is used to eliminate this undesired, discontinuous behaviour:

$$\begin{aligned}
 V_{attr}(L_k, r) &= \alpha_1(L_k, r) C E_p^{4/3}(L_k, r) \\
 \alpha_1(L_k, r) &= 0 & E_p(L_{k+1}, r) &\leq E_{p,min} & [5.52] \\
 \alpha_1(L_k, r) &= \frac{\ln(E_p(L_{k+1}, r)) - \ln(E_{p,min})}{\ln(E_p(L_{k+1}, r)) - \ln(E_p(L_k, r))} & E_p(L_k, r) &< E_{p,min} \wedge \\
 & & E_p(L_{k+1}, r) &> E_{p,min} \\
 \alpha_1(L_k, r) &= 1 & E_p(L_k, r) &\geq E_{p,min}
 \end{aligned}$$

5.5.4.2 Fragment distribution equation

The second conditional equation that was identified as a source of discontinuity in the attrition model describes the distribution of attrition fragments as a result of a collision between a crystal of size L with the impeller at radial position r (Eq. 4.18). Similar to the attrition volume equation, a first, obvious implementation of the fragment distribution equation on a discrete crystal size domain is given by:

$$\begin{aligned}
 q_{frag}(L_k, r_j, L_{frag,i}) &= \alpha_2(L_k, r_j, L_{frag,i}) \frac{2.25 L_{frag,i}^{-3.25}}{L_{frag,min}^{-2.25} - L_{frag,max}^{-2.25}(L_k, r_j)} \\
 \alpha_2(L_k, r_j, L_{frag,i}) &= 0 & L_{frag,i+1} &\leq L_{frag,min} & [5.53] \\
 \alpha_2(L_k, r_j, L_{frag,i}) &= 1 & L_{frag,i+1} &> L_{frag,min} \wedge L_{frag,i} &\leq L_{frag,max}(L_k, r_j) \\
 \alpha_2(L_k, r_j, L_{frag,i}) &= 0 & L_{frag,i} &> L_{frag,max}(L_k, r_j)
 \end{aligned}$$

This implementation gives rise to discontinuities because the maximum fragment size, $L_{frag,max}$, is a function of the collision energy, which in its turn is influenced by operating conditions such as the impeller frequency and design and variables related to the crystalliser and impeller geometry. Again, consider the impeller frequency as an example. On a continuous crystal size domain an infinitesimally small increase in impeller frequency would lead to an infinitesimally small size range between an ‘old’ $L_{frag,max}$ and a marginally larger, ‘new’ $L_{frag,max}$ joining the fragment distribution. On a discrete crystal size domain however, an infinitesimally small increase in frequency may lead to either a zero size range or a whole volume element joining the distribution. The first case arises when there is no computational node, $L_{frag,j}$, between the ‘old’ and ‘new’ $L_{frag,max}$, whereas the second case occurs when $L_{frag,max}$ moves past a computational node. This behaviour combined with the fact that the birth rate of the fragments that have just joined the fragment distribution is not zero but a finite positive amount can clearly cause undesired discontinuities. In this work, the fragment distribution equation was made continuous by means of the following implementation:

$$q_{frag}(L_k, r_j, L_{frag,i}) = \alpha_2(L_k, r_j, L_{frag,i}) \frac{2.25 L_{frag,i}^{-3.25}}{L_{frag,min}^{-2.25} - L_{frag,max}^{-2.25}(L_k, r_j)}$$

$$\alpha_2(L_k, r_j, L_{frag,i}) = 0 \quad L_{frag,i+1} \leq L_{frag,min}$$

$$\alpha_2(L_k, r_j, L_{frag,i}) = 1 \quad L_{frag,i+1} > L_{frag,min} \wedge \quad [5.54]$$

$$\alpha_2(L_k, r_j, L_{frag,i}) = \frac{\ln(L_{frag,max}(L_k, r_j)) - \ln(L_{frag,i-1})}{\ln(L_{frag,i}) - \ln(L_{frag,i-1})} \quad \begin{array}{l} L_{frag,i} \leq L_{frag,max}(L_k, r_j) \\ L_{frag,i} > L_{frag,max}(L_k, r_j) \wedge \\ L_{frag,i-1} < L_{frag,max}(L_k, r_j) \\ L_{frag,i-1} \geq L_{frag,max}(L_k, r_j) \end{array}$$

The combined effect of converting the relationship between attrition volume and potential energy as well as the fragment distribution equation into a continuous function on a discretised crystal size grid is illustrated by Figure 5.17 and Figure 5.18.

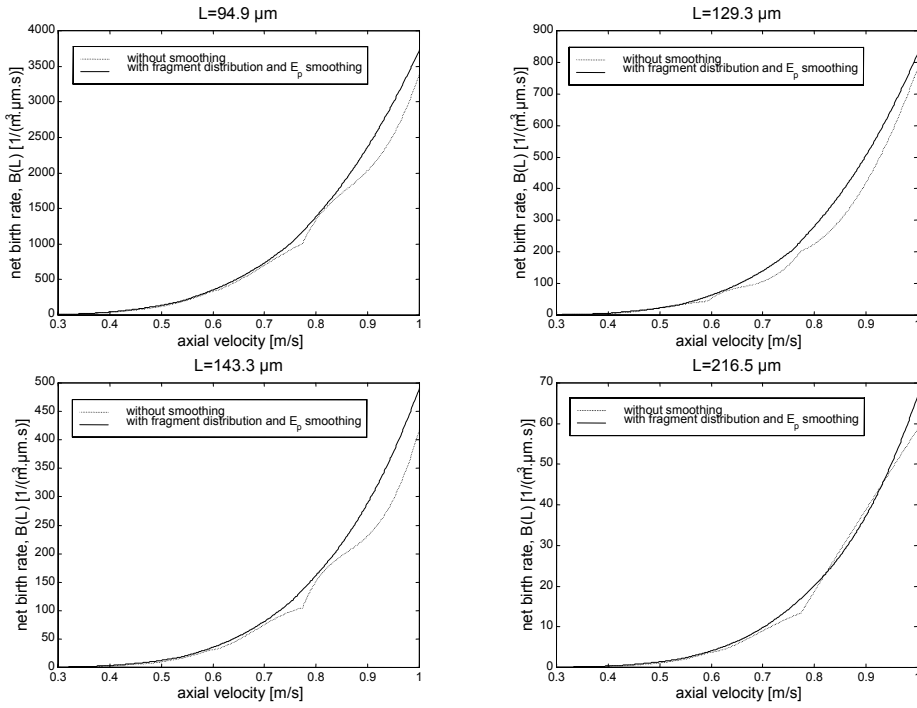


Figure 5.17: Axial velocity dependence of the combined birth and death term for four crystal sizes as predicted with the first and second implementation of the Gahn kinetic model, i.e. respectively without and with discontinuity smoothing.

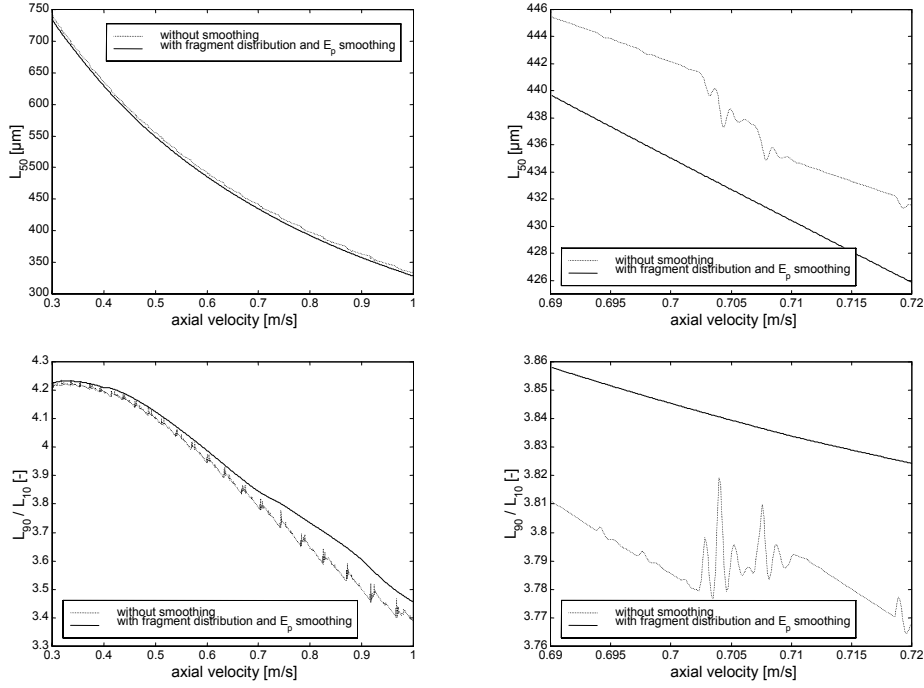


Figure 5.18: Axial velocity dependence of the median size (above) and a quantile ratio (below) as predicted with the first and second implementation of the Gahn kinetic model, i.e. respectively without and with discontinuity smoothing.

5.6 ACCURACY OF NUMERICAL SOLUTION - GAHN KINETIC MODEL

This subparagraph is concerned with the influence on the overall simulation accuracy of:

- The grid type used for the crystal size domain (linear or logarithmic).
- The discretisation resolution for the crystal size grid (25-400 grid points).
- The discretisation resolution for the radial impeller co-ordinate (1-10 impeller segments).

The effect of the form in which the number density appears in the PBE, i.e. ‘normal’ number density or its logarithm, could unfortunately not be studied. All simulations using the logarithm of the number density in the PBE resulted in integrator failures. This suggests that the transformation of the PBE presented in subparagraph 5.3.4 leads to stiffer dynamics. This problem was not resolved within the time frame of this thesis. However, considering the promising results

obtained for the MSMPR case (paragraph 5.4), it is strongly recommended to further pursue this option.

The following test case was used to investigate the accuracy of the numerical solution of the PBE obtained with different crystal size grids and discretisation resolutions:

- Evaporative crystallisation of ammonium sulphate from water.
- The UNIAK 0.022 m³ DT crystalliser (see Chapter 6.2.1 for a detailed description of this crystalliser).
- An operating temperature of 50°C.
- A residence time of 75 minutes.
- Two compartments, a zero volume compartment containing the impeller and a 0.022 m³ compartment where crystal growth and dissolution take place; and
- The following values for the kinetic parameters in the Gahn model: $\Gamma_s = 10^{-4} \text{ J}\cdot\text{m}\cdot\text{mol}^{-1}$ and $k_r = 1.59\cdot 10^{-5} \text{ m}\cdot\text{s}^{-1}$.

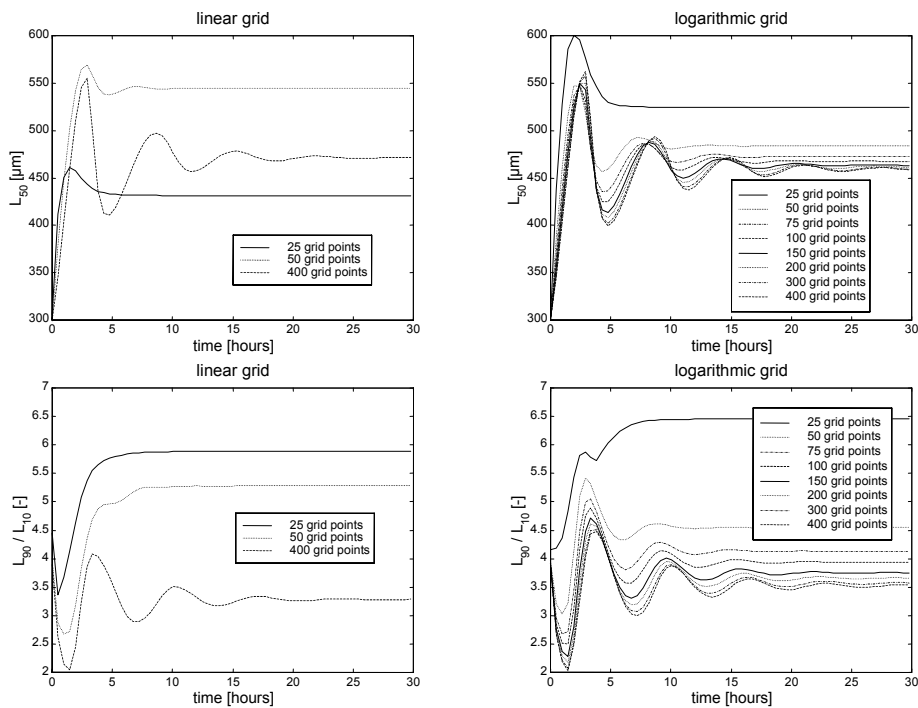


Figure 5.19: Accuracy of numerical solution: dynamics of the median size (above) and a quantile ratio (below) simulated using a linear crystal size grid (left) and logarithmic crystal size grid (right) with different discretisation resolutions.

5.6.1 INFLUENCE OF GRID TYPE AND RESOLUTION FOR CRYSTAL SIZE DISCRETISATION

The before mentioned test case was simulated using 25, 50, 75, 100, 150, 200, 300 and 400 grid points on both a linear and logarithmic grid. The linear grid simulations were only completed successfully for 25, 50 and 400 grid points. Other simulations employing this grid all encountered time integration difficulties. In strong contrast, all simulations with the logarithmic grid were successful.

Not only does the logarithmic grid appear to be more robust than the linear grid, it also provides more accurate results (see Figure 5.19). This is in contrast with the MSMR case where the linear grid was more accurate than the logarithmic grid (see paragraph 5.4). This turnaround can be explained by the strong size dependency of the growth and birth/death term in the crystal size range of 0 – 50 μm , which can only be captured by a linear grid when an excessive number of grid points is used. Figure 5.20, which shows the strong size dependency of the size distribution below 100 μm , supports this explanation.

Due to the limited robustness of simulations employing a linear grid, it was decided to abandon this grid for the remainder of this work.

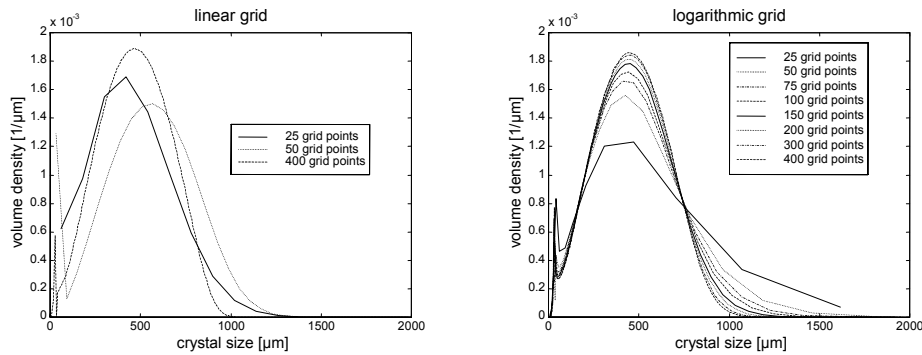


Figure 5.20: Accuracy of numerical solution: steady-state volume density distribution simulated using a linear crystal size grid (left) and logarithmic crystal size grid (right) with different discretisation resolutions.

Next, the steady-state CSD is investigated in terms of the cumulative volume density distribution and normalised cumulative volume density distribution to provide insight into respectively the total volume of crystals and the entire shape of the distribution (Figure 5.21).

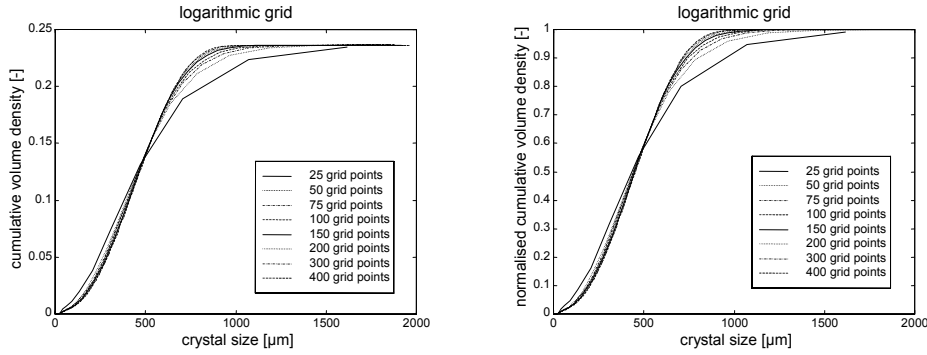


Figure 5.21: Accuracy of numerical solution: steady-state cumulative volume density distribution (left) and normalised cumulative volume density distribution (right) simulated using a logarithmic crystal size grid with different discretisation resolutions.

Note that the overestimation of the total amount of crystals observed for the MSMPR case (Figure 5.10) is not seen here. This may seem surprising at first, but is easily explained by the fact that the simulations performed with the Gahn kinetic model involved simultaneous solution of the PBE, mass balances, energy balance and solid-liquid phase equilibrium, whereas those performed for the MSMPR case involved solution of the PBE only. The mass of crystals obtained with simulations using the Gahn kinetic model is thus not determined by the number of grid points used to solve the PBE, but by the combined solution of the mass balances, energy balance and phase equilibrium. However, the shape of the crystal size distribution is influenced by the number of grid points used to discretise the crystal size domain (Figure 5.20 and Figure 5.21). This influence is further illustrated in Table 5.7.

Table 5.7: Relative deviation between the median size and quantile ratio obtained for 25 to 300 grid points and the median size and quantile ratio obtained for 400 grid points.

Number of grid points	Relative deviation in L_{50} [%]	Relative deviation in L_{90}/L_{10} [%]
25	14.16	83.12
50	5.33	28.98
75	2.88	17.21
100	1.83	11.75
150	0.93	6.43
200	0.53	3.82
300	0.17	1.25

5.6.2 INFLUENCE OF RESOLUTION FOR RADIAL IMPELLER CO-ORDINATE DISCRETISATION

The simulations in the previous section were all performed with five segments for the discretisation of the radial impeller co-ordinate, but with different grids and resolutions for the crystal size discretisation. In this section all simulations are performed on a logarithmic crystal size grid using 200 grid points, but with varying discretisation resolutions for the radial impeller coordinate. The results of these simulations are shown in Figure 5.22 and Figure 5.23, which show predictions for respectively the dynamic evolution of the CSD and the steady-state CSD. As can be seen from Table 5.8, an accuracy of over 99 percent for the predicted median size and spread is already obtained when using three impeller segments.

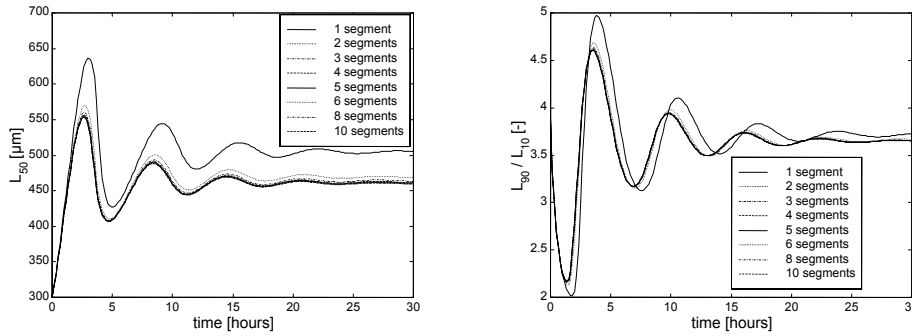


Figure 5.22: Accuracy of numerical solution: dynamics of the median size (left) and a quantile ratio (right) simulated using a logarithmic crystal size grid with 200 grid points and different numbers of impeller segments.

5.6.3 COMPUTATIONAL REQUIREMENTS

Finally, after studying the influence of the resolution and grid type for the discretisation of the crystal size domain on the numerical solution accuracy, the impact of the discretisation resolution on the computational requirements is investigated.

Table 5.9 illustrates the increase in the problem size and consequently computational time as the number of grid points employed in the simulation is increased.

An increase in the number of grid points causes a linear increase in the number of algebraic and differential variables, but an almost quadratic increase in the number of nonzero elements in the Jacobian. A similar increase is seen for the simulation CPU times, whether using variable time step/variable order Backward Differentiation Formulae (DASOLV) or a fully-implicit Runge-Kutta method (SRADAU) for the time-integration.

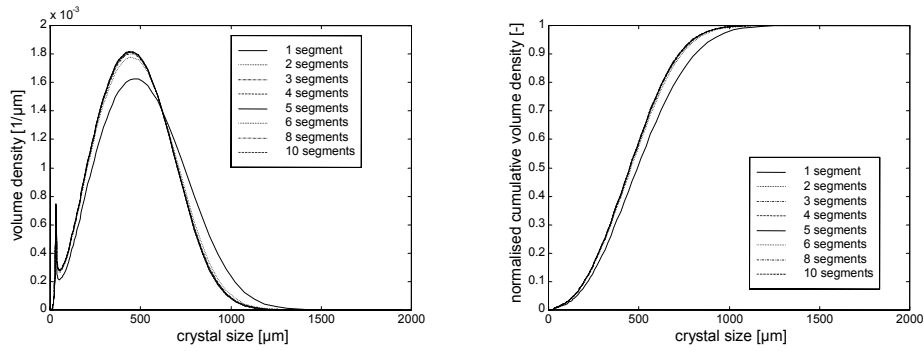


Figure 5.23: Accuracy of numerical solution: steady-state volume density distribution (left) and normalised cumulative volume density distribution (right) simulated using a logarithmic crystal size grid with 200 grid points and different numbers of impeller segments.

Table 5.8: Relative deviation between the L_{50} and L_{90}/L_{10} obtained for 1 to 8 impeller segments and the L_{50} and L_{90}/L_{10} obtained for 10 impeller segments.

Number of segments	Relative deviation in L_{50} [%]	Relative deviation in L_{90}/L_{10} [%]
1	9.65	1.82
2	1.99	0.34
3	0.81	0.11
4	0.42	0.05
5	0.24	0.02
6	0.14	0.01
8	0.04	0.00

Table 5.9: Computational requirements³ as a function of the number of grid points used for discretisation of the crystal size domain.

grid points	25	50	75	100	150	200	300	400
variables	810	1335	1860	2385	3435	4485	6585	8685
differential variables	35	60	85	110	160	210	310	410
non-zeros in Jacobian	4151	8751	14601	21701	39651	62601	123501	204401
DASOLV								
simulation time								
[CPU sec]	17	58	149	265	567	1002	2606	6348
FO calculations								
[CPU sec]	0.48	2.2	6.3	13	29	54	128	264
function evaluations	2865	4691	7415	8684	11315	11440	12881	15415
Jacobian evaluations	320	550	957	1242	1309	1497	1695	1999
SRADAU								
simulation time								
[CPU sec]	7	24	54	104	330	831	3898	12521
FO calculations								
[CPU sec]	0.16	0.56	1.4	2.5	7.5	15	45	110
function evaluations	1193	1973	2714	3302	4582	5903	8957	12836
Jacobian evaluations	70	116	123	149	211	255	370	522

5.7 CONCLUSIONS

The developed crystallisation process modelling framework has been successfully implemented in a commercial modelling tool that can deal with integro-partial differential equations and supports steady-state and dynamic simulation, parameter estimation and optimisation.

The finite volume method was selected for the numerical solution of the population balance equation, because it is known to be robust for highly convective PDEs such as the PBE, even when the sign of the convective term changes (e.g. from growth to dissolution). A downside of this method is that it involves only a first order approximation of the partial derivatives, thus requiring relatively high discretisation resolutions. More importantly, it is not possible to a priori estimate the error in the numerical solutions obtained with such a method. Consequently, the influence of factors such as discretisation resolution, grid type and form of the number density in the PBE is assessed by performing numerous simulations for two different kinetic models.

Analysis of results obtained by employing a kinetic model with size independent crystal growth rates and crystal birth at one crystal size only, leads to the following qualitative conclusions:

- When using the same number of grid points and the same form for the number density in the PBE, the accuracy of the numerical solution

³ The simulation times were obtained on a PC with a Pentium III 1.2 GHz processor.

obtained on a linear grid is better than that obtained on a logarithmic grid; and

- When using the same number of grid points and the same type of grid, the accuracy of the numerical solution obtained when using the logarithm of the number density in the PBE is better than that obtained with the ‘normal’ number density.

Analysis of simulation results obtained with the kinetic model of Gahn, which has a strong crystal size dependency for the birth and growth rates at small crystal sizes, yields different conclusions:

- Using the logarithm of the number density in the PBE seems to increase the stiffness of the resulting DAE system and as such led to numerous time integration failures; and
- When using the same number of grid points, the accuracy of the numerical solution obtained on a logarithmic grid is better than that obtained on a linear grid.

In addition to the above, a number of conclusions were drawn that are independent of the employed kinetic model:

- Numerical solution of an integral equation with a certain accuracy requires significantly less grid points than solving a partial differential equation with the same accuracy.
- Using the logarithm of the number density instead of the ‘normal’ number density in the PBE leads to a significantly better scaled problem from a numeric point of view (whereas values for the number density may range from $1e-20$ to $1e20$, the corresponding values for the natural logarithm of the number density ranges from -46 to 46); and
- As expected, when using the same type of grid and the same form for the number density in the PBE, the accuracy of the numerical solution increases with the number of grid points.

In the remainder of this thesis a logarithmic crystal size grid is used with a spacing of $\ln(L_{i+1}/L_i) = 0.099$ when using the kinetic model of Gahn.

Based on two of the above-mentioned conclusions, it is recommended to revisit the use of the logarithm of the number density in the PBE in combination with the Gahn kinetic model.

Initial simulations and optimisations with the Gahn kinetic model revealed unexpected changes in the crystal size distribution when the discretisation resolution of the crystal size domain was varied and/or when the crystalliser geometry or impeller frequency was varied. These unexpected changes were tracked down to two conditional equations in the kinetic model, where the condition is directly or indirectly related to crystal size. Because discretisation transforms the crystal size domain from a continuous into a discrete domain, conditional equations with respect to crystal size need to be smoothed between neighbouring nodes of the discrete domain. This smoothing is probably not crucial

for simulation purposes, but is expected to be essential for optimisation calculations that require gradient information of for instance the CSD evolution with respect to degrees of freedom, such as the impeller frequency.

6 PARAMETER ESTIMATION, MODEL VALIDATION AND DESIGN OF EXPERIMENTS

Before applying a crystallisation process model for optimal design purposes of a new chemical system, one firstly needs to estimate the values of unknown model parameters, in particular parameters of the employed kinetic model, and secondly validate the model with respect to the predictive capabilities required for design. To this effect, experimental data is collected from two crystallisers of a different scale and type, viz a 22-litre Draft Tube crystalliser and an 1100-litre Draft Tube Baffle crystalliser, which are both equipped with online measurement techniques to characterise the evolution of the crystal size distribution during start-up and subsequent operation. Both crystallisers are operated continuously in an evaporative mode for the crystallisation of ammonium sulphate from water. In order to provide a reference frame for the descriptive and predictive capabilities of the Gahn kinetic model, parameter estimation and validation are also carried out with the kinetic models of Ottens, Eek and Ó Meadhra. The model of Ó Meadhra (eight unknown parameters) is shown to have the best descriptive value, while the model of Gahn (only two unknown parameters) has the best predictive value with respect to both changes in crystalliser scale/type and impeller frequency. Finally, it is shown how the same crystallisation process model can be applied for experiment design, by either estimating whether an additional measurement provides significant additional information and/or determining the control profiles that lead to the experiment with the highest information content.

6.1 INTRODUCTION

To obtain the data required for (1) estimation of the unknown (kinetic) parameters in the model framework presented in Chapter 4 and (2) validation of the model framework's predictive capabilities, two crystalliser configurations are employed. The first configuration is a Draft Tube (DT) crystalliser with an operating volume of 22 litres. This laboratory scale crystalliser is used to derive intrinsic kinetic parameters for growth and secondary nucleation and to study the effect of different operating conditions on the kinetics and the resulting product quality (CSD). The second configuration is a Draft Tube Baffle (DTB) crystalliser with a volume of 1100 litre. This crystalliser is used to validate the model framework (kinetic model and compartmental model approach), i.e. can the model framework predict the influence of changes in crystalliser geometry, scale and operating conditions on the resulting product quality and its related product performance. Both configurations are operated in a continuous mode as evaporator-type crystallisers using ammonium sulphate/water as the model

system. They are also both equipped with a number of on-line measurement sensors to capture the dynamics of the product quality (CSD).

6.2 EQUIPMENT SET-UP

The description that follows, is of the crystallisers and CSD measurement devices that were used to produce the experimental data presented in this thesis, and is a summary of Chapters 3 and 4 of Neumann (2001), a thesis by a colleague PhD student in the UNIAK project. The reader is referred to this thesis for more detailed information on the crystallisers and measurement devices, as well as for information on ancillary equipment, such as the feed and dilution system, and condenser and rinse water system.

6.2.1 CRYSTALLISER PLANTS

6.2.1.1 22-litre Draft Tube crystalliser plant

A flow sheet of this plant is shown in Figure 6.1.

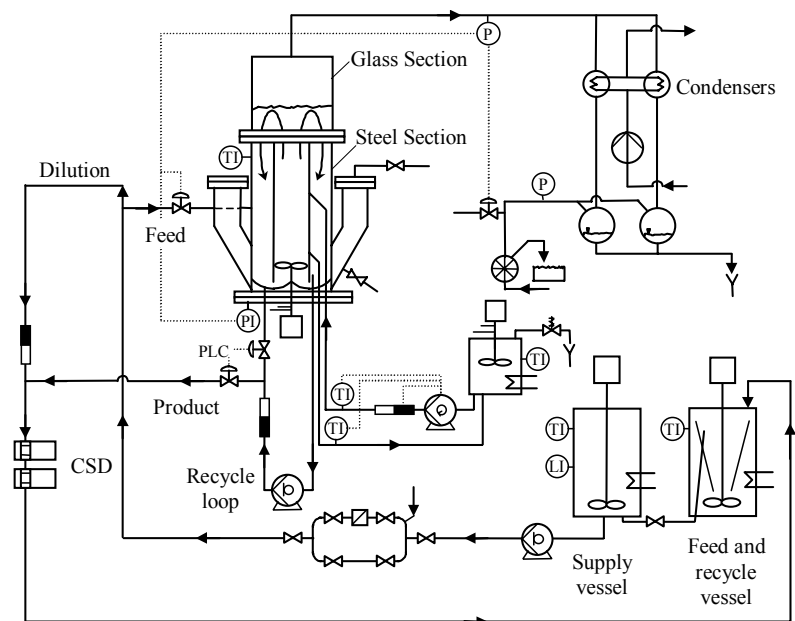


Figure 6.1: Flowsheet of the 22-litre DT crystalliser plant (Neumann, 2001). Solid lines represent process streams, dotted lines represent control loops.

Draft Tube Crystalliser

The crystalliser is an evaporator-type draft tube (DT) agitated crystalliser, which can be operated in a fed-batch as well as in a continuous mode. A schematic view of the crystalliser is given in Figure 6.2. The crystalliser body is a cylindrical

vessel having a height of 1 m and an internal diameter of 0.23 m with a flat head and a contour-shaped base. Its nominal volume is approximately 22 litres. The crystalliser is fitted with a draft tube (height 0.5 m; internal diameter 0.15 m and outer diameter 0.17 m) that consists of two segments. The lower segment is a spirally baffled jacket heat exchanger through which hot water is pumped to supply the heat for evaporation of the solvent. Both jacket walls, the inner draft tube side and the outer down-comer side, function as heat transfer surfaces. The height of this segment is 0.25 m. The upper segment is made of solid stainless steel.

A marine-type impeller with a diameter of 0.14 m is used to pump the suspension through the draft tube upwards to the boiling zone. The impeller frequency can be varied up to 1400 rpm and the corresponding attainable superficial fluid velocity was measured to be 1.3 m/s. The vessel and draft tube are fitted with vertical baffles to reduce the impeller-induced rotational momentum by diverting it to the axial direction.

Fines removal arms are located on each side of the crystalliser with a volume of 3.2 litres each. They were implemented by Ó Meadhra so as to represent a DTB crystalliser configuration. Operation of this fines removal system is, however, not possible due to cavitation in the fines withdrawal tubes caused by the small height difference between the boiling zone and the fines withdrawal location.

All parts of the crystalliser, piping and vessels are constructed from glass or stainless steel (SS304) and are insulated.

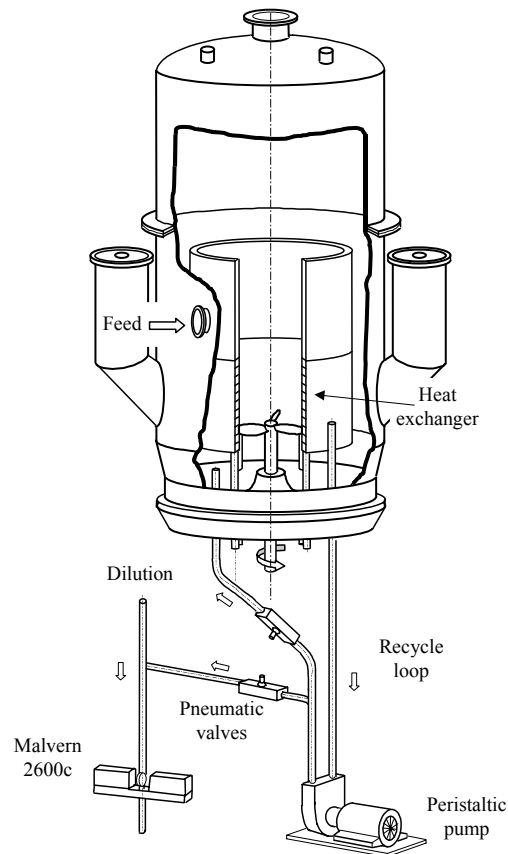


Figure 6.2: Schematic drawing of the 22-litre DT crystalliser (Neumann, 2001).

Product Removal System

The product removal system of the 22-litre DT crystalliser plant is of a semi-continuous nature. Magma is continuously removed from the down-comer of the crystalliser by means of a peristaltic pump and recycled to the crystalliser. The withdrawal tube diameter was chosen in such a way that the criterion of isokinetic product withdrawal (Mersmann, 1995) is met for an impeller frequency of 775 rpm. For the experiments performed at a lower frequency (550 and 640 rpm) and a higher frequency (850, 910, 970 and 1090 rpm) the ratio of the velocity in the crystalliser's outer draft tube and the withdrawal velocity ranges between 0.9 and 1.4 (optimum should be between one and 1.2). It is assumed that this deviation has a negligible effect on the product removal.

At regular time intervals, the product stream is injected into the dilution stream of saturated crystal-free mother liquor by switching the position of the pneumatic valves (see Figure 6.2). Next, the diluted product sample is transported through the on-line laser diffraction measurement systems, Malvern and HELOS, to measure the CSD and subsequently discharged into the feed and recycle vessel.

The residence time in the crystalliser is adjusted, at a fixed flow rate in the recycle loop, by the period the magma is injected into the dilution stream.

Monitoring and control system

A description of the monitoring and control system for the liquid level, temperature, heat input, residence time and dilution flow of the 22-litre DT crystalliser is given by Neumann (2001).

6.2.1.2 1100-litre DTB crystalliser plant

A simplified flow sheet of this crystalliser plant is depicted in Figure 6.3.

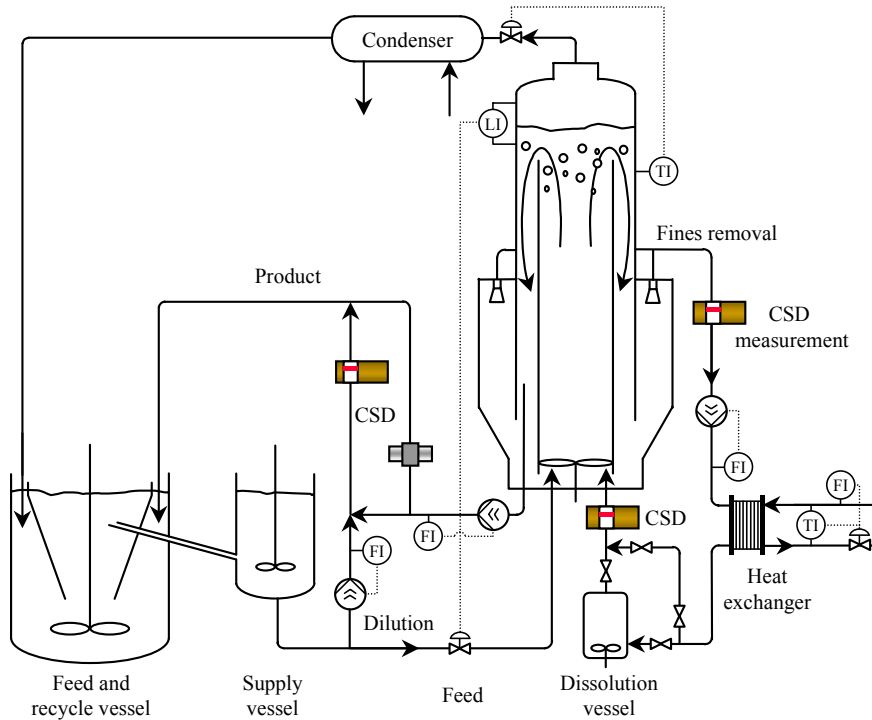


Figure 6.3: Flowsheet of the 1100-litre DTB crystalliser plant; solid lines represent process lines, dotted lines represent control loops (Neumann, 2001).

Draft Tube Baffle Crystalliser

The crystalliser is a draft tube baffle evaporator-type crystalliser that can be operated in either a fed-batch or a continuous mode. A schematic view of the 1100-litre DTB crystalliser is given in Figure 6.4. The crystalliser body is a cylindrical vessel with a dished head and a contoured base. The body has a total height of 4 m and an outer diameter of 0.7 m; its effective volume is estimated to be 1100 litre. The lower part of the crystalliser body is surrounded by an annular zone with a height of 1.5 m, an outer diameter of 1.2 m and a total volume of approximately 775 litre. The hull that separates the annular zone from the

crystalliser body is a so-called skirt baffle. The crystalliser body is equipped with a draft tube with a height of 2.3 m and a diameter of 0.5 m. A marine-type impeller with a diameter of 0.484 m is used to circulate the contents of the crystalliser through the draft tube upwards to the boiling zone. The maximum impeller frequency is 370 rpm and the corresponding superficial fluid velocity was measured to be 1.1 m/s. All process streams enter the bottom section of the crystalliser in the vicinity of the impeller. The top part of the crystalliser body is connected via air driven valves to two condensers. All parts of the crystalliser, piping and vessels are constructed from stainless steel (SS316) and are insulated.

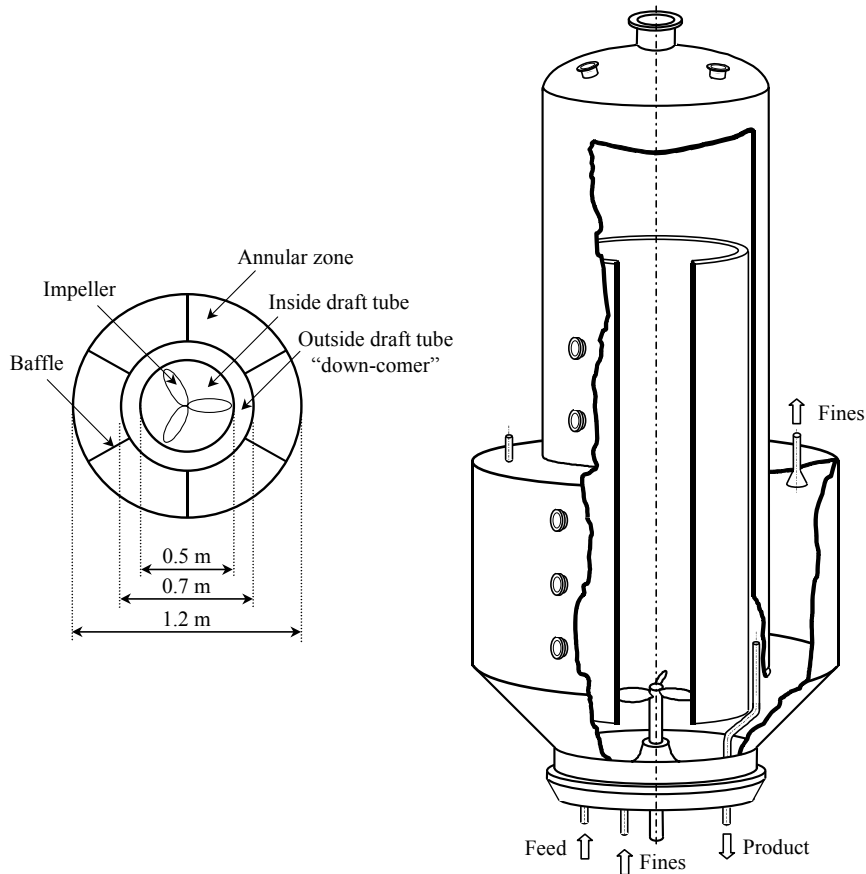


Figure 6.4: Top down, cross sectional view of the 1100-litre DTB crystalliser (left), schematic drawing of the same crystalliser (right).

The annular zone surrounding the crystalliser body has a cross-sectional area of 0.746 m^2 . Large baffles divide this zone across the entire height into six equally spaced, independent compartments. From the top of each compartment, a so-called fines flow is removed via a withdrawal tube (see Figure 6.4). The bottom of each compartment has an open connection to the crystalliser body. The

relatively large cross-sectional area in combination with a low fines removal rate (up to 3.5 l/s) leads to a low vertical upward velocity inside the compartments. Due to this low velocity the annular zone will act as a settling zone in which small crystals are separated from larger crystals by gravitational forces. Larger crystals will subsequently return to the crystalliser body whereas small crystals are removed with the fines flow.

The partition of the annular zone in compartments is made to 1) prevent the generation of a swirl in the annular zone due to the rotation of the impeller and to 2) de-couple to a certain extent the fines removal rate and the vertical upward velocity in the compartments; thus increasing the flexibility of the system.

In order to access the inside of the crystalliser from the outside for the purpose of local sampling or in-line measurements, flange connections are made in the crystalliser hull at five different height locations. Where necessary, corresponding holes are made in the skirt baffle and in the draft tube respectively. To prevent shortcut streams through the holes when no local measurement or sampling is performed, sealing rods are implemented.

Classification in the Annular Zone

Due to the low upward superficial velocity in the annular zone, classification occurs as a result of gravitational forces/settling. The classification performance of the annular zone can be expressed by means of a classification function, $h_{fines}(L)$, as defined by Eq. 4.47. Under the assumption of unclassified product removal, i.e. $n_{prod}(L) = n_{bulk}(L)$, the classification function is determined from experimental CSD data of the fines and product stream. Measurement of the product CSD is discussed above. In order to measure the CSD of the fines removed from the annular zone a Malvern MasterSizer X laser diffraction measurement system (see Figure 6.3), equipped with a 300 mm lens, was placed before the plate heat exchanger. The classification function is given by the ratio of these two size distributions, viz $n_{fines}(L)$ and $n_{prod}(L)$.

Fines Removal and Dissolving System

The fines removal and dissolving system is used to 1) supply the required heat for evaporation of the solvent and 2) to remove and partially dissolve small crystals in order to decrease the overall crystal surface area. This decrease in surface area leads to higher growth rates and thus to an increased median crystal size L_{50} . As shown by Eek (1995) this system can be used as an effective actuator to control the dynamic start-up behaviour of the CSD in the crystalliser.

In the current configuration the fines flow rate can be varied in the range of 1 to 3.5 l/s. The upper limit has to be maintained to avoid cavitation in the withdrawal tubes and the lower limit to avoid cavitation at the re-entry location. Next, the stream passes through a plate heat exchanger in which the necessary heat for the crystallization process is added to the system. The temperature increase of the fines flow is determined by the set heat duty and the fines flow rate. The plate heat exchanger is fed with water of 90 °C from a hot water supply vessel. The fines flow is subsequently fed back to the crystalliser either directly or via a dissolving vessel. This vessel with a volume of 220 litres is installed to

increase the residence time of the fines stream in the external loop and thus their degree of dissolution. The degree of dissolution can be monitored by measuring the CSD of the fines stream being returned to the crystalliser body and comparing it with the CSD of the fines removed from the annular zone. Both CSD measurements are performed with a Malvern MasterSizer X laser diffraction measurement system (see Figure 6.3), equipped with a 300 mm lens.

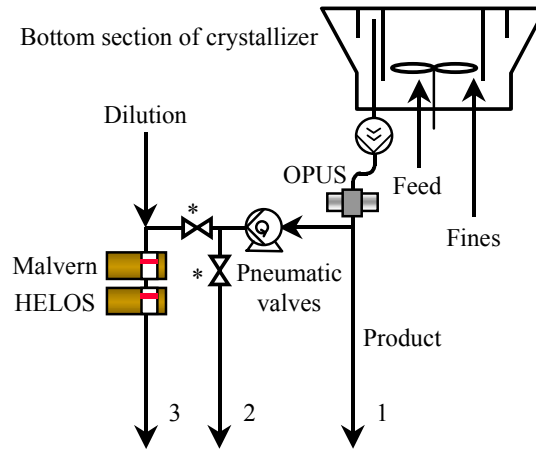


Figure 6.5: Product removal and dilution system of the 1100-litre DTB crystalliser (Neumann, 2001).

Product Removal and Dilution System

Product is continuously removed from the down-comer of the crystalliser, in the direction of the internal circulation flow, by means of a progressive cavity pump situated at the ground floor of the plant (see Figure 6.5). The criterion for isokinetic product withdrawal is met for an impeller frequency of 370 rpm. For the other experiments, performed at a frequency of 320 rpm, the ratio of crystalliser and withdrawal velocity is 1.26. It is assumed that this small deviation has no significant effect on the product removal.

After passing through the product removal pump, the flow is passed through an on-line CSD measurement device (OPUS), which is based on ultrasonic extinction measurements, to measure the size distribution of the product crystals in undiluted form. At regular time intervals, a part of this product stream is injected into a dilution stream of saturated crystal-free mother liquor. The resulting diluted product sample is transported through two on-line laser diffraction measurement systems, Malvern and HELOS, to measure the CSD. By using this dilution technique the original product solid concentration of approximately 11 vol.% can be lowered to a solid concentration of approximately 1.5 vol.%; the maximum solid concentration which avoids multiple scattering and thus enables an accurate measurement using the laser diffraction measurement systems.

Monitoring and control system

A description of the monitoring and control system for the liquid level, temperature, heat input, residence time, fines removal flow and dilution flow of the 1100-litre DTB crystalliser is given by Neumann (2001).

6.2.2 CSD MEASUREMENT DEVICES

For parameter estimation and model validation purposes it would be very useful to have techniques for the direct measurements of the rates at which the various crystallisation phenomena occur. This is only possible to a limited extent in dedicated laboratory scale equipment and not at all possible in industrial applications. Instead, measurement techniques relating the various crystallisation phenomena to common process and product denominators, such as supersaturation and CSD are used.

The evolution of the crystal size distribution during start-up and subsequent operation of the 22-litre DT and 1100-litre DTB crystallisers is measured using two forward laser diffraction instruments, the Malvern 2600 Particle Sizer and Sympatec Helos Vario, and an acoustic attenuation instrument, the Sympatec Opus. The principles, advantages and disadvantages of these measurement techniques are discussed by Neumann (2001), who also performed a comparative study focusing on measurement quality. This study revealed that the measurements obtained with the Helos and Malvern are in good agreement and of superior quality than that provided by the Opus. For the remainder of this work Helos data was chosen above Malvern data, because the Malvern is an older instrument of which the calibration is consequently probably less reliable than that of the Helos measurement device. Although the same Helos device was used for experiments on both crystallisers, a 1000 mm and 2000 mm lens, corresponding to a smaller and larger crystal size range, are used for experiments on respectively the 22-litre DT and 1100-litre DTB crystallisers. For presentation and parameter estimation purposes, the evolution of the CSD is captured in the form of 10, 25, 50, 75 and 90% quantiles. These measures, symbolically denoted as L_{10} , L_{25} , L_{50} , L_{75} and L_{90} , are defined as the crystal size for which respectively 10, 25, 50, 75 and 90% of the observed volume density distribution has a size smaller than or equal to this value. Quantiles were chosen over volume densities because they constitute more robust measures of the CSD (Boxman, 1992).

6.3 EXPERIMENTS AND MEASUREMENT DATA

This section provides an overview of selected experiments performed on the 22-litre DT crystalliser (two experiments) and 1100-litre DTB crystalliser (four experiments). In total, 64 continuous experiments, corresponding to approximately 3000 hours of operation, were performed. Details on many of the experiments not included in this thesis are given by Neumann (2001).

Initial conditions

All experiments were started from the same initial conditions as regards temperature, solute concentration and CSD: 50°C, an ammonium sulphate/water solution saturated at that temperature and no solids.

Experiment design parameters

The experiment design parameters selected to vary between the experiments presented in this chapter are the impeller frequency (DT and DTB crystallisers), fines removal rate (DTB crystalliser) and volume of fines dissolution loop (DTB crystalliser). These experiment design parameters were selected because of the different physical processes through which they affect the product quality and in particular the CSD:

- The impeller frequency influences (i) the frequency and intensity of crystal-impeller collisions, (ii) the degree of internal solids classification and (iii) the internal supersaturation profile.
- The fines removal rate has an effect on (i) the residence time of the fine crystals in the main body of the crystalliser, (ii) the upward velocity in the annular zone and hence the cut size of the fines classification and (iii) the residence time of the fine crystals in the fines dissolution loop, i.e. the amount of time that these crystals are exposed to undersaturation or the time available for dissolution of these crystals.
- The volume of the fines dissolution loop is varied to allow investigation of the influence of the fines crystals' residence time in this loop at a fixed fines removal rate. This separates the effect the degree of fines dissolution in this loop has on the CSD from changes in the CSD through a modified fines classification cut size and/or residence time of fine crystals in the crystalliser main body.

Other experimental design parameters that were considered but not selected to be varied in the experiments presented here include the product residence time (DT and DTB crystallisers) and the cross-sectional area of the annular zone (DTB crystalliser).

- The product residence time can be changed by varying the liquid level in the crystalliser and/or the product flow rate, but both are heavily constrained by respectively undesired hydrodynamic effects, such as short-circuiting and stagnation of the circulation, and pump limitations /blockages.
- The annular zone is divided into six vertically separated compartments in order to enable discrete changes in the cross-sectional area of the annular zone. This allows investigation of the influence of the upward velocity in the annular zone at a fixed fines removal rate. This separates the effect the cut size of the fines classification has on the CSD from changes in the CSD through a modified degree of fines dissolution and/or residence time of fine crystals in the crystalliser

main body. However, this experiment design parameter could not be used effectively because closing one or more of the vertical compartments led to cavitation in the fines pump.

Finally, it is worth noting that although all experiments presented here were conducted with time-invariant design parameters, there is no practical reason preventing variation of design parameters within an experiment (this in addition to variations between experiments). However, at the outset of this research project there were two major reasons for not designing experiments with time-variant parameters. Firstly, it was uncertain whether the still-to-be-developed parameter estimation facility would be able to handle experiments with time-variant parameters. Secondly, the vast majority of crystallisation experiments had been performed with time-invariant parameters.

The default values for the experiment design parameters and other key operating conditions are listed in Table 6.1.

Table 6.1: Default operating conditions for the experiments presented in this chapter.

	DT	DTB
crystalliser volume [l]	22	1100
temperature [°C]		50
impeller frequency [rpm]	775	370
fines removal flow rate [$\text{l}\cdot\text{s}^{-1}$]	-	2
volume for fines dissolution [l]	-	240
volume specific heat input [$\text{kW}\cdot\text{m}^{-3}$]		120
feed temperature [°C]		53
feed density [$\text{kg}\cdot\text{m}^{-3}$]		1248 ⁴
product residence time [s]		4500
product flow [$\text{l}\cdot\text{s}^{-1}$]	$4.88\cdot 10^{-3}$	$2.44\cdot 10^{-1}$

6.3.1 22-LITRE DT CRYSTALLISER

The influence of the impeller frequency on the CSD produced in the 22-litre DT crystalliser is illustrated by experiments DT25 and DT26, operated at impeller frequencies of respectively 775 and 910 rpm (see Table 6.2). Operating conditions not listed in this table were kept at the default values listed in Table 6.1.

⁴ density corresponding to an ammonium sulphate / water solution saturated at 50°C

Table 6.2: Experiment design parameter values for DT25 and DT26.

	DT25	DT26
impeller frequency [rpm]	775	910
tip speed [$\text{m}\cdot\text{s}^{-1}$]	5.6	6.6
specific power input [$\text{W}\cdot\text{kg}^{-1}$]	1.96	3.18
internal circulation velocity [$\text{m}\cdot\text{s}^{-1}$]	0.65	0.74
turnover time [s]	2.0	1.8

The measured transients of the quantiles L_{10} , L_{25} , L_{50} , L_{75} and L_{90} are shown in Figure 6.6 for experiments DT25 and DT26.

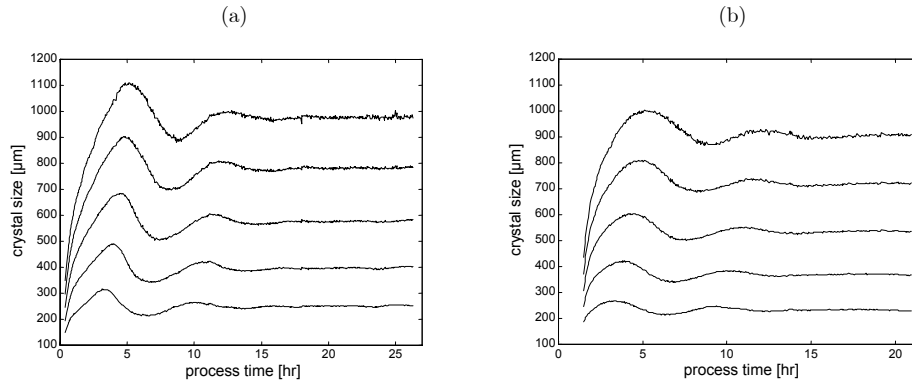


Figure 6.6: measured transients of the quantiles L_{10} , L_{25} , L_{50} , L_{75} and L_{90} for experiments DT25 (a) and DT26 (b).

Both experiments performed with the DT crystalliser initially exhibit oscillations as regards the CSD evolution. These oscillations dampen out after approximately 1.5 to 2 periods (5-7 hours) and are more pronounced in DT25, the experiment performed at a lower impeller frequency. Furthermore, a lower impeller frequency also results in higher steady-state values for the quantiles. The impeller frequency is clearly an effective actuator for the crystallisation of ammonium sulphate from water in a crystalliser of this type and scale.

6.3.2 1100-LITRE DTB CRYSTALLISER

Four experiments, viz DTB03, DTB05, DTB06 and DTB12, are used to demonstrate and study the effect of the impeller frequency, fines removal flow rate and fines dissolution loop volume on the CSD produced in the 1100-litre DTB crystalliser. The values of the experiment design parameters and related quantities for these four experiments are given in Table 6.3. Operating conditions not listed in this table were kept at the default values listed in Table 6.1. The measured transients of the quantiles L_{10} , L_{25} , L_{50} , L_{75} and L_{90} for these four experiments are shown in Figure 6.7.

All experiments performed on the 1100-litre DTB crystalliser exhibit a significantly more pronounced oscillatory behaviour of the CSD evolution than is observed in the 22-litre DT crystalliser experiments. A rough estimation of the time averaged quantiles indicates a CSD shift towards larger crystal sizes when comparing the 1100-litre DTB with the 22-litre DT experiments. The increased crystal size is attributed to mainly two factors. First of all, the removal and subsequent dissolution of large numbers of small crystals (fines), which results in a decreased volume specific crystal surface area available for growth, which in its turn implies a higher growth rate for the same volume specific crystal production rate. All experiments on the 22-litre DT and 1100-litre DTB crystalliser have the same volume specific production rate because they were performed with the same residence time and volume specific heat input. The second factor attributing to a change in crystal size is the frequency and intensity of crystal-impeller collisions. The collision frequency is determined by (i) the average time between two subsequent passes of the impeller by a single specific crystal and (ii) the chance of collision per pass. An indication for the time between two subsequent passes is the so-called turnover time, defined as the crystalliser volume over the volumetric internal circulation flow rate, which is approximately two seconds on the 22-litre DT crystalliser and five seconds on the 1100-litre DTB crystalliser (see Table 6.2 and Table 6.3 respectively). Comparison of the collision chance per pass between the two crystallisers is less straightforward as this chance depends on both the superficial axial velocity in the draft tube, which is nearly twice as high in the 1100-litre DTB crystalliser, and geometric considerations, for which the influence of the differences between the two crystalliser configurations is more difficult to assess. The same reasoning holds for the intensity or potential energy of the crystal-impeller collision, which is determined by the superficial axial velocity and the impeller geometry. The latter determines the impact angle and thus the effective velocity of the crystal-impeller collision.

Influence of impeller frequency

Comparison of experiments DTB03 and DTB12 reveals the effect of the impeller frequency, 370 and 320 RPM respectively, on the CSD transients obtained from a given crystalliser while maintaining all other operating conditions at their default values (see Table 6.1). As can be seen from Figure 6.7.a and Figure 6.7.b a 14 percent decrease in impeller frequency results in a marked increase in the crystal sizes corresponding to the various quantiles. For instance, the time averaged median crystal size increases from approximately 700 and 900 μm . At the same time, the time averaged quantile ratio remains relatively unchanged. Roughly speaking, decreasing the impeller frequency from 370 to 320 rpm shifts the location of the CSD to a higher crystal size without increasing the width of the distribution. The shift to higher crystal sizes is expected because, for a given crystalliser, the decrease in impeller frequency leads to higher turnover times, lower collision chances and lower collision energies. On the other hand, the influence of the impeller frequency on the distribution's width cannot easily be explained by reasoning. Another observation that is difficult to explain is the fact

that the oscillations of the quantiles are more pronounced for the experiment performed at the higher impeller frequency. Moreover, this behaviour is actually counterintuitive because these kinds of oscillations are generally assumed to be the result of alternating periods with a shortage of nuclei and periods with an excess of nuclei. Consequently one would expect that a higher impeller frequency would reduce the length of the periods with a shortage of nuclei and hence the magnitude of the oscillations.

Influence of fines removal rate

The influence of the fines removal flow rate on the CSD evolution can be seen by comparing experiments DTB05 and DTB06, which were conducted with fines flow rates of respectively 3 and 2 l/s. All other operating conditions were kept at the default values listed in Table 6.1. Comparison of Figure 6.7.c and Figure 6.7.d reveals a slight increase in the time averaged median crystal size due to the increase in the fines removal flow rate. There is again no significant influence in the time averaged quantile ratios. The increased crystal size is a result of a larger number of fine crystals being removed from the crystalliser and being dissolved in the fines dissolution loop, which decreases the volume specific crystal surface area available for growth and thus increases the crystal growth rate as described above. Besides influencing the number of crystals removed from the crystalliser, the fines flow rate also influences the classification behaviour in the annular zone as well as the temperature increase in the fines dissolution loop for a given heat input. It is therefore worth noting that if one keeps increasing the fines removal flow rate the average crystal size will cease to increase and start decreasing. A too high flow rate can result in a lack of classification selectivity with respect to crystal size, i.e. the CSD of the crystals removed from the annular zone is (practically) the same as the product CSD, and/or such a low temperature increase that the corresponding undersaturation provides an inadequate driving force for dissolution of the removed crystals.

Influence of fines residence time in dissolution loop

The efficiency of the fines dissolution is not only determined by the temperature increase over the fines loop and the amount of crystals removed from the annular zone, but also by the time available for dissolution. Experiments DTB03 and DTB06 were performed using fines dissolution loop volumes of respectively 240 and 20 litres, which for a fines removal flow rate of 2 litres per second corresponds to residence times in the loop of respectively 120 and 10 seconds. Figure 6.7.a and Figure 6.7.c show no significant effect of this fines residence time on the location and width of the produced CSD. This seems to indicate that fines dissolution is already complete with a fines residence time of 10 s for the employed product residence time, heat input and fines removal flow rate.

Table 6.3: Experiment design parameter values for the 1100-litre DTB experiments.

	DTB03	DTB05	DTB06	DTB12
impeller frequency [rpm]	370	370	370	320
tip speed [$\text{m}\cdot\text{s}^{-1}$]	9.4	9.4	9.4	8.1
specific power input [$\text{W}\cdot\text{kg}^{-1}$]	2.29	2.29	2.29	1.48
internal circulation velocity [$\text{m}\cdot\text{s}^{-1}$]	1.12	1.12	1.12	1.01
turnover time [s]	5.0	5.0	5.0	5.5
fines removal flow rate [$\text{l}\cdot\text{s}^{-1}$]	2	3	2	2
fines residence time in main body [s]	550	367	550	550
cut size of fines classification [μm]	80	100	80	80
fines dissolution loop volume [l]	240	20	20	240
fines residence time in dissolution loop [s]	120	7	10	120
effect of impeller frequency	x			x
effect of fines removal flow rate		x	x	
effect of volume for fines dissolution	x		x	

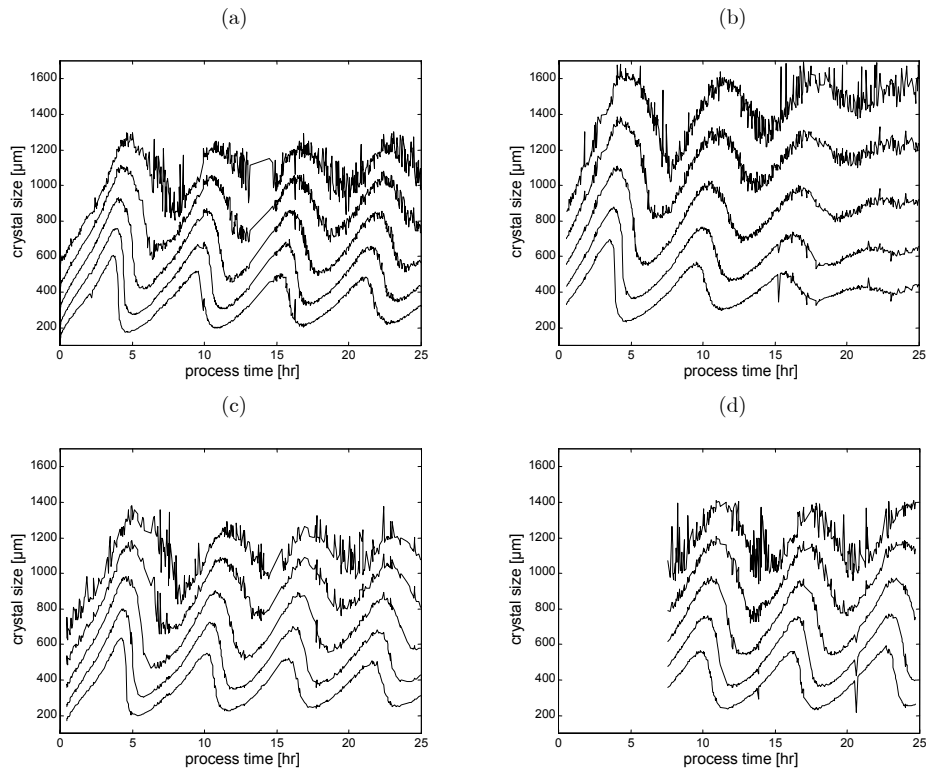


Figure 6.7: measured transients of the quantiles L_{10} , L_{25} , L_{50} , L_{75} and L_{90} for the first 25 hours of experiments DTB03 (a), DTB12 (b), DTB06 (c) and DTB05 (d).

6.3.3 MEASUREMENT ERRORS

The relative standard deviations in the quantiles of the measured crystal size distributions are estimated by fitting a linear relationship through subsets of the quantile time series of experiments DT25 and DTB03, shown in respectively Figure 6.6.a and Figure 6.7.a, and calculating the average standard deviation of all data points in the subset under consideration. This approach is considered a valid approximation as the time interval between two successive data points is of the order of two minutes while the characteristic time of the quantile dynamics is in the order of hours.

Table 6.4: Estimated relative standard deviations in quantile measurements.

quantile	22-litre DT experiments (based on DT25)	1100-litre DTB experiments (based on DTB03)
L_{10}	0.42%	3.93%
L_{25}	0.34%	2.45%
L_{50}	0.32%	2.07%
L_{75}	0.35%	2.85%
L_{90}	0.43%	4.75%

The significant difference in the estimated standard deviations for experiments DT25 and DTB03 can be attributed to the higher sensitivity for environmental disturbances (draft, temperature fluctuations, etc.) of the 2000 mm lens used for the 1100-litre DTB experiments and/or differences in the sampling and dilution system of the two crystalliser configurations. The estimated standard deviations of the measurements are used either as fixed values in the maximum likelihood function (see 6.4) or as lower bounds for the standard deviations estimated simultaneously with the kinetic parameters.

6.4 PARAMETER ESTIMATION

The two 22-litre DT crystalliser experiments presented in the previous section are to be used to estimate the unknown kinetic parameters of the model framework presented in Chapter 4. These parameters are the rate constant for surface integration, k_r , and the condition of deformation, Γ_s . Gahn and Mersmann (1999) used steady state median size and supersaturation measurements to estimate values for these two unknown kinetic parameters. However, this approach is infeasible for (i) continuous crystallisation processes where the supersaturation is difficult to measure and (ii) batch crystallisation processes, which by definition have no steady state. The ammonium sulphate crystallisation experiments used in this work fall under the first category, i.e. difficult to obtain accurate supersaturation measurements. Neumann et al. (1999) showed that, as expected, an unambiguous determination of the kinetic parameters is not possible on the basis of the steady state median size alone. Subsequently, they used other characteristics of the steady state CSD, such as quantiles and the quartile ratio, as additional information. However, this did not lead to a significantly less unambiguous determination. Therefore, *dynamic* parameter estimation is used here as an alternative approach to compensate for the absence of a steady-state supersaturation measurement.

The two kinetic parameters, k_r and Γ_s , providing the best correspondence between measurements and model predictions will be determined using gPROMS' built-in parameter estimation capabilities, which combine formal mathematically based optimisation techniques with a maximum likelihood formulation for the objective function (Process Systems Enterprise Ltd, 2002). This formulation consists of three terms:

$$\Phi = \underbrace{\frac{N}{2} \ln(2\pi)}_{\text{constant term}} + \frac{1}{2} \min_{\theta} \left\{ \sum_{i=1}^{NE} \sum_{j=1}^{NV_i} \sum_{k=1}^{NM_{ij}} \left[\underbrace{\ln(\sigma_{ijk}^2)}_{\text{variance term}} + \underbrace{\frac{(\tilde{z}_{ijk} - z_{jk})^2}{\sigma_{ijk}^2}}_{\text{weighted residual term}} \right] \right\} \quad [6.1]$$

where	N	total number of measurements taken during all experiments.
	θ	set of model parameters to be estimated, which may be subject to given bounds, <i>i.e.</i> $\theta \leq \theta \leq \theta^U$.
	NE	number of experiments performed.
	NV_i	number of variables measured in experiment i .
	NM_{ij}	number of measurements of variable j in experiment i .
	σ_{ijk}^2	variance of the k^{th} measurement of variable j in experiment i .
	\tilde{z}_{ijk}	k^{th} measured value of variable j in experiment i .
	z_{jk}	k^{th} (model-)predicted value of variable j in experiment i .

For the parameter estimation calculations in this chapter, a two-compartment model is used to represent the 22-litre DT crystalliser, one compartment for the impeller and one for the remaining volume. The justification for use of this compartmental model will be given in Chapter 7.

6.4.1 PARAMETER SENSITIVITIES

Before proceeding with parameter estimation on the basis of measured data, the sensitivity of the CSD predicted by the model for both unknown and 'known' parameters is evaluated. The unknown parameters are the kinetic parameters whereas the 'known' parameters include material properties such as the critical work for indentation, Vicker's hardness, shear modulus, density and viscosity, operating conditions such as the residence time and impeller frequency, and finally the binary diffusion coefficient of the solute in the solvent. The purpose of this parameter sensitivity study is to identify model parameters that may be worthwhile estimating simultaneously with the kinetic parameters in order to obtain a satisfactory fit. Finite differencing using results from steady-state simulations and dynamic simulations as well as parameter estimation on the basis of artificial measurements are used to evaluate these parameter sensitivities. It is worth noting that, as the crystallisation model is non-linear, the parameter sensitivities will depend on the values taken as the starting point for these parameters. The material property values and their references can be found in Appendix B.4. For the operating conditions the default values of the 22-litre DT experiments as shown in Table 6.1 are used. Finally, the kinetic parameter values were chosen to be of the same order of magnitude as those obtained from preliminary parameter estimation calculations.

Finite differencing on the basis of simulations is aimed at determining the parameter sensitivity on an individual basis as well as identifying parameters that may have a limited influence on the steady-state CSD but a significant influence on the transient behaviour of the CSD or vice versa. The measure for the parameter sensitivity determined by finite differencing on the basis of steady-state

simulations is defined as the relative change in the steady-state median crystal size over the relative perturbation of the parameter in question:

$$\frac{L_{50,ss}(p^0 + \Delta p) - L_{50,ss}(p^0 - \Delta p)}{L_{50,ss}(p^0)} \frac{p^0}{2\Delta p} \quad [6.2]$$

The measure for the parameter sensitivity determined by finite differencing on the basis of dynamic simulations is given by the time averaged relative difference between the transients of the median crystal size obtained with the default set of parameter values and the median crystal size obtained with one of these parameters perturbed by a factor of Δp over the relative perturbation of the parameter in question:

$$\frac{\int_{t=0}^T \left[|L_{50}(p^0 + \Delta p, t) - L_{50}(p^0, t)| + |L_{50}(p^0, t) - L_{50}(p^0 - \Delta p, t)| \right] dt}{\int_{t=0}^T L_{50}(p^0, t) dt} \frac{p^0}{2\Delta p} \quad [6.3]$$

The parameter sensitivities determined by finite differencing on the basis of steady-state and dynamic simulations with relative perturbation factors, $\Delta p/p^0$, of 0.1% and 10% are shown in Table 6.5.

Table 6.5: Parameter sensitivities determined for each parameter individually by means of finite differencing using steady-state and dynamic simulation.

par.	p^0	steady-state parameter		dynamic parameter		rank
		sensitivity according to Eq. 6.2		sensitivity according to Eq. 6.3		
		$\frac{\Delta p}{p^0} = 10^{-3}$	$\frac{\Delta p}{p^0} = 10^{-1}$	$\frac{\Delta p}{p^0} = 10^{-3}$	$\frac{\Delta p}{p^0} = 10^{-1}$	
k_r	$2.00 \cdot 10^{-5}$	0.145	0.141	0.137	0.138	5
Γ_S	$2.00 \cdot 10^{-4}$	0.395	0.399	0.377	0.387	3
W_C	$4.10 \cdot 10^{-9}$	0.077	0.077	0.073	0.073	7
D_{AB}	$2.50 \cdot 10^{-9}$	0.071	0.071	0.070	0.069	9
H	$3.55 \cdot 10^8$	0.231	0.233	0.220	0.221	4
ρ_S	$1.77 \cdot 10^3$	-0.730	-0.747	0.697	0.717	2
ρ_L	$1.25 \cdot 10^3$	0.121	0.127	0.116	0.121	6
μ	$8.90 \cdot 10^9$	0.000	0.000	0.002	0.000	11
$\eta_{L/S}$	$1.45 \cdot 10^{-3}$	0.050	0.050	0.048	0.048	10
τ_{prod}	$4.50 \cdot 10^3$	0.075	0.072	0.137	0.136	8
N_{imp}	$1.29 \cdot 10^1$	-0.782	-0.787	0.743	0.746	1

The measures for the parameter sensitivities have been defined such to enable direct comparison between sensitivities for different parameters. For instance, a one percent change in the impeller speed results in a -0.78% percent change in the steady state median crystal size, while a one percent change in the critical work required for indentation leads to a 0.08 percent increase in the steady state median crystal size. Interestingly, there is not much difference between the

sensitivities determined from steady-state versus dynamic simulations. According to the measures for the sensitivities listed in Table 6.5, the two kinetic parameters, T_s and k_v , have relatively speaking only the third and fifth largest influence on the median crystal size. Furthermore, from the last column of this table it may appear there is more benefit to be gained by estimating the material density of the solid phase and the Vicker's hardness than by estimating the kinetic parameters. However, one additional factor that significantly influences the choice which parameters to estimate has not yet been taken into account. That factor is the uncertainty in the parameter values before any crystallisation experiment is performed. The kinetic parameter values are completely unknown besides perhaps their orders of magnitude, while the impeller frequency will typically be known within 5 to 10 percent. Multiplying the measures in columns 3 through 6 with an estimate of the relative uncertainty of each parameter and ranking the results will therefore provide a more useful indication of which parameters to include in estimation calculation. Due to the absence of reasonable estimates for these uncertainties, educated engineering guesses are used to illustrate the influence of this operation on the parameter sensitivity ranking (Appendix C.1).

So far, the study into the sensitivity of the CSD for changes in model parameters and operating conditions has been limited to their effect on the median crystal size, L_{50} . In order to not only investigate the impact on the location of the CSD but also on its width, other quantiles, viz the L_{10} , L_{25} , L_{75} and L_{90} , will be included in the next sensitivity analysis. This analysis also differs from the previous analyses in that it employs parameter estimation calculations as opposed to simulations. The advantage of this approach is a simultaneous determination of the CSD's sensitivities with respect to all parameters, which also estimates and takes into account the cross correlation between all the parameters. To separate the effects of the cross correlations and of including additional quantiles, this parameter estimation based approach will first be performed on the basis of the median crystal size alone and secondly on the basis of all five quantiles. For this sensitivity study approach artificial measurements, created by superimposing normally distributed noise on simulated (ideal) measurements, are used.

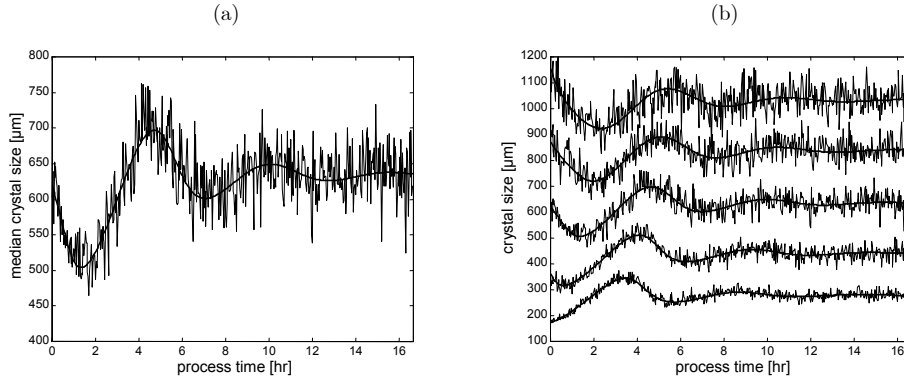


Figure 6.8: Simulated measurements and model predictions for the transients of the median crystal size alone (a) and five quantiles L_{10} , L_{25} , L_{50} , L_{75} and L_{90} (b) used for parameter sensitivity analysis.

The simulated measurements and model predictions for the parameter sensitivity analyses based on median crystal size alone and on all five quantiles are depicted in Figure 6.8. For all measurements normally distributed noise with a 5% relative standard deviation was used. The parameter estimates and standard deviations corresponding to the model predictions in Figure 6.8 are listed in Table 6.6. Unlike Table 6.5, Table 6.6 does not contain the shear modulus, μ . This parameter was omitted from the parameter estimation exercise, because including a parameter to which the objective function is insensitive results in an ill-conditioned problem for the calculation of the variance and correlation matrices.

Table 6.6: Parameter sensitivities determined via simultaneous estimation of these parameters using simulated, ideal measurements with addition of normally distributed noise.

par.	p^0	sensitivity analysis based on transient of median crystal size (L_{50}) alone			sensitivity analysis based on transients of L_{10} , L_{25} , L_{50} , L_{75} and L_{90}		
		$p^* \pm \sigma$	$\ln(p^*/\sigma)$	rank	$p^* \pm \sigma$	$\ln(p^*/\sigma)$	rank
k_r	$2.00 \cdot 10^{-5}$	$(0 \pm 1.3) \cdot 10^{-3}$	-4.13	4	$(0.2 \pm 1.2) \cdot 10^{-4}$	-1.81	4
Γ_S	$2.00 \cdot 10^{-4}$	$(0 \pm 8.0) \cdot 10^{-3}$	-3.67	3	$(2.0 \pm 6.2) \cdot 10^{-4}$	-1.13	3
W_C	$4.10 \cdot 10^{-9}$	$(0 \pm 3.1) \cdot 10^{-3}$	-13.55	9	$(0 \pm 1.3) \cdot 10^{-6}$	-5.75	8
D_{AB}	$2.50 \cdot 10^{-9}$	$(0 \pm 2.1) \cdot 10^{-7}$	-4.57	6	$(0.2 \pm 2.5) \cdot 10^{-8}$	-2.28	6
H	$3.55 \cdot 10^8$	$(0 \pm 8.8) \cdot 10^{13}$	-12.43	7	$(0 \pm 3.8) \cdot 10^{10}$	-4.68	7
ρ_S	$1.77 \cdot 10^3$	$(0 \pm 1.6) \cdot 10^5$	-4.51	5	$(0.2 \pm 1.4) \cdot 10^4$	-2.06	5
ρ_L	$1.25 \cdot 10^3$	$(0 \pm 8.3) \cdot 10^8$	-13.40	8	$(0 \pm 8.5) \cdot 10^6$	-8.83	9
$\eta_{L/S}$	$1.45 \cdot 10^{-3}$	$(0 \pm 4.9) \cdot 10^3$	-15.06	10	$(0 \pm 3.1) \cdot 10^1$	-9.98	10
τ_{prod}	$4.50 \cdot 10^3$	$(4.66 \pm 0.59) \cdot 10^3$	2.06	1	$(4.493 \pm 0.039) \cdot 10^3$	4.74	1
N_{imp}	$1.29 \cdot 10^1$	$(1.3 \pm 1.1) \cdot 10^1$	0.13	2	$(1.289 \pm 0.094) \cdot 10^1$	2.62	2

Here the ratio of a parameter's estimated value over its standard deviation is used as a measure to compare the CSD transient's sensitivities with respect to the

model parameters and operating conditions. A higher value for this ratio implies that the agreement between model predictions and measurements will be affected more strongly by a given relative change in a parameter. The most marked difference between this simultaneous study of all parameter sensitivities and the individual study of the parameter sensitivities is observed for the product residence time, which has moved up from eighth position to become the parameter the CSD is most sensitive to for a given relative change. At the same time the Vicker's hardness, H , and the critical work for indentation, W_c , have dropped in the ranking to below the rate constant for surface integration, k_r . However, caution must again be exercised in using this ranking to determine the parameters to be included in the estimation calculations. For this purpose, the sensitivities should be multiplied by an estimate of the uncertainty in the respective parameter, as described earlier. The differences between the rankings shown in Table 6.5 and Table 6.6 are mainly the result of going from an individual to simultaneous determination of parameter sensitivities and thus including the effects of the parameter cross-correlations (see Appendix C.1).

6.4.2 DATA WINDOW AND INITIAL CONDITIONS

Two additional issues require attention when performing parameter estimation with dynamic or transient data as opposed to merely steady-state data. These issues are data window selection and initial conditions.

For determination of the data window (time horizon), the following criteria are used:

- The initial, start-up phase of the crystallisation experiments described in section 6.3 involves two nucleation mechanisms: primary and secondary nucleation. As the experiment progresses and crystal growth produces crystals sufficiently large to be prone to attrition, secondary nucleation becomes the dominant mechanism. Therefore, as primary nucleation is not included in the model framework, CSD data from the first four to five hours of the experiment will not be used for parameter estimation. After this time, equal to approximately three residence times, it is expected that practically no primary nuclei will be present in the crystalliser.
- Due to fouling in the sampling and/or dilution system, the noise in the measurements tends to increase towards the end of the experiment. For each experiment, a judicious decision is taken which data to exclude due to noise exceeding a certain, subjective level.

The second issue is the initial condition. As we are using dynamic, as opposed to steady state data, for parameter estimation, the initial condition will have a significant effect on the model predictions and thus on the optimal estimates of the kinetic parameters. The initial condition is given by the CSD, solids concentration, solute concentration and temperature at time zero. Note that time zero now does not refer to the beginning of the experiment but to the time of the

first CSD measurement used for parameter estimation purposes, i.e. the lower bound of the data window. The initial conditions are usually known with varying degrees of certainty: high certainty for the temperature (accurate measurements), high certainty for the solids concentration (easily at steady state after three hours and can be calculated from mass and energy balances alone), lower certainty for the CSD (measurement technique) and even lower certainty for the solute concentration (no supersaturation measurement). As a result, the temperature and solids concentration are assigned a measured respectively calculated value whereas the initial solute concentration will be estimated simultaneously with the kinetic parameters. How to deal with the initial CSD in parameter estimation calculations is slightly more complicated.

First, the crystallisation model requires, as an initial condition, values for the crystal number density at each node of the discretised crystal size domain. However, the CSD measurements typically encompass fewer points on the crystal size domain than the number of nodes. Furthermore, the nodes of the size domain used by the crystallisation model do usually not coincide with the points on the size domain used by the CSD measurement technique. This discrepancy is overcome by using CSD measurements to estimate the parameters of a continuous distribution function approximating the initial CSD. Here the initial CSD is parameterised as a bimodal distribution consisting of two log normal distributions on a volume density basis:

$$v(L, t = 0) = \frac{\phi}{L \ln(\sigma_{g,1}) \sqrt{2\pi}} \exp \left[- \frac{\left(\ln \left(\frac{L}{L_{0g,1}} \right) \right)^2}{2 \left(\ln(\sigma_{g,1}) \right)^2} \right] + \frac{(1-\phi)}{L \ln(\sigma_{g,2}) \sqrt{2\pi}} \exp \left[- \frac{\left(\ln \left(\frac{L}{L_{0g,2}} \right) \right)^2}{2 \left(\ln(\sigma_{g,2}) \right)^2} \right] \quad [6.4]$$

where	$v(L, t=0)$	initial crystal concentration expressed as a volume density	$[\text{m}^{-1}]$
	ϕ	relative weighting of the two log-normal distributions	$[-]$
	$L_{0g,1}, L_{0g,2}$	location parameters of log-normal distributions 1 and 2 respectively	$[\text{m}]$
	$\sigma_{g,1}, \sigma_{g,2}$	spread parameters of log-normal distributions 1 and 2 respectively	$[-]$

Secondly, two approaches can be considered for estimation of this distribution function's parameters: (i) estimation of these parameters before estimating the kinetic parameters and (ii) simultaneous estimation of the initial CSD's distribution function parameters and the kinetic parameters. For the first approach, the parameters of the distribution function describing the initial CSD are estimated on the basis of the CSD measurement ($L_{10}, L_{16}, L_{25}, L_{50}, L_{75}, L_{84}$ and

L_{90}) at time zero of the data window alone. The second approach uses all CSD measurements (L_{10} , L_{25} , L_{50} , L_{75} and L_{90}) within the data window to determine the parameters of this distribution function. In both cases, the kinetic parameters are estimated using all CSD measurements (L_{10} , L_{25} , L_{50} , L_{75} and L_{90}) within the data window. The 16 and 84 percent quantiles are brought into the picture for the first approach in order to have more measured variables than parameters to be estimated.

The effect of data window selection and including the initial conditions in the parameter estimation procedure is illustrated for experiment DT25 by Figure 6.9. The same effects are shown for experiment DT26 in Appendix C.2.

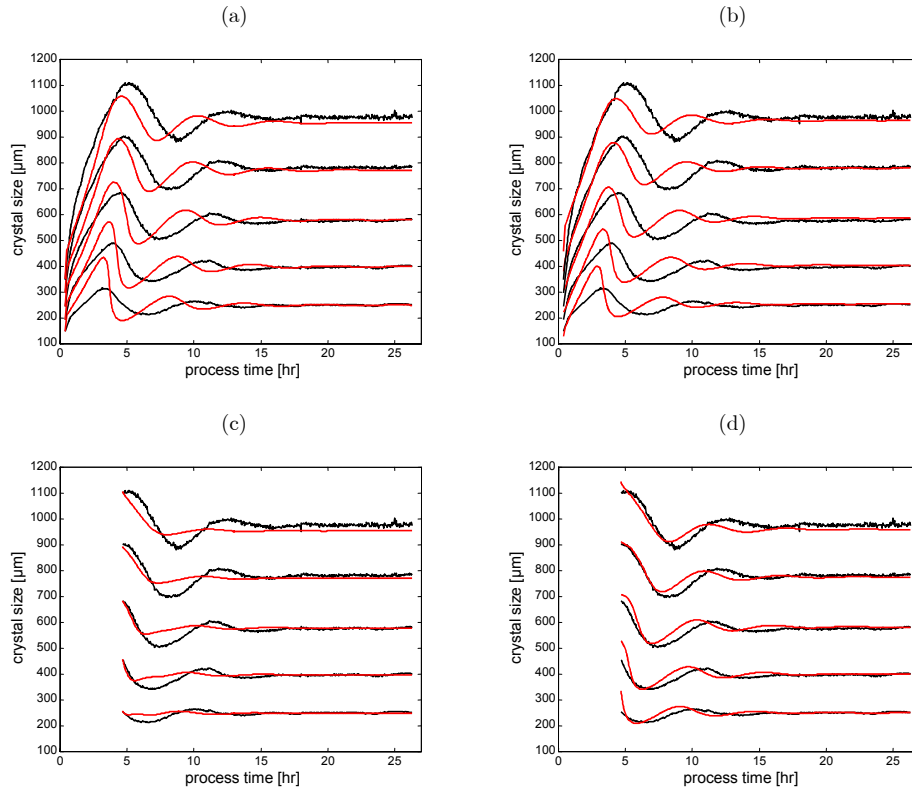


Figure 6.9: Effect of data window selection and estimation of initial conditions on quality of fit for measured quantiles of DT25. Data window: (a) and (b) include first four hours of data, (c) and (d) exclude these data. Initial conditions: (a) and (c) have initial CSD estimated prior to kinetic parameters, (b) and (d) have initial CSD estimated simultaneously with kinetic parameters.

This exercise yields the same trends in the results of both experiments. Selecting a data window, which excludes the first four to five hours of CSD measurements and estimating simultaneously the kinetic parameters and initial CSD (at time zero of the data window) significantly improves the agreement between the

measured quantiles and those predicted by the model. The better fits of Figure 6.9.c and Figure 6.9.d in comparison with Figure 6.9.a and Figure 6.9.b are attributed to the fact that the measured dynamic behaviour during the first four to five hours of the experiment is strongly influenced by primary nucleation, a phenomenon that is currently not included in the model framework. Figure 6.9.d shows a better agreement between measurements and model predictions than Figure 6.9.c for the time horizon as a whole. However, Figure 6.9.c provides a much better fit at the lower bound of the data window. This is not surprising as estimating the parameters of the initial CSD's distribution function before estimating the kinetic parameters can in fact be considered as simultaneous estimation of the initial CSD and kinetic parameters where the CSD measured at time zero has been given a higher weighting than all other measurements combined. At time zero, Figure 6.9.d shows the largest discrepancy between predictions and measurements, but apparently this discrepancy is required to provide a better fit for the remainder of the experiment. The second approach, simultaneous estimation of the initial CSD and kinetic parameters, ensures a better overall fit because all measurements are taken equally into account. The discrepancy between predictions and measurements at time zero indicates an inadequacy in the crystallisation model, parameterisation of the initial CSD and/or measurement inaccuracies.

Based on these results, all remaining parameter estimation calculations will exclude the initial four to five hours of the CSD measurements and involve simultaneous estimation of the initial CSD, initial solute concentration and kinetic parameters.

6.4.3 FITTING EXPERIMENTAL DATA OBTAINED FROM 22-LITRE DT CRYSTALLISER

The CSD measurements of experiments DT25 and DT26 to be used for parameter estimation are identified using the approach for data window selection outlined in the previous section. In order to provide a reference frame for the quality of fit and statistics of the parameter estimates, the experiments will not only be fitted with the Gahn kinetic model but also with the kinetic models of Ottens et al. (1972), Eek et al. (1995b) and Ó Meadhra et al. (1996). The nucleation and growth rate expressions of these three models are listed in Appendix C.3. A discussion of these models' characteristics and in particular their predictive value can be found in Chapter 4.

6.4.3.1 Model predictions versus measurements

The fits obtained with the kinetics models of Ottens, Eek, Ó Meadhra and Gahn are shown in Figure 6.10 for DT25 and in Appendix C.4 for DT26. For both experiments the kinetic model of Ottens clearly emerges as the model least capable of describing the observed CSD transients, while the kinetic model of Ó Meadhra produces the best fits by far. The kinetic models of Eek and Gahn provide comparable agreement between model predictions and measurements,

better than Ottens and worse than Ó Meadhra. The kinetic model of Gahn results in a better agreement for the (nearly) steady-state quantile values, whereas the kinetic model of Eek is more capable of reproducing the periods of the initial oscillations of the quantiles. Interestingly enough, the three other kinetic models all describe the periods of the oscillations more closely than the kinetic model of Gahn. To improve this aspect of the fit obtained with the Gahn kinetic model, additional parameter estimation studies were performed that involved estimation of the product residence time in addition to the kinetic parameters and the parameter of the initial CSD's distribution function (see Appendix C.4). For both experiments a residence time of approximately 5900 seconds was found to be the optimal value. Although this exercise does provide a better reproduction of the oscillation periods and a better fit of the median crystal size, the mismatch between model predictions and measurements increases for most other quantiles. Furthermore, it is unlikely to have such a large uncertainty in the product residence time (set to 4500 seconds) and, even if the residence time would be substantially different, to not identify this difference via a significant increase in the solids concentration (from approximately 10 to 13% when going from 4500 to 5900 seconds). Simultaneous estimation of the kinetic parameters, initial CSD and product residence time is thus not particularly meaningful from a physical point of view, but may be of use for certain optimisation and control applications that require good descriptive capabilities in a limited operation range. In order to obtain an improved predictive value with the Gahn kinetic model, it would be worthwhile investigating whether better fits can be obtained by including certain material properties in the parameter estimation calculations. Obvious candidates, based on the results of the parameter sensitivity studies in section 6.4.1, are the critical work for indentation, W_C , and the Vicker's hardness, H .

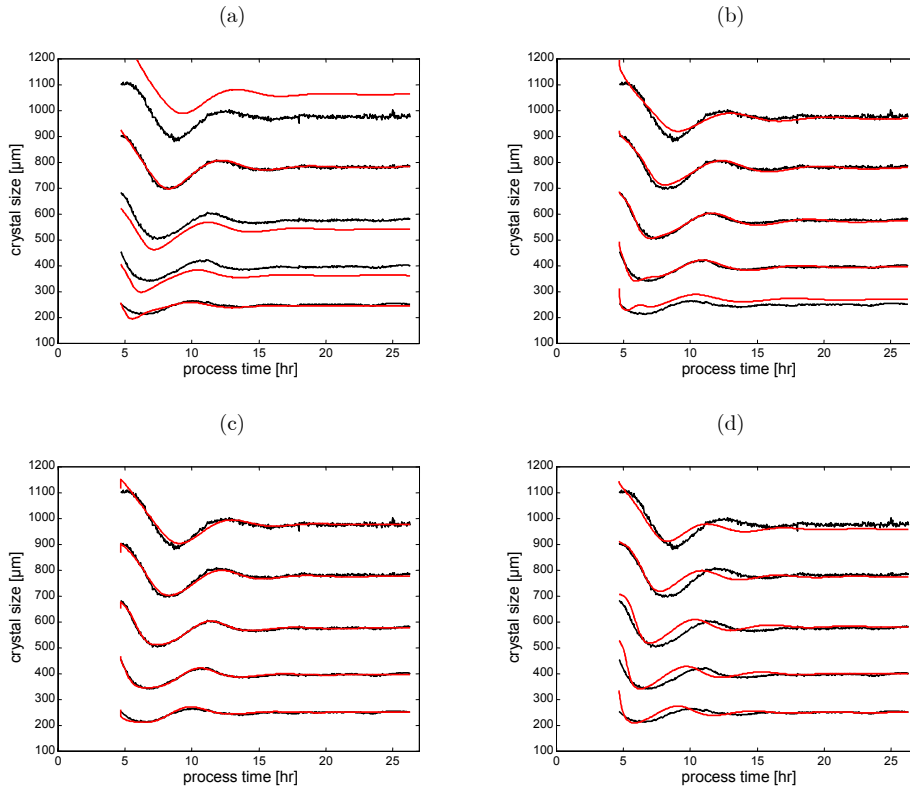


Figure 6.10: Measurements versus model predictions of quantiles L_{10} , L_{25} , L_{50} , L_{75} and L_{90} using the Ottens (a), Eek (b), Ó Meadhra (c) and Gahn (d) kinetic model for experiment DT25.

A more quantitative representation of the fits obtained with the kinetics models of Ottens, Eek, Ó Meadhra and Gahn is shown in Table 6.7 and Table 6.8. Table 6.7 contains the relative standard deviations of the fits for the various quantiles. Comparison of this table with Table 1.4 reveals that for all kinetic models the relative standard deviations of all *quantile fits* (i.e. model prediction versus measurement) are larger than the estimated relative standard deviation of the corresponding *quantile measurements*. The ratios between these relative standard deviations range from 1.6 to 4.5 for Ó Meadhra and from 2.0 to 24.4 for Ottens. The fact that all these ratios are larger than one indicates that there are structural errors in the measurements and/or varying degrees of model inadequacies. The last row of this table shows the average standard deviation over all quantile measurements, which is calculated as follows:

$$\sqrt{\frac{1}{5} \sum_{qq=10,25,50,75,90} \sigma_{L_{qq}}^2} \quad [6.5]$$

Table 6.7: Relative standard deviations of quantile fits for experiments DT25 and DT26.

Quantile	experiment DT25				experiment DT26			
	Ottens	Eek	Ó Meadhra	Gahn	Ottens	Eek	Ó Meadhra	Gahn
L_{10}	3.2%	8.2%	1.9%	4.9%	2.3%	10.0%	1.1%	4.9%
L_{25}	8.1%	1.6%	0.8%	4.5%	8.3%	1.5%	0.9%	5.1%
L_{50}	5.7%	1.1%	0.6%	3.8%	5.4%	0.7%	0.5%	2.4%
L_{75}	0.7%	1.1%	0.9%	2.2%	1.6%	0.6%	0.7%	2.6%
L_{90}	9.8%	1.5%	1.0%	2.1%	9.2%	1.1%	1.4%	7.4%
average	6.40%	3.86%	1.13%	3.69%	6.17%	4.57%	0.97%	4.84%

Table 6.8 contains values for a quality of fit measure defined as:

$$\frac{1}{nm - np} \sum_{i=1}^{nm} \frac{(\tilde{z} - z)^2}{(\sigma_{rel,meas} \tilde{z})^2} \quad [6.6]$$

where

- nm number of measurements
- np number of estimated model parameters
- \tilde{z} measured value
- z predicted value
- $\sigma_{rel,meas}$ relative standard deviation in measurement (see Table 6.4)

This measure assigns weights to the fits of the various quantiles on the basis that the mismatch between measurement and prediction is a result of measurement noise and model inadequacy alone (i.e. no mismatch due to structural measurement errors). As the results of Table 6.7 and Table 6.8 reveal similar trends between the various kinetic models, the assumption of no significant structural measurement errors appears to be valid.

Table 6.8: Quality of fit for experiments DT25 and DT26 according to a measure defined by Eq. 6.6. A lower value for this measure indicates a better fit.

quantile	experiment DT25				experiment DT26			
	Ottens	Eek	Ó Meadhra	Gahn	Ottens	Eek	Ó Meadhra	Gahn
L_{10}	65	433	21	121	34	515	6	85
L_{25}	625	22	6	168	568	20	6	184
L_{50}	372	11	3	105	307	5	2	53
L_{75}	3	10	6	41	23	3	4	70
L_{90}	494	13	5	27	525	6	10	243
total	1559	489	41	462	1457	549	28	635

Due to the high number of measurements for each quantile in the data windows of experiments DT25 and DT26, respectively 592 and 303, the results in this table do not significantly reflect the value of having a kinetic model with fewer parameters, e.g. 2 kinetic parameters in the Gahn model as opposed to 6 or 8 kinetic parameters for the kinetic model of respectively Eek or Ó Meadhra.

6.4.3.2 Parameter estimates

The parameter estimates corresponding to the fits obtained with the kinetic models of Ottens, Eek, Ó Meadhra and Gahn for experiments DT25 and DT26 are listed in the following four tables.

Table 6.9: Kinetic parameter estimates for the model of Ottens.

kinetic parameter	experiment DT25		experiment DT26	
	estimated value and standard deviation	rel. stand. dev. (%)	estimated value and standard deviation	rel. stand. dev. (%)
$P_{ott,1}$	$(2.8 \pm 2.4) \cdot 10^{-7}$	84	$(2.0 \pm 3.1) \cdot 10^{-7}$	152
$P_{ott,2}$	$(6.6 \pm 2.5) \cdot 10^{-1}$	38	$(5.9 \pm 4.6) \cdot 10^{-1}$	78
$P_{ott,3}$	$(6.370 \pm 0.098) \cdot 10^{-4}$	1.5	$(5.61 \pm 0.34) \cdot 10^{-4}$	6.0
$P_{ott,4}$	$(7.61 \pm 0.24) \cdot 10^2$	3.2	$(5.21 \pm 0.57) \cdot 10^2$	11

Table 6.10: Kinetic parameter estimates for the model of Eek.

kinetic parameter	experiment DT25		experiment DT26	
	estimated value and standard deviation	rel. stand. dev. (%)	estimated value and standard deviation	rel. stand. dev. (%)
$P_{eek,1}$	$(9.470 \pm 0.095) \cdot 10^{-1}$	1.0	$(1.150 \pm 0.025) \cdot 10^0$	2.2
$P_{eek,3}$	$(3.55 \pm 5.64) \cdot 10^{+5}$	159	$(2.83 \pm 5.53) \cdot 10^{+5}$	195
$P_{eek,4}$	$(8.250 \pm 0.075) \cdot 10^{-4}$	0.9	$(6.340 \pm 0.079) \cdot 10^{-4}$	1.2
$P_{eek,5}$	$(2.22 \pm 0.25) \cdot 10^0$	11	$(2.33 \pm 0.25) \cdot 10^0$	11
$P_{eek,8}$	$(4.390 \pm 0.096) \cdot 10^0$	2.2	$(3.240 \pm 0.078) \cdot 10^0$	2.4
$P_{eek,9}$	$(1.0200 \pm 0.0044) \cdot 10^{-3}$	0.4	$(9.930 \pm 0.057) \cdot 10^{-4}$	0.6

Table 6.11: Kinetic parameter estimates for the model of Ó Meadhra.

kinetic parameter	experiment DT25		experiment DT26	
	estimated value and standard deviation	rel. stand. dev. (%)	estimated value and standard deviation	rel. stand. dev. (%)
$P_{mea,1}$	$(2.30 \pm 0.76) \cdot 10^{-5}$	33	$(1.93 \pm 1.01) \cdot 10^{-5}$	52
$P_{mea,2}$	$(1.02 \pm 0.061) \cdot 10^0$	6.0	$(9.93 \pm 0.96) \cdot 10^{-1}$	9.7
$P_{mea,3}$	$(1.46 \pm 0.095) \cdot 10^{-1}$	6.5	$(2.23 \pm 0.17) \cdot 10^{-1}$	7.7
$P_{mea,4}$	$(1.55 \pm 0.012) \cdot 10^{-4}$	0.8	$(1.54 \pm 0.015) \cdot 10^{-4}$	0.9
$P_{mea,5}$	$(1.96 \pm 0.087) \cdot 10^0$	4.4	$(2.17 \pm 0.15) \cdot 10^0$	7.1
$P_{mea,6}$	$(2.63 \pm 0.13) \cdot 10^{-8}$	5.1	$(2.78 \pm 0.27) \cdot 10^{-8}$	9.8
$P_{mea,7}$	$(7.08 \pm 0.14) \cdot 10^{-4}$	2.0	$(7.11 \pm 0.31) \cdot 10^{-4}$	4.4
$P_{mea,8}$	$(3.29 \pm 0.20) \cdot 10^0$	6.0	$(3.02 \pm 0.31) \cdot 10^0$	10

Table 6.12: Kinetic parameter estimates for the model of Gahn.

kinetic parameter	experiment DT25		experiment DT26	
	estimated value and standard deviation	rel. stand. dev. (%)	estimated value and standard deviation	rel. stand. dev. (%)
k_r	$(1.020 \pm 0.061) \cdot 10^{-5}$	6.0	$(1.14 \pm 0.11) \cdot 10^{-5}$	9.6
Γ_s	$(2.060 \pm 0.049) \cdot 10^{-4}$	2.4	$(2.280 \pm 0.090) \cdot 10^{-4}$	4.0

The parameter estimates of all kinetic models except Gahn include at least one parameter with a relative standard deviation of 33 percent or more. For all models, these large standard deviations are not a result of inadequate data and/or an inadequate model but of cross-correlation and thus overparameterisation. As can be seen from the correlation matrices for the estimated kinetic parameters (Appendix C.5), the highest cross-correlation factors always include the parameter with the highest relative standard deviation: 0.998774 for $(p_{ott,1}, p_{ott,2})$, 0.999762 $(p_{eek,3}, p_{eek,5})$ and 0.99709 for $(p_{mea,1}, p_{mea,2})$.

In the previous section, the quality of the kinetic models was judged on the basis of agreement between model predictions and measurements. Here another quality aspect is considered, viz the agreement between the parameter estimates obtained using data from experiment DT25 on the one hand and those obtained using data from experiment DT26 on the other hand. For this quality aspect, the following measure is used:

$$ss = \left(\underline{p}_{DT25} - \underline{p}_{DT26} \right)^T \left(\text{cov} \left(\underline{p}_{DT25} \right) + \text{cov} \left(\underline{p}_{DT26} \right) \right)^{-1} \left(\underline{p}_{DT25} - \underline{p}_{DT26} \right) \quad [6.7]$$

This measure represents the squared distance between the two sets of parameter estimates obtained with data from DT25 and DT26 over the sum of the (co-)variances of these parameter estimate sets. Therefore, if the kinetic model describes the data adequately and the covariance matrices are exact, this measure will be equal to the sum of np squared variables that have a standard normal distribution. This measure is listed in Table 6.13 for the kinetic models of Ottens, Eek, Ó Meadhra and Gahn. From this quality perspective, Ottens is now the best kinetic model, followed by Ó Meadhra, Eek and Gahn.

Table 6.13: Agreement between parameter sets for the kinetic models of Ottens, Eek, Ó Meadhra and Gahn obtained using data from experiments DT25 and DT26.

	ss	\sqrt{ss} / np	rank
Ottens	542	12	1
Eek	4404	27	3
Ó Meadhra	2311	17	2
Gahn	9306	68	4

If one does not take into account the parameter cross-correlations, i.e. $\text{cov}(i,j) = 0$ for $i \neq j$, a very different ranking of the kinetic models is obtained: 1. Ó Meadhra, 2. Gahn, 3. Ottens and 4. Eek. This illustrates the importance of using the entire

covariance matrix to determine the agreement between parameter sets. The effect of the covariances or the cross correlations on the calculated agreement between the two parameter sets derived using data from DT25 and DT26 is further illustrated by Figure 6.11, which shows the confidence ellipsoids for k_r and Γ_s , two parameters of the Gahn kinetic model, estimated using data from experiments DT25 and DT26.

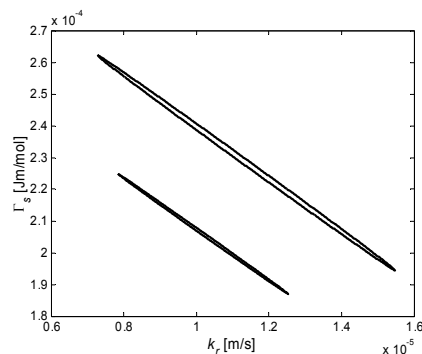


Figure 6.11: Confidence ellipsoids for k_r and Γ_s estimated using data from experiments DT25 and DT26.

These parameters are clearly highly correlated and the confidence ellipsoids corresponding to the two experiments do not overlap. The estimated correlation factor between k_r and Γ_s is -0.999652 for experiment DT25 and -0.999501 for experiment DT26. If these two parameters were not correlated and retained their current standard deviations, the two confidence ellipsoids would be spherical and overlap, thus indicating agreement between the two sets of parameter estimates. This is clearly not the case here, so we should conclude that both experiments clearly give different results. The last section of this Chapter will investigate the origin of this high cross correlation between the two kinetic parameters of the Gahn model. The cross-correlation matrices for the estimated parameters of the kinetic models of Ottens, Eek and Ó Meadhra can be found in Appendix C.5.

Leaving aside the cross correlation between the two kinetic parameters in the Gahn model, there are at least two factors that may result in a disagreement between the parameter sets obtained from DT25 and DT26.

- Firstly, the Gahn model, as opposed to the three other kinetic models, contains a very detailed description of the attrition process related to crystal-impeller collisions. This description is based on the detailed geometry of the impeller and contains no parameters that need to be estimated from the crystallisation experiments. Although this description is theoretically an advantage of the Gahn model over the other kinetic models, it may be a disadvantage here as it is applied for parameter estimation using data from two experiments performed at different impeller frequencies. The reason being that, as can be seen from Figure 6.2, the 22-litre DT crystalliser contains an additional

mechanical attrition source, viz the pump of the external circulation loop. As this additional attrition source is not considered explicitly in the model, the attrition caused by the external circulation pump is in fact attributed to the internal impeller. When fitting the model to the experimental data, the two kinetic parameters, k_r and Γ_s , describing crystal growth (including the outgrowth of attrition fragments) can only account for this additional attrition by assuming different values for the different impeller frequencies. Admittedly, the attrition caused by the internal impeller and external circulation pump is also lumped when using the kinetic model of Ottens, Eek or Ó Meadhra. However, because these models do not rely on an accurate description of the impeller geometry (the models of Eek and Ó Meadhra do not use any description of the impeller) and contain sufficient parameters directly related to the attrition process that are estimated when fitting the experimental data, the kinetic parameters relating to crystal growth are much less affected by the lumping of these two attrition sources. As a result, it is not surprising that the two estimates (DT25 and DT26) for the kinetic parameters relating to crystal growth are in better agreement for the models of Ottens, Eek or Ó Meadhra than for Gahn.

- Secondly, for similar reasons as discussed above, incorrect values of the material properties used in the Gahn model framework, such as the shear modulus, Vicker's hardness, material densities, etc. may also lead to different estimates for the two kinetic parameters, k_r and Γ_s , when fitting the CSD data from the experiments performed at different impeller frequencies. If correct, this argument strengthens the case for including certain material properties in the parameter estimation calculation. Likely candidates, determined in the parameter sensitivity studies (section 6.4.1), are the Vicker's hardness and critical work for indentation.

6.5 PREDICTIVE QUALITY OF THE KINETIC MODELS

This section is concerned with a third approach for determining and comparing the quality of the kinetic models of Ottens, Eek, Ó Meadhra and Gahn. This latest approach considers the agreement between model predictions and measurements of a certain experiment using parameters estimated using data from an independent experiment. In this case, parameter sets determined using 22-litre experiment DT25 will be used to predict the measured CSD transients of an experiment on the same crystalliser at different operating conditions (6.5.1) and of an experiment on a crystalliser of different scale and type (6.5.2). These predictions are not obtained from straightforward simulations but from parameter estimation calculations excluding the kinetic parameters but involving the parameters of the initial size distribution function and the initial supersaturation. This ensures the best possible fit for fixed kinetic parameter values.

6.5.1 DIFFERENT OPERATING CONDITIONS ON THE SAME CRYSTALLISER

The capability of the kinetic models of Ottens, Eek, Ó Meadhra and Gahn to predict (as opposed to fit or describe) the effect of the impeller frequency on the CSD is shown in Figure 6.12. This figure contains model predictions versus measurements for the 10, 50 and 90% quantile trends of two 22-litre DT crystalliser experiments, viz DT25 and DT26, using kinetic parameters estimated on the basis of data from experiment DT25 alone.

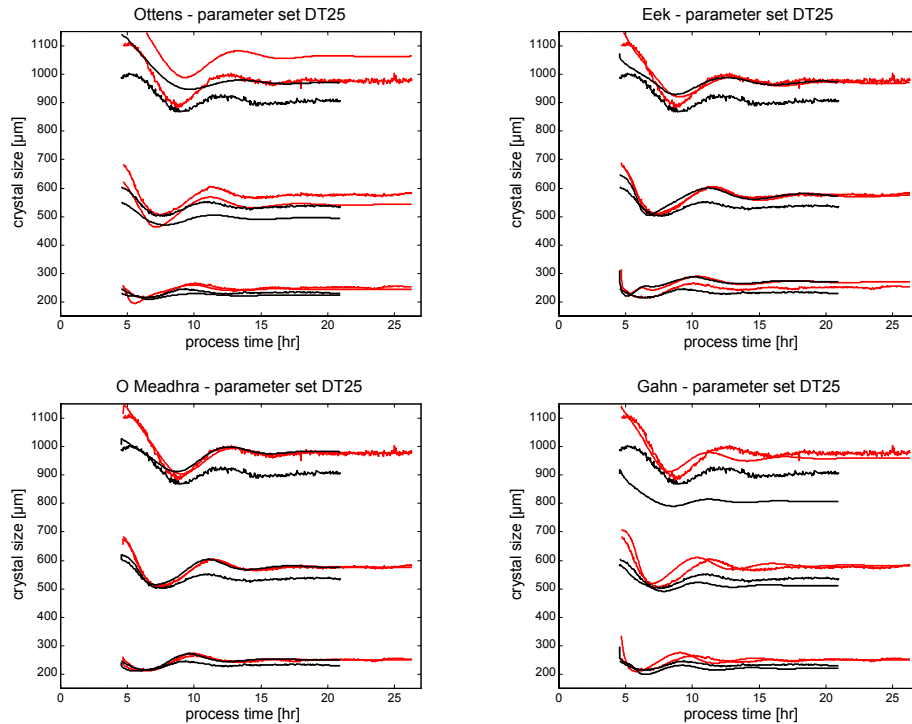


Figure 6.12: Model predictions versus measurements for the L_{10} , L_{50} , and L_{90} of experiments DT25 and DT26 using kinetic parameters estimated from DT25.

Note that of the two experiments DT25 has the longer duration and higher quantile values, and that the smoother trend lines constitute the model predictions.

As one may expect from the structure of their equations, the kinetic models of Eek and Ó Meadhra fail to predict the influence of a change in impeller frequency on the CSD. The slight differences in the predictions of each of these models for experiments DT25 and DT26 are purely a result of different estimates for the initial conditions of these experiments. The models of Ottens and Gahn on the other hand do predict significantly different quantile trends for the two experiments, because they have an intrinsic dependency of the birth rate of

secondary nuclei on the impeller frequency. A more quantitative analysis of the ability of the various kinetic models to capture the effect of the impeller frequency on the CSD is provided by Table 6.14 and Table 6.15. The first of these tables compares the quality of fit for experiment DT26 obtained using kinetic parameters estimated from that same experiment with the quality of fit obtained using kinetic parameters estimated on the basis of experiment DT25. For this comparison the measure defined by Eq. 6.6 and also used in section 6.4.3.1 is employed.

Table 6.14: Quality of fit for experiment DT26 using kinetic parameters estimated from the same experiment DT26 and another experiment DT25.

quantile	using kinetic parameters estimated from same experiment (DT26)				using kinetic parameters estimated from another experiment (DT25)			
	Ottens	Eek	Ó Meadhra	Gahn	Ottens	Eek	Ó Meadhra	Gahn
L_{10}	34	515	6	85	95	1446	312	176
L_{25}	568	20	6	184	855	466	359	81
L_{50}	307	5	2	53	542	431	422	159
L_{75}	23	3	4	70	10	453	369	512
L_{90}	525	6	10	243	361	222	235	694
total	1457	549	28	635	1864	3019	1698	1623

Table 6.15 focuses on the capability of the various kinetic models to predict the effect of the impeller frequency on the steady-state quantile values. For this purpose, the measured quantiles of experiments DT25 and DT26 are compared with the predicted quantiles for these experiments, where both predictions are obtained using kinetic parameter values estimated on the basis of experimental data from DT25 alone:

$$\frac{L_{qq,DT26}(p_{DT25}, t_{f,DT26}) - L_{qq,DT25}(p_{DT25}, t_{f,DT25})}{\tilde{L}_{qq,DT26}(t_{f,DT26}) - \tilde{L}_{qq,DT25}(t_{f,DT25})} \quad \text{where } qq=10,25,50,75,90 \quad [6.8]$$

Using the absolute differences between respectively the two predicted and the two observed quantile values as opposed to the ratios of respectively the predicted and observed values gives this measure two convenient properties. For kinetic models that have no dependency on the impeller frequency this measure will be zero and for kinetic models that correctly predict the absolute change in steady-state quantiles and the measure will equal unity. Note that this measure is an approximation as the observed and predicted quantile trends have not completely reached steady-state at the end of the experiment. This immediately explains why the values listed in Table 6.15 for the kinetic models of Eek and Ó Meadhra are close to zero but not exactly zero. The values listed for the kinetic model of Ottens are closest to unity, thus indicating that this model may be the most suitable kinetic model from a predictive point of view. The fact that the values shown in this table for the kinetic model of Gahn are all considerably larger than unity signals an over prediction of the impeller frequency's influence on the birth rate of secondary nuclei and hence the CSD. The most likely explanation for this

over prediction is the fact that the attrition caused by the (unmodelled) external circulation pump of the 22-litre DT crystalliser is also attributed to the internal impeller (see section 6.4.3.2).

Table 6.15: Capability of the kinetic models to capture the effect of the impeller frequency (as defined by Eq. 6.8). Experiment DT25 versus experiment DT26 using kinetic parameter values estimated on the basis of experiment DT25.

quantile	steady-state			
	Ottens	Eek	Ó Meadhra	Gahn
L_{10}	1.01	0.07	-0.02	1.41
L_{25}	0.91	0.07	-0.01	1.19
L_{50}	1.03	0.05	0.00	1.51
L_{75}	1.09	-0.02	-0.02	1.77
L_{90}	1.36	-0.06	-0.05	2.25
average	1.08	0.02	-0.02	1.63

6.5.2 DIFFERENT OPERATING CONDITIONS ON A CRYSTALLISER OF DIFFERENT TYPE AND SCALE

This section investigates the capability of the kinetic models of Ottens, Eek, Ó Meadhra and Gahn to predict not only changes in the CSD due to changes in impeller frequency but also because of differences in crystalliser type (DT versus DTB) and crystalliser scale (22 versus 1100 litre). To this effect, kinetic parameter values estimated on the basis of measured CSD data of experiment DT 25 are used to predict the CSD transients of two 1100-litre DTB experiments, viz DTB03 and DTB12 (see Table 6.1 and Table 6.3 for the operating conditions).

The 1100-litre DTB crystalliser is modelled using a perfectly mixed compartment for the main body of crystalliser, a zero hold up compartment for the annular zone and a zero hold up compartment with complete dissolution for the fines loop. The classification function for the stream from the main body to the annular zone is calculated using the model equations presented in Chapter 4. A justification for the use of zero hold up compartments and the assumption of complete fines dissolution will be given in Chapter 7.

The model predictions and measurements of the median size trends for the two 1100-litre DTB experiments are shown in Figure 6.13. Although the trends of the 10, 25, 75 and 90 percent quantiles are not shown here, they were taken into account for the estimation of the parameters of the initial size distribution. They are also included in Table 6.16 where the quality of fit measure as defined in Eq. 6.6 is listed for the five quantile trends of experiments DTB03 and DTB12, using the kinetic models of Ottens, Eek, Ó Meadhra and Gahn for the model predictions.

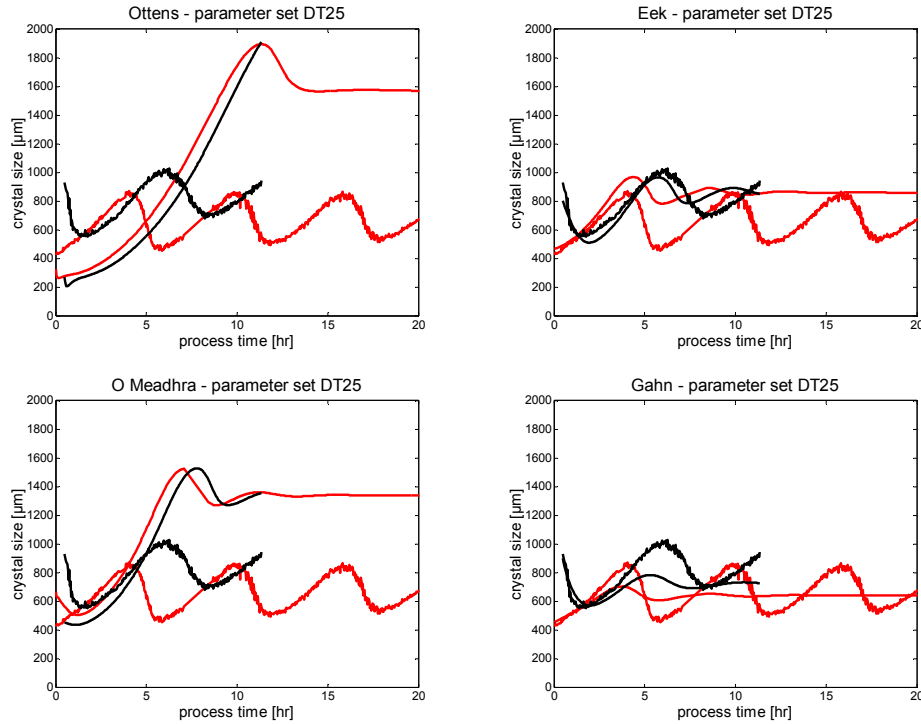


Figure 6.13: Model predictions versus measurements for the median size trends of experiments DTB03 and DTB12 using kinetic parameters estimated from DT25.

Note that of the two experiments DTB03 has the longer duration and lower median sizes, and that the smoother trend lines constitute the model predictions.

Table 6.16: Quality of fit for experiments DTB03 and DTB12 according to measure defined by Eq. 6.6.

quantile	experiment DTB03				experiment DTB12			
	Ottens	Eek	Ó Meadhra	Gahn	Ottens	Eek	Ó Meadhra	Gahn
L_{10}	103146	17614	92917	3762	52584	2256	28624	1711
L_{25}	141414	17640	106471	4096	49862	1989	29325	2023
L_{50}	167892	12114	102880	2631	37751	1021	27239	1705
L_{75}	169790	5033	92539	1466	24055	742	22350	1941
L_{90}	134955	1512	72626	1142	11293	1089	13691	1948
total	717197	53911	467434	13097	175545	7097	121229	9328

From both Figure 6.13 and Table 6.16 it is obvious that the kinetic models of Ottens and Ó Meadhra are completely unable to correctly predict the effect of differences in crystalliser scale and type. Furthermore, as explained and observed in the previous section, the kinetic models of Eek and Ó Meadhra do not predict any influence of the impeller frequency on the CSD. Of the four kinetic models

investigated in this chapter, the Gahn kinetic model is clearly the only one capable of a reasonable prediction of the CSD as a function of crystalliser type, crystalliser scale and operating conditions.

Nevertheless, the Gahn kinetic model exhibits one significant shortcoming in this specific study: the inability to predict the very pronounced and in some cases even sustained oscillations of the product CSD in the 1100-litre DTB crystalliser, when using kinetic parameters obtained from an experiment performed on a 22-litre DT crystalliser. At this stage it is not clear whether this inability is a result of the uncertainties surrounding the parameter estimates (see section 6.4.3.2), an incorrect prediction of the fines classification function or whether it is intrinsic to the kinetic model. To analyse the first possible cause, Monte Carlo simulations of the 1100-litre DTB crystalliser were performed to study the dynamic behaviour for various random combinations of values for the two kinetic parameters of the Gahn model (see Appendix C.7). In the same appendix results are shown of dynamic simulations performed with a fixed set of kinetic parameter values but varying cut sizes for the fines classification function. These results do not reject the hypothesis that the Gahn kinetic model cannot describe the CSD oscillations observed in the 1100-litre DTB crystalliser. One aspect of the Gahn kinetic model that merits further investigation is the influence that the physical and material properties determined from independent (i.e. non-crystallisation) experiments, such as the diffusion coefficient, critical work for indentation and Vicker's hardness, may have on the CSD dynamics. If this investigation were not to lead to the Gahn kinetic model being capable of describing pronounced and sustained oscillations, it should be concluded from the 1100-litre DTB crystallisation experiments that the crystallisation model framework presented in Chapter 4 needs revision. The most likely candidate for improvement of this model framework is the inclusion of primary nucleation.

6.6 DESIGN OF EXPERIMENTS

So far, this chapter has mainly been concerned with the use of models for processing experimental data in the light of parameter estimation and model validation. In the final section of this chapter, the focus is on the use of models to guide the experimental programme, i.e. the design of experiments. As design of experiments is ultimately a model-based activity, the outcome depends largely on the model parameters. Although these often need to be estimated more precisely using information from the designed experiments, reasonable parameter values are required for a meaningful design of experiments.

The objective of an experiment design activity is to maximise the information content from experiments in order to discriminate between alternative models or to maximise parameter precision for a selected model. In order to achieve this goal there are two classes of decision variables for which optimal values need to be determined, viz sensors (what to measure, where and when) and controls (initial conditions, duration of control intervals and values for each interval).

Model discrimination versus parameter precision

The main difference between design of experiments for model discrimination and parameter precision is the formulation of the objective function. The aim in experiment design for model discrimination is to maximise the difference between the alternative models' predictions for the variables that will be measured in the designed experiment(s). For example, to discriminate between two crystallisation models on the basis of quantile measurements the objective function could be as follows:

$$\max_{x(0), t_f, \tau_I, u(t), v, \rho} \left\{ \sum_{qq} \sum_{k=1}^{nm} \left[\frac{(L_{qq,k,\text{model A}} - L_{qq,k,\text{model B}})^2}{\sigma_{L_{qq,k}}^2} \right] \right\} \quad [6.9]$$

where	$x(0)$	initial conditions of the experiment.
	t_f	duration of experiment.
	τ_I	duration of control intervals.
	$u(t)$	time varying controls
	v	time-invariant controls
	$L_{qq,k}$	k^{th} prediction for the qq percent quantile
	$\sigma_{L_{qq,k}}^2$	variance of the k^{th} prediction for the qq percent quantile
	qq	indices relating to used quantiles, viz 10, 25, 50, 75 and 90 percent quantile

The objective of experiment design for parameter precision is to minimise some function of the variance-covariance matrix, V . Three frequently used functions refer to respectively A, D and E-optimality and correspond to respectively the trace, determinant and largest eigenvalue of the variance-covariance matrix.

Influence of measurement selection on parameter statistics

Models can also be used to address questions such as 'to what extent is the cross-correlation between the two kinetic parameters of the Gahn model intrinsic of the kinetic model and to what extent does it depend on the choice and quality of measurements?' This purpose can be served by performing parameter estimation using various combinations of simulated measurements, with and without superimposed randomly distributed noise. This approach is illustrated here for the two main parameters of the Gahn kinetic model using measurements for the supersaturation and a number of quantiles. The ideal measurements were obtained by simulating a 22-litre DT crystalliser using the operating conditions listed in Table 6.1 and the material property and kinetic parameter values shown in Table 6.5. The measurements with noise were generated by superimposing normally distributed noise with a relative standard deviation of five and seven percent for respectively the quantile and supersaturation measurements. The results of the parameter estimation calculations using various combinations of measured quantities are presented in Table 6.17 and Figure 6.14. As expected, the determinant of the variance-covariance matrix, a measure for the area of the parameters' confidence ellipsoid, increases when noise is added to the measurements. More interesting results are the fact that (i) a supersaturation measurement contains more information than four additional quantile measurements and (ii) a median size measurement on its own contains more

information than a supersaturation measurement on its own. In fact, all attempted parameter estimation calculations using only a supersaturation measurement failed to converge. Finally, the confidence ellipsoids in Figure 6.14 clearly show that the supersaturation measurement strongly determines the value of the rate constant for surface integration, k_r , whereas the shape of the crystal size distribution is strongly linked to the condition of deformation, Γ_s .

Table 6.17: Parameter estimation results obtained with simulated dynamic data excluding and including normally distributed noise. A smaller value for $\ln(\det|\text{variance matrix}|)$, a measure for the volume of the parameters' confidence ellipsoid, indicates a better estimate.

measured quantities	excluding noise		including noise	
	correlation	$\ln(\det \text{variance}$	correlation	$\ln(\det \text{variance}$
	factor between	matrix)	factor between	matrix)
	k_r and Γ_s		k_r and Γ_s	
$L_{10}, L_{25}, L_{50}, L_{75}, L_{90}$ and σ	-0.8201	-87.15	-0.9012	-61.55
L_{50} and σ	-0.1809	-85.05	-0.4635	-59.51
$L_{10}, L_{25}, L_{50}, L_{75}$ and L_{90}	-0.9990	-81.86	-0.9989	-56.85
L_{10}, L_{50} and L_{90}	-0.9987	-81.31	-0.9988	-56.28
L_{50}	-0.9999	-75.26	-0.9998	-50.75
σ	-	-	-	-

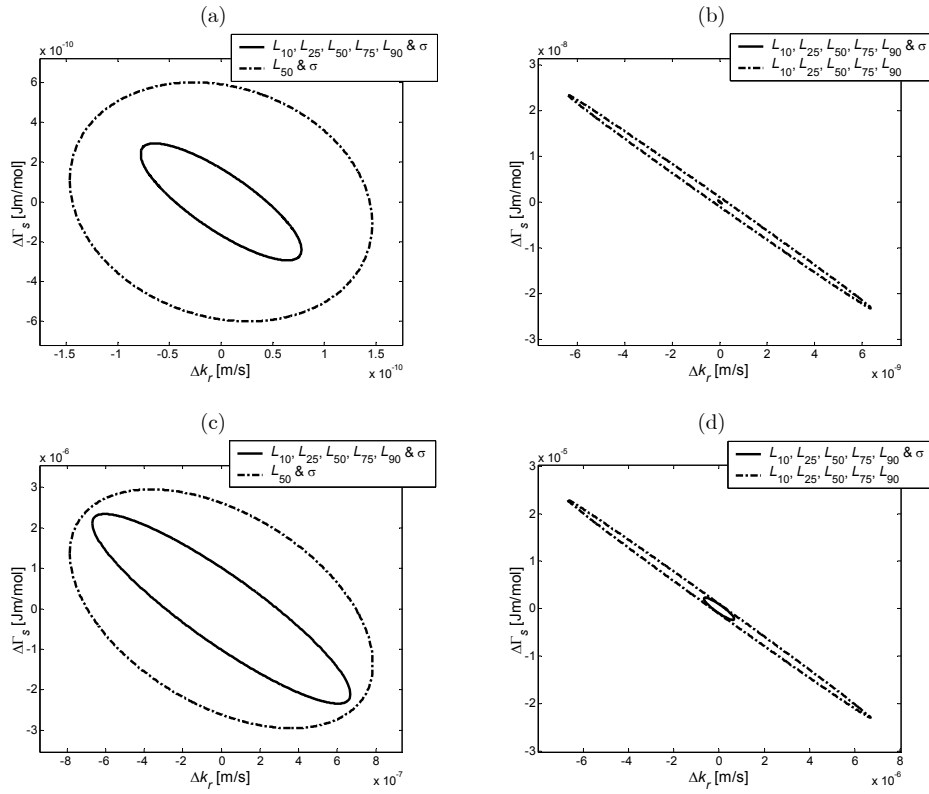


Figure 6.14: Confidence ellipsoids for k_r and Γ_s estimated using simulated dynamic data excluding (a, b) and including (c, d) normally distributed noise corresponding to different combinations of sensors (see legends).

6.7 CONCLUSIONS AND RECOMMENDATIONS

A detailed crystallisation modelling framework and comprehensive data of CSD transients have been successfully combined to estimate the parameters of the Gahn kinetic model presented and implemented in respectively Chapters 4 and 5. In order to provide a reference frame for determining the quality of the Gahn model, the same modelling framework and data were used to estimate the parameters of three other kinetic models, viz the models of Ottens, Eek and Ó Meadhra. The quality of these four kinetic models was compared from three different perspectives:

1. Descriptive value, i.e. agreement between model predictions and measurements for the actual parameter estimation calculation. The kinetic models of Ó Meadhra and Ottens are respectively the best and worst from this perspective.

2. Agreement between the parameter estimation sets obtained from two independent parameter estimation calculations using data from respectively experiments DT25 and DT26. The best agreement is seen for the Ottens kinetic model, while the worst agreement is seen for the Gahn kinetic model. To perform this test properly, it is essential to take into account both the variances and covariances. If only the variances are considered, a very different ranking is obtained for the four kinetic models.
3. Predictive value, i.e. agreement between model predictions and measurements for experiments other than the experiment used to estimate the unknown model parameters. The kinetic models of Eek and Ó Meadhra are both completely incapable of predicting the influence a change in impeller frequency has on the CSD. This is a direct result of the secondary nucleation rate expressions in these kinetic models not having any dependency on the impeller frequency. As regards predictive capabilities with respect to differences in crystalliser scale and type, the kinetic models of Ottens and Ó Meadhra fail to produce predictions that would even approximate the measurements. The models of Eek and Gahn do give a reasonable agreement between measurements and predictions as regards the time-averaged median size, but fail to predict the sustained oscillations that are observed in the experiments.

Based on the outcome of these three tests, it is concluded that the model of Ó Meadhra has the best descriptive value for this crystallisation system, thus making it an interesting candidate for control purposes. The model of Gahn on the other hand exhibits the best predictive capabilities with respect to both changes in crystalliser scale/type and impeller frequency, thus confirming its selection in Chapter 4, which was based purely on theoretical reasoning, as the best model currently available for design purposes.

Furthermore, there are clear opportunities for improving the descriptive and predictive capabilities of the Gahn kinetic model. Firstly, it is suggested to estimate certain 'known' model parameters of the Gahn model in addition to the two kinetic parameters currently estimated, viz the rate constant for surface integration, k_s , and the condition of deformation, F_s . Obvious candidates, based on the results of parameter sensitivity studies, are material properties such as the critical work for indentation, W_C , and the Vicker's hardness, H . Secondly, it is proposed to extend the kinetic model with primary nucleation. If this mechanism were to prove dominant during continuous operation, it may help describe the observed sustained oscillations of the CSD, as primary nucleation rates typically have a high order supersaturation dependency.

Finally, considering the significant human effort and economic cost associated with the crystallisation experiments, it is well worth employing crystallisation process models *before* conducting these experiments, i.e. for experiment design purposes. Crystallisation process models can be used to either estimate whether

an additional measurement will provide significant additional information and/or to determine the control profiles that lead to the experiment with the highest information content. For instance, in the case of the Gahn model, it is shown that measurements of the width of the CSD and of the supersaturation contribute to an increase in accuracy of the estimates for respectively the condition of deformation, I_s , and the rate constant for surface integration, k_v .

7 OPTIMAL DESIGN

The first part of this chapter concerns the compartmental modelling of the UNIAK 1100-litre DTB crystalliser and a 360 m³ DTB crystalliser. For this purpose, the various compartmental models presented in Chapter 4 are employed. The resulting simulations provide a general indication of the importance of (i) the use of real dissolution kinetics as opposed to the assumption of complete dissolution for the fines removal system of a DTB crystalliser, (ii) taking into account the hold-up of the annular zone, (iii) compartmentation of the crystalliser main body, and (iv) the modelling of internal classification. The results of these simulations also serve to justify the compartmental models used in Chapter 6 to describe the 22-litre DT and 1100-litre DTB crystalliser for parameter estimation and model validation purposes.

The second part of this chapter is concerned with the generation of optimal crystalliser designs. For this purpose, standard mathematical optimisation techniques are used that allow a flexible formulation of constraints and an objective function. The design problem considered here involves a DTB crystalliser for the crystallisation of ammonium sulphate from water with a production capacity of 94 kton per annum. The optimisation problem relates to steady-state process behaviour only and involves an economic objective function comprising capital and operational costs, four inequality constraints and five continuous decision variables. The constraints include both product quality related constraints and operational constraints, whereas the decision variables relate to both design and operational aspects.

7.1 INTRODUCTION

The final chapter of this thesis will address three questions. Firstly, having discussed the need for compartmental modelling and introduced a variety of compartmental models in Chapter 4, why were only a single and a two-compartment model used in Chapter 6 to describe the UNIAK 22-litre DT and 1100-litre DTB crystalliser? Secondly, under what circumstances are more detailed compartmental models required? Finally, having estimated the unknown model parameters in Chapter 6, how can the crystallisation modelling framework presented in Chapter 4 be applied for design purposes?

7.2 COMPARTMENTAL MODELLING

In Chapter 4, compartmental modelling was selected as the modelling approach to achieve a separation between kinetics and overall hydrodynamics. This separation is seen as one of the major requirements for the development of process models with sufficient predictive capabilities for design purposes. However, the predictive quality of a multi-compartment crystallisation process model does not only depend on the quality of the single compartment model, in particular that of the

kinetic model, but also on the structure of the compartmental model. This structure is characterised by parameters such as the number of compartments, the size of the compartments, and the exchange rates between the compartments. Obtaining correct values for these parameters is thus a key issue in compartmental modelling. To this effect, a compartmentation procedure was developed in Chapter 4. As this procedure contains many steps of a heuristic nature, it is advisable to check the validity of the resulting compartmental model. Due to the lack of significantly accurate experimental data and an uncertainty with respect to the quality of the employed kinetic model, this validation is performed by simulating the crystalliser of interest with various compartmental models and comparing the resulting numerical solutions. In a similar way a number of other modelling issues are investigated in this chapter:

- The use of real dissolution kinetics versus a complete dissolution assumption for the fines removal system of a DTB crystalliser.
- The effect of taking into account the hold-up of the annular zone.
- The modelling of internal classification.

Whether a given compartmental model, use of the complete fines dissolution assumption, not modelling the hold-up in the annular zone and/or neglecting internal classification are valid for a certain crystalliser type and scale depends both on the chemical system and the operating conditions. Here we will limit ourselves to the crystallisation of ammonium sulphate from water, for which we will use the modelling framework presented in Chapter 4 including the Gahn kinetic model. For this system two crystallisers will be investigated, viz the UNIAK 1100-litre DTB crystalliser and a 360 m³ DTB crystalliser. Both crystallisers are simulated for two different impeller frequencies. Information on the various compartmental model configurations used to simulate these two crystallisers can be found in Table 7.1 and the references contained within this table.

Table 7.1: The various compartmental model configurations used to simulate the 1100-litre and 360 m³ DTB simulations.

configuration	A	B	C	D	E	F	G
compartmental model according to:	Figure 4.2	Figure 4.2	Figure 4.2	Figure 4.3	*	Figure 4.4	Figure 4.3
compartment numbers, location and volumes according to:	Table D.1	Table D.2	Table D.3	Table D.4	Table D.5	#	Table D.4

* see Figure 6 in Bermingham et al. (2000); # see ten Cate et al. (2000)

By comparing simulation results obtained with the different compartmental models listed in Table 7.1, the importance of modelling certain phenomena and further compartmentation can be assessed for a given crystalliser and set of operating conditions (see Table 7.2). For instance, if there is no significant difference between the numerical solutions obtained using compartmental models

D and G, it can be concluded that an adequate description of the crystalliser under investigation does not require the use of internal classification functions.

Table 7.2: Compartmental model configurations used to illustrate a certain effect. Letters in second column refer to a configuration in Table 7.1.

effect of using real dissolution kinetics vs complete dissolution assumption	A vs B
effect of taking into account the hold-up of the annular zone	B vs C
effect of describing the main body with multiple compartments (4)	C vs D
effect of describing the main body with multiple compartments (10)	C vs E
effect of describing the main body with multiple compartments (20)	C vs F
effect of internal classification	D vs G

7.2.1 UNIAC 1100-LITRE DTB CRYSTALLISER

For the simulations of the UNIAC 1100-litre DTB crystalliser, impeller frequencies of 320 and 370 rpm are used, which correspond to the settings of experiments DTB12 and DTB03 respectively. The other settings used for these simulations are shown in Table 7.3.

Table 7.3: Settings (top half) and selected characteristic quantities (lower half) of the 1100-litre DTB simulations.

	DTB12	DTB03
volume crystalliser main body [l]		1100
volume annular zone [l]		900
volume fines dissolution loop [l]		240
diameter crystalliser main body [m]		0.7
diameter annular zone [m]		1.0
feed temperature [°C]		50
feed density [kg·m ⁻³]		1248
crystalliser temperature [°C]		50
volume specific heat input [kW·m ⁻³]		120
product residence time [s]		4500
impeller frequency [rpm]	320	370
fines flow rate [l·s ⁻¹]		2
impeller specific power input [W·kg ⁻¹]	1.5	2.3
internal circulation velocity [m·s ⁻¹]	1.0	1.2
crystalliser turnover time [s]	5.6	4.9
product flow rate [l·s ⁻¹]		0.244
fines flow rate over product flow rate [-]		8.2
fines residence time in main body [s]		550
superficial upward velocity in annular zone [m·s ⁻¹]		2.6·10 ⁻³
cut size of fines classification [µm]		80
fines residence time in dissolution loop [s]		120

Appendix D.1.2 contains the simulation results for the 1100-litre DTB crystalliser operated at the settings listed in Table 7.3. This appendix shows the evolution of the crystal size distribution obtained with each compartmental model configuration listed in Table 7.1 in order to show the incremental effect of the various modelling assumptions and compartmentation resolutions. Figure 7.1 presents the combined effect of these assumptions and differing numbers of compartments for the crystalliser main body on the predicted CSD evolution.

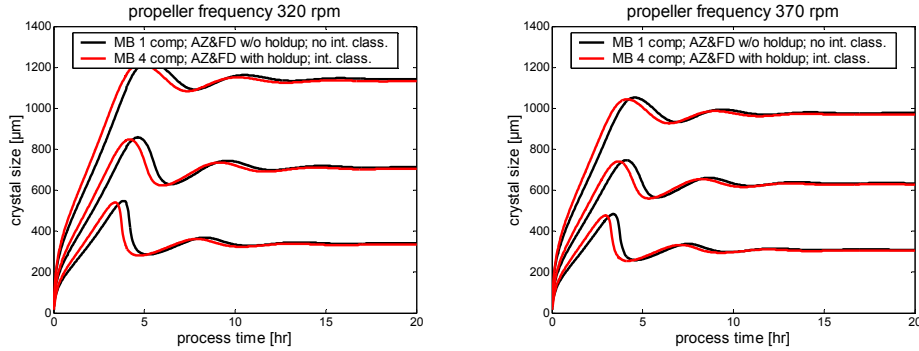


Figure 7.1: 1100-litre DTB crystalliser simulations illustrating the combined effect on the predicted CSD transient of (i) using real dissolution kinetics versus complete dissolution assumption, (ii) taking into account the hold-up of the annular zone and (iii) describing the main body with multiple compartments.

As can be seen from Figure D.1 through Figure D.4 in Appendix D.1.2, taking into account the hold-up in the annular zone, compartmentation of the main body and the modelling of internal classification have no visible effect on the predicted evolution of the CSD in this 1100-litre DTB crystalliser. The most important effect is the use of dissolution kinetics as opposed to the assumption of complete dissolution for the fines loop of this crystalliser. Although compartmentation of the main body does result in a spatial supersaturation profile (see Table D.6 through Table D.8 in Appendix D.1.2), it hardly affects the predicted CSD.

7.2.2 A 360 m³ DTB CRYSTALLISER

Bermingham et al. (2000) presented a large number of simulations of a 360 m³ DTB crystalliser, of which the dimensions were obtained by scaling up from the UNIAK 1100-litre DTB crystalliser. The first set of dimensions for the main body, annular zone and fines dissolution loop of this large scale DTB crystalliser was determined by keeping constant the product residence time, residence time of fines in the main body, superficial velocity in the annular zone and residence time of fines in the dissolution loop. However, these scale-up rules led to a very large annular zone and fines dissolution loop. As a result, other sets of dimensions were generated by among others increasing the superficial velocity in the annular zone and decreasing the residence time of the fines in the dissolution loop. The effects

of these changes in dimensions on the crystal size distribution are presented stepwise by Bermingham and co-workers. Although their final configuration for a 360 m³ DTB crystalliser possesses reasonable dimensions for the annular zone and dissolution loop, it is operated at a lower product residence time (4500 s) and lower solids concentration (10%) than is typical in practice for large-scale ammonium sulphate DTB crystallisers; see for example Mersmann and Rennie (1995). It was therefore decided to generate a new set of dimensions and operating conditions for a 360 m³ DTB crystalliser that will result in a solids concentration of approximately 20 percent, a product residence time in the order of 10 hours, whilst satisfying constraints related to vapour release velocities, crystal growth rates and temperature increase of the fines stream (see 7.3.1.2). The resulting set of dimensions and operating conditions that will be used for the simulations with the various compartmental models is presented in Table 7.4.

Table 7.4: Settings (top half) and selected characteristic quantities (lower half) of the 360 m³ DTB simulations.

	$v_{ax}=0.5 \text{ m}\cdot\text{s}^{-1}$	$v_{ax}=1.0 \text{ m}\cdot\text{s}^{-1}$
volume crystalliser main body [m ³]		360
volume annular zone [m ³]		102
volume fines dissolution loop [m ³]		3
diameter crystalliser main body [m]		4.8
diameter annular zone [m]		6.3
feed temperature [°C]		50
feed density [kg·m ⁻³]		1248
crystalliser temperature [°C]		50
volume specific heat input [kW·m ⁻³]		30
product residence time [s]		36000
impeller frequency [rpm]	23	47
fines flow rate [m ³ ·s ⁻¹]		0.33
impeller specific power input [W·kg ⁻¹]	0.03	0.22
internal circulation velocity [m·s ⁻¹]	0.5	1.0
crystalliser turnover time [s]	77	39
product flow rate [m ³ ·s ⁻¹]		0.01
fines flow rate over product flow rate [-]		33
fines residence time in main body [s]		1100
superficial upward velocity in annular zone [m·s ⁻¹]		$2.6\cdot 10^{-2}$
cut size of fines classification [µm]		340
fines residence time in dissolution loop [s]		10

Appendix D.1.3 contains the simulation results for the 360 m³ DTB crystalliser operated at the settings listed in Table 7.4. This appendix shows the evolution of the crystal size distribution obtained with each compartmental model configuration listed in Table 7.1 in order to show the incremental effect of the various modelling assumptions and compartmentation resolutions. Figure 7.2

presents the combined effect of these assumptions and differing numbers of compartments for the crystalliser main body on the predicted CSD evolution. Analogue to the 1100-litre DTB crystalliser, the most significant effect is the use of dissolution kinetics as opposed to assuming complete dissolution in the fines loop. However, in contrast to the smaller scale DTB crystalliser, the effect of taking into account the hold-up in the annular zone, compartmentation of the main body and the modelling of internal classification are all clearly visible.

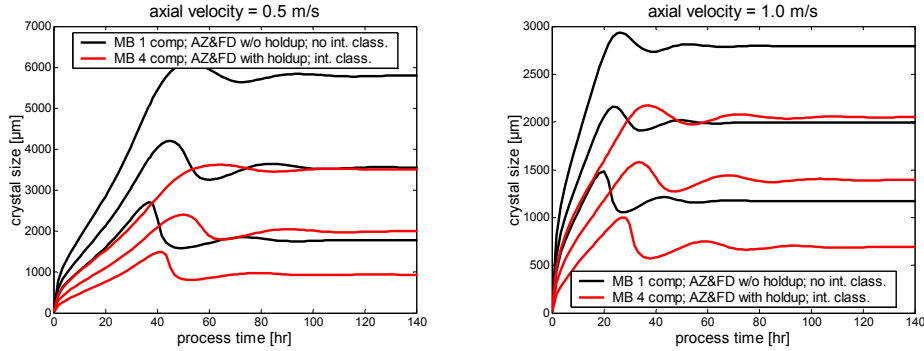


Figure 7.2: 360 m³ DTB crystalliser simulations illustrating the effect on the predicted CSD transient of (i) using real dissolution kinetics versus complete dissolution assumption (top) and (ii) taking into account the hold-up of the annular zone (bottom).

7.2.3 DISCUSSION AND CONCLUSIONS

Modelling the kinetics of crystal dissolution instead of following the conventional assumption of complete dissolution, to describe the behaviour of the fines destruction system of a DTB crystalliser is the most significant modelling improvement for the crystallisation of ammonium sulphate from water.

For the 1100-litre DTB crystalliser this is the only aspect of compartmental modelling that has a visible effect on the predicted evolution of the CSD. Other aspects such as taking into account the hold-up of the annular zone, the use of multiple compartments for the main body and internal classification had little effect on the model predictions. Apparently, the time-delay effect of taking into account the annular zone's hold-up is negligible. The fact that the use of multiple compartments for the main body is of little importance, is not surprising since the half-time for supersaturation decay for this crystallisation system is in the range of 30 to 80 seconds (Bermingham et al., 1998), which is an order of magnitude larger than the turnover time (approximately five seconds, see Table 7.3) in the 1100 litre DTB crystalliser. This is the same engineering rule of thumb used in step four of the compartmentation procedure presented in Chapter 4 to decide upon further subdivision of compartments to account for internal supersaturation gradients. Finally, the effect of internal classification is insignificant due to the relatively high circulation velocities, the low density difference between the solid

and liquid phase, and the relatively low average crystal size. Based on the results of the modelling studies presented here for the 1100-litre DTB crystalliser and 22-litre DT crystalliser, it is considered justified to use respectively a two compartment and single compartment model to describe these crystallisers.

For the 360 m³ DTB crystalliser, all aspects of compartmental modelling that were investigated in this chapter have a visible effect on the predicted evolution of the CSD. Taking into account the kinetics of the fines dissolution again has the most significant effect. The influence of modelling the hold-up in the annular zone is believed to be a result of taking into account the additional time available for growth of crystals that are in the size range corresponding to those crystals that are on the borderline of surviving the fines destruction system due to a limited dissolution time and/or driving force. As the turnover time of this large-scale crystalliser (see Table 7.4 is of the same order of magnitude as the half-time for supersaturation decay, compartmentation of the main body expectedly results in the prediction of an internal supersaturation gradient. However, it is thought that the main effect of this gradient on the predicted CSD is through the level of supersaturation in the fines removal stream. This hypothesis is based on the observation that the kinetic model employed for the simulation studies presented in this chapter, which concern the crystallisation of ammonium sulphate from water, does not contain any phenomena whose kinetics are not roughly first order in the supersaturation. To confirm or reject this hypothesis it is proposed to predict the CSD evolution of this crystallisation system when employing a DT crystalliser of a similar scale. The reason for the sensitivity of the predicted product CSD for the supersaturation level of the stream entering the annular zone and subsequently the fines dissolution loop, is the fact that the fines dissolution system of this 360 m³ crystalliser is operated far away from the complete dissolution assumption. As a result, small changes in the supersaturation of the fines stream entering the dissolution loop can significantly affect the degree of fines dissolution and thus the product CSD. However, if the recommendations made in Chapter 6 are followed and primary nucleation is included for the description of this crystallisation system, compartmentation will also affect the predicted product CSD directly as a result of the presence of internal supersaturation gradients. The increased importance of internal classification with respect to the 1100-litre DTB crystalliser is primarily related to the lower axial velocities and to a lesser extent to the increased average crystal size.

Finally, some general conclusions with respect to compartmental modelling. Whether a compartmental model is valid for a certain crystalliser depends on:

- Its scale – most effects of the various compartmental modelling aspects studied in this chapter are more visible on a larger scale
- Employed operating conditions – for instance, internal classification has a visible effect on the predicted CSD of the 360 m³ DTB crystalliser when operated with an axial velocity of 0.5 m·s⁻¹ but not with an axial velocity of 1.0 m·s⁻¹.

- Crystallisation system – mainly via the dominant crystallisation kinetics of the crystallisation system as these determine factors such as the half-time for supersaturation depletion and how strongly supersaturation gradients will effect the predicted CSD. If all dominant mechanisms are taken into account and their kinetics possess more or less a first-order dependency on the supersaturation, supersaturation gradients do not have to be accounted for in great detail. However, if primary nucleation were important but omitted, the importance of a spatial supersaturation profile would not be acknowledged, thus possibly leading to false conclusions with respect to the need for further compartmentation of the main body.

7.3 OPTIMAL DESIGN OF A CONTINUOUS PROCESS

In Chapter 6 the unknown parameters were estimated and the predictive value with respect to crystalliser scale and type was investigated for four different kinetic models. The Gahn model emerged from this study as the most promising kinetic model for improving the design and operation of processes for the crystallisation of ammonium sulphate from water, a crystallisation process dominated by secondary nucleation and growth. Using this kinetic model in combination with the crystallisation process modelling framework presented in Chapter 4, the time-averaged median crystal size obtained from a continuously operated 1100-litre DTB crystalliser was predicted within a margin of 20 percent using parameters estimated on the basis of CSD measurements obtained from a continuously operated 22-litre DT crystalliser. However, the model failed to predict the sustained oscillations of the CSD exhibited by the 1100-litre DTB crystalliser during undisturbed operation. Consequently, it was considered appropriate to use the crystallisation process modelling framework developed in this thesis in combination with the Gahn kinetic model for model-based steady-state design of continuously operated crystallisation processes. The dynamic characteristics including controllability of the design process are thus ignored for the time being, but should be included in future studies (after improving the predictive capabilities of the crystallisation process model with respect to process dynamics).

The remainder of this chapter illustrates the application of the crystallisation modelling framework for design purposes. To this effect, we will successively have a look at the problem formulation (i.e. possible objective functions, inequality constraints and decision variables), the use of simulations to explore the design space and to motivate the use of mathematical methods for optimisation, and finally the actual optimal design calculations. For both the simulations and optimisations, compartmental model C (Table 7.1) is used, which consists of three compartments: one for the main body, one for the annular zone and one for the fines dissolution loop. As the use of this compartmental model involves ignoring the effect of internal classification and of spatially distributed process variables in

the main body, the resulting optimal designs should be verified with more detailed compartmental models.

7.3.1 PROBLEM FORMULATION

The first design specification is the production of 94 kton·annum⁻¹ ammonium sulphate through evaporative crystallisation from water. Assuming 300 operating days per year, this implies a crystal mass flow from the crystalliser of 3.61 kg·s⁻¹. The product solids concentration should be 20 vol%, a higher concentration is expected to significantly increase the chance of blockages in piping, while a lower concentration will require a larger crystalliser volume to provide the same product residence time and thus lead to increased capital costs for this process. Finally, the process will be designed to operate at 50°C with a saturated feed of the same temperature. The abovementioned production rate, solids concentration and temperature, require a crystalliser feed flow rate of 17.8 kg·s⁻¹ and a heat input of 11 MW as can be seen from the overall mass and energy balance shown in Figure 7.3. Note that the crystalliser feed consists of fresh mother liquor and mother liquor returned from the S/L separation downstream of the crystalliser. The feed to the crystallisation plant as a whole will therefore be of the order of 8 kg·s⁻¹, the exact amount depending on the amount of mother liquor that adheres to the crystalline product.

Taking these flow rates and heat input as a start, the objective is to use mathematical, model-based optimisation techniques to obtain the economically most attractive design that satisfies both product quality related constraints and operational constraints, whereas the decision variables relate to both design and operational aspects.

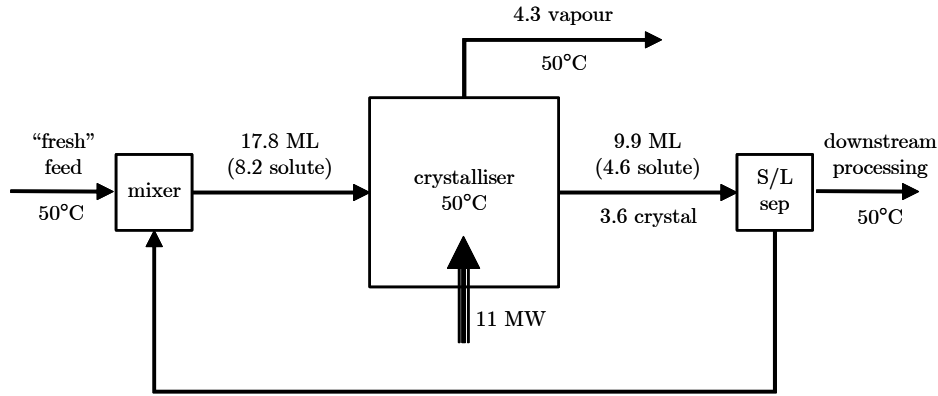


Figure 7.3: Overall mass and energy balance for design study
(numbers without engineering units denote mass flow rates in $\text{kg}\cdot\text{s}^{-1}$).

7.3.1.1 Objective

The objective of the design problem is to minimise or maximise a certain function of product and/or process performance criteria. For this case study three objective functions are considered, viz minimise costs of the process, minimise the median crystal size or maximise the median crystal size. The latter two are simply aimed at determining the attainable region. The economic objective function consists of capital expenditure (CAPEX) and operational expenditure (OPEX), and is described in detail in Appendix D.2.

7.3.1.2 Inequality constraints

Product quality related constraints

The most prominent quality characteristics of a crystalline product are its lattice structure, morphology and size distribution as discussed in Chapter 2. As the crystallisation process modelling framework used for this design study does not relate equipment design variables and operational variables to the resulting lattice structure and morphology, the size distribution is the most important product quality related constraint for this design study. Here the median crystal size is used.

A second quality characteristic that is considered here is the crystal purity. A constraint on this characteristic can be formulated indirectly via the crystal growth rate. Imposing a maximum growth rate ensures regular incorporation of building blocks in the crystal lattice, thus resulting in an acceptable, low impurity content.

Operational constraints

In order to prevent flashing of the fines flow on return to the crystalliser main body, an upper limit is imposed on the temperature increase in the fines dissolution loop. From a physical point of view, the value for this limit depends among others on the hydrostatic pressure at the fines return location in the crystalliser main body. Here simply a value of 20°C is used for all configurations.

A second operational constraint is aimed at preventing the entrainment of liquid droplets into the condenser zone. This requires a minimum cross-sectional area for a given vapour flow. This constraint is imposed by forcing the superficial vapour velocity to be less than a maximum value calculated using the following formula (van Rosmalen et al., 1997):

$$v_{vap,max} = 0.0244 \sqrt{\frac{\rho_{liq} - \rho_{vap}}{\rho_{vap}}} \quad [7.1]$$

7.3.1.3 Decision variables

Both design and operational variables are used as decision variables for the optimal design problem (see Table 7.5). The main design variables that are present in the process model but not considered here, relate to more detailed aspects of the geometry, such as the crystalliser's height over diameter ratio and the impeller geometry including the clearance with the draft tube. These variables are all deduced from the 1100-litre DTB crystalliser geometry.

Table 7.5: Decision variables for the optimal design problem.

decision variable	lower bound	default value	upper bound
product residence time in main body [hr]	1.4	9.1	14
axial velocity in draft tube induced by impeller [m·s ⁻¹]	0.5	1.0	1.5
fines flow rate over product flow rate [-]	5	14.7	100
superficial upward velocity in annular zone [m·s ⁻¹]	0.002	0.14	0.5
fines residence time in dissolution loop [s]	5.0	35	1000

All decision variables taken into account for the design of a single crystalliser are of a continuous nature. Later in this chapter the design problem formulation will be extended to include the question ‘what is the economically optimal number of crystallisers in parallel to meet the production capacity and satisfy the various constraints?’. This introduces an integer decision variable, which is not handled by the mathematical optimisation algorithm and therefore requires user intervention.

7.3.2 EXPLORING THE DESIGN SPACE

Before initiating large-scale optimisation calculations, it is useful to explore the design space manually by means of simulations and/or smaller optimisation problems with less decision variables and constraints. Here, homotopy is used to study the steady-state response of the median crystal size as a function of one of the decision variables. During these homotopy simulations the four remaining decision variables are kept at the default values listed in Table 7.5.

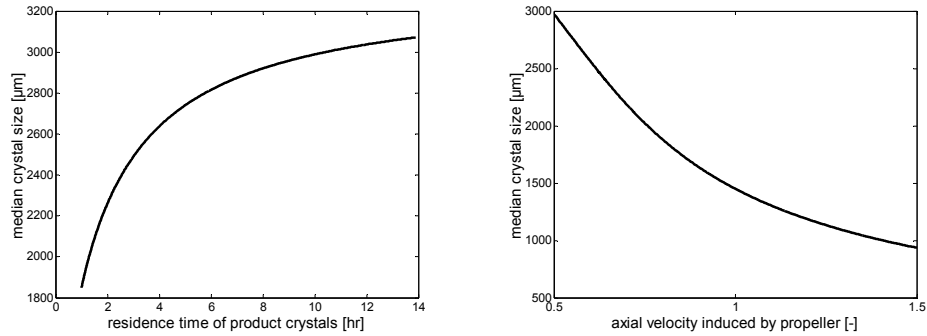


Figure 7.4: Steady-state response of the median crystal size as a function of the product residence time (left) and the axial velocity induced by the impeller (right).

As expected, the steady-state median crystal size exhibits a monotonous increase and decrease as a function of respectively the product residence time and actual velocity. It is worth noting that the relationship between median crystal size and product residence time is far from linear: increasing the product residence time by a factor of 10 only increases the median crystal size by 60 percent.

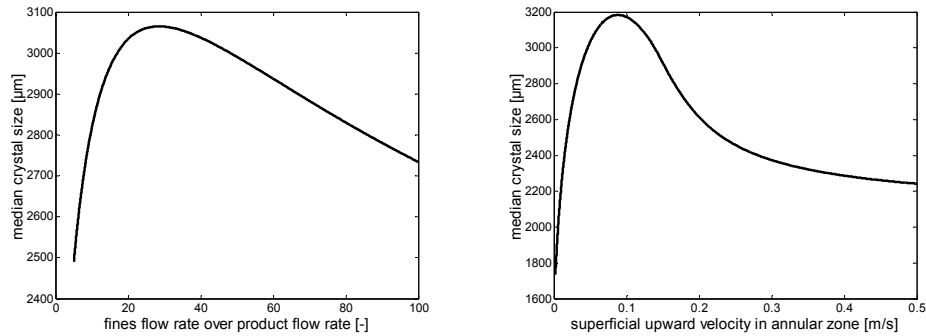


Figure 7.5: Steady-state response of the median crystal size as a function of the ratio of the fines flow rate over the product flow rate (left) and the superficial upward velocity in the annular zone (right).

The effect of the fines flow rate and upward velocity in the annular zone on the steady-state median crystal size is far more complex than that of the previous two decision variables. In the case of the fines flow rate, there are two counteracting effects. An increase in the fines flow rate naturally increases the number of fines that are removed per unit of time, however, at the same time it reduces the temperature increase of the fines flow in the dissolution loop, thereby decreasing the driving force for dissolution. Initially, the second effect is of little significance and the median crystal size increases. Later, the degree of dissolution decreases to such an extent that the median crystal size also drops. As regards the upward velocity in the annular zone, an increase in this decision variable also has two counteracting effects. An increased upward velocity leads to a higher cut size of the classification function, which on the one hand increases the number of crystals removed with the fines flow, but on the other hand it decreases the driving force per crystal for dissolution. Again, the decrease in driving force only starts affecting the median crystal size after a certain increase in this decision variable.

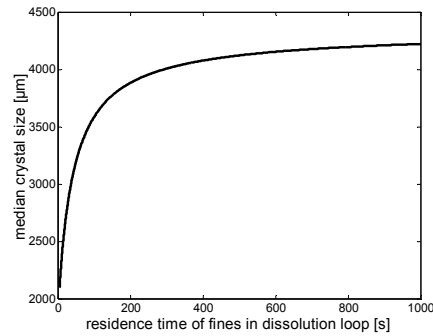


Figure 7.6: Steady-state response of the median crystal size as a function of the fines residence time in the dissolution loop.

The relationship between the fines residence time in the dissolution loop and the steady-state median crystal size is also highly nonlinear. Initially the median size increases rapidly with this fines residence time, but this effect decreases gradually. Increasing the residence time of the fines may provide additional time for dissolution, but this will have little effect on the product CSD if the driving force for dissolution has been depleted.

7.3.3 MATHEMATICAL OPTIMISATION

The exploratory homotopy simulations presented in the previous section strongly indicate that manual trial and error manipulation of all five decision variables in order to find an economically optimal design that satisfies all product quality and operational constraints will be very time-consuming, as it may literally require hundreds of simulations. Furthermore, this approach is not guaranteed to deliver a (local) optimum. A more time- and cost-efficient as well as effective method for the solution of inverse problems, the class of problems that optimal design belongs to, embraces formal, mathematically-based methods. gPROMS, the tool used to implement the crystallisation process modelling framework developed as part of this PhD work, has built-in capabilities for optimisation using such methods. For the optimal design calculations in this chapter an SQP optimisation algorithm is used (Process Systems Enterprise Ltd, 2002). Formulation of the optimal design problem outlined in Chapter 7.3.1 involves specifying:

- Initial guesses, lower bounds and upper bounds for the decision variables (see Table 7.5).
- Lower and/or upper bounds for the operational constraints; the temperature increase of the fines flow in the dissolution loop may not exceed 20°C and the superficial vapour velocity above the boiling zone may not exceed $3 \text{ m}\cdot\text{s}^{-1}$ (from Eq. 7.1 for a crystalliser operating temperature of 50°C).

- Lower and/or upper bounds for the product quality related constraints; the crystal growth rate should not exceed $50 \text{ nm}\cdot\text{s}^{-1}$ and the median crystal size should be within a specified narrow range, e.g. $1000 \mu\text{m} \pm 1\%$.
- The objective function, which is typically related to the economics of the process. However, objective functions involving key process or product performance indicators, such as the median crystal size, may also be used. Such objective functions are useful to determine the attainable region with respect to these indicators before switching to the economic objective function.

Table 7.6: Optimal crystalliser designs for a range of median crystal sizes at a production capacity of $94 \text{ kton}\cdot\text{annum}^{-1}$ and an operating temperature of $50 \text{ }^\circ\text{C}$.

		steady-state median crystal size [μm]	1000	2000	3000
objective function	total annualised costs [k€]		1032	158	160
	annualised capital costs [k€]		93	93	95
	annualised operational costs [k€]		939	65	65
decision variables	product residence time in main body [hr]		9.1	9.1	9.1
	axial velocity in draft tube induced by impeller [$\text{m}\cdot\text{s}^{-1}$]		1.27	0.50	0.50
	finer flow rate over product flow rate [-]		14.6	14.7	15.1
	superficial velocity in annular zone [$\text{m}\cdot\text{s}^{-1}$]		0.50	0.50	0.14
	finer residence time in dissolution loop [s]		5.0	5.5	34.9
constraint variables	superficial vapour velocity [$\text{m}\cdot\text{s}^{-1}$]		3.03	3.03	3.03
	finer temperature increase [K]		20.2	20.2	20.2
	maximum crystal growth rate [$\text{nm}\cdot\text{s}^{-1}$]		15	16	25
other selected variables	finer flow rate [$\text{m}^3\cdot\text{s}^{-1}$]		0.15	0.15	0.15
	finer residence time in main body [s]		2238	2225	2167
	volume main body [m^3]		328	328	328
	volume annular zone [m^3]		2.3	2.3	8.4
	volume finer dissolution loop [m^3]		0.73	0.81	5.27
	diameter main body [m]		4.67	4.67	4.67
	diameter annular zone [m]		4.71	4.71	4.82
	area annular zone [m^2]		0.29	0.29	1.06

The first optimisation calculations were aimed at determining the lowest and the highest median crystal size that can be obtained in a single DTB crystalliser with a production capacity of $94 \text{ kton}\cdot\text{annum}^{-1}$ and an operating temperature of $50 \text{ }^\circ\text{C}$.

These calculations resulted in a lower bound of 858 μm and an upper bound of approximately 4000 μm (the calculation for this bound did not fully converge). Based on this range it was decided to determine the economically optimal designs capable of delivering a crystalline product with a median crystal size of 1000, 2000 or 3000 μm . The results of the corresponding optimisation calculations are shown in Table 7.6, from which one can make a number of observations.

Capital costs either stay the same or increase with the steady-state median crystal size. Operational costs, however, are higher for a median size of 1000 μm than for 2000 μm . This is a result of having to use an increased impeller frequency to prevent the crystals from becoming too large and the impeller frequency largely dominates the operational costs of the crystalliser. Note that the operational costs constituting part of the economic objective function do not include the heating duty required for evaporation. Given the fixed production capacity, the heating duty is not used as a decision variable. The reason why the impeller frequency has to be used to control the median size is that other decision variables that can decrease the median size are bound by operational constraints. For instance, the residence time cannot be reduced as this would result in a too high vapour velocity. Furthermore, the fines destruction system is already operating at its least effective settings, i.e. the highest superficial velocity in the annular zone (resulting in a cut size higher than the product median size) and the shortest residence time in the dissolution loop (resulting in practically no dissolution).

It is not until a product median size of approximately 3000 μm is required that the fines destruction system becomes an essential mechanism for satisfying this product quality constraint. Consequently, for this production capacity and operating temperature, one does not require a DTB crystalliser to obtain a product median size of 2000 μm or less, as the fines destruction system is only acting as an external heating loop. Instead, it would be just as effective and probably considerably cheaper to employ a DT crystalliser with internal or external heating.

For all three designs, the product residence time is determined by the vapour velocity constraint. If this constraint were not taken into account, designs with shorter product residence times and thus lower capital costs would be obtained. Also, in that case one would expect the product residence time to increase with the required median crystal size and to see an increase in the ratio of the fines flow rate over the product flow rate as well as lower superficial velocities in the annular zone and higher residence times in the fines dissolution loop. The reason for the latter expectations is that fines destruction is a cheaper and more effective technique to increase the crystal size than increasing the product residence time. This is also illustrated by the homotopy simulations in Chapter 7.3.2. As dropping the vapour velocity constraint is not realistic, two other approaches are followed to test the hypotheses with respect to the product residence time and operation of the fines destruction system. Firstly, we will look at the use of multiple crystallisers in parallel with a combined production capacity of 94 $\text{kton}\cdot\text{annum}^{-1}$ and all operating at a temperature of 50 $^{\circ}\text{C}$ (see Table 7.7). Secondly, we will

determine the optimal designs for a single crystalliser operating at a temperature of 100 °C (see Table 7.8).

Table 7.7: Optimal designs for a median crystal size of 1500 μm when using 1, 3, 5 or 10 crystallisers in parallel for a production capacity of 94 kton $\cdot\text{annum}^{-1}$ and an operating temperature of 50 °C.

	number of crystallisers in parallel	1	3	5	10
objective function	total annualised costs for all crystallisers [k€]	300	210	193	215
	annualised capital costs for all crystallisers [k€]	93	103	115	147
	annualised operational costs for all crystallisers [k€]	207	107	78	69
	total annualised costs per crystalliser [k€]	300	70	39	22
	annualised capital costs per crystalliser [k€]	93	34	23	15
	annualised operational costs per crystalliser [k€]	207	36	16	7
decision variables	product residence time in main body [hr]	9.1	5.3	4.1	2.9
	axial velocity in draft tube induced by impeller [$\text{m}\cdot\text{s}^{-1}$]	0.76	0.60	0.53	0.50
	finer flow rate over product flow rate [-]	14.7	14.7	14.7	14.7
	superficial velocity in annular zone [$\text{m}\cdot\text{s}^{-1}$]	0.50	0.50	0.50	0.41
	finer residence time in dissolution loop [s]	5.0	5.0	5.0	8.2
constraint variables	superficial vapour velocity [$\text{m}\cdot\text{s}^{-1}$]	3.03	3.03	3.03	3.03
	finer temperature increase [K]	20.2	20.2	20.2	20.2
	maximum crystal growth rate [$\text{nm}\cdot\text{s}^{-1}$]	15	23	28	41
other selected variables	finer flow rate [$\text{m}^3\cdot\text{s}^{-1}$]	0.15	0.05	0.03	0.01
	finer residence time in main body [s]	2231	1288	997	705
	volume main body [m^3]	328	63	29	10
	volume annular zone [m^3]	2.33	0.45	0.21	0.09
	volume finer dissolution loop [m^3]	0.73	0.24	0.15	0.12
	diameter main body [m]	4.67	2.70	2.09	1.48
	diameter annular zone [m]	4.71	2.72	2.11	1.49
	area annular zone [m^2]	0.29	0.10	0.06	0.04

From Table 7.7 one can see that the capital and operational costs respectively increase and decrease in going from one to ten crystallisers in parallel, which leads to an overall economic optimum for a process configuration consisting of somewhere between four and nine crystallisers in parallel. Similarly to the single crystalliser designs (see Table 7.6), the operation of the finer destruction system does not move away from the highest superficial velocity in the annular zone and

the lowest residence time in the fines dissolution loop before the axial velocity induced by the impeller reaches its lowest value. The other trend worth noting is that the product residence time decreases with the number of crystallisers in parallel. The design calculations ensure at the same time that the crystal growth rate increases with the number of crystallisers to obtain the required median crystal size.

Table 7.8: Optimal crystalliser designs for a range of median crystal sizes at a production capacity of 94 kton·annum⁻¹ and an operating temperature of 100 °C.

		steady-state median crystal size [μm]	1000	2000	3000
objective function	total annualised costs [k€]		270	88	117
	annualised capital costs [k€]		41	43	57
	annualised operational costs [k€]		230	45	60
decision variables	product residence time in main body [hr]		2.3	2.3	3.7
	axial velocity in draft tube induced by impeller [$\text{m}\cdot\text{s}^{-1}$]		1.04	0.50	0.50
	fines flow rate over product flow rate [-]		14.4	15.1	15.3
	superficial velocity in annular zone [$\text{m}\cdot\text{s}^{-1}$]		0.50	0.08	0.06
	fines residence time in dissolution loop [s]		5.0	7.4	31.5
constraint variables	superficial vapour velocity [$\text{m}\cdot\text{s}^{-1}$]		1.14	1.14	0.83
	fines temperature increase [K]		20.2	20.2	20.1
	maximum crystal growth rate [$\mu\text{m}\cdot\text{s}^{-1}$]		39	50	50
other selected variables	fines flow rate [$\text{m}^3\cdot\text{s}^{-1}$]		0.14	0.15	0.15
	fines residence time in main body [s]		576	548	862
	volume main body [m^3]		83	83	132
	volume annular zone [m^3]		1.4	9.6	14.2
	volume fines dissolution loop [m^3]		0.72	1.12	4.82
	diameter main body [m]		2.96	2.96	3.45
	diameter annular zone [m]		3.02	3.34	3.87
	area annular zone [m^2]		0.29	1.91	2.42

Increasing the operating temperature from 50 to 100 °C leads to roughly a tenfold increase in the crystalliser's operating pressure. As a result, the optimal designs listed in Table 7.8 can operate at considerably lower product residence times than the optimal designs for operating temperatures of 50 °C without violating the vapour velocity constraint. The crystalliser designs aimed at delivering a crystalline product with a steady-state median size of 1000 and 2000 μm both operate exactly on this constraint. In addition, the design for a 2000 μm median

size also operates on the maximum growth rate constraint. This constraint is the only active constraint providing a lower bound for the product residence time of the crystalliser design aimed at producing a CSD with a median size of 3000 μm . Thanks to the lower product residence times, these crystalliser designs have considerably lower capital costs than their counterparts operating at 50 °C.

7.3.4 CONCLUSIONS

Based on the results of the homotopy simulations, in particular those where the fines flow rate over the product flow rate and the superficial upward velocity in the annular zone were varied, one can easily imagine that finding an optimal solution through the use of simulations may require hundreds of simulations, even though the number of decision variables (5) is still relatively small. Furthermore, this manual exercise becomes increasingly more complex when one needs to ensure that a number of inequality constraints, related to product quality and operational factors, are satisfied. One invisible, but important outcome of the optimal design work performed in this chapter is that the additional effort required to set up design calculations using formal mathematically-based optimisation techniques is relatively small once a crystallisation process model is available. Using these techniques, large numbers of decision variables and inequality constraints can be handled in a transparent manner.

There are a number of issues hampering the quality assessment of the solutions found for the optimal crystalliser design problem formulated in this chapter. Firstly, there is considerable uncertainty in some of the financial parameters used by the objective function. Secondly, we had no access to reference designs either from literature or industry to demonstrate that the use of formal optimisation techniques results in designs with a better product and process performance. However, the dependencies of the objective function, the number of decision variables, and the number of constraints under consideration ensure that the optimisation problem is of a realistic complexity. Furthermore, the optimal designs for various target crystal sizes and differing numbers of crystallisers show trends that are intuitive and consistent. As such, this chapter has succeeded in demonstrating proof of concept and practical feasibility for a sufficiently complex industrial problem.

Finally, it should be reiterated that the optimal design work performed in this chapter only concerns the steady-state behaviour of a continuous process. The dynamic characteristics including controllability of the process design are thus ignored for the time being, but should be included in future studies (after improving the predictive capabilities of the crystallisation process model with respect to process dynamics).

8 RECOMMENDATIONS AND PERSPECTIVES

As important a result of this PhD thesis as the developed design procedure and predictive models, is the identification of areas that require further research and development and opportunities for application of the current tools and results.

The foremost need for development with respect to the overall design process is an expert driven environment that (i) guides the user through the various design levels with differing degrees of user interaction and (ii) interfaces with the relevant heuristic and rigorous models at the various design levels identified in Chapter 3. This development is currently being undertaken by Delft University of Technology in co-operation with two companies that develop and supply design software. These companies have expertise in respectively combining heuristics and ‘simplified, reduced’ models for process synthesis and the use of rigorous predictive models for design analysis and optimisation.

As regards the availability and quality of models at the various design levels, it is the author's opinion that the models relating product composition to product performance constitute the weakest link in the chain. As such, further research into the systematic design of crystallisation processes should pay more attention to the domain knowledge required for design level I than was the case in this research. The main emphasis from the process systems engineering point of view should however not be on the development of models with improved predictive capabilities, but on dealing with the significant uncertainties in the predictions obtained with the current models.

The predictive models developed as part of this thesis work have been successfully applied for synthesis and analysis purposes at design levels III and IV. However, their predictive capabilities still need to and can be improved, in particular with respect to the dynamic behaviour of the CSD as observed on the 1100 litre DTB crystalliser. The first recommendation in this respect is to extend the kinetic model of Gahn with not only a birth rate expression but also a growth rate expression for primary nuclei. Further improvements may be expected by including certain material properties that are currently determined from independent experiments (often with large variances) in parameter estimation calculations based on CSD data from crystallisation experiments.

Other aspects of the crystallisation process modelling framework that require further attention are related to thermodynamics and hydrodynamics. Currently the supersaturation is calculated on a concentration basis as opposed to an activity basis. This did not pose a problem for the work presented here, as a feedstock with a consistently high purity was used for all experimental work. However, in industrial practice the use of concentration based driving forces may significantly limit the predictive value of the model with respect to changes in feed composition. With respect to the hydrodynamics, it is recommended to explore the use of automatic zoning techniques for setting up compartmental models, as the current procedure for constructing these models is largely heuristic. On the longer term, as computer hardware becomes more powerful, and as process

modelling and CFD packages evolve (and perhaps converge), the choice between a compartmental modelling approach and CFD approach should be revisited.

Another category of model improvements is related to the numerical solution of the model equations. The first suggestion is to revisit the use of the logarithm of the number density instead of the 'normal' number density in the PBE, as this leads to a significantly better scaled problem from a numeric point of view. A second and more important improvement would be the use of numerical techniques with built-in error control for the solution of PDEs and IEs. Realistically, this is a matter of either waiting for a generic process modelling and optimisation tool (e.g. Aspen Custom Modeller and gPROMS) to incorporate such techniques, or to switch to a modelling tool dedicated to the efficient and accurate solution of PDEs using adaptive techniques, such as PARSIVAL. However, tools belonging to the latter category typically lack one or more of the following: powerful parameter estimation and optimisation capabilities, a flexible and powerful modelling language and physical property interfaces.

In its current form, the developed crystallisation process modelling framework already possesses sufficient descriptive and predictive capabilities as well as computational performance to be applied routinely and effectively in academia and industry. As the requirements for predictive capabilities become more stringent as one goes from experimentation to control, optimisation of operation and further to grassroots design, it makes sense to demonstrate the value of a model based approach by performing case studies for a certain crystallisation system in the same or a similar sequence. Design of experiments and parameter estimation respectively also make good starting points as crystallisation experiments are typically very resource intensive and many alternative kinetic models have been postulated. In contrast, the effort required to take a model that has been successfully used for simulation and configure it for use in a parameter estimation, optimisation or experiment design activity is considerably less than the model development effort. As confidence in the crystallisation models and modelling tools grows through successful applications in experimentation and control, model-based optimisation for the operation of existing plants and for grassroots design will be the next logical steps.

Not only the process modelling framework can be used throughout the lifecycle of a process, the same holds for the developed systematic design procedure. Besides grassroots design, the hierarchical design procedure can also be used for retrofitting and optimisation of operation. Using the procedure for these activities mainly reduces the degrees of freedom available for design. Another lifecycle perspective concerns operational effectiveness of the process, which requires additional development to integrate the process design or retrofit objectives with the operational and control objectives. The existing predictive models form a stepping stone in this respect as they can be applied for controllability studies and dynamic optimisation of operation.

Many of the above-mentioned development and application activities are being performed within the European section of SINC-PRO, an IMS project on model-

based design and control of crystallisation processes. This project uses the crystallisation process modelling framework developed at Delft University of Technology as a basis, with the aim of substantially reducing the effort for the development of crystallisation design models.

References

- Bamforth, A.W. (1965). *Industrial crystallization*. Leonard Hill, UK.
- Barnea, E. and J. Mizrahi (1973). A generalised approach to fluid dynamics of particulate systems. *Chem. Eng. J.*, **5**, 171-189.
- Barton, P.I. and C.C. Pantelides (1994). The modelling of combined discrete/continuous processes. *AIChE J.*, **40**, 966-979.
- Bennett, R.C. (1984). Crystallization from solution. In D.W. Green and J.O. Maloney (Ed.), *Perry's Chemical Engineer's Handbook*, 6th ed., McGraw-Hill, New York, USA, chapter 19, pp. 25-40.
- Bennett, R.C. (1993). Crystallizer selection and design. In A.S. Myerson (Ed.), *Handbook of Industrial Crystallization*, Butterworth-Heinemann, Boston, USA.
- Bermingham, S.K., A.M. Neumann, J.P. Muusze, H.J.M. Kramer, and P.J.T. Verheijen (1997). Modelling the settling, dissolution and non-uniform nucleation kinetics in a 150-litre forced circulation crystalliser. *Part. Part. Syst. Charact.*, **15**, 125-130.
- Bermingham S.K., H.J.M. Kramer, G.M. van Rosmalen (1998). Towards on-scale crystalliser design using compartmental models. *Comput. Chem. Eng.*, **22**, S355-S362.
- Bermingham, S.K., A.M. Neumann, H.J.M. Kramer, J. Grievink and G.M. van Rosmalen (1998). The influence of crystallizer scale and type on product quality. *Proceedings of the International Symposium on Industrial Crystallization, Tokyo, Japan, 17-18 September 1998*. pp. 37-46.
- Bermingham, S.K., M. Jonkers, G.J. Kruizinga, J.L.B. van Reisen and P.J.T. Verheijen (1999). Monitoring heat exchanger fouling for optimal operation of a multiple effect evaporator. *Comp. Chem. Engng.*, **23**, S771-S774.
- Bermingham, S.K., A.M. Neumann, H.J.M. Kramer, P.J.T. Verheijen, G.M. van Rosmalen and J. Grievink (2000). A design procedure and predictive models for solution crystallisation processes. *AIChE Symp. Series 323*, **96**, pp. 250-264.
- Berry, D.A. and K.M. Ng (1997). Synthesis of reactive crystallization processes. *AIChE J.*, **43**, 1737-1750.
- Boxman, A. (1992). *Particle size measurement for the control of industrial crystallizers*. PhD Thesis, Delft University of Technology, The Netherlands.
- Chen, B.H., S.P. Asprey, S. K. Bermingham, A.M. Neumann and H.J.M. Kramer (2003). On the design of optimally informative experiments for model discrimination among dynamic crystallization process models. *Proceedings Foundations of Computer-Aided Process Operations (FOCAPO2003)*, pp. 455-458.
- Chen, M.-Q., C. Hwang and Y-P Shih (1996). A Wavelet-Galerkin method for solving population balance equations. *Comput. Chem. Eng.*, **20**, 131-145.
- Daudey, P.J. (1987). *Crystallisation of ammonium sulphate*. PhD Thesis, Delft University of Technology, The Netherlands.

- De Jong, E.J. (1984). The one or the other. In S.J. Jancic and E.J. de Jong (Ed.), *Industrial Crystallization 84*, Elsevier Science Publishers B.V., Amsterdam, The Netherlands, p. 177-184.
- De Jong, M.D., R.E. Breslau, A.M. Neumann, H.J.M. Kramer, B. Scarlett (1998). Modelling the Hydrodynamics of a 22 litre DT Crystalliser. *Proceedings of the World Conference on Particle Technology III, Brighton, UK*.
- De Jong, M.D. (2003). *Developing and validating a hydrodynamic model for a draft tube crystalliser*. PhD Thesis, Delft University of Technology, The Netherlands.
- Derksen J. and H.E.A. Van den Akker (1999). Large eddy simulations on the flow driven by a Rushton turbine. *AIChE J.*, **45**, 209-221.
- Douglas, J.M. (1985). A hierarchical decision procedure for process synthesis. *AIChE J.*, **31**, 353-362.
- Dye, S.R. and K.M. Ng (1995). Fractional crystallization: design alternatives and tradeoffs. *AIChE J.*, **41**, 2427-2438.
- Eek, R.A. (1995a). *Control and dynamic modelling of industrial suspension crystallizers*. PhD Thesis, Delft University of Technology, The Netherlands.
- Eek, R.A, Sj. Dijkstra and G.M. van Rosmalen (1995b). Dynamic modelling of suspension crystallizers using experimental data. *AIChE J.*, **41**(3), 571-584.
- Eek, R.A., H.A.A Pouw and O.H. Bosgra (1995c). Design and experimental evaluation of stabilizing feedback controllers for continuous crystallizers. *Powder Technology*, **82**, 21-35.
- EKATO (1991). *EKATO-Handbook of Mixing Technology*. EKATO Rühr-und Mischtechnik GmbH, Schopfheim, Germany.
- Erasmus, L.D., D. Eyre and R.C. Everson (1994). Numerical treatment of the population balance equation using a Spline-Galerkin method. *Comput. Chem. Eng.*, **18**, 775-783.
- Ferziger, J.H. and M. Peric (1996). *Computational methods for fluid dynamics*, Springer-Verlag, Berlin, German. pp. 67-84.
- Gahn, C. (1996). The effect of impact energy and the shape of crystals on their attrition rate. *J. Crystal Growth*, **166**, 1058-1063.
- Gahn, C. and A. Mersmann (1997). Theoretical prediction and experimental determination of attrition rates. *Trans IChemE.*, **75(A)**, 125-131.
- Gahn, C. (1997). *Die Festigkeit von Kristallen und ihr Einfluß auf die Kinetik in Suspensions-kristallisatoren*, PhD thesis, München University of Technology, Herbert Utz Verlag Wissenschaft, München, Germany.
- Gahn, C. and A. Mersmann (1999a). Brittle fracture in crystallisation processes. Part A. Attrition and abrasion of brittle solids. *Chem Engng Sci.*, **54**, 1273-1282.
- Gahn, C. and A. Mersmann (1999b). Brittle fracture in crystallisation processes. Part B. Growth of fragments and scale-up of suspension crystallizers. *Chem Engng Sci.*, **54**, 1283-1292.
- Garside, J. (1985). Industrial crystallization from solution. *Chem. Engng. Sci.*, **40**, 3-26.

- Gavrila, I.S. (1998). *Automating Process Design. A knowledge-based approach*. PhD Thesis, University of Amsterdam, The Netherlands.
- Gerla, J.H. (1995). *Modeling, measurement and manipulation of crystallizers*. PhD thesis, Delft University of Technology, The Netherlands.
- Gerstlauer, A., A. Mitrovic, S. Motz and E.-D. Gilles (2001). A population model for crystallization processes using two independent particle properties. *Chem. Engng. Sci.*, **56**, 2553-2565.
- Grievink, J. (2001). *A formal specification of a compartment and its attributes*. Private communications.
- Herder, P.M. (1999). *Process Design in a Changing Environment - Identification of Quality Demands Governing the Design Process*. PhD thesis, Delft University of Technology, The Netherlands.
- Herndl, G. (1982). *Stoffübergang in gerührten Suspensionen*. PhD thesis, München University of Technology.
- Hill, P.J. and K.M. Ng (1997). Simulation of solids processes accounting for particle-size distribution. *AIChE J.*, **43**, 715-726.
- Hollander, E.D., J.J. Derksen, O.S.L. Bruinsma, H.E.A. van den Akker, G.M. van Rosmalen (1999). A numerical study on the coupling of hydrodynamics and agglomeration. *Proceedings of 14th International Symposium on Industrial Crystallization*. 12-16 September 1999, Cambridge, United Kingdom.
- Jager, J. (1990). *Control of industrial crystallizers – the physical aspects*. PhD Thesis, Delft University of Technology, The Netherlands.
- Jager, J., S. de Wolf, H.J.M. Kramer, B. Scarlett and E.J. de Jong (1991). The effect of the scale of operation on CSD dynamics in evaporative crystallizers. *AIChE J.*, **37**, 182-192.
- Jancic, S.J. and P.A.M. Grootcholten (1984). In S.J. Jancic and E.J. de Jong (Ed.), *Industrial Crystallization 84*, Elsevier Science Publishers B.V., Amsterdam, The Netherlands.
- Klein, J.P. (1991). In J. Garside, R.J. Davey and A.G. Jones (Ed.), *Advances in Industrial Crystallisation.*, Butterworth Heinemann Ltd., Oxford, UK, pp. 182-196.
- Kramer, H.J.M., J.W. Dijkstra, A.M. Neumann, R. Ó Meadhra and G.M. van Rosmalen (1996). Modelling of industrial crystallizers, a compartmental approach using a dynamic flow-sheeting tool. *J. Crystal Growth*, **166**, 1084-1088.
- Kramer, H.J.M., S.K. Bermingham and G.M. van Rosmalen (1999). Design of industrial crystallisers for a required product quality. *J. Crystal Growth*, **198/199**, 729-737.
- Kramers, H. and K.R. Westerterp (1963). *Elements of Chemical Reactor Design and Operation*. Netherlands University Press, The Netherlands.
- Kumar, S. and D. Ramkrishna (1996). On the solution of population balance equations by discretization – I. A fixed pivot technique. *Chem. Engng. Sci.*, **51**, 1311-1332.
- Lapidus, L. and G.F. Pinder (1982). *Numerical solution of partial differential equations in science and engineering*, Wiley, New York, USA.

- Levenspiel, O. (1972). *Chemical Reactor Engineering, Second Edition*. John Wiley & Sons, USA.
- Mersmann, A. (1988). Design of crystallizers. *Chem. Eng. Process.*, **23**, 213-228.
- Mersmann, A., R. Sangl, M. Kind and J. Pohlisch (1988). Attrition and secondary nucleation in crystallizers. *Chem. Eng. Technol.*, **11**, 80-88.
- Mersmann, A. (1995). Fundamentals of Crystallization. In A. Mersmann (Ed.), *Crystallization Technology Handbook*, Marcel Dekker, New York, USA. pp. 1-78.
- Mersmann, A. and F.W. Rennie (1995). Design of Crystallizers and Crystallization Processes. In A. Mersmann (Ed.), *Crystallization Technology Handbook*, Marcel Dekker, New York, USA. pp. 215-326.
- Miller, S.M. and J.B. Rawlings (1994). Model identification and control strategies for batch cooling crystallisers. *AIChE J.*, **40**, 1312-1326.
- Mitrovic, A. (2002). Population Balance based Modeling, Simulation, Analysis and Control of Crystallization Processes, PhD thesis, University of Stuttgart, Germany.
- Moyers Jr. C.G. and R.W. Rousseau (1987). In R.W. Rousseau (Ed.), *Handbook of Separation Processes*, 1st ed., chapter 11, pp. 587-643.
- Muhr, H., R. David, J. Villiermaux and P.H. Jezequel (1995). Crystallization and precipitation engineering – V. Simulation of the precipitation of silver bromide octahedral crystals in a double-jet semi-batch reactor. *Chem. Engng. Sci.*, **50**, 345-355.
- Muhr, H., R. David, J. Villiermaux and P.H. Jezequel (1995). Crystallization and precipitation engineering – VI. Solving population balance in the case of the precipitation of silver bromide crystals with high primary nucleation rates by using the first order upwind differentiation. *Chem. Engng. Sci.*, **51**, 309-319.
- Mullin, J.W. (1993). *Crystallization*, Butterworth-Heinemann, Boston.
- Mumtaz, H.S., M.J. Hounslow, N.A. Seatan and W.R. Paterson (1997). Orthokinetic aggregation during precipitation: A computational model for calcium oxalate monohydrate. *Chem. Eng. Res. Des.*, **75(A2)**, 152-159.
- Myerson, A.S. and R. Ginde (1993). Crystals, crystal growth and nucleation. In A.S. Myerson (Ed.), *Handbook of Industrial Crystallization*, Butterworth-Heinemann, Boston.
- Nelson, S.A. (1999). Lecture Notes ‘Geology 211’. Tulane University, USA. <http://www.tulane.edu/~sanelson/geol211/lect5.htm>.
- Neumann, A.M., S.K. Bermingham, H.J.M. Kramer and G.M. van Rosmalen (1998a). The effect of the impeller speed on the product crystal size distribution (CSD) in a 22 litre draft tube (DT) crystalliser. *J. Crystal Growth*, **198/199**, 723-728.
- Neumann, A.M., S.K. Bermingham, H.J.M. Kramer and G.M. van Rosmalen (1998b). Modelling the attrition process in a 22 litre DT crystallizer. *Proceedings of the International Conference on Mixing and Crystallization*, Malaysia, April 22-25, Paper no. 36.

- Neumann, A.M., S.K. Bermingham, H.J.M. Kramer and G.M. van Rosmalen (1998c). Modelling the dynamic behaviour of a 22 litre evaporative draft tube crystallizer. *Proceedings of the International Symposium on Industrial Crystallization*, Tianjin, China, 21-25 September 1998. pp. 222-226.
- Neumann, A.M., S.K. Bermingham, H.J.M. Kramer and G.M. van Rosmalen (1999). Modeling industrial crystallizers of different scale and type. *Proceedings of the 14th Symposium on Industrial Crystallisation*, Cambridge, UK, 12th-16th September 1999.
- Neumann, A.M. (2001). *Characterizing Industrial Crystallizers of Different Scale and Type*. PhD Thesis, Delft University of Technology, The Netherlands.
- Nicmanis, M. and M.J. Hounslow (1998). A finite elements analysis of the steady-state population balance equation for particulate systems: aggregation and growth. *Comput. Chem. Eng.*, **20**, S261-S266.
- Nicmanis, M. and M.J. Hounslow (1998). A finite element method for the steady-state population balance equation. *AIChE J.*, **44**, 2253-2272.
- Oh, M. (1995). *Modelling and simulation of combined lumped and distributed processes*. PhD Thesis, Imperial College London, UK.
- Oldshue, J.Y. (1993). Agitation and mixing. In A.S. Myerson (Ed.), *Handbook of Industrial Crystallization*, Butterworth-Heinemann, Boston, USA.
- Ó Meadhra, R. (1995). *Modelling of the kinetics of suspension crystallizers – a new model for secondary nucleation*. PhD Thesis, Delft University of Technology, The Netherlands.
- Ó Meadhra, R., H.J.M. Kramer and G.M. van Rosmalen (1996). A model for secondary nucleation in a suspension crystalliser. *AIChE J.*, **42**, 973-982.
- Ottens, E.P.K., A.H. Janse and E.J. de Jong (1972). Secondary nucleation in a stirred vessel cooling crystalliser. *J. Crystal Growth*, **13/14**, 500-505.
- Ottens, E.P.K. and E.J. de Jong (1973). A model for secondary nucleation in a stirred vessel cooling crystallizer. *Ind. Engng Chem Fundls*, **12**, 179-183.
- Pantelides, C.C. (1988). SpeedUp – recent advances in process simulation. *Comp. Chem. Engng.*, **12**, 745-755.
- Ploß, R., T. Tengler, A. Mersmann (1985). *Chem.-Ing.-Tech.*, **MS 1364**, 1-24.
- Ploß, R., T. Tengler, A. Mersmann (1989). A new model of the effect of stirring intensity on the rate of secondary nucleation. *Chem. Eng. Technol.*, **12**, 137-146.
- Patankar, S.V. (1980). *Numerical heat transfer and fluid flow*, Hemisphere, New York, USA.
- Process Systems Enterprise Ltd (2002). *gPROMS Advanced User Guide*. London, UK.
- Qian, R.-Y. and G.D. Botsaris (1996). Laboratory Simulation of Industrial Crystallizer Cycling. *Ind.Eng.Chem.Res.*, **35**, 1163-1172.
- Randolph, A.D. and M.A. Larson (1988). *Theory of Particulate Processes, Second Edition*, Academic Press, San Diego, USA.
- Rajagopal, S., K.M. Ng and J.M. Douglas (1992). A hierarchical procedure for the conceptual design of solids processes. *Comp. Chem. Engng.*, **16**, 675-689.

- Richardson, J.F. and W.N. Zaki (1954). Sedimentation and fluidization. *Trans. Inst. Chem. Engrs.*, **32**, 35-53.
- Ristic, R.I., J.N. Sherwood, T. Shripathi (1990). Strain variation in the (100) growth sectors of Potash Alum single-crystals and its relationship to growth-rate dispersion. *J. Cryst Growth.*, **102**, 245-248.
- Rosmalen, G.M. van, S.K. Bermingham, G.J. Witkamp, D. Bruinsma and H.J.M. Kramer (1997). *Industrial crystallisation and precipitation. Handbook of the PAON course*. Delft University of Technology, The Netherlands.
- Rossiter, A.P. and J.M. Douglas (1986). Design and optimisation of solids processes. I: A hierarchical decision procedure for process synthesis of solids systems. *Chem. Eng. Res. Des.*, **64**, 175-183.
- Rousseau, R.W. (1993). Crystallization. In J.I. Kroschwitz and M. Howe-Grant (Ed.) *Kirk-Othmer Encyclopedia of Chemical Technology*, 4th ed., Wiley, New York, USA (1993).
- Tanguy, D. and P. Marchal (1996). Relations between the properties of particles and their process of manufacture. *Trans IChemE*, **74**, 715-722.
- Ten Cate, A., S.K. Bermingham, J.J. Derksen and H.J.M. Kramer (2000). Compartmental modelling of an 1100L DTB crystallizer based on large eddy flow simulation. *10th European Conference on Mixing*. July 2-5, 2000, Delft, The Netherlands.
- Urban, Z. and L. Liberis (1999). Hybrid gPROMS-CFD modelling of an industrial scale crystalliser with rigorous crystal nucleation and growth kinetics and a full population balance. *Presented at Chemputers 1999*. Düsseldorf, Germany.
- Van der Heijden, A.E.D.M., M. Elwenspoek and J.P. van der Eerden (1989). Size distribution of embryos produced by crystal-rod contacts. *J. Crystal Growth*, **98**, 398-410.
- Van der Heijden, A.E.D.M. (1992). *Secondary Nucleation and Crystallization Kinetics*. PhD thesis, University of Nijmegen, The Netherlands.
- Van der Heijden, A.E.D.M., J.P. van der Eerden and G.M. van Rosmalen (1994). The secondary nucleation rate - a physical model. *Chem. Engng. Sci.*, **49**(18), 3103-3113.
- Villadsen, J. (1997). Putting structure into chemical engineering. *Chem. Eng. Sci.*, **52**, 2857-2864.
- Westhoff, G.M. (2002). *Design and analysis of suspension crystallisers - Aspects of crystallisation kinetics and product quality*. PhD Thesis, Delft University of Technology, The Netherlands.
- Wöhlk, W., G. Hofmann and E.J. de Jong (1991). Die Kristallisationstheorie in der Praxis. *Chem.-Ing.-Tech.*, **63**, 293-297.
- Wójcik J.A. and A.G. Jones (1998). Dynamics and stability of continuous MSMPR agglomerative precipitation: numerical analysis of the dual particle coordinate model. *Comp. Chem. Engng.*, **22**, 535-545.
- Yadhav, N., M. van der Stappen, R. Boom, G. Bierman and J. Grievink (2002). On Mass Balance and Capacity Optimisation for the Conceptual Design of

- Processes for Structured Products. *Computer Aided Chemical Engineering*, **10**, 85.
- Zacher, U. (1995). *Die Kristallwachstumsdispersion in einem kontinuierlichen Suspensions-kristallisator*. PhD thesis, München University of Technology, Germany.
- Zimmels, Y. (1983). Theory of hindered sedimentation of polydisperse mixtures. *AIChE J.*, **29**, 669-676.

List of symbols

A_T	crystal surface area	$[\text{m}^2 \cdot \text{m}^{-3}]$
B_0	birth rate of crystals at L_0	$[\text{s}^{-1}]$
c	molar concentration	$[\text{mole} \cdot \text{m}^{-3}]$
c^*	molar saturation concentration of stress free crystals	$[\text{mole} \cdot \text{m}^{-3}]$
$c^*_{real}(L)$	molar saturation concentration of crystals of size L	$[\text{mole} \cdot \text{m}^{-3}]$
c_s	molar concentration in solid phase	$[\text{mole} \cdot \text{m}^{-3}]$
D_{AB}	binary diffusion coefficient	$[\text{m}^2 \cdot \text{s}^{-1}]$
D_{dis}	dissolution rate	$[\text{m}^{-3} \cdot \text{s}^{-1}]$
D_{dt}	draft tube diameter	$[\text{m}]$
D_{imp}	impeller diameter	$[\text{m}]$
e	edge of the impeller blade	$[\text{m}]$
f	face of the impeller blade	$[\text{m}]$
G	linear crystal growth rate	$[\text{m} \cdot \text{s}^{-1}]$
H	enthalpy	$[\text{J}]$
H	hardness	$[\text{N} \cdot \text{m}^{-2}]$
k	concentration (expressed as unit mass per unit volume)	$[\text{kg} \cdot \text{m}^{-3}]$
k_d	mass transfer coefficient	$[\text{m} \cdot \text{s}^{-1}]$
k_r	rate constant for surface integration	$[\text{m} \cdot \text{s}^{-1}]$
k_v	volumetric shape factor	$[-]$
K_r	radial efficiency factor in crack formation	$[-]$
L	crystal length	$[\text{m}]$
m	mass	$[\text{kg}]$
M	molar mass	$[\text{kg} \cdot \text{mole}^{-1}]$
$n(L,t)$	crystal number density	$[\text{m}^{-3} \cdot \text{m}^{-1}]$
$N(L,t)$	cumulative crystal number density	$[\text{m}^{-3}]$
N_{blades}	number of impeller blades	$[-]$
NC	number of components	$[-]$
Ne	Newton number or power number	$[-]$
N_{frag}	number of fragments from a single collision	$[-]$
NI	number of solid/liquid inlet streams	$[-]$
N_{imp}	impeller frequency	$[\text{s}^{-1}]$
NK	number of compartments	$[-]$
NO	number of solid/liquid outlet streams	$[-]$
NP	number of phases	$[-]$
N_{pump}	pumping capacity or discharge coefficient	$[-]$
NR	number of reactions	$[-]$
P	pressure	$[\text{Pa}]$
r	reaction rate	$[\text{mole} \cdot \text{s}^{-1}]$
r	radial position on impeller	$[\text{m}]$
R	ideal gas constant ($= 8.314$)	$[\text{J} \cdot \text{mole}^{-1} \cdot \text{K}^{-1}]$
t	time	$[\text{sec}]$
T	temperature	$[\text{K}]$

T	characteristic length	[m]
$v(L,t)$	crystal number density	[m ⁻¹]
v^*	molar volume	[m ³ ·mole ⁻¹]
$v_{L,i}^*$	partial molar volume	[m ³ ·mole ⁻¹]
v_{ax}	axial velocity	[m·s ⁻¹]
v_{coll}	collision velocity	[m·s ⁻¹]
v_{rel}	relative velocity	[m·s ⁻¹]
v_{tan}	tangential velocity	[m·s ⁻¹]
V	size of control volume	[m ³]
V_{attr}	attrition volume from a single collision	[m ³]
w	weight fraction	[-]
W_C	critical work of indentation for crack formation	[J]
x	mole fraction	[-]
y	flag indicating whether a component can be present in a certain phase	[-]

Greek

β	moles of solvent incorporated in crystal lattice per mole solute	[-]
ε	specific power input	[W·kg ⁻¹]
ε	fraction of total volume occupied by continuous phase	[-]
ϕ_H	enthalpy flow rate or enthalpy flux	[J·s ⁻¹]
ϕ_m	mass flow rate or mass flux	[kg·s ⁻¹]
ϕ_{mol}	molar flow rate or molar flux	[mole·s ⁻¹]
ϕ_n	number density production rate	[m ⁻³ ·m ⁻¹ ·s ⁻¹]
$\phi_{n,coll}$	crystal collision rate at a certain radial position	[m ⁻¹ ·m ⁻¹ ·s ⁻¹]
ϕ_V	volumetric flow rate or volumetric flux	[m ³ ·s ⁻¹]
$\phi_{V,dt}$	volumetric flow rate through draft tube	[m ³ ·s ⁻¹]
η_{coll}	collision efficiency	[m ⁻¹]
η_{geom}	geometric target efficiency	[m ⁻¹]
η_{target}	target efficiency	[-]
η_L	dynamic viscosity of the liquid	[N·m ⁻² ·s]
$\eta_{L/S}$	apparent dynamic viscosity of the slurry	[N·m ⁻² ·s]
Γ	fraction surface energy	[J·m ⁻²]
Γ_S	surface related energy increase or condition of deformation	[J·m·mol ⁻¹]
μ	shear modulus	[N·m ⁻²]
ν	stoichiometric coefficient matrix	[-]
ν_L	kinematic viscosity of the liquid	[m ² ·s ⁻¹]
ρ_L	material density of the liquid phase	[kg·m ⁻³]
ρ_S	material density of the solid phase	[kg·m ⁻³]
σ	relative supersaturation	[-]
Ψ	Stokes parameter	[-]
τ	residence time	[s]

Indices

<i>i</i>	index of a liquid phase component
<i>j</i>	index of a compartment
<i>k</i>	index of a solid/liquid inlet
<i>l</i>	index of a solid/liquid outlet
<i>p</i>	index of a liquid phase reaction
<i>q</i>	index of a solid phase and of the corresponding crystallisation reaction

Subscripts

<i>aggl</i>	agglomeration
<i>attr</i>	attrition
<i>break</i>	breakage
<i>dis</i>	dissolution
<i>edge</i>	edge of the impeller blade
<i>face</i>	face of the impeller blade
<i>grow</i>	growth
<i>nucl</i>	primary nucleation
<i>L</i>	liquid phase, i.e. the continuous phase
<i>S</i>	solid phase, i.e. the dispersed phase
<i>V</i>	vapour phase

Abbreviations

<i>CFD</i>	Computational Fluid Dynamics
<i>CSD</i>	Crystal Size Distribution
<i>DT</i>	Draft Tube (Crystalliser)
<i>DTB</i>	Draft Tube Baffle (Crystalliser)
<i>FC</i>	Forced Circulation (Crystalliser)
<i>LES</i>	Large Eddy Simulation
<i>MSMPR</i>	Mixed Suspension Mixed Product Removal
<i>PBE</i>	Population Balance Equation
<i>UNIAK</i>	Universele Instrumentatie en Automatisering van Kristallisatoren (A Dutch acronym which stands for Universal Instrumentation and Automation of Crystallisers)

A ON PRODUCT COMPOSITION

The most important product composition characteristics and their influence on product performance characteristics are described in the following sections.

A.1 LATTICE STRUCTURE

The three-dimensional repeating periodic structure of atoms, ions or molecules in a crystal is called a lattice structure. Crystal properties such as material density and mechanical properties are largely determined by the lattice structure. In addition, the lattice structure also determines the possible morphologies that a crystal may exhibit.

It is possible to have two or more substances that are chemically identical, but possess different lattice structures. This phenomenon is called polymorphism and the involved substances are consequently denoted as polymorphs. The most well-known example of polymorphism involves diamond and graphite, two crystalline materials consisting of carbon atoms only. Diamond has an isometric crystal structure that is stable at high pressure. As temperature and/or pressure are decreased, the hexagonal structure of graphite becomes the more stable form, although this reconstructive transformation from diamond to graphite is extremely slow at environmental temperatures. Pseudo-polymorphism is a special form of polymorphism, and involves two or more substances, which are chemically identical except for the amount of solvent incorporated in the lattice.

If a substance can exhibit polymorphism, the polymorph that will be formed in a specific crystallisation process, depends on factors such as process conditions (pressure, temperature, supersaturation), the prevailing nucleation mechanism, and whether seeds are added to the process.

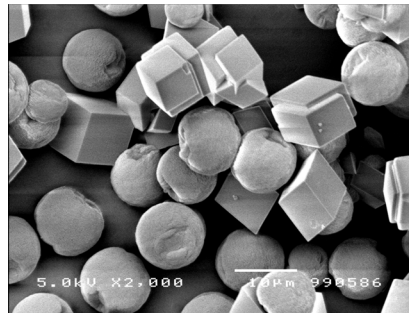


Figure A.1: Two polymorphs: the same chemical composition but different lattice structures. This figure does not show the lattice structures, but the differences in resulting morphology.

A.2 MORPHOLOGY AND HABIT

The external appearance of a crystal is described in terms of morphology and habit. In literature the terms morphology, habit and shape are often freely interchanged. However, there is an important distinction between habit and morphology, as depicted in Figure A.2.

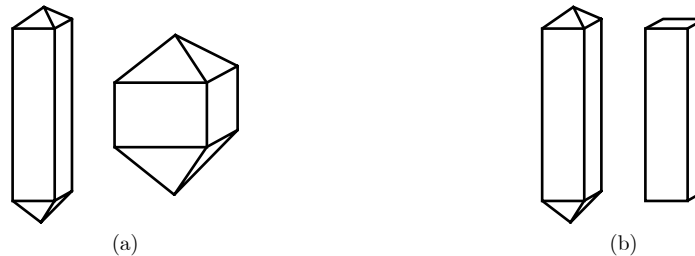


Figure A.2: Difference between habit and morphology after Randolph and Larson (1988). (a) Same morphology but different habit. (b) Same habit but different morphology.

Crystal habit refers to the general shape of a crystal given by the relative length to width of the crystal faces. Some common terms used to describe crystal habit are cubic, octahedral, tabular, columnar, equant, acicular, etc. (Nelson, 1999). Crystal habit affects crystal performance characteristics, such as settling velocities, centrifuge drainage rates, and product purity (Moyers, 1987). More specific, long, needle-like crystals tend to be easily broken during centrifugation and drying, whereas flat, plate-like crystals are very difficult to wash during filtration or centrifugation and result in relatively low filtration rates. Complex or twinned crystals tend to be more easily broken in transport than chunky, compact crystal habits. Spherical crystals, generally caused by attrition during growth, tend to give considerably less difficulty with caking than do cubical or other compact sizes (Bennett, 1984).

Crystal morphology describes the appearance of faceted crystals due to the specific crystallographic faces showing. As mentioned above, the lattice structure of a crystal determines the possible morphologies it may assume: the morphology reflects the periodic structure of the crystal lattice, which is imposed by the bond energies between the atoms, ions or molecules in the lattice. Crystal faces are represented using so-called Miller indices $\{hkl\}$. The morphologically most important faces are those with the lowest growth rates. This statement may seem strange at first, but can easily be explained (see Figure A.3). A crystal face with a large growth rate, R_3 , is positioned far from the origin, and thus its surface area, A_3 , will be relatively small. In contrast, a face with a small growth rate, R_1 , will be close to the origin and have a relatively large surface area, A_1 .

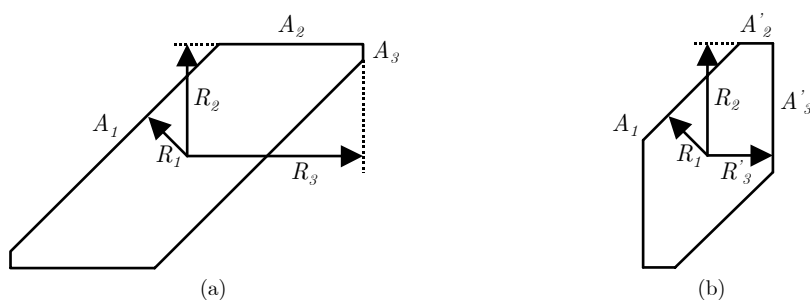


Figure A.3: The relative growth rates of the faces determine the crystal morphology. If the growth rate of a face decreases from R_3 to R'_3 the corresponding surface area increases from A_3 to A'_3 . After Ter Horst (2000).

If one knows the relative growth rates of all the different faces, the morphology and habit of a crystal can be predicted. Nowadays a number of general prediction methods are available to determine vacuum morphologies, i.e. the morphology in the absence of any foreign compounds such as solvents, impurities, etc. (Ter Horst, 2000). A frequently used prediction method is based on calculated attachment energies of the various crystal faces. It is assumed that the growth rate of a face is linearly proportional to its attachment energy.

Morphology prediction of crystals in the presence of a solvent and possible impurities requires calculation of the interaction energies between each foreign compound and the various crystal faces. Using these interaction energies, the attachment energies calculated in vacuum conditions can be corrected to account for morphology changes due to the presence of foreign compounds. A change in morphology as depicted in Figure A.3 can for instance be explained by a selective adsorption of a solvent on crystal face number three. The corresponding interaction energy decreases the absolute attachment energy and thus the growth rate of that face.

The morphology and habit, which a crystal develops during a specific crystallisation process, depend on the growth conditions (solvent, additives and impurities) and may vary with the level of supersaturation.

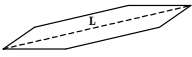
A.3 CRYSTAL SIZE

Usually one expects the ‘size’ of a crystal to be reported in terms of some linear dimension, d or L ; and indeed it usually is. However, in certain situations it may be more convenient to report ‘size’ in terms of volume, v , and occasionally in terms of projected area or surface area, a . Only spheres and regular polyhedra can be specified by a single linear ‘size’, whereas the volume of any crystal can always be given by a single number. This fact makes it extremely convenient to define a volume-equivalent sphere diameter:

$$d_v = \sqrt[3]{\left(\frac{6v}{\pi}\right)} \quad [1.1]$$

Area-equivalent diameters can be defined in a similar way, but note that the ‘area’ of a crystal is not so uniquely defined, or so easily measured, as its volume. Although volume is clearly the best quantity to denote crystal size, in practice mostly linear dimensions are used. The employed dimension is determined by installed measurement techniques, applied modelling methods and personal preferences. An overview of linear dimensions used to represent crystal size is given in Table A.1.

Table A.1: Linear dimensions used for the representation of crystal size.

Linear dimension	Definition	Associated measurement technique
length	maximal visible length 	imaging
sieve diameter	width of the minimum square aperture through which the particle will pass	sieve analysis
volume-equivalent sphere diameter	diameter of a sphere having the same volume	Coulter counter
surface-area-equivalent sphere diameter	diameter of a sphere having the same surface area	light diffraction
projected-area-equivalent sphere diameter	diameter of a sphere having the same projected area as the crystal viewed from a fixed direction	imaging

Directly correlated with the definition of the crystal length, L , are the definitions of the surface shape factor, k_a , and volume shape factor, k_v :

$$\text{crystal surface} = k_a L^2 \quad [1.2]$$

$$\text{crystal volume} = k_v L^3 \quad [1.3]$$

Crystal size influences performance characteristics such as filterability, settling behaviour, caking behaviour, bulk density and dissolution rates. For instance, small crystals contain more adhering mother liquor after filtration due to the relatively large surface area compared to a similar mass comprising larger crystals. This results in a less pure product after drying and a higher tendency towards

caking. Another example is the permeability of a crystal cake during solid-liquid separation. Although this permeability is a function of crystal size as expected, it is much stronger related to the width of the crystal size distribution. Finally, although for many applications large crystals are preferred, this is not the case if the crystals need to be dissolved or digested for their final use, e.g. pharmaceutical use.

A.4 CRYSTAL PURITY

If crystals are grown at relatively low rates and under constant conditions, normally purities of about 99.5 to 99.8 percent can be achieved in one process step. Under certain conditions, the purity may be significantly lower due to one or more of the following mechanisms:

- inclusion of mother liquor in the lattice
- entrapment of mother liquor in cracks, processes and agglomerates
- incorporation of impurities in the crystal lattice
- adsorption of impurities or solvent on crystal surfaces.

Impurities are undesirable for one or more of the following reasons: they increase the caking tendency, may lead to further reactions, incorrect chemical composition. The latter is a serious concern in pharmaceutical applications.

Mother liquor inclusions

The inclusion of mother liquor by the crystal lattice is strongly dependent on the supersaturation. At supersaturations where growth instabilities occur, mother liquor inclusions are almost unavoidable. For instance, at high supersaturations macrosteps may be formed on the crystal surface.

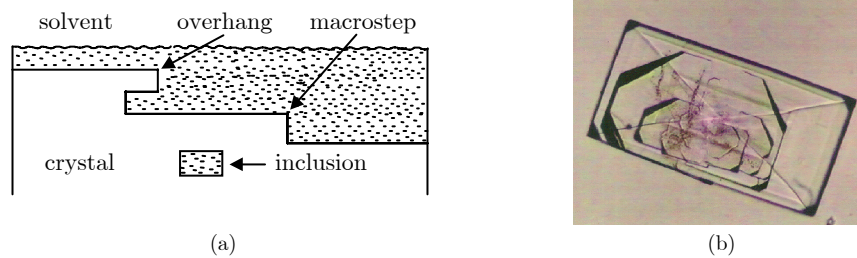
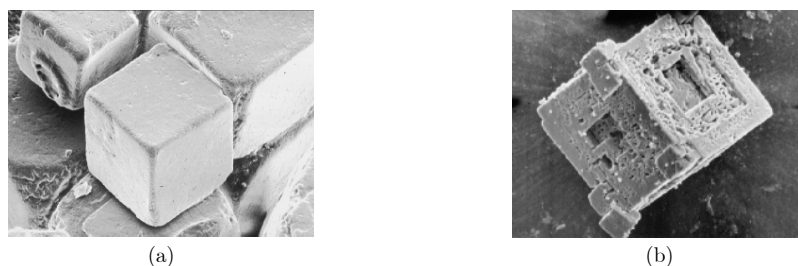


Figure A.4: (a) Macrosteps with overhangs. (b) Solvent inclusions in a crystal due to macrostep formation.

When macrosteps are present, overhangs can be formed that lead to mother liquor inclusions (see Figure A.4.a). These inclusions are therefore aligned along the outer crystal faces (see Figure A.4.b). At even higher supersaturations, the edges and corners of the crystals start exhibiting higher growth rates than the centres of the faces because, for geometric reasons, they suffer less from mass transfer limitation. Under such circumstances hopper crystals, which have more inclusions than crystals with flat faces, can be formed (see Figure A.5).



**Figure A.5: (a) Crystal grown with a relatively low growth rate.
(b) Same substance grown at a too high supersaturation.**

Another cause for the formation of liquor inclusions is attrition of crystals due to collisions with other crystals, pump blades or other equipment surfaces. Above a certain size, which depends on the material strength and the collision energies, the edges and in particular the corners of the crystals are attrited. If an attrited crystal is in a supersaturated region, the edges and corners will 'heal' as a result of crystal growth. During this healing, mother liquor is included because the growth layers propagating along two faces no longer fit perfectly. This phenomenon of solvent inclusions towards the corners of the crystals beyond a certain crystal size as well as the occurrence of other inclusions can easily be visualised under a microscope when the crystals are embedded in a non-dissolving liquid with the same refractive index: only the boundaries of the crystals and the mother liquor inclusions show up (see Figure A.6).

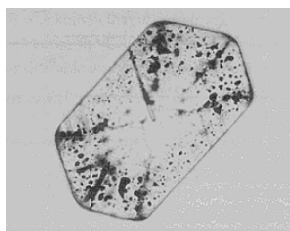


Figure A.6: A crystal with mother liquor inclusions due to attrition of its corners and edges.

Incorporation of impurities in the crystal lattice

As a crystalline material has a very rigid structure, incorporation of impurities by occupation of crystal lattice positions that are normally occupied by the growth units will only occur if the impurity fits reasonably well into the lattice.

A.5 SUPERFICIAL PROPERTIES

Superficial properties, such as hydrophobicity, polarity, and susceptibility to electrostatic charging also influence product performance. Many problems observed during industrial operations on powders (e.g. pneumatic conveyance,

drying and sieving) are the consequence of particle charging (Tanguy and Marchal, 1996).

B A PREDICTIVE CRYSTALLISATION PROCESS MODEL

B.1 MODEL ASSUMPTIONS

B.1.1 MODEL ASSUMPTIONS FOR THE GENERAL COMPARTMENT MODEL

The assumptions underlying the development of the general compartment model in Chapter 4 are given below (Grievink, 2001):

- Shape of compartment:
 - a bounded volume in 3-D space, which may have symmetric features, lowering the effective dimensionality to 2-D.
 - a fixed position, shape and size in time and space; and
 - a finite number of surfaces, which form the interface with the remainder of the process and its environment.
- Contents of compartment:
 - a liquid phase as a continuous medium.
 - a dispersed phase of solid particles.
 - no (dispersed) vapour phase.
 - each phase in the bulk is spatially homogeneous.
 - a particle population with one or more distributed properties.
 - the particle distribution can change in time due to rate phenomena.
 - the rate phenomena are spatially uniform.
 - the liquid and solid phases in the bulk are in thermal and mechanical equilibrium, i.e. same temperature and pressure.
 - the phases in the bulk are not in chemical equilibrium, i.e. different chemical compositions.
 - when phases are not in chemical equilibrium internal fluxes between the phases will arise.
 - there is no work done on or by the compartment.
 - the hydrodynamic state of the bulk is represented by a viscosity and an average energy dissipation rate.
 - the bulk has conservative properties with respect to mass, energy and momentum (no sources or sinks).
 - the contents of the bulk can change in time due to exchange fluxes with the environment.
 - the temporal change of the (averaged) hold-up of the momentum of the bulk can be ignored as well as the effects of the gravitational field; and

- the following laws of change are applied to the bulk of the compartment:
 - component mass balances for the liquid phase.
 - population balance for solid phase particles; and
 - energy balance over both phases.
- Surfaces of compartment and associated external fluxes:
 - the compartment is an open system capable of exchanging mass and energy with its environment by means of fluxes through one or more of its surfaces.
 - a surface can be isolated (no exchange fluxes at all), closed (heat exchange only) or open (mass and/or heat exchange).
 - the fluxes are uniform over the area of a surface and perpendicular to the surface.
 - the mass related fluxes are phase specific: liquid or solids.
 - a mass flux associated with the liquid phase has the properties of the bulk of the compartment it is leaving.
 - a mass flux between a liquid phase and a vapour phase in the outer world, may partially or totally change phase (evaporate, condense) at the interface.
 - a particle flux associated with the solid phase may have a particle size distribution that is different from the distribution in the bulk of the compartment it is leaving (classification effects).
 - the liquid phase related mass fluxes are characterised by (the product of) a convective velocity and a concentration (no dispersive contribution).
 - the particle related fluxes are characterised by the product of a size dependent velocity and a particle number or mass related concentration.
 - a surface may have two opposing mass related fluxes (in and out); and
 - the momentum exchange between phase and a solid ‘wall’ is characterised by the relative velocities of the wall and the phase and the mechanical impact energy.

B.1.2 FURTHER MODEL ASSUMPTIONS

In addition to the model assumptions made for the development of a general compartment model, assumptions were made for the crystallisation of ammonium sulphate from water in the UNIAK crystallisers. These are listed below.

- constant feed temperature
- a crystal free but saturated feed
- constant temperature in the crystalliser
- constant liquid level in the crystalliser

- constant fines flow
- constant product flow
- constant heat input
- no heat of crystallisation
- no heat loss to the environment
- no energy input via the mechanical action of the impeller
- solid phase only contains a single pure component
- the vapour flow only contains solvent(s); no solute or crystals
- the product removal is iso-kinetic and (thus) non-classified
- the particle shape is independent of size and constant in time
- agglomeration negligible
- primary nucleation negligible during continuous operation
- growth rate dispersion does not occur

B.2 GENERAL COMPARTMENT MODEL

A general crystallisation model for a control system/volume, with volume V , temperature T , pressure P , NC_L components in the liquid phase, NR_L liquid phase reactions, NP_S solid (crystalline) phases, NI S/L inlets, NO S/L outlets and one vapour outlet. It is assumed that each solid phase is created or depleted via one reaction only. The general model is set up to include primary nucleation, growth, dissolution, attrition, breakage and agglomeration.

B.2.1 EQUATIONS OF CONSERVATION

Mass balance for liquid phase component i

$$\begin{aligned}
 \overbrace{\frac{dm_{L,i}}{dt}}^{\text{mass rate of accumulation}} &= \overbrace{\sum_{k=1}^{NI} \phi_{m,L,i,in,k} - \sum_{l=1}^{NO} \phi_{m,L,i,out,l} - \phi_{m,V,i,out}}^{\text{mass rates in and out via convective transport}} \\
 &+ \overbrace{M_i \cdot \sum_{p=1}^{NR_L} v_{L,p,i} \cdot r_p}^{\text{mass production rate due to liquid phase reactions}} \\
 &+ \overbrace{M_i \cdot \sum_{q=1}^{NP_S} v_{S,q,i} \cdot [\phi_{mol,nucl,q} + \phi_{mol,grow,q} - \phi_{mol,dis,q}]}^{\text{interphase mass flux due to crystal growth and due to primary nucleation and dissolution at the critical nucleus size}}
 \end{aligned} \quad i = 1, \dots, NC_L \quad [2.1]$$

Initial condition:

$$n_{L,i}(t = 0) = n_{L,i,0} \quad i = 1, \dots, NC_L$$

Population balance for solid phase q

$$\begin{aligned}
 \overbrace{\frac{\partial n_q(L,t)V(t)}{\partial t}}^{\text{number rate of accumulation}} &= \overbrace{-V(t) \frac{\partial (n_q(L,t) \cdot G_q(L,\sigma))}{\partial L}}^{\text{rate of number gain by crystal growth and dissolution}} \\
 &+ \overbrace{\sum_{k=1}^{NI} \phi_{V,in,k} \cdot n_{q,in,k} - \sum_{l=1}^{NO} \phi_{V,out,l} \cdot n_{q,out,l}}^{\text{number rate in} \quad \text{number rate out}} \\
 &+ \overbrace{(\phi_{n,q,nucl}^+ - \phi_{n,q,dis}^-) V(t)}^{\text{number production rate due to primary nucleation and dissolution at the critical nucleus size}} \\
 &+ \overbrace{(\phi_{n,q,attr}^\pm + \phi_{n,q,break}^\pm + \phi_{n,q,aggl}^\pm) V(t)}^{\text{number production rate due to attrition, breakage and agglomeration}}
 \end{aligned} \quad q = 1, \dots, NP_S \quad [2.2]$$

Initial condition:

$$n_q(L, t = 0) = n_{q,0}(L) \quad q = 1, \dots, NP_s$$

Boundary condition:

$$n_q(L = 0, t) = \frac{B_{q,0}(t)}{G_q(L = 0, t)} \quad \text{if } G \geq 0 \quad q = 1, \dots, NP_s$$

$$n_q(L = \infty, t) = 0 \quad \text{if } G < 0 \quad q = 1, \dots, NP_s$$

Energy balance

$$\begin{aligned} \frac{dE}{dt} &= \overbrace{\sum_{k=1}^{NI} \phi_{E,in,k}}^{\text{rate of total energy in by convection}} - \overbrace{\sum_{l=1}^{NO} \phi_{E,out,l}}^{\text{rate of total energy out by convection}} - \overbrace{\phi_{E,V,out}}^{\text{rate of total energy out by convection via vapour}} \\ &+ \overbrace{\hat{Q}}^{\text{net rate of heat addition}} - \overbrace{\hat{W}_s}^{\text{net rate of shaft work}} - \overbrace{\hat{W}_{vc}}^{\text{net rate of work due to volume change}} \\ &+ \overbrace{\sum_{k=1}^{NI} \phi_{m,in,k} \cdot \frac{P_{m,k}}{\rho_{in,k}}}^{\text{work needed to introduce inlet streams}} - \overbrace{\sum_{l=1}^{NO} \phi_{m,out,l} \cdot \frac{P_{out,l}}{\rho_{out,l}}}^{\text{work needed to remove outlet streams}} - \overbrace{\phi_{m,V,out} \cdot \frac{P_{V,out}}{\rho_{V,out}}}^{\text{work needed to remove vapour stream}} \end{aligned} \quad [2.3]$$

Initial condition:

$$E(t = 0) = E_0$$

$$E = U + E_k + E_p \quad [2.4]$$

$$\phi_E = \phi_m \cdot (\hat{U} + \hat{E}_k + \hat{E}_p) \quad [2.5]$$

For crystallisation processes, kinetic energy, potential energy and shaft work can usually be neglected, thus reducing Eq. 2.3 to:

$$\begin{aligned} \frac{dU}{dt} &= \sum_{k=1}^{NI} \phi_{m,in,k} \cdot \left(\hat{U}_{in,k} + \frac{P_{m,k}}{\rho_{in,k}} \right) \\ &- \sum_{l=1}^{NO} \phi_{m,out,l} \cdot \left(\hat{U}_{out,l} + \frac{P_{out,l}}{\rho_{out,l}} \right) - \phi_{m,V,out} \cdot \left(\hat{U}_{V,out} + \frac{P_{V,out}}{\rho_{V,out}} \right) \\ &+ Q - W_{vc} \end{aligned} \quad [2.6]$$

The sum of internal energy and work due to the entrance and exit of mass is the enthalpy:

$$\hat{H} = \hat{U} + P\hat{V} = \hat{U} + \frac{P}{\rho} \quad [2.7]$$

$$\phi_H = \phi_m \cdot \hat{H} \quad [2.8]$$

$$\frac{dU}{dt} = \sum_{k=1}^{NI} \phi_{H,k} - \sum_{l=1}^{NO} \phi_{H,l} - \phi_{H,V,out} + Q - W_{vc} \quad [2.9]$$

$$\frac{d(H - PV)}{dt} = \frac{dH}{dt} - \frac{dPV}{dt} = \sum_{k=1}^{NI} \phi_{H,k} - \sum_{l=1}^{NO} \phi_{H,l} - \phi_{H,V,out} + Q - W_{vc} \quad [2.10]$$

and as

$$\frac{dPV}{dt} = W_{vc} \quad [2.11]$$

Eq. 2.10 reduces to the enthalpy balance as is frequently used in process engineering problems:

$$\frac{dH}{dt} = \sum_{k=1}^{NI} \phi_{H,k} - \sum_{l=1}^{NO} \phi_{H,l} - \phi_{H,V,out} + Q \quad [2.12]$$

Initial condition:

$$H(t = 0) = H_0$$

B.2.2 DERIVATIVE/RELATED/ASSOCIATED STATES

$$n_L = \sum_{i=1}^{NC_L} n_{L,i} \quad [2.13]$$

$$x_{L,i} = \frac{n_{L,i}}{n_L} \quad i = 1, \dots, NC_L \quad [2.14]$$

$$v_{L,i}^* = v_{L,i}^*(x_{L,j}, P, T) \approx v_{L,i}^*(x_{L,j}, T) \quad j = 1, \dots, (NC_L - 1), \quad i = 1, \dots, NC_L \quad [2.15]$$

$$V_L = \sum_{i=1}^{NC_L} n_{L,i} \cdot v_{L,i}^* \quad [2.16]$$

$$V_L = n_L \cdot v_L^* \quad [2.17]$$

$$m_{L,i} = n_{L,i} \cdot M_i \quad i = 1, \dots, NC_L \quad [2.18]$$

$$m_{L,i} = V_L \cdot k_{L,i} \quad i = 1, \dots, NC_L \quad [2.19]$$

$$m_L = \sum_{i=1}^{NC_L} m_{L,i} \quad [2.20]$$

$$w_{L,i} = \frac{m_{L,i}}{m_L} \quad i = 1, \dots, NC_L \quad [2.21]$$

$$m_L = V_L \cdot \rho_L = n_L \cdot v_L^* \cdot \rho_L \quad [2.22]$$

$$V_{S,q} = k_v \cdot \int_0^{\infty} N_q(L,t) \cdot L^3 \cdot dL \quad q = 1, \dots, NP_S \quad [2.23]$$

$$m_{S,q} = V_{S,q} \cdot \rho_{S,q} \quad q = 1, \dots, NP_S \quad [2.24]$$

$$V_S = \sum_{q=1}^{NP_S} V_{S,q} \quad [2.25]$$

$$m_S = \sum_{q=1}^{NP_S} m_{S,q} \quad [2.26]$$

$$V = V_S + V_L \quad [2.27]$$

$$m = m_S + m_L \quad [2.28]$$

$$m = V \cdot \rho \quad [2.29]$$

$$dH = \left(\frac{\partial H}{\partial T} \right)_P dT + \left(\frac{\partial H}{\partial P} \right)_T dP \quad [2.30]$$

$$C_P \equiv \left(\frac{\partial H}{\partial T} \right)_P \quad [2.31]$$

$$\left(\frac{\partial H}{\partial P} \right)_T \approx 0, \quad [2.32]$$

for any constant pressure process, regardless of the substance.

Whenever the enthalpy of the substance is independent of pressure, regardless of the process. This is exactly true for ideal gases and approximately true for low pressure gases

$$\hat{H}_{S,q} = \hat{H}_{f,q}^0 + \int_{T_0}^T C_{p,S,q} dT \quad q = 1, \dots, NP_S \quad [2.33]$$

$$\hat{H}_L = \sum_{i=1}^{NC_L} w_{L,i} \hat{H}_{f,i}^0 + \Delta \hat{H}_{solution}^0 + \int_{T_0}^T C_{p,L} dT \quad [2.34]$$

$$H = \sum_{q=1}^{NP_S} M_{S,q} \cdot \hat{H}_{S,q} + M_L \cdot \hat{H}_L \quad [2.35]$$

B.2.3 SLURRY (S/L) INLET

analogue to previous paragraph

B.2.4 SLURRY (S/L) OUTLET

analogue to previous paragraph

B.2.5 VAPOUR OUTLET

analogue to previous paragraph

$$\phi_{n,V,i,out} = \phi_{n,V,out} \cdot x_{V,i,out} \quad [2.36]$$

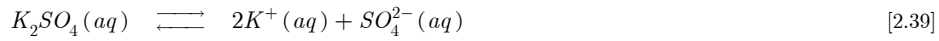
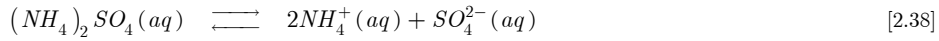
$$\sum_{i=1}^{NC_L} x_{V,out,i} = 1 \quad [2.37]$$

$$x_{V,out,i} = \frac{n_{L,i}}{\sum_{i=1}^{NC_L} y_i \cdot n_{L,i}},$$

where y is an integer with a value of zero or one! this relation assumes the same ratio in liquid and vapour phase

B.2.6 LIQUID PHASE REACTIONS

Example: Crystallisation of ammonium sulphate and potassium sulphate from water



$$NC_L = 6$$

$$NR_L = 2$$

		Liquid Phase Component					
		1	2	3	4	5	6
		(NH ₄) ₂ SO ₄	K ₂ SO ₄	NH ₄	K	SO ₄	H ₂ O
Liquid Phase	1	-1		2		1	
Reaction	2		-1		2	1	

Matrix of stoichiometric coefficients for liquid phase reactions

$$v_L = \begin{pmatrix} -1 & 0 & 2 & 0 & 1 & 0 \\ 0 & -1 & 0 & 2 & 1 & 0 \end{pmatrix} \quad [2.40]$$

Note that although the liquid phase reactions in the example system are all dissociation reactions, the model framework may also be used for systems with chemical reactions, as is the case in precipitation systems.

B.2.7 CRYSTALLISATION REACTIONS



$$NP_s = 2$$

		Liquid Phase Component					
		1	2	3	4	5	6
		(NH ₄) ₂ SO ₄	K ₂ SO ₄	NH ₄	K	SO ₄	H ₂ O
Solid Phase	(NH ₄) ₂ SO ₄	-1					
	K ₂ SO ₄		-1				

Matrix of stoichiometric coefficients for crystallisation reactions

$$v_s = \begin{pmatrix} -1 & 0 & 0 & 0 & 0 & 0 \\ 0 & -1 & 0 & 0 & 0 & 0 \end{pmatrix} \quad [2.45]$$

		Liquid Phase Component					
		1	2	3	4	5	6
		(NH ₄) ₂ SO ₄	K ₂ SO ₄	NH ₄	K	SO ₄	H ₂ O
Solid Phase	(NH ₄) ₂ SO ₄			-2		-1	
	K ₂ SO ₄				-2	-1	

Matrix of stoichiometric coefficients for crystallisation reactions

$$v_s = \begin{pmatrix} 0 & 0 & -2 & 0 & -1 & 0 \\ 0 & 0 & 0 & -2 & -1 & 0 \end{pmatrix} \quad [2.46]$$

B.3 CRYSTAL-IMPELLER COLLISION MODEL

The models of Mersmann, Ploß, Polish and Sangl can be used to determine and calculate the following quantities (all as a function of the parent crystal size and the impeller radius co-ordinate):

- the velocity profile around the impeller.
- the chance of collision and therefore the number of colliding crystals.
- the impact energy of the crystal.

The impeller blade is discretised along its radial co-ordinate; the minimal radius is the impeller point at which α (angle of the approaching crystal) is equal to β (angle of the impeller blade). Normally $\alpha < \beta$ (Figure B.1), however, for very small impeller radii, α may be larger than β . Physically this means that the crystal collides with the back of the impeller. Next to stirring, the impeller also acts as a pump; this results in both a pressure and a suction side. For $\alpha < \beta$ the crystals are pumped upwards, however, the case of $\alpha > \beta$ means that there is no pumping effect. Since this makes no sense, the discretisation of the impeller is started at $r(\alpha=\beta)$.

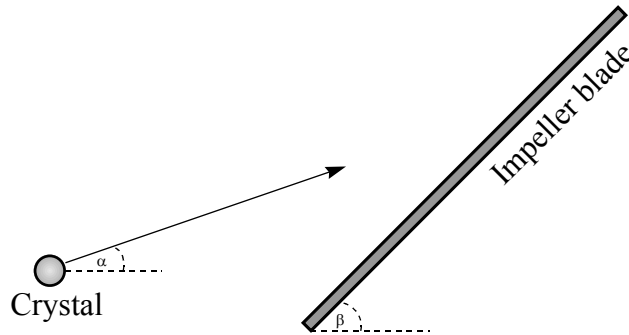


Figure B.1: definitions of the angles α and β

B.3.1 THE VELOCITY PROFILE AROUND THE IMPELLER

The volume flow in the draft tube is related to the impeller diameter and frequency via the pumping number:

$$\phi_{V,dt} = N_{pump} D_{imp}^3 N_{imp} \quad [2.47]$$

By assuming that the crystal follows the fluid flow in the crystalliser, its axial velocity can be calculated by determining the axial fluid velocity:

$$v_{ax} = \frac{\phi_{V,dt}}{\frac{\pi}{4} D_{dt}^2} \quad [2.48]$$

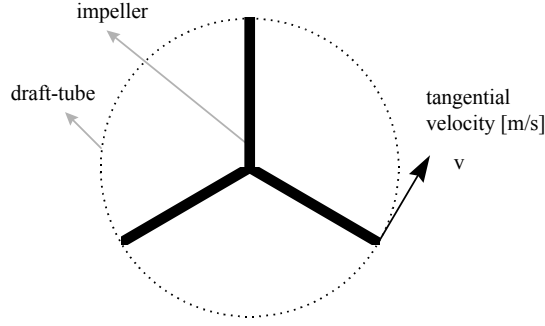


Figure B.2: Top view of the draft-tube and the impeller showing the definition of the tangential velocity

The tangential velocity of the impeller (Figure B.2) is a function of the impeller radius co-ordinate.

$$v_{tan}(r) = 2\pi r N_{imp} \quad [2.49]$$

Finally, the relative velocity of the crystal can be calculated by summing the axial and the tangential velocity vectors:

$$v_{rel}(r) = \sqrt{v_{ax}^2 + v_{tan}^2(r)} \quad [2.50]$$

These vectors also determine the angle between the crystal and the horizontal plane:

$$\alpha(r) = \arctan\left(\frac{v_{ax}}{v_{tan}(r)}\right) \quad [2.51]$$

B.3.2 THE CHANCE OF COLLISION OF A CRYSTAL

The models of Mersmann, Ploß, Polish and Sangl use two efficiencies:

- A geometric target efficiency which describes the chance that a crystal will be on a streamline heading for an impeller blade.
- A target efficiency, which indicates the chance that a crystal on such a streamline will collide with the impeller. In addition, the target efficiency also influences the collision velocity of the crystal.

The geometric target efficiency of the impeller edge respectively face is defined as the quotient of two areas: (1) the ‘effective’ area of the impeller edge respectively face and (2) the cross-sectional area of the draft-tube:

$$\eta_{geom,edge/face}(r) = \frac{4T_{edge/face}(r)N_{blades}}{\pi D_{dt}^2 \sin(\alpha(r))} \quad [2.52]$$

where the characteristic length of the impeller edge and face, $T_{edge/face}$, is given by:

$$T_{edge}(r) = e(r) \cos(\beta(r) - \alpha(r)) \quad [2.53]$$

$$T_{face}(r) = f(r)|\sin(\beta(r) - \alpha(r))| \quad [2.54]$$

The relation for the target efficiency was developed in research on dust collection equipment, describing the chance that a particle approaching a fibre thread would actually stick to it. The main focus in the determination of the target efficiency is the inertia of the particle (crystal) that approaches a specific geometry (Figure B.3). A particle with a small inertia (low mass and/or velocity) will probably follow the fluid flow lines around the object, while a particle with a high inertia (high mass and/or velocity) will not follow these fluid flow lines and will therefore collide with the object.

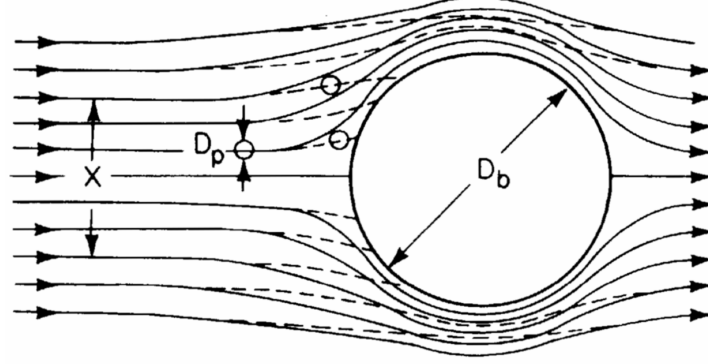


Figure B.3: A crystal approaching an object

There are several relations available for calculating the target efficiency of a particle approaching a specific geometry. Ploß uses the relation for a particle approaching a cylindrical shaped body (*i.e.* the impeller). The target efficiency for a cylindrical body is a fitted function of the Stokes parameter:

$$\eta_{target,edge/face}(L,r) = \left(\frac{\Psi_{edge/face}(L,r)}{\Psi_{edge/face}(L,r) + 0.32} \right)^{2.1} \quad [2.55]$$

where the Stokes parameter is defined as:

$$\Psi_{edge/face}(L,r) = \frac{(\rho_s - \rho_l)v_{rel}(r)L^2}{18T_{edge/face}(r)\eta_L} \quad [2.56]$$

The product of the geometric and target efficiency equals the chance that a crystal will collide with the impeller surface:

$$\eta_{coll,edge/face}(L,r) = \eta_{geom,edge/face}(r)\eta_{target,edge/face}(L,r) \quad [2.57]$$

B.3.3 THE COLLISION VELOCITY OF A CRYSTAL

The perpendicular collision velocity of a crystal with the impeller edge or blade is determined by multiplying the perpendicular relative velocity of the crystal with the above-mentioned target efficiency:

$$v_{coll,edge/face}(L,r) = \eta_{target,edge/face}(L,r)v_{rel,\perp,edge/face}(L,r) \quad [2.58]$$

The relative velocity of a crystal perpendicular to the impeller edge and face is calculated as follows:

$$v_{rel,\perp,edge}(L,r) = v_{rel,edge}(L,r)\cos(\beta(r) - \alpha(r)) \quad [2.59]$$

$$v_{rel,\perp,face}(L,r) = v_{rel,face}(L,r)|\sin(\beta(r) - \alpha(r))| \quad [2.60]$$

B.4 MATERIAL PROPERTIES

This appendix on material properties is after Neumann (2001).

B.4.1 SOLUBILITY

Solubility (Daudey, 1987 and Jager, 1990):

$$c_w = 0.41179 + 9.121 \cdot 10^{-4} \cdot T \quad [\text{kg solute/kg solution}] \quad [2.61]$$

$$-6^\circ\text{C} \leq T \leq 90^\circ\text{C}$$

Solubility (Westhoff et al., 2001):

$$c_w = 0.7008 + 26.8 \cdot 10^{-4} \cdot T + 2 \cdot 10^{-6} \cdot T^2 \quad [\text{kg solute/kg H}_2\text{O}] \quad [2.62]$$

$$35^\circ\text{C} \leq T \leq 55^\circ\text{C}$$

B.4.2 DENSITY

Solid phase ((NH₄)₂SO₄) – (Jager, 1990):

$$\rho_c = 1777.5 - 0.19697 \cdot T \quad [\text{kg/m}^3] \quad [2.63]$$

$$0^\circ\text{C} \leq T \leq 80^\circ\text{C}$$

$$0 \leq c_w \leq 50 \text{ wt\%}$$

Saturated crystal free solution ((NH₄)₂SO₄-H₂O) – (Jager, 1990):

$$\rho_l = A_0 + A_1 \cdot c_w + A_2 \cdot c_w^2 + A_3 \cdot c_w^3 + A_4 \cdot T + A_5 \cdot T^2 + A_6 \cdot T^3 \quad [\text{kg/m}^3] \quad [2.64]$$

$$0^\circ\text{C} \leq T \leq 100^\circ\text{C}$$

$$0 \leq c_w \leq 50 \text{ wt\%}$$

with

$$A_0 = 1003.51$$

$$A_1 = 6.00874$$

$$A_2 = -7.77478 \cdot 10^{-3}$$

$$A_3 = 3.10023 \cdot 10^{-5}$$

$$A_4 = -0.222764$$

$$A_5 = -2.76467 \cdot 10^{-3}$$

$$A_6 = 6.25116 \cdot 10^{-6}$$

$$0^\circ\text{C} \leq T \leq 100^\circ\text{C}$$

$$0 \leq c_w \leq 50 \text{ wt\%}$$

Vapour (H₂O):

$$\rho_v = 2500 - 0.19697 \cdot T \quad [\text{kg/m}^3] \quad [2.65]$$

$$0^\circ\text{C} \leq T \leq 80^\circ\text{C}$$

$$0 \leq c_w \leq 50 \text{ wt\%}$$

B.4.3 VISCOSITY

Saturated crystal free solution ((NH₄)₂SO₄-H₂O) – (Jager, 1990):

$$\eta_l = 10^{B_0 + B_1 \cdot c_w + B_2 \cdot c_w^2 + B_3 \cdot c_w^3 + B_4 \cdot T + B_5 \cdot T^2 + B_6 \cdot T^3} \quad [\text{mPa}\cdot\text{sec}] \quad [2.66]$$

$$0^{\circ}\text{C} \leq T \leq 80^{\circ}\text{C}$$

$$0.02 \leq c_w \leq 0.42$$

with	$B_0 = 0.219497$	$B_l = 5.71007 \cdot 10^{-3}$	$B_2 = 1.22202 \cdot 10^{-4}$
	$B_3 = -1.92549 \cdot 10^{-7}$	$B_4 = -1.25024 \cdot 10^{-2}$	$B_5 = 7.81444 \cdot 10^{-5}$
	$B_6 = -2.66152 \cdot 10^{-7}$		

B.4.4 DIFFUSIVITY

The volume diffusivity - Stokes-Einstein equation (Mersmann, 1995)

$$D_{AB} = \frac{k \cdot T}{2 \cdot \pi \cdot \eta_l \cdot d_m} \approx \frac{k \cdot T \cdot (c_s \cdot N_A)^{1/3}}{2 \cdot \pi \cdot \eta_l} \quad [\text{m}^2/\text{s}] \quad [2.67]$$

with

$$c_s = \frac{\rho_s}{M} \quad [\text{mol solute}/\text{m}^3 \text{ solution}] \quad [2.68]$$

According to Mersmann, the experimental diffusivity data published in the literature can be described by Stokes-Einstein's equation with a mean accuracy of $\pm 50\%$ and maximum deviation of $\pm 100\%$.

Effective volume diffusivity (Westphal and Rosenberger, 1978)

$$D_{AB,eff} = D_{AB} \cdot \frac{1 - c_w \cdot \frac{\partial \rho_l}{\partial c_c}}{1 - c_w} \approx D_{AB} \cdot \frac{1}{1 - c_w} \quad [\text{m}^2/\text{s}] \quad [2.69]$$

with

$$c_w = \frac{c_c}{\rho_l} \quad [\text{kg solute}/\text{kg solution}] \quad [2.70]$$

Due to the advective flux towards a growing crystal the mass transfer is larger than predicted if a stagnant liquid is assumed. To correct for this effect an effective diffusion coefficient must be used (Daudey, 1987).

B.4.5 SPECIFIC HEAT CAPACITY

Solid phase $((\text{NH}_4)_2\text{SO}_4)$ - (Jager, 1990):

$$c_{ps} = 1.3760 + 2.13 \cdot 10^{-2} \cdot T \quad [\text{kJ}/\text{kg} \cdot ^{\circ}\text{C}] \quad [2.71]$$

$$25^{\circ}\text{C} \leq T \leq 323^{\circ}\text{C}$$

Saturated crystal free solution $((\text{NH}_4)_2\text{SO}_4\text{-H}_2\text{O})$ - (Jager, 1990):

$$c_{pl} = 4.259 - 3.0321 \cdot c_w - 1.7668 \cdot 10^{-3} \cdot T + 4.2874 \cdot 10^{-6} \cdot T^2 \quad [\text{kJ}/\text{kg} \cdot ^{\circ}\text{C}] \quad [2.72]$$

$$25^{\circ}\text{C} \leq T \leq 323^{\circ}\text{C}$$

B.4.6 ADDITIONAL MATERIAL PROPERTIES

#	Material Properties of $(\text{NH}_4)_2\text{SO}_4$	Value	Units
1	Vickers hardness, H_v	$355 \cdot 10^6$	$[\text{N} \cdot \text{m}^{-2}]$
2	Shear modulus, μ	$8.90 \cdot 10^9$	$[\text{N} \cdot \text{m}^{-2}]$
3	Young's modulus, E	$23.4 \cdot 10^9$	$[\text{N} \cdot \text{m}^{-2}]$
4	Critical work to form visible cracks, W_c	$41 \cdot 10^{-10}$	$[\text{J}]$
5	Average atomic distance, l_0	$2 \cdot 10^{-10}$	$[\text{m}]$
6	Effective fracture surface energy, Γ/K_r	3.2^1	$[\text{J} \cdot \text{m}^{-2}]$
7	Attrition constant, C	$11.73 \cdot 10^{-6}$	$[\text{m}^3 \cdot \text{J}^{-4/3}]$
8	Minimum impact energy, $E_{p,min}$	$2.624 \cdot 10^{-10}$	$[\text{J}]$
9	Minimum attrition fragment size, L_{min}	2.411	$[\mu\text{m}]$
10	Molar mass, \tilde{M}	0.1321	$[\text{kg} \cdot \text{mol}^{-1}]$
11	Diffusivity, D_{AB} ²	$1.66 \cdot 10^{-9}$	$[\text{m}^2 \cdot \text{s}^{-1}]$
12	Effective diffusivity, $D_{AB,eff}$ ²	$3.06 \cdot 10^{-9}$	$[\text{m}^2 \cdot \text{s}^{-1}]$

¹calculated using Eq. 4.12; ²taken from Daudey (1987).

NOTE: The material properties (item # 1-5) are taken from Galn (1997 b).

C PARAMETER ESTIMATION, MODEL VALIDATION AND DESIGN OF EXPERIMENTS

C.1 PARAMETER SENSITIVITIES

Table C.1: parameter sensitivities determined for each parameter individually by means of finite differencing using dynamic simulation and adjusted for estimated relative uncertainties in the parameter values.

par.	p^0	sensitivity for $\frac{\Delta p}{p^0} = 10^{-3}$ (Eq. 6.3)	rank	estimated $\frac{\Delta p}{p^0}$	sensitivity for estimated $\frac{\Delta p}{p^0}$ (weighted sensitivity)	rank
k_r	$2.00 \cdot 10^{-5}$	0.137	5	0.10	0.014	7
Γ_S	$2.00 \cdot 10^{-4}$	0.377	3	0.10	0.038	2
W_C	$4.10 \cdot 10^{-9}$	0.073	7	0.50	0.037	4
D_{AB}	$2.50 \cdot 10^{-9}$	0.070	9	0.20	0.014	6
H	$3.55 \cdot 10^8$	0.220	4	0.50	0.110	1
ρ_S	$1.77 \cdot 10^3$	0.697	2	0.01	0.007	8
ρ_L	$1.25 \cdot 10^3$	0.116	6	0.01	0.001	10
μ	$8.90 \cdot 10^9$	0.002	11	0.20	0.000	11
$\eta_{L/S}$	$1.45 \cdot 10^{-3}$	0.048	10	0.30	0.014	5
τ_{prod}	$4.50 \cdot 10^3$	0.137	8	0.05	0.007	9
N_{imp}	$1.29 \cdot 10^1$	0.743	1	0.05	0.037	3

Table C.2: parameter cross-correlations determined via simultaneous estimation of these parameters using simulated, ideal median crystal size measurements with addition of normally distributed noise.

	k_r	Γ_S	W_C	D_{AB}	H	ρ_S	ρ_L	$\eta_{L/S}$	τ_{prod}	N_{imp}
k_r	1.00	-0.16	0.87	0.71	-0.85	0.49	***	-0.94	-0.35	-0.05
Γ_S	-0.16	1.00	-0.51	0.53	0.50	0.76	-0.70	0.55	0.98	0.96
W_C	0.87	-0.51	1.00	0.38	-0.98	0.14	***	***	-0.64	-0.35
D_{AB}	0.71	0.53	0.38	1.00	-0.44	0.95	0.60	-0.48	0.33	0.58
H	-0.85	0.50	-0.98	-0.44	1.00	-0.14	***	***	0.65	0.36
ρ_S	0.49	0.76	0.14	0.95	-0.14	1.00	0.17	-0.14	0.63	0.81
ρ_L	***	-0.70	***	0.60	***	0.17	1.00	***	***	-0.79
$\eta_{L/S}$	-0.94	0.55	***	-0.48	***	-0.14	***	1.00	0.74	0.35
τ_{prod}	-0.35	0.98	-0.64	0.33	0.65	0.63	***	0.74	1.00	0.92
N_{imp}	-0.05	0.96	-0.35	0.58	0.36	0.81	-0.79	0.35	0.92	1.00

Table C.3: parameter cross-correlations determined via simultaneous estimation of these parameters using simulated, 10, 25, 50, 75 and 90 percent quantile measurements with addition of normally distributed noise.

	k_r	Γ_S	W_C	D_{AB}	H	ρ_S	ρ_L	$\eta_{L/S}$	τ_{prod}	N_{imp}
k_r	1.00	-0.21	-0.24	0.87	0.29	0.62	0.00	0.00	-0.18	-0.18
Γ_S	-0.21	1.00	-0.06	0.30	0.12	0.63	0.00	0.00	0.40	0.47
W_C	-0.24	-0.06	1.00	-0.24	-1.00	-0.23	0.02	-0.01	-0.20	-0.33
D_{AB}	0.87	0.30	-0.24	1.00	0.33	0.93	0.00	0.00	0.03	0.06
H	0.29	0.12	-1.00	0.33	1.00	0.32	-0.02	0.01	0.22	0.34
ρ_S	0.62	0.63	-0.23	0.93	0.32	1.00	0.00	0.00	0.18	0.23
ρ_L	0.00	0.00	0.02	0.00	-0.02	0.00	1.00	***	0.00	-0.01
$\eta_{L/S}$	0.00	0.00	-0.01	0.00	0.01	0.00	***	1.00	0.00	0.00
τ_{prod}	-0.18	0.40	-0.20	0.03	0.22	0.18	0.00	0.00	1.00	0.81
N_{imp}	-0.18	0.47	-0.33	0.06	0.34	0.23	-0.01	0.00	0.81	1.00

C.2 DATA WINDOW AND INITIAL CONDITIONS

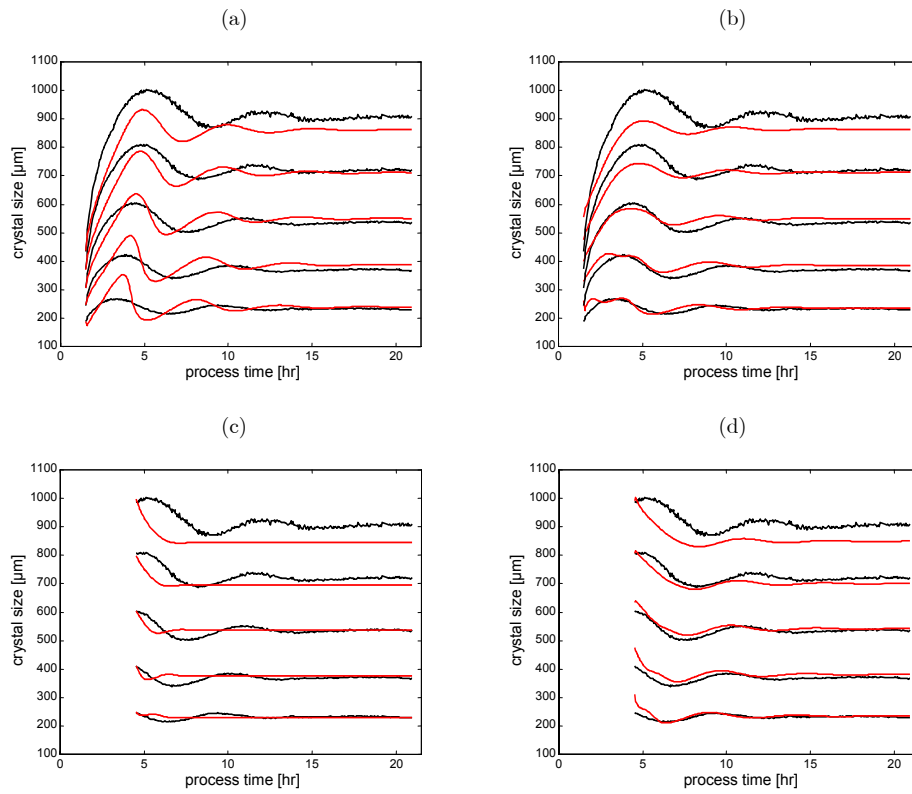


Figure C.1: Effect of data window selection and estimation of initial conditions on quality of fit for measured quantiles of DT26. Data window: (a) and (b) include first four hours of data, (c) and (d) exclude these data. Initial conditions: (a) and (c) have initial CSD estimated prior to kinetic parameters, (b) and (d) have initial CSD estimated simultaneously with kinetic parameters.

C.3 KINETIC MODELS OF OTTENS, EEK AND O MEADHRA

C.3.1 OTTENS

$$B_0(t) = p_{ott,4} \frac{N^2 \rho_s \pi}{8\tau_{circ}} \int_{L=p_{ott,3}}^{\infty} n(L,t) L^3 dL \quad [3.1]$$

$$G(t) = p_{ott,1} \left(\frac{C(t) - C_{sat}(t)}{C_{sat}(t)} \right)^{p_{ott,2}} \quad [3.2]$$

Table C.4: Overview of parameters in the kinetic model of Ottens.

$p_{ott,1}$	to be estimated	$[\text{m}\cdot\text{s}^{-1}]$	$p_{ott,3}$	to be estimated	$[\text{m}]$
$p_{ott,2}$	to be estimated	$[-]$	$p_{ott,4}$	to be estimated	$[\text{s}^2\cdot\text{kg}^{-1}]$

C.3.2 EEK

$$B_0(t) = p_{EEK,3} (C(t) - C_{sat}(t))^{p_{EEK,2}} \left(\int_{L=p_{EEK,4}}^{\infty} n(L,t) L^{p_{EEK,5}} dL \right)^{p_{EEK,1}} \quad [3.3]$$

$$G(L,t) = p_{EEK,6} (C(t) - C_{sat}(t))^{p_{EEK,7}} \left(1 - \frac{L^{p_{EEK,8}} (L_{max}^{p_{EEK,8}} + p_{EEK,9}^{p_{EEK,8}})}{L_{max}^{p_{EEK,8}} (L^{p_{EEK,8}} + p_{EEK,9}^{p_{EEK,8}})} \right) \quad [3.4]$$

Following Eek's recommendations, parameters $p_{EEK,2}$, $p_{EEK,6}$ and $p_{EEK,7}$ are not included in the parameter estimation calculations.

Table C.5: Overview of parameters in the kinetic model of Eek.

$p_{EEK,1}$	to be estimated	$[-]$	$p_{EEK,6}$	$1.0\cdot 10^{-8}$	$[\text{m}^4\cdot\text{kg}^{-1}\cdot\text{s}^{-1}]$
$p_{EEK,2}$	0.0	$[-]$	$p_{EEK,7}$	1.0	$[-]$
$p_{EEK,3}$	to be estimated	$[\text{m}^{-3}]$	$p_{EEK,8}$	to be estimated	$[-]$
$p_{EEK,4}$	to be estimated	$[\text{m}]$	$p_{EEK,9}$	to be estimated	$[\text{m}]$
$p_{EEK,5}$	to be estimated	$[-]$			

C.3.3 O MEADHRA

$$B(L,t) = \eta_{survival} H(L) \int_{L=0}^{\infty} n(L,t) G_{attr}(L,t) L^2 dL \quad [3.5]$$

$$\eta_{survival} = \max\left(0, \min\left(1, p_{mea,9} (C(t) - C_{sat}(t))\right)\right) \quad [3.6]$$

$$H(L) = \frac{\exp\left(-\frac{(L - p_{mea,10})^2}{2p_{mea,11}^2}\right)}{\int_{L=0}^{\infty} \exp\left(-\frac{(L - p_{mea,10})^2}{2p_{mea,11}^2}\right) L^3 dL} \quad [3.7]$$

$$G(L, t) = G_{kin}(L, t) - G_{attr}(L, t) \quad [3.8]$$

$$G_{kin}(L, t) = p_{mea,1} \left(\frac{C(t) - C_{sat}(t)}{C_{sat}(t)} \right)^{p_{mea,2}} \left(1 - (1 - p_{mea,3}) \exp\left(-\left(\frac{L}{p_{mea,4}}\right)^{p_{mea,5}}\right) \right) \quad [3.9]$$

$$G_{attr}(L, t) = p_{mea,6} \left(1 - \frac{1}{1 + \left(\frac{L}{p_{mea,7}}\right)^{p_{mea,8}}} \right) \quad [3.10]$$

Table C.6: Overview of parameters in the kinetic model of Ó Meadhra.

$p_{mea,1}$	to be estimated	$[\text{m}\cdot\text{s}^{-1}]$	$p_{mea,7}$	to be estimated	$[\text{m}]$
$p_{mea,2}$	to be estimated	$[-]$	$p_{mea,8}$	to be estimated	$[-]$
$p_{mea,3}$	to be estimated	$[-]$	$p_{mea,9}$	$3.5\cdot 10^{-2}$	$[\text{m}^3\cdot\text{kg}^{-1}]$
$p_{mea,4}$	to be estimated	$[\text{m}]$	$p_{mea,10}$	$2.0\cdot 10^{-5}$	$[\text{m}]$
$p_{mea,5}$	to be estimated	$[-]$	$p_{mea,11}$	$1.0\cdot 10^{-5}$	$[\text{m}]$
$p_{mea,6}$	to be estimated	$[\text{m}\cdot\text{s}^{-1}]$			

C.4 FITTING EXPERIMENTAL DATA OBTAINED FROM 22 LITRE DT CRYSTALLISER

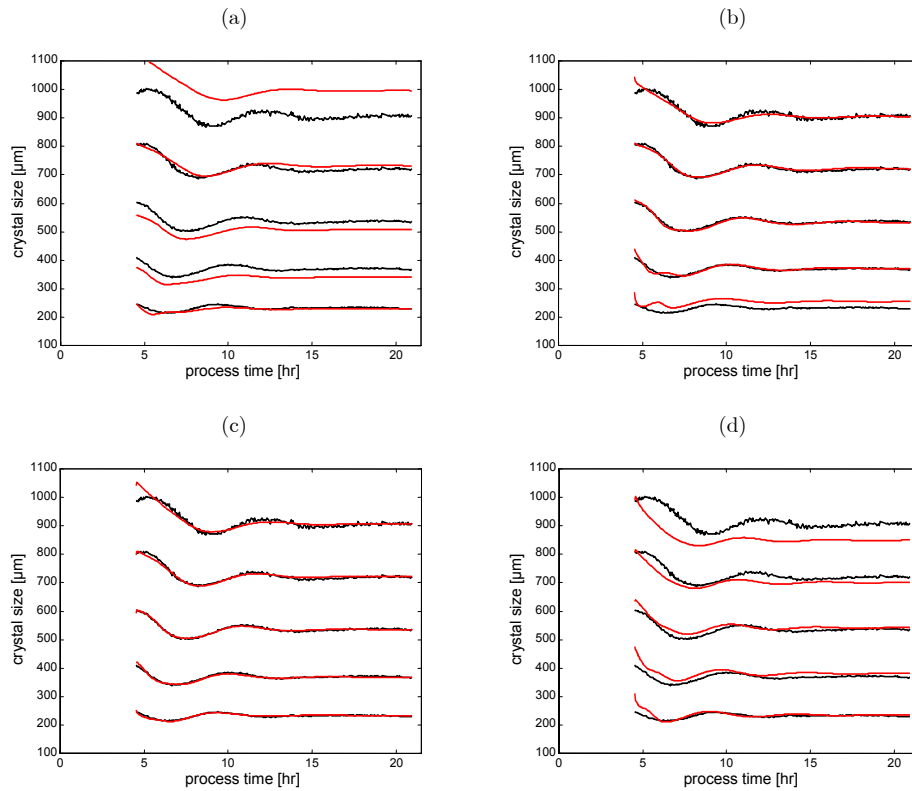


Figure C.2: Measurements versus model predictions of quantiles L_{10} , L_{25} , L_{50} , L_{75} and L_{90} using the Ottens (a), Eek (b), Meadhra (c) and Gahn (d) kinetic model for experiment DT26.

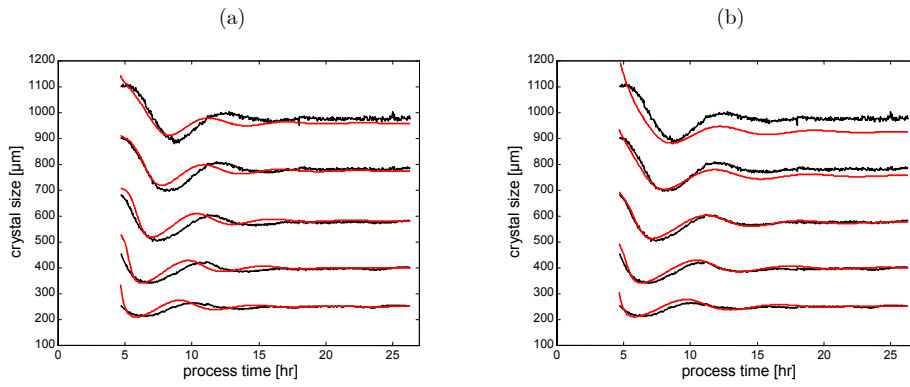


Figure C.3: Effect of product residence time on quality of fit for measured quantiles of DT25. Residence times of 4500 seconds (a) and 5898 seconds (b).

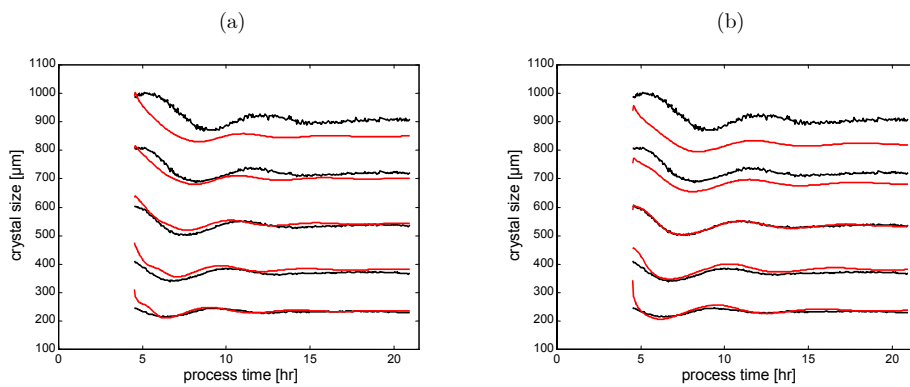


Figure C.4: Effect of product residence time on quality of fit for measured quantiles of DT26. Residence times of 4500 seconds (a) and 5909 seconds (b).

C.5 PARAMETER CROSS-CORRELATIONS

Table C.7: Correlation matrix for the Ottens kinetic parameters estimated from experiments and DT25.

	$P_{ott,1}$	$P_{ott,2}$	$P_{ott,3}$	$P_{ott,4}$
$P_{ott,1}$	1.000000	0.998774	-0.868110	-0.862176
$P_{ott,2}$	0.998774	1.000000	-0.868602	-0.863018
$P_{ott,3}$	-0.868110	-0.868602	1.000000	0.998699
$P_{ott,4}$	-0.862176	-0.863018	0.998699	1.000000

Table C.8: Correlation matrix for the Eek kinetic parameters estimated from experiments and DT25.

	$P_{eek,1}$	$P_{eek,3}$	$P_{eek,4}$	$P_{eek,5}$	$P_{eek,8}$	$P_{eek,9}$
$P_{eek,1}$	1.000000	0.035587	-0.280836	0.054038	0.002822	0.014104
$P_{eek,3}$	0.035587	1.000000	-0.841483	0.999762	0.006465	0.042824
$P_{eek,4}$	-0.280836	-0.841483	1.000000	-0.851448	0.027585	-0.046993
$P_{eek,5}$	0.054038	0.999762	-0.851448	1.000000	0.004918	0.043821
$P_{eek,8}$	0.002822	0.006465	0.027585	0.004918	1.000000	-0.893536
$P_{eek,9}$	0.014104	0.042824	-0.046993	0.043821	-0.893536	1.000000

Table C.9: Correlation matrix for the Ó Meadhra kinetic parameters estimated from experiments and DT25.

	$P_{mea,1}$	$P_{mea,2}$	$P_{mea,3}$	$P_{mea,4}$	$P_{mea,5}$	$P_{mea,6}$	$P_{mea,7}$	$P_{mea,8}$
$P_{mea,1}$	1.00000	0.99709	0.77484	-0.67947	0.58253	-0.86720	-0.50046	0.89481
$P_{mea,2}$	0.99709	1.00000	0.79701	-0.71522	0.61711	-0.87786	-0.48731	0.90630
$P_{mea,3}$	0.77484	0.79701	1.00000	-0.48627	0.94313	-0.57910	-0.05917	0.61007
$P_{mea,4}$	-0.67947	-0.71522	-0.48627	1.00000	-0.38478	0.72692	0.31876	-0.75777
$P_{mea,5}$	0.58253	0.61711	0.94313	-0.38478	1.00000	-0.38215	0.13408	0.40494
$P_{mea,6}$	-0.86720	-0.87786	-0.57910	0.72692	-0.38215	1.00000	0.79690	-0.99070
$P_{mea,7}$	-0.50046	-0.48731	-0.05917	0.31876	0.13408	0.79690	1.00000	-0.74130
$P_{mea,8}$	0.89481	0.90630	0.61007	-0.75777	0.40494	-0.99070	-0.74130	1.00000

C.6 PREDICTIVE QUALITY OF THE KINETIC MODELS

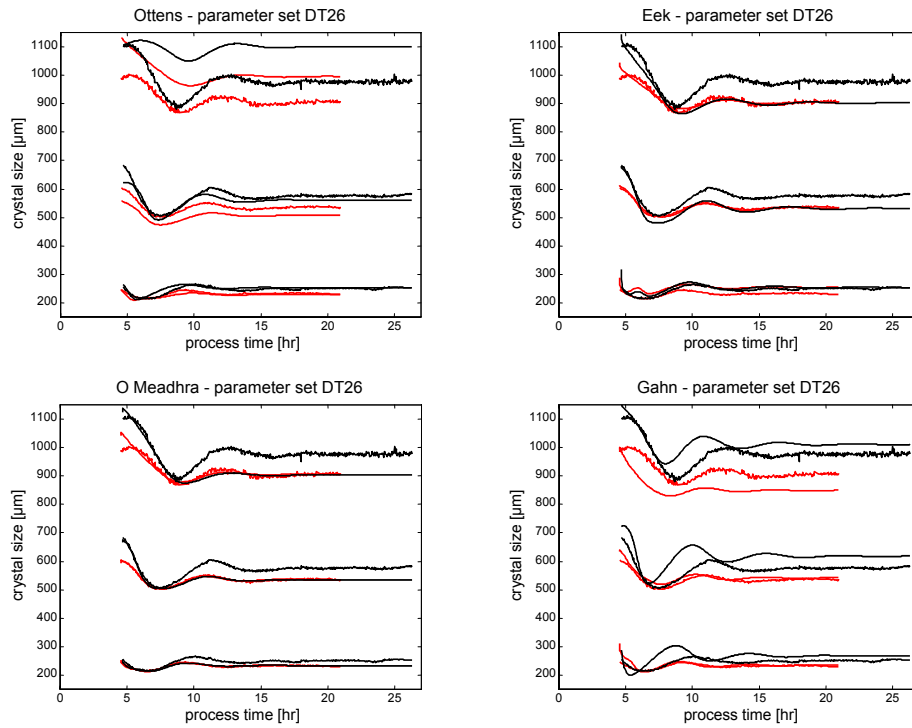


Figure C.5: Model predictions versus measurements for the L_{10} , L_{50} , and L_{90} of experiments DT25 and DT26 using kinetic parameters estimated from DT26. Note that of the two experiments DT25 has the longer duration and higher quantile values, and that the smoother trend lines constitute the model predictions.

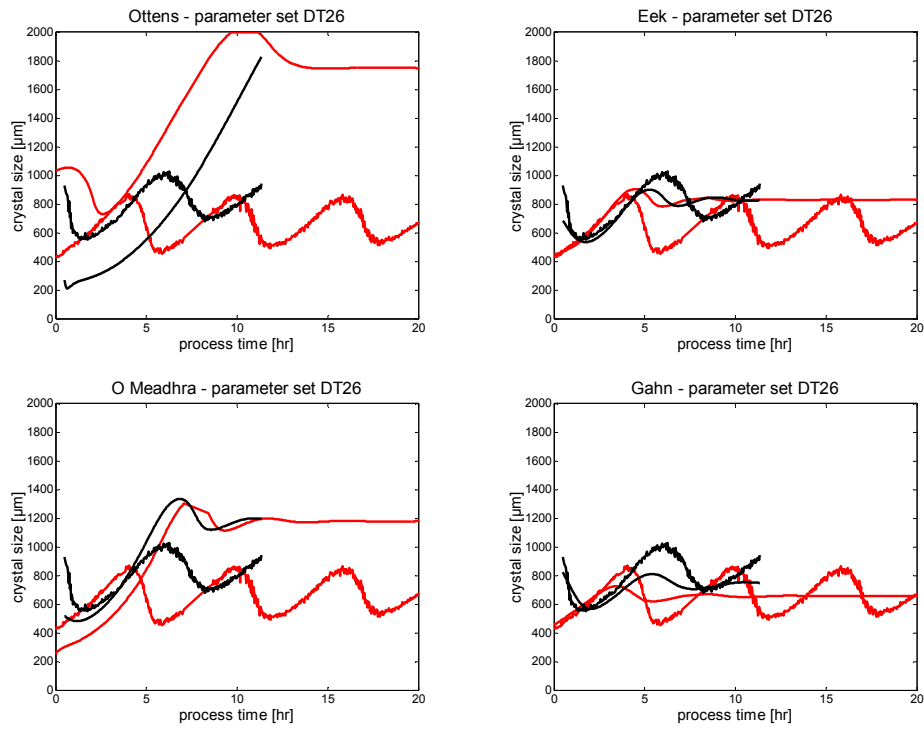


Figure C.6: Model predictions versus measurements for the median size trends of experiments DTB03 and DTB12 using kinetic parameters estimated from DT26.

Note that of the two experiments DTB03 has the longer duration and lower median sizes, and that the smoother trend lines constitute the model predictions.

C.7 DYNAMICS IN THE GAHN KINETIC MODEL

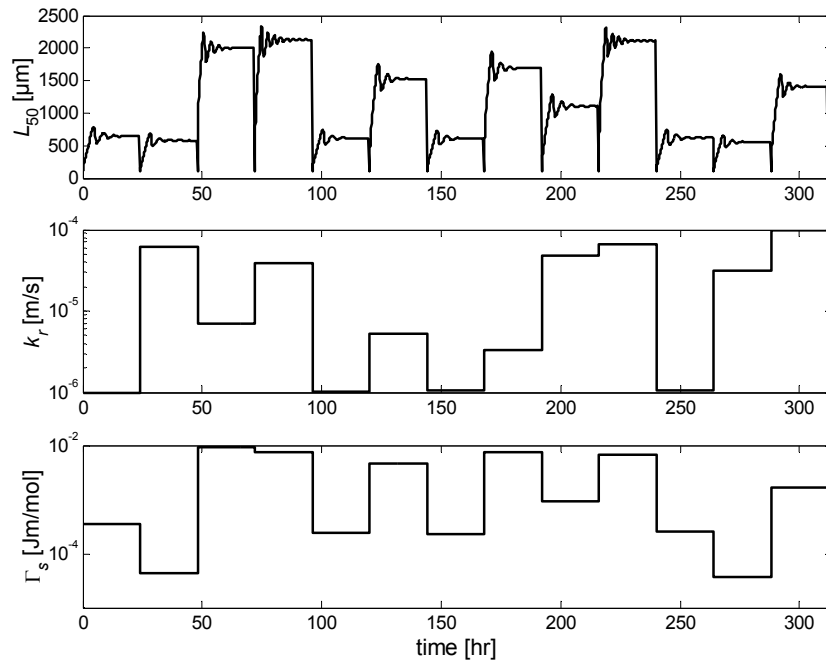


Figure C.7: Monte Carlo simulations of the 1100-litre DTB crystalliser using various random combinations of values for the two parameters of the Gahn kinetic model.

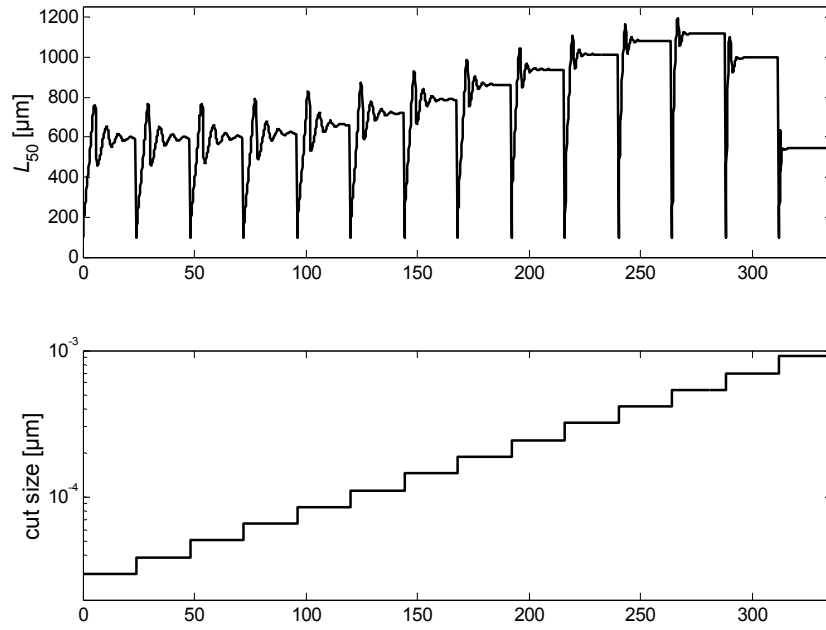


Figure C.8: Simulations of the 1100-litre DTB crystalliser using the Gahn kinetic model and various cut sizes for the fines classification function in the range of 30-1000 μm .

C.8 INFLUENCE OF MEASUREMENT SELECTION ON PARAMETER STATISTICS

Table C.10: Parameter estimation results obtained with simulated dynamic data.

measured quantities (501 sampling points)	standard deviation in k_r [m·s ⁻¹]	standard deviation in Γ_s [J·m·mol ⁻¹]	correlation factor between k_r and Γ_s	ln(det variance matrix)
$L_{10}, L_{25}, L_{50}, L_{75}, L_{90}$ and σ	2.35E-10	8.85E-10	-0.8201	-87.15
L_{50} and σ	2.91E-10	1.19E-09	-0.1809	-85.05
$L_{10}, L_{25}, L_{50}, L_{75}$ and L_{90}	3.19E-09	1.16E-08	-0.9990	-81.86
L_{10}, L_{50} and L_{90}	3.45E-09	1.26E-08	-0.9987	-81.31
L_{50}	2.53E-08	9.13E-08	-0.9999	-75.26
σ	-	-	-	-

Table C.11: Parameter estimation results obtained with simulated dynamic data including normally distributed noise.

measured quantities (501 sampling points)	standard deviation in k_r [m·s ⁻¹]	standard deviation in Γ_s [J·m·mol ⁻¹]	correlation factor between k_r and Γ_s	ln(det variance matrix)
$L_{10}, L_{25}, L_{50}, L_{75}, L_{90}$ and σ	1.69·10 ⁻⁷	5.89·10 ⁻⁷	-0.9012	-61.55
L_{50} and σ	1.90·10 ⁻⁷	7.12·10 ⁻⁷	-0.4635	-59.51
$L_{10}, L_{25}, L_{50}, L_{75}$ and L_{90}	1.70·10 ⁻⁶	5.81·10 ⁻⁶	-0.9989	-56.85
L_{10}, L_{50} and L_{90}	1.86·10 ⁻⁶	6.47·10 ⁻⁶	-0.9988	-56.28
L_{50}	1.34·10 ⁻⁵	3.70·10 ⁻⁵	-0.9998	-50.75
σ	-	-	-	-

D COMPARTMENTAL MODELLING AND OPTIMAL DESIGN

D.1 COMPARTMENTAL MODELLING

D.1.1 COMPARTMENT NUMBERING, LOCATIONS AND VOLUMES OF THE COMPARTMENTAL MODELS USED IN CHAPTER 7

Table D.1: Compartmental model according to Figure 4.2; no hold-up in annular zone; no hold-up in dissolution loop.

compartment	location*	volume	details
1	MB	V_{MB}	target for feed and fines return; source for AZ and product
2	AZ	-	source for fines dissolution loop
3	FD	-	

*MB = main body; AZ = annular zone; FD = fines dissolution loop.

Table D.2: Compartmental model according to Figure 4.2; no hold-up in annular zone; hold-up in dissolution loop.

compartment	location*	volume	details
1	MB	V_{MB}	target for feed and fines return; source for AZ and product
2	AZ	-	source for fines dissolution loop
3	FD	V_{FD}	

*MB = main body; AZ = annular zone; FD = fines dissolution loop.

Table D.3: Compartmental model according to Figure 4.2; hold-up in annular zone; hold-up in dissolution loop.

compartment	location*	volume	details
1	MB	V_{MB}	target for feed and fines return; source for AZ and product
2	AZ	V_{AZ}	source for fines dissolution loop
3	FD	V_{FD}	

*MB = main body; AZ = annular zone; FD = fines dissolution loop.

Table D.4: Compartmental model according to Figure 4.3.

compartment	location*	volume	details
1	IDT	$1/6 * V_{MB}$	
2	TZ	$1/3 * V_{MB}$	boiling zone
3	ODT	$1/6 * V_{MB}$	source for AZ and product
4	BZ	$1/3 * V_{MB}$	target for feed and fines return
5	AZ	V_{AZ}	source for fines dissolution loop
6	FD	V_{FD}	

* MB = main body; BZ = bottom zone; IDT = inside draft tube; ODT = outside draft tube; TZ = top zone; AZ = annular zone; FD = fines dissolution loop.

Table D.5: Compartmental model according to Bermingham et al. (2000).

compartment	location*	volume	details
1	BZ	$1/20 * V_{MB}$	target for feed and fines return
2	IDT	$9/80 * V_{MB}$	
3	IDT	$9/80 * V_{MB}$	
4	IDT	$9/80 * V_{MB}$	
5	IDT	$9/80 * V_{MB}$	
6	TZ	$1/20 * V_{MB}$	boiling zone
7	ODT	$9/80 * V_{MB}$	
8	ODT	$9/80 * V_{MB}$	
9	ODT	$9/80 * V_{MB}$	
10	ODT	$9/80 * V_{MB}$	source for AZ and product
11	AZ	V_{AZ}	source for fines dissolution loop
12	FD	V_{FD}	

* MB = main body; BZ = bottom zone; IDT = inside draft tube; ODT = outside draft tube; TZ = top zone; AZ = annular zone; FD = fines dissolution loop.

D.1.2 UNIAK 1100-LITRE DTB CRYSTALLISER

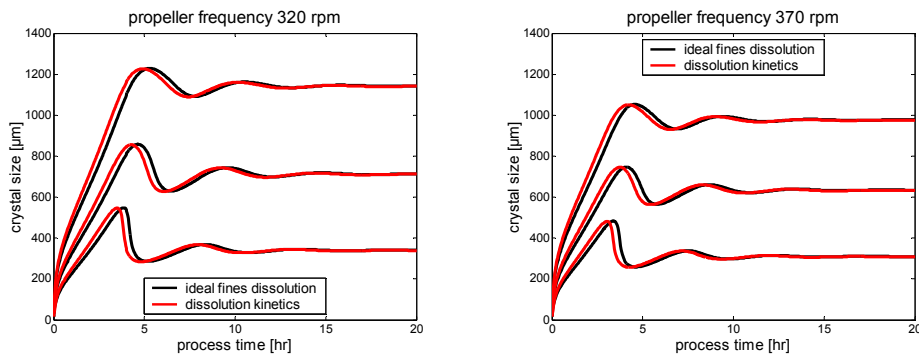


Figure D.1: 1100-litre DTB crystalliser simulations illustrating the effect on the predicted CSD transient of using real dissolution kinetics versus complete dissolution assumption.

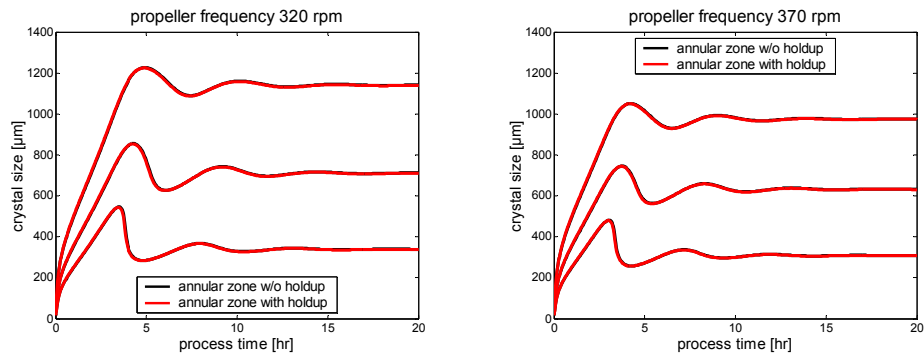


Figure D.2: 1100-litre DTB crystalliser simulations illustrating the effect on the predicted CSD transient of taking into account the hold-up of the annular zone.

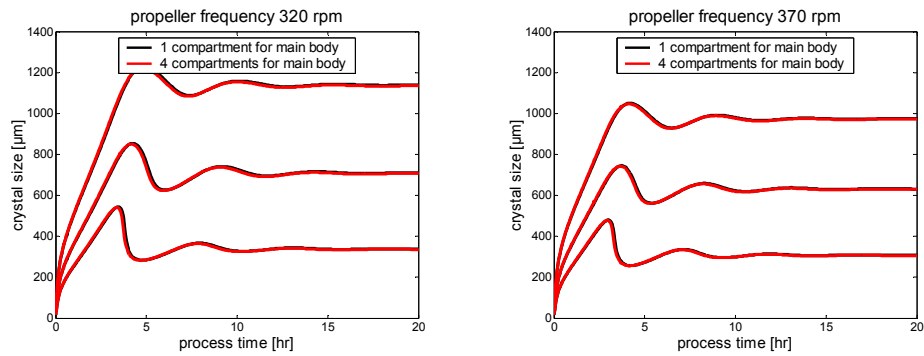


Figure D.3: 1100-litre DTB crystalliser simulations illustrating the effect of describing the main body with multiple compartments on the predicted CSD transient.

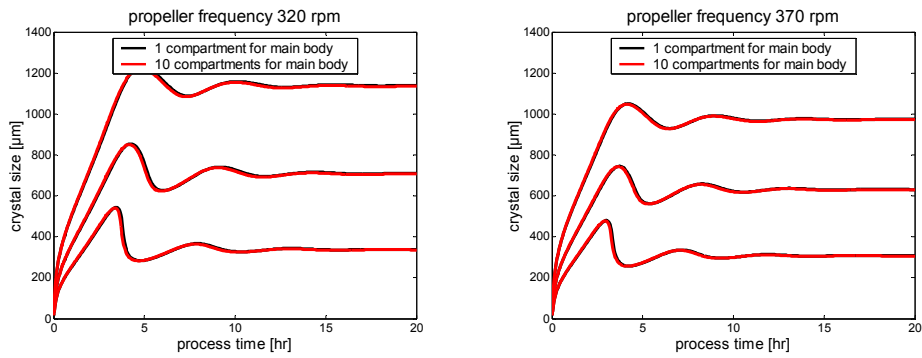


Figure D.4: 1100-litre DTB crystalliser simulations illustrating the effect of describing the main body with multiple compartments on the predicted CSD transient.

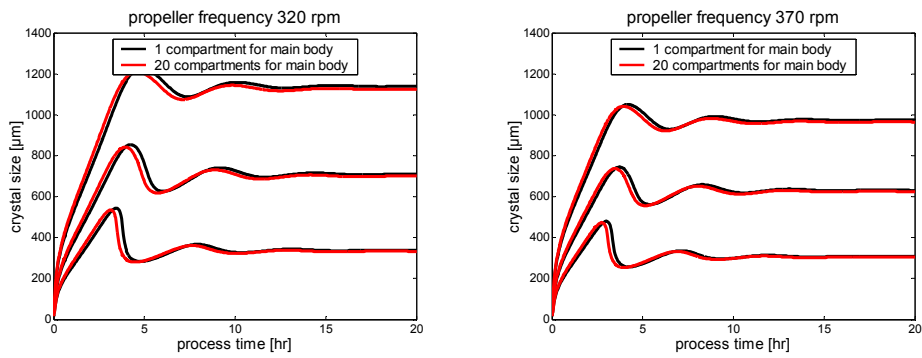


Figure D.5: 1100-litre DTB crystalliser simulations illustrating the effect of describing the main body with multiple compartments on the predicted CSD transient.

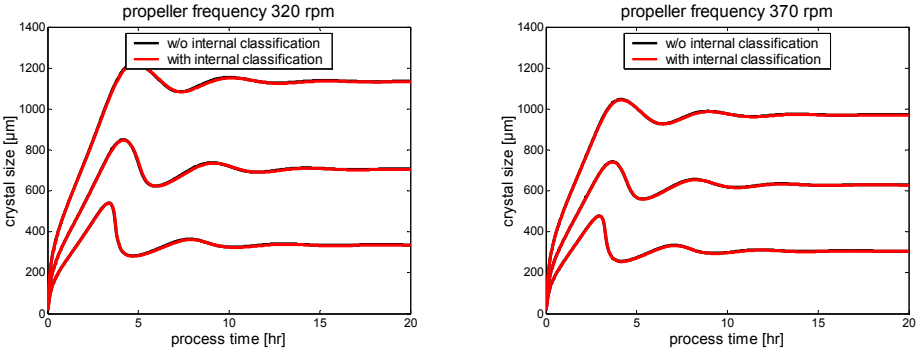


Figure D.6: 1100-litre DTB crystalliser simulations illustrating the effect of internal classification on the predicted CSD transient.

Table D.6: Selected simulation results using the compartmental model according to Figure 4.2; hold-up in annular zone; hold-up in dissolution loop.

comp	320 rpm					370 rpm				
	L_{50} [μm]	L_{90}/L_{10} [-]	σ [-]	G [$\mu\text{m}\cdot\text{s}^{-1}$]	prod [$\text{kg}\cdot\text{m}^{-3}\cdot\text{s}^{-1}$]	L_{50} [μm]	L_{90}/L_{10} [-]	σ [-]	G [$\mu\text{m}\cdot\text{s}^{-1}$]	prod [$\text{kg}\cdot\text{m}^{-3}\cdot\text{s}^{-1}$]
1	711	3.4	0.0017	0.049	0.049	631	3.2	0.0017	0.049	0.053
2	80	3.2	0.0016	0.044	0.000	77	3.1	0.0016	0.044	0.000
3	85	3.4	-0.0338	-3.125	-0.009	83	3.4	-0.0334	-3.313	-0.013

Table D.7: Selected simulation results using the compartmental model according to Figure 4.3.

comp	320 rpm					370 rpm				
	L_{50} [μm]	L_{90}/L_{10} [-]	σ [-]	G [$\mu\text{m}\cdot\text{s}^{-1}$]	prod [$\text{kg}\cdot\text{m}^{-3}\cdot\text{s}^{-1}$]	L_{50} [μm]	L_{90}/L_{10} [-]	σ [-]	G [$\mu\text{m}\cdot\text{s}^{-1}$]	prod [$\text{kg}\cdot\text{m}^{-3}\cdot\text{s}^{-1}$]
1	707	3.4	0.0015	0.038	0.034	629	3.2	0.0015	0.039	0.038
2	707	3.4	0.0020	0.061	0.064	629	3.2	0.0019	0.060	0.068
3	707	3.4	0.0019	0.058	0.061	629	3.2	0.0019	0.057	0.065
4	707	3.4	0.0015	0.037	0.036	629	3.2	0.0015	0.038	0.039
5	84	3.3	0.0017	0.048	0.000	81	3.3	0.0017	0.047	0.000
6	91	3.6	-0.0336	-3.107	-0.010	87	3.6	-0.0333	-3.297	-0.013

Table D.8: Selected simulation results using the compartmental model according to Bermingham et al. (2000).

comp	320 rpm					370 rpm				
	L_{50} [μm]	L_{90}/L_{10} [-]	σ [-]	G [$\mu\text{m}\cdot\text{s}^{-1}$]	prod [$\text{kg}\cdot\text{m}^{-3}\cdot\text{s}^{-1}$]	L_{50} [μm]	L_{90}/L_{10} [-]	σ [-]	G [$\mu\text{m}\cdot\text{s}^{-1}$]	prod [$\text{kg}\cdot\text{m}^{-3}\cdot\text{s}^{-1}$]
1	707	3.4	0.0015	0.038	0.037	629	3.2	0.0015	0.039	0.041
2	707	3.4	0.0015	0.039	0.036	629	3.2	0.0015	0.041	0.039
3	707	3.4	0.0015	0.038	0.036	629	3.2	0.0015	0.040	0.040
4	707	3.4	0.0015	0.037	0.035	629	3.2	0.0015	0.039	0.039
5	707	3.4	0.0014	0.036	0.034	629	3.2	0.0015	0.038	0.038
6	707	3.4	0.0020	0.065	0.069	629	3.2	0.0020	0.063	0.072
7	707	3.4	0.0020	0.062	0.066	629	3.2	0.0019	0.061	0.070
8	707	3.4	0.0020	0.060	0.063	629	3.2	0.0019	0.059	0.067
9	707	3.4	0.0019	0.058	0.061	629	3.2	0.0019	0.057	0.064
10	707	3.4	0.0019	0.056	0.059	629	3.2	0.0018	0.055	0.062
11	83	3.3	0.0017	0.048	0.000	80	3.2	0.0016	0.046	0.000
12	90	3.5	-0.0336	-3.111	-0.010	86	3.5	-0.0333	-3.301	-0.013

D.1.3 A 360 M³ DTB CRYSTALLISER

Note the difference in y-axis scale between Figure D.7 on the one hand and Figure D.8 through Figure D.11 on the other hand for the simulation results obtained for an axial velocity of 0.5 m·s⁻¹.

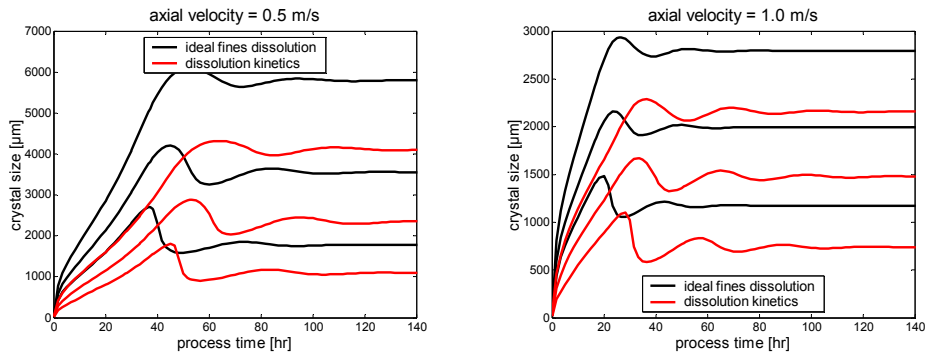


Figure D.7: 360 m³ DTB crystalliser simulations illustrating the effect on the predicted CSD transient of using real dissolution kinetics versus complete dissolution assumption.

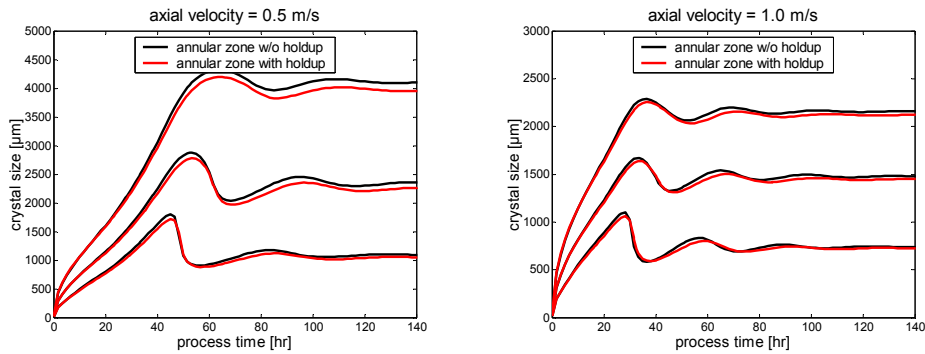


Figure D.8: 360 m³ DTB crystalliser simulations illustrating the effect on the predicted CSD transient of taking into account the hold-up of the annular zone.

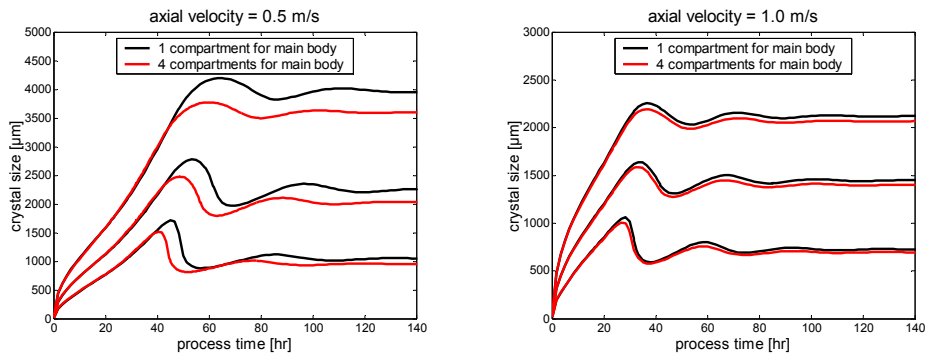


Figure D.9: 360 m³ DTB crystalliser simulations illustrating the effect of describing the main body with multiple compartments on the predicted CSD transient.

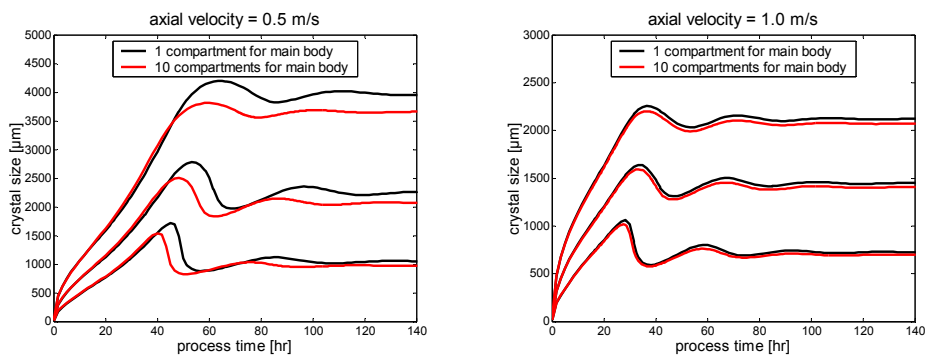


Figure D.10: 360 m³ DTB crystalliser simulations illustrating the effect of describing the main body with multiple compartments on the predicted CSD transient.

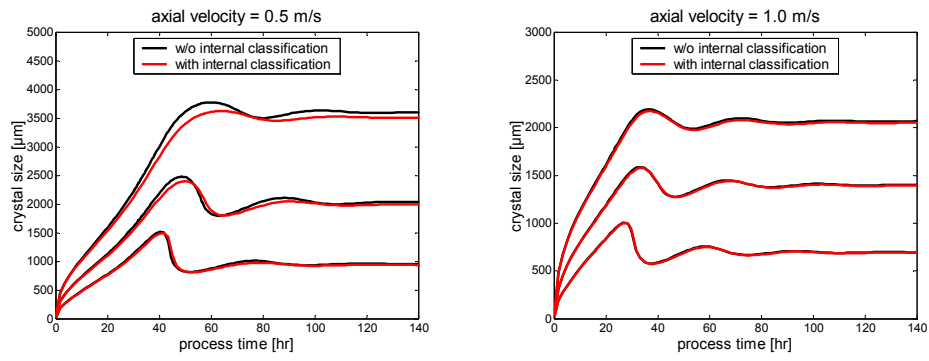


Figure D.11: 360 m³ DTB crystalliser simulations illustrating the effect of internal classification on the predicted CSD transient.

Table D.9: Selected simulation results using the compartmental model according to Figure 4.2; hold-up in annular zone; hold-up in dissolution loop.

comp	$v_{ax} = 0.5 \text{ m}\cdot\text{s}^{-1}$					$v_{ax} = 1.0 \text{ m}\cdot\text{s}^{-1}$				
	L_{50} [μm]	$L_{90}/$ L_{10} [-]	σ [-]	G [$\mu\text{m}\cdot\text{s}^{-1}$]	prod [$\text{kg}\cdot\text{m}^{-3}\cdot\text{s}^{-1}$]	L_{50} [μm]	$L_{90}/$ L_{10} [-]	σ [-]	G [$\mu\text{m}\cdot\text{s}^{-1}$]	prod [$\text{kg}\cdot\text{m}^{-3}\cdot\text{s}^{-1}$]
1	2268	3.8	0.0010	0.015	0.011	1447	2.9	0.0009	0.014	0.015
2	319	3.3	0.0010	0.013	0.000	273	4.0	0.0008	0.011	0.000
3	321	3.1	-0.0172	-0.608	-0.038	280	3.7	-0.0160	-0.785	-0.184

Table D.10: Selected simulation results using the compartmental model according to Figure 4.3.

comp	$v_{ax} = 0.5 \text{ m}\cdot\text{s}^{-1}$					$v_{ax} = 1.0 \text{ m}\cdot\text{s}^{-1}$				
	L_{50} [μm]	$L_{90}/$ L_{10} [-]	σ [-]	G [$\mu\text{m}\cdot\text{s}^{-1}$]	prod [$\text{kg}\cdot\text{m}^{-3}\cdot\text{s}^{-1}$]	L_{50} [μm]	$L_{90}/$ L_{10} [-]	σ [-]	G [$\mu\text{m}\cdot\text{s}^{-1}$]	prod [$\text{kg}\cdot\text{m}^{-3}\cdot\text{s}^{-1}$]
1	2026	3.8	0.0001	0.000	0.000	1400	3.0	0.0006	0.006	0.004
2	2027	3.8	0.0016	0.028	0.023	1400	3.0	0.0013	0.024	0.027
3	2028	3.8	0.0013	0.021	0.018	1401	3.0	0.0011	0.019	0.021
4	2027	3.8	0.0001	0.000	0.000	1401	3.0	0.0005	0.005	0.003
5	341	2.8	0.0012	0.017	0.001	281	3.6	0.0009	0.013	0.001
6	340	2.7	-0.0170	-0.601	-0.035	286	3.5	-0.0159	-0.781	-0.184

Table D.11: Selected simulation results using the compartmental model according to Bermingham et al. (2000).

comp	$v_{ax} = 0.5 \text{ m}\cdot\text{s}^{-1}$					$v_{ax} = 1.0 \text{ m}\cdot\text{s}^{-1}$				
	L_{50} [μm]	$L_{90}/$ L_{10} [-]	σ [-]	G [$\mu\text{m}\cdot\text{s}^{-1}$]	prod [$\text{kg}\cdot\text{m}^{-3}\cdot\text{s}^{-1}$]	L_{50} [μm]	$L_{90}/$ L_{10} [-]	σ [-]	G [$\mu\text{m}\cdot\text{s}^{-1}$]	prod [$\text{kg}\cdot\text{m}^{-3}\cdot\text{s}^{-1}$]
1	2063	3.8	0.0000	0.000	0.000	1405	3.0	0.0004	0.004	0.003
2	2062	3.8	0.0000	0.000	0.000	1404	3.0	0.0005	0.006	0.003
3	2062	3.8	0.0000	0.000	0.000	1404	3.0	0.0005	0.005	0.004
4	2062	3.8	0.0000	0.000	0.000	1404	3.0	0.0005	0.005	0.004
5	2062	3.8	0.0000	0.000	0.000	1404	3.0	0.0005	0.005	0.003
6	2062	3.8	0.0021	0.040	0.033	1404	3.0	0.0015	0.031	0.037
7	2062	3.8	0.0018	0.033	0.027	1404	3.0	0.0013	0.026	0.030
8	2062	3.8	0.0016	0.027	0.022	1405	3.0	0.0012	0.022	0.025
9	2062	3.8	0.0014	0.023	0.018	1405	3.0	0.0011	0.019	0.021
10	2063	3.8	0.0012	0.019	0.016	1405	3.0	0.0010	0.017	0.018
11	338	2.8	0.0011	0.016	0.000	279	3.7	0.0008	0.012	0.001
12	338	2.7	-0.0171	-0.605	-0.034	284	3.5	-0.0159	-0.783	-0.185

D.2 OBJECTIVE FUNCTION FOR OPTIMISATION

In industry, utilising an optimisation procedure will above all be aimed at finding the cheapest process with respect to design and operation, given a set process and product specifications. Economic objective functions typically consist of capital investment costs on the one hand and operating costs on the other hand. The capital investment costs include all hardware expenses:

- main body
- annular zone
- fines dissolution loop
- impeller
- vacuum system
- pumps
- internals

Note: grey items were omitted in the economic objective function

To the operating costs, the following items contribute:

- impeller duty
- pump duty
- vacuum duty
- heat duty

Note: grey items were omitted in the economic objective function

These lists are not exhaustive, but give the most important capital and operating costs. Unfortunately, it is difficult to find accurate cost references for crystallisation processes, which can be attributed to the mere fact that most crystallisation equipment is tailor-made (Perry, 1984; Bennett, 1993).

On the other hand, at a preliminary stage there is no real need to make use of an objective function that includes all equipment and operational costs. It is more important that the ratio between capital and operating costs is approximately right to give a sensible direction to the optimisation. Moreover, such an approach does not call for a detailed equipment design, which would otherwise be the case. Hence, the optimisation procedure will give trends, rather than real results. Note that the heat duty can be omitted from the objective function since it is fixed.

Of the capital costs, only the volume of the main crystalliser body is considered. Column costs are typically related to the diameter of the column. For an indication of column costs, the ratio of height over diameter (H/D) is important. This ratio is fixed at 4, the H/D ratio of the UNIAK 1100-litre crystalliser, which is used as a scaling basis for this design study. The cost of the crystalliser body was derived from prices found for distillation columns (DACE, 1995). The investment costs are written of for depreciation in a period of five years.

The following relations are used to provide a rough approximation of the total capital costs in the objective function:

$$V_{CR} = V_{MB} + V_{AZ} + V_{FD} \quad [4.1]$$

$$V_{CR} = \frac{\pi}{4} D_{CR}^2 H_{CR} = \pi D_{CR}^3 \Rightarrow D_{CR} = \sqrt[3]{\frac{V_{CR}}{\pi}} \quad [4.2]$$

$$obj_{cap} = \frac{(20.857 D_{CR}^2 - 7.7776 D_{CR} + 38.25)}{5} \quad [4.3]$$

in which $obj_{cap,CR}$ capital costs for objective function [k€·yr⁻¹]
 D_{CR} average crystalliser diameter taking into account the volume of the main body, annular zone and fines dissolution loop [m]

Of the operational costs, only the impeller and fines pump duty are taken into account. For the impeller duty a simple relation between the specific power and the axial power applies. The impeller efficiency is assumed to be 40%.

$$W_{ax} = \frac{P_{spec} \rho_{liq} V_{MB}}{\eta} \quad [4.4]$$

in which: W_{ax} = axial power [W]
 P_{spec} = specific power input [W·kg⁻¹]
 ρ_{liq} = liquid density [kg·m⁻³]
 V_{MB} = volume main body [m³]
 η = impeller efficiency [-]

The above power duties are converted to costs by multiplying with the electrical costs, which results in the operating part of the objective function (Obj_{op}):

$$obj_{op} = (W_{ax} + W_{fines}) cost_{elec} \quad [4.5]$$

in which: $cost_{elec}$ = electrical costs [k€·W⁻¹·yr⁻¹]

The complete objective function, composed of a capital and an operating part, is as follows:

$$obj = obj_{cap} + obj_{op} \quad [4.6]$$

SAMENVATTING

Dit proefschrift beschrijft de ontwikkeling en toepassing van een systematische ontwerpprocedure en voorspellende modellen gericht op zowel procesgedrag en productkwaliteit.

Het inleidende hoofdstuk behandelt allereerst de toepassing, voordelen en problemen van kristallisatieprocessen in de chemische industrie. De problemen zijn gerelateerd aan productkwaliteit en procesgedrag. Hoewel sommige problemen kunnen worden opgelost met behulp van procesregeling, zijn de meeste problemen gerelateerd aan beslissingen genomen tijdens de ontwerpfasen. Desondanks bestaat er weinig op het gebied van systematische procedures en hulpmiddelen voor het betrouwbaar ontwerpen van kristallisatieprocessen. Het doel van dit promotieonderzoek is daarom het ontwikkelen van een prototype ontwerp pakket voor kristallisatieprocessen bestaand uit een systematische procedure en hulpmiddelen. Het kader van dit onderzoek is gedefinieerd in termen van de aard van het chemisch systeem (relatief goed oplosbare stoffen), kristallisatiemethode (indirect koelen, flashkoelen en verdampen), operatiewijze (batch, semi-batch en continu), flowsheet configuratie (één- en meertraps) en kristallisorotype (geroerde tank, draft tube, draft tube baffle en forced circulation).

De relaties tussen productkwaliteit, kristallisatiemechanismen, procescondities, geometrie van de kristallisor en operatiecondities staan ter discussie in Hoofdstuk 2. Voor wat betreft productkwaliteit is er een onderscheid gemaakt tussen productgedrag en productsamenstelling. Klantenspecificaties worden over het algemeen gedefinieerd met betrekking tot productgedrag, terwijl kristallisatiemodellen productkwaliteit voorspellen in termen van productsamenstelling. Daarna volgt een overzicht van de kristallisatiemechanismen die de productsamenstelling van de kristallen bepalen. Ten slotte volgt een uiteenzetting van de voorwaarden voor een ontwerpprocedure en fenomenologische modellen die noodzakelijk worden geacht voor het betrouwbaar ontwerpen van kristallisatieprocessen die voldoen aan hun product- en procescriteria. De gevolgen van een beperkte domeinkennis, beperkte rekencapaciteit en, waarschijnlijk het belangrijkste, beperkingen van de menselijke procesontwerper, staan centraal.

Systematische ontwerpprocedures hebben als doel het verbeteren van zowel de kwaliteit van het ontwerp als van het ontwerpproces. Hoofdstuk 3 introduceert een nieuwe hiërarchische procedure voor het conceptueel ontwerpen van kristallisatieprocessen. De hiërarchie bestaat uit vier ontwerpniveaus. De eerste twee niveaus hebben voornamelijk betrekking op het productontwerp, terwijl de laatste twee ontwerpniveaus meer op procesontwerp zijn gericht. Op ieder niveau van de ontwerpprocedure wordt gekeken naar de ontwerpspecificaties, de ontwerpvariabelen en de domeinkennis nodig voor het genereren, analyseren en optimaliseren van ontwerpalternatieven. De ontwerpprocedure is geschikt voor meerdere scenario's voor wat betreft het kristallijne product (eindproduct, bijproduct of afvalproduct) en de rol van het kristallisatieproces (conversie, scheiding of zuivering).

Het genereren, evalueren en optimaliseren van ontwerpalternatieven vereist kristallisatieprocesmodellen die beschikken over een voorspellend vermogen met betrekking tot de verhoudingen tussen productkwaliteit en procesontwerp- en procesoperatievariabelen. Hoofdstuk 4 betreft de ontwikkeling van een modelleerraamwerk gericht op het snel genereren van consistente procesmodellen voor een groot bereik aan kristallisatieprocessen. Scheiding van kinetiek en hydrodynamica wordt gezien als een essentiële hoeksteen voor het ontwikkelen van voorspellende kristallisatieproces- en productmodellen. Voor deze scheiding zijn twee alternatieve modelleerbenaderingen geëvalueerd die als basis kunnen dienen van het te ontwikkelen modelleerraamwerk, te weten *compartmental modelling* en *computational fluid dynamics*. De eerste modelleerbenadering is gekozen omdat het een rigoureuzere beschrijving toelaat van de kristalgrootteverdeling (KGV of *CSD*) en de procesdynamica, ten koste van een als acceptabel beschouwd verlies in resolutie voor het beschrijven van veranderingen in de ruimtelijke dimensies. Daarna volgt de presentatie van een compartimentatieprocedure, dat wil zeggen een procedure voor het vormen van een netwerk van compartimenten dat de belangrijkste hydrodynamische kenmerken van een bepaalde kristallisator benadert. De compartimenten vertegenwoordigen volumes van de kristallisator met uniforme omstandigheden. Hetzelfde model van een enkel compartiment wordt gebruikt voor de beschrijving van alle volumes. Het hart van dit hoofdstuk behandelt de aannames, kenmerken, behoudsvergelijkingen, kinetiekvergelijkingen en sedimentatievergelijkingen van dit generieke compartimentmodel. Ten slotte wordt ingegaan op de toepassing van het ontwikkelde kristallisatieproces- en productmodelleerraamwerk op de hele reeks kristallisatieprocessen die binnen het kader van dit onderzoek liggen.

Rigoureuze kristallisatieprocesmodellen hebben over het algemeen geen analytische oplossingen. Daarom concentreert Hoofdstuk 5 zich op numerieke oplossingen voor deze modellen. Voor dit doel worden verschillende commercieel beschikbare modelleerpakketten beschouwd. Het gekozen pakket is een generiek procesmodelleerpakket dat gebruikt kan worden voor stationaire en dynamische simulaties, parameterschattingsberekeningen en optimalisaties. Hoewel dit pakket stelsels van differentiële en algebraïsche vergelijkingen tot een vooraf bepaalde precisie kan oplossen, is dit niet het geval voor partiële differentiaalvergelijkingen, zoals bijvoorbeeld de populatiebalansvergelijking, en integraalvergelijkingen zoals de berekening van momenten. Teneinde oplossingen te vinden voor dergelijke vergelijkingen, moeten ze eerst worden omgezet in eenvoudige differentiaalvergelijkingen of algebraïsche vergelijkingen. Voor deze transformatie wordt in dit onderzoek de eindigevolumemethode toegepast. De precisie van deze transformatie of benadering wordt bepaald door de discretisatiereolutie van het kristalgrootte-domein en de formulering van de populatiebalansvergelijking. Het meest geschikte discretisatietype, namelijk lineair of logaritmisch, hangt af van het toegepaste kristallisatiekinetiekmodel. Voor het kinetiekmodel van Gahn, het voor dit onderzoek meest interessante model, levert een logaritmisch kristalgroottegrid de

meest precieze resultaten voor een gegeven aantal gridpunten. Het optimale aantal gridpunten is een compromis tussen precisie en numerieke oplossnelheid. Initieel werk met het Gahn-model bracht enkele vreemde discontinuïteiten aan het licht tijdens de implementatie van conditionele vergelijkingen met betrekking tot de kristal grootte op een gediscrètiseerd domein. Het gladstrijken van deze niet fysische discontinuïteiten is essentieel voor de modelgebaseerde optimalisatieberekeningen voor ontwerp en operatie in Hoofdstuk 7.

Voordat een kristallisatieprocesmodel kan worden toegepast voor optimale ontwerpdoeleinden van een nieuw chemisch systeem, dient men eerst de waarden te schatten van de onbekende modelparameters, in het bijzonder de parameters van het kristallisatiekinetiekmodel, en in tweede instantie het model te valideren met betrekking tot het voorspellend vermogen, welk noodzakelijk is voor ontwerpdoeleinden. Dit is het onderwerp van Hoofdstuk 6. Hiertoe worden experimentele gegevens verzameld van twee types kristallisatoren met een verschillende schaal grootte, namelijk een 22-liter Draft Tube kristallisator en een 1100-liter Draft Tube Baffle kristallisator. Beide zijn continue verdampingskristallisatoren en uitgerust met *on-line* meettechnieken die de ontwikkeling tonen van de kristal grootteverdeling tijdens het opstarten en het verdere procesverloop. Het modelsysteem voor deze experimenten is de kristallisatie van ammoniumsulfaat uit water. Teneinde te voorzien in een referentiekader voor het beschrijvende en voorspellende vermogen van het kinetiekmodel van Gahn, worden de parameterschat- en validatie-exercities ook uitgevoerd met de kinetiekmodellen van Ottens, Eek en Ó Meadhra. Het model van Ó Meadhra (acht onbekende parameters) heeft het beste beschrijvende vermogen, terwijl het model van Gahn (slechts twee onbekende parameters) de beste voorspellende waarde heeft met betrekking tot zowel veranderingen in schaal en type kristallisator als roerdersnelheid. Tot slot wordt geïllustreerd hoe hetzelfde kristallisatieprocesmodel kan worden gebruikt om vooraf het nut van additionele metingen te bepalen en om experimenten te ontwerpen met een maximale hoeveelheid informatie.

In Hoofdstuk 7 wordt de gevoeligheid bepaald van het voorspelde procesgedrag en productkwaliteit voor veranderingen in de compartimentenstructuur van een kristallisator, alvorens het in dit onderzoek ontwikkelde en gevalideerde procesmodelleerraamwerk te gebruiken voor ontwerpdoeleinden. Het eerste deel van dit hoofdstuk behandelt het modelleren in compartimenten van de UNIAK 1100 liter DTB kristallisator en de 360 m³ DTB kristallisator. Hiertoe worden de verschillende compartimentstructuren uit Hoofdstuk 4 gebruikt. De simulaties met deze verschillende structuren geven algemene indicaties over het belang van (i) het gebruik van een kinetiekmodel voor het oplossen van kristallen in tegenstelling tot de aanname van volledige oplossing voor het kiemvernietigingssysteem van een DTB kristallisator, (ii) het in acht nemen van de *hold-up* van de annulaire zone, (iii) het indelen in compartimenten van het kristallisatorlichaam, en (iv) het modelleren van interne classificatie. De resultaten van deze simulaties dienen dan ook ter validatie van de compartimentstructuren, gebruikt voor de beschrijving

van de 22-liter DT en de 1100-liter DTB kristallisator voor het parameterschatten en de modelvalidatie in Hoofdstuk 6. Het tweede deel van Hoofdstuk 7 beschouwt het genereren van optimale kristallisatorontwerpen. Hiertoe worden standaard rekenkundige optimalisatietechnieken gebruikt die ruimte laten voor een flexibele formulering van randvoorwaarden en een doelfunctie. Het probleem dat hier wordt bestudeerd is het ontwerp van één of meer DTB kristallisatoren voor het kristalliseren van ammoniumsulfaat uit water met een gezamenlijke productiecapaciteit van 94 kton-jaar⁻¹. Om dit probleem op te lossen met behulp van het ontwikkelde modelleerraamwerk, zijn er vijf vrijheidsgraden, vijf randvoorwaarden en een economische doelfunctie geformuleerd. De randvoorwaarden zijn zowel productkwaliteit als operationeel gerelateerd en de vrijheidsgraden hebben betrekking op zowel ontwerpaspecten als operationele aspecten.

In het laatste hoofdstuk van dit proefschrift worden perspectieven geboden voor het gebruik van de resultaten van dit onderzoek en aanbevelingen gedaan voor verder onderzoek.

ACKNOWLEDGMENTS

A great number of people have contributed to the completion of my thesis, some with respect to the contents, some by making life more enjoyable at and away from university and a few in both respects. Avoiding the risk of being sued for emotional damage, I will refrain from categorising anyone mentioned in this acknowledgement.

Let me start with my extensive team of advisors, who, with their different areas of expertise, provided me insight in many new topics and steered this research in various directions, while allowing me the freedom to pursue my own interests. Balancing all these interests proved to be one of the biggest challenges of this project, and some may quite rightly wonder whether I did cope, considering the duration of this thesis work. Firstly, I would like to thank Johan Grievink, who initiated my quest for a PhD by suggesting a ‘design’ research position with the UNIAK crystallisation project, when I visited him for a second opinion on a position at a research institute in France. Johan, thank you also for showing me how to link conceptual thinking to hard mathematical formulations and for serving excellent tea (loose tea leaves, no tea bags!). Secondly, Herman Kramer, my 24/7 supervisor and friend, his knowledge of and enthusiasm for crystallisation research has proven an invaluable contribution to this research. Herman, apart from our lengthy technical discussions, I also enjoyed the fruitless and even lengthier discussions about the French and the English. Thirdly, Peter Verheijen, who provided a lot of input for the modelling work in general and parameter estimation in particular. I especially appreciated your pro-active contact after I had moved to London, which always helped me speed up my thesis work. Finally, Gerda van Rosmalen, who not only taught me some of her extensive knowledge on crystallisation, but also gave me the opportunity to develop and teach material for the postgraduate training course on industrial crystallisation.

I would now like to move on to my colleagues at the Process Systems Engineering group (PSE). During my PhD study the composition of the PSE group changed dramatically and rather suddenly. Before 1997 we had a relatively small group consisting of among others Monique, Peter, Folmer, Bertjan, Jan and Jos. Folmer and I collaborated on a number of interesting topics ranging from uncertainty analysis to an extension of Douglas’ hierarchical design procedure to explicitly incorporate decisions relating to social and environmental ethics. More importantly, Folmer, I enjoyed the various meals we shared, (Krashna) concerts we attended and parties we visited. Thanks! In and after 1997 most of the initial group left and a whole batch of new PhD students (Andreas, Gijsbert, Michiel, Michiel, Pieter and Wouter) arrived as well as Panos, our first postdoc, a Greek from Canada. This slightly larger group was socially very active with large lunch sessions usually involving hefty discussions, the odd sailing trip here and there, dinners to mark the start of each season where the table arrangements changed for each course based on randomly generated Matlab output. Most of these activities also involved a close group of MSc students (Bas, Denes, Jantien,

Judith, Maurice, ...). Bas and Maurice both performed valuable research that respectively ended up in my thesis and a publication. Many thanks for that work! I also performed some interesting research with Andreas ten Cate on compartmental modelling, which found its way into Chapter 7. Above all, Andreas, thanks for being a true friend and introducing me to Funkadelic et al. Finally, I would also like to thank Aat, Caroline, Cees, Henk and other PSE staff members for an enjoyable time in the PSE group.

During my PhD I was in the fortunate position of having two offices, one at PSE and the other one at the Laboratory for Process Equipment (LPE or *API* in Dutch). It is at *API* that I spent most of my time, as this is where the experimental facilities of the UNIAK project were located. Many days and nights were spent here with fellow project members to gather the experimental data required by the various PhD students and postdocs (Andreas, Bronwen, Gerrit, Joost, Maarten and myself) of the UNIAK project. Andreas was the first to join the project and although he had the most extensive experimental programme, the effort he invested to get the crystallisers up and running was extraordinary. Andreas, thanks for your determination and friendship (I really miss the second hand stuff you always tried and often managed to flog me, although I have met a German with similar skills in London). Maarten joined as number four and became my roommate at *API*, which turned out to be a great partnership. Not only are you a dedicated tea drinker, you are also one of the funniest storytellers I know! Thanks for keeping up the friendship since we left and your help on gjoin. Bronwen, you were only with the UNIAK project for a year as a postdoc, but it was a great year in which you and Mitch became some of Jilda's and my best friends. Having visited you in South Africa, we look forward to seeing you in Oz. Gerrit, you did an entire PhD, but didn't seem to be around much longer than Bronwen. Congratulations and thanks for being the first person to apply the design procedure presented in this thesis! A significant part of the results and atmosphere at *API* was created by the MSc students. Bart (my first MSc student and the first to write a gPROMS crystalliser model in Delft), Bing (Smashing Pumpkins), Gerben (Linvision and Lowlands), Jelte (loads of classified experiments), Joppe (knows Gahn inside out), Jos (FC and skate freak), Palmiro (Italian control freak), Reinier (master of the downloads), Sander (maniac driver), Sandra (thanks for the writing tip, it worked), etc. Thanks for all your work and creating a good atmosphere (Kamer 1, UNIAK T-shirts, carting, downloads, pizzas, etc.). Finally, I would like to thank our plant managers, Harmen and Bas, André, Paul, Theo, Jan and other members of the mechanical and electrical workshops for their support and for making *API* an enjoyable place to work.

Being keen on travelling, I was fortunate to have a few collaborations with researchers outside Delft. Firstly, the co-operation with Achim Gerstlauer, Aleksander Mitrovic and Stefan Motz of the University of Stuttgart, which greatly improved our numerical solution of the population balance equation. Secondly, Costas Pantelides of the Centre for Process Systems Engineering at Imperial College, who helped improve the implementation of the Gahn kinetic model,

which led to a one order increase in simulation speed. Finally, Steven Asprey and Bing Chen, also from the Centre at IC, and Irene Bauer of PSE Ltd, who independently demonstrated the practical feasibility of using the crystallisation models developed in Delft for experiment design purposes.

Before switching to those who made life away from university so much fun, I would like to thank the industrial partners of the UNIAK project (Akzo Nobel, BASF, Bayer, Dow, DSM, DuPont and Purac Biochem), who contributed both financially and scientifically. The input received during the six-monthly progress meetings and the various company visits has had a significant impact on the contents of this thesis.

One of the reasons I never had one of those infamous ‘promotie-dipje’ were the many distractions provided by friends: the ‘delftseonzin’ or Lowlands group with many friends from my earlier student days (Dinand, Frank, Gijs, Jeroen, ...), Allard and my housemates of the Smitsteeg. Claartje, Kelly, Niels and Jonts thanks for the good food, reasonable wine and bad (but oh so enjoyable) TV we enjoyed together. Also a big thank you to Christian and Peter for providing ample distraction in London.

Femke and Arthur, not only thanks for being such good friends, but also for facing the assault with me as my paronymphs. Femke, many thanks for putting me up so frequently for a few nights and being such a caring host on all my visits to Delft over the last two years.

I would also like to acknowledge the continued support and interest shown by my parents. In particular, I appreciate the fact that there was no nagging about completion dates, but that you have checked your holiday dates for the last three years to ensure you would not miss the defence of this thesis.

Of course, the biggest thank you by far goes to Jilda, who has read my entire thesis, shown extreme patience and has always ensured I led a healthy social life in between *work* work and *thesis* work. I look forward to being able to give you more of my time and more space in the house.

Apologies to anyone I may have forgotten.

Sean

London, February 2003

*He who hurries has one foot in the grave
(Moroccan saying)*

CURRICULUM VITAE

Sean Bermingham was born on 31 August 1970 in Terneuzen.

1982-1988	VWO, R.S.G. Petrus Hondius, Terneuzen
1988-1989	Industrial Design, Delft University of Technology
1989-1995	Chemical Engineering, Delft University of Technology
1995-2000	PhD with the Process Systems Engineering group and the Laboratory for Process Equipment, Delft University of Technology
2000-2001	Process modelling consultant, Process Systems Enterprise Ltd
2001-present	Consulting group manager, Process Systems Enterprise Ltd